



Universitat Autònoma de Barcelona

ADVERTIMENT. L'accés als continguts d'aquesta tesi queda condicionat a l'acceptació de les condicions d'ús establertes per la següent llicència Creative Commons:  http://cat.creativecommons.org/?page_id=184

ADVERTENCIA. El acceso a los contenidos de esta tesis queda condicionado a la aceptación de las condiciones de uso establecidas por la siguiente licencia Creative Commons:  <http://es.creativecommons.org/blog/licencias/>

WARNING. The access to the contents of this doctoral thesis it is limited to the acceptance of the use conditions set by the following Creative Commons license:  <https://creativecommons.org/licenses/?lang=en>

Universitat Autònoma de Barcelona



**Universitat Autònoma
de Barcelona**

1240 – Programa de Doctorat en Física
Physics Department

Doctoral Dissertation

Qualification of an X-ray Unit for Dosimetrical Application

PhD Candidate: Matteo Treccani

Supervisor: Prof. Carles Domingo Miralles
Dr. Roberto Bedogni

Thesis deposit year: 2019

A Mariele

Index

English abstract	15
Spanish (Castellano) abstract	17
<i>Part I – Introduction</i>	20
1. X-RAYS PRODUCTION	21
1.1 X-ray tube: structure and operating principle.....	21
1.2 X-ray tube spectra	25
2. RADIATION PROTECTION QUANTITIES	31
2.1 Dosimetry	31
2.2 Limiting quantities.....	38
2.3 Operational quantities.....	40
2.4 Calibration principle	44
2.5 New ICRU approach on operational quantities.....	44
3 THE X-RAY IRRADIATION FACILITY: description of the experimental setup	47
3.1 Description of the laboratory	47
3.2 The irradiation room.....	49
3.3 Radiological safety system.....	78
<i>Part II – The complete qualification and characterisation of the X-ray irradiation unit</i>	80
4 MONITOR ION CHAMBER	81
5 FOCUS REGRESSION	85
6 HALF VALUES LAYERS EVALUATION	87
6.1 HVL evaluation procedure	87
6.2 PTW HVLs measurements	88
6.3 Example of the procedure for determining the additional filtration	93
6.4 2 nd HVL and homogeneity coefficient.....	94
7 FIELD UNIFORMITY MEASUREMENTS	95
7.1 Gafchromic measurements	96
7.2 Silicon detector measurements.....	99
7.3 Silicon and Gafchromic comparison	102
7.4 Concluding remarks about X-ray field uniformity	104

8	N-SERIES SPECTRAL MEASUREMENTS.....	107
8.1	Silicon detector calibration.....	107
8.2	Si N-series experimental spectra	113
8.3	CdTe calibration.....	117
8.4	CdTe N-series experimental spectra.....	125
8.5	Concluding remarks about spectral measurements.....	129
<i>Part III – R&D on a need for operational dosimetry.....</i>		<i>134</i>
9	EYE LENS DOSIMETRY	135
9.1	Introduction: why is the eye lens dose monitoring important?.....	135
9.2	Choice of the operational quantity to monitor eye lens exposures.....	138
9.3	Calibration and type testing for a dosimeter to measure $H_p(3)$	140
9.4	Wearing conditions and state of art.....	143
9.5	Design a dosimeter for monitoring $H_p(3)$	145
9.6	Eye lens dosimeter prototype based on active detector	145
9.7	Concluding remarks about energy and angular response of the prototype.....	155
10	APPENDIX.....	159
10.1	RTC 1000 HS 0.6/1.2 X-ray tube	159
10.2	TZM properties	162
10.3	C100 CT tube assembly.....	163
10.4	PTW ionization chamber	166
10.5	PTW calibration certificate	171
10.6	MPXAZ4115A pressure sensor	173
10.7	TSic 301/306 temperature sensor.....	175
10.8	Hamamatsu s3590-09.....	177
10.9	CdTe detector	180
10.10	PR16-H preamplifier	182
10.11	CREMAT CR-110 charge sensitive preamplifier	184
10.12	CREMAT CR-200 gaussian shaping amplifier	185
10.13	ImageJ macro for the coloured uniformity map	186
10.14	Voltage divider.....	192
10.15	Monitor ion chamber operating point measurements	195
Conclusions.....		198

Bibliography..... 200
Ringraziamenti..... 205

Index of Figures

<p>Figure 1.1 - (a) Schematic diagram of X-ray tube and circuit. (b) Tube current as a function of tube voltage. Curves 1 and 2, Siemens B150 RGS tube. Curve 3, typical data for tube operating at a lower current (Johns e Cunningham s.d.).....</p>	<p>21</p>
<p>Figure 1.2 - (On the left) Rotating anode tube, adapted from diagram by Philips. (On the right) Rotating targets damaged by excessive loading or improper rotation of the target. A: target cracked by lack of rotation. B: target damaged by slow rotation and excessive loading. C: target damaged by slow rotation (Johns e Cunningham s.d.).....</p>	<p>23</p>
<p>Figure 1.3 - Illustration of the line-focus principle, which reduces the apparent size of the focal spot (J. T. Bushberg 2012).</p>	<p>23</p>
<p>Figure 1.4 - On the left: a dual-focus X-ray tube with a rotating anode. Picture of an X-ray tube insert and partially cut-away housing, shows the various components of the X-ray tube. On the right: cathode assembly of a dual-focus X-ray tube. The small filament provides a smaller focal spot and a radiograph with greater detail, provided that the patient does not move. The larger filament is used for high-intensity exposures of short duration (J. T. Bushberg 2012).</p>	<p>24</p>
<p>Figure 1.5 - The focusing cup shapes the electron distribution when it is at the same voltage as the filament (left). Isolation of the focusing cup from the filament and application of a negative bias voltage (-100 V) reduces electron distribution further by increasing the repelling electric fields surrounding the filament and modifying the electron trajectories (middle). At the top are typical electron distributions incident on the target anode (the focal spot) for the unbiased and biased focusing cups. Application of -4000 V on an as a grid biased or grid pulsed tube (right) (J. T. Bushberg 2012).</p>	<p>24</p>
<p>Figure 1.6 - The X-ray tube collimator assembly is attached to the housing at the tube port, typically on a collar that allows it to be rotated. A light source, positioned at a virtual focal spot location, illuminates the field from a 45° angle mirror. Lead collimator blades define both the X-ray and light fields (J. T. Bushberg 2012).</p>	<p>25</p>
<p>Figure 1.7 - Emission spectrum for a tungsten target X-ray tube operated at 100 kVp. K-characteristic X-ray emission occurs for tungsten whenever the tube voltage exceeds 69 keV, the K-shell binding energy for tungsten. The dotted line represents the theoretical bremsstrahlung emission from a tungsten target. The solid line represents the spectrum after self-, inherent, and added filtration. The area under the spectrum represents the total number of X-rays (J. T. Bushberg 2012).</p>	<p>26</p>
<p>Figure 1.8 - (On the left) Bremsstrahlung radiation arises from energetic electron interactions with an atomic nucleus of the target material. In a “close” approach, the positive nucleus attracts the negative electron, causing deceleration and redirection, resulting in a loss of kinetic energy that is converted to an X-ray. The X-ray energy depends on the interaction distance between the electron and the nucleus; it decreases as the distance increases. (On the right) Generation of a characteristic X-ray in a target atom occurs in the following sequence: (1) the incident electron interacts with the K-shell electron via a repulsive electrical force. (2) The K-shell electron is removed (only if the energy of the incident electron is greater than the K-shell binding energy), leaving a vacancy in the K-shell. (3) An electron from the adjacent L-shell (or possibly a different shell) fills the vacancy. (4) A K_{α} characteristic X-ray photon is emitted with energy equal to the difference between the binding energies of the two shells. In this case, a 59.3 keV photon is emitted (J. T. Bushberg 2012).</p>	<p>26</p>

Figure 1.9 - The filtered spectrum of bremsstrahlung and characteristic radiation from a tungsten target with a potential difference of 90 kV illustrates specific characteristic radiation energies from K_{α} and K_{β} transition (J. T. Bushberg 2012).....	27
Figure 1.10 - The heel effect is a loss of intensity on the anode side of the X-ray field of view. It is caused by attenuation of the X-ray beam by the anode. Upper right is an expanded view that shows electrons interacting at depth within the anode and the resultant “self attenuation” of produced X-rays that have a trajectory towards the anode side of the field (J. T. Bushberg 2012).	29
Figure 1.11 - Heel effect is usually exploited in mammography where there is need to penetrate different tissue thicknesses (Radiology C. - Mammography 2019).	30
Figure 2.1 - Relationship between physical protection and operational quantities (IAEA 2000).....	31
Figure 2.2 - Collision kerma and absorbed dose as a function of depth in a medium, irradiated by a high-energy photon beam for (a) the hypothetical case of no photon attenuation or scattering and for (b) the realistic case (J.P. Seuntjens n.d.).	37
Figure 2.3 - Radiation weighting factor for neutrons versus neutron energy (ICRP 103 2007).....	39
Figure 2.4 - Actual, expanded and aligned radiation field (Kutkov 2018).	42
Figure 2.5 - Diagram of an expanded (a) and an oriented (b) radiation field (Kutkov 2018).....	42
Figure 2.6 - Comparison of skin absorbed dose conversion coefficients for the male phantom for antero-posterior geometry as calculated for ICRP Publication 116 (ICRP publication 116 2010) and those of ICRP Publication 74 (ICRP publication 74 1995).	45
Figure 2.7 - Comparison of the breast absorbed dose conversion coefficients of the female phantom for antero-posterior geometry as calculated for ICRP Publication 116 (ICRP publication 116 2010) and those of ICRP Publication 74 (ICRP 74 1996).	46
Figure 3.1 - Work in progress in the irradiation room: assembling and setting up the X-ray irradiation unit. .	47
Figure 3.2 - Control room and experimental hall schematic view from above. The light blue walls are the external walls of the ASI building; the yellow ones are the walls that delimit the rooms and the blue ones are lead walls placed for staff radioprotection. The numbers are the walls identification names.	48
Figure 3.3 - Photograph of the control room (on the top), control console (bottom right) and device for the X-ray tube ignition (bottom left). On the latter, it has been placed a passive dosimeter for the necessary radioprotection tests.	48
Figure 3.4 - Complete vision of the experimental hall. X-ray tube with the additional lead shielding (blue walls in Figure 3.2), collimator, monitor chamber support, metal filters, mechanical bench, a cart with PTW chamber, NI DAQ.....	50
Figure 3.5 - The collimator and support for the monitor ionization chamber.....	50
Figure 3.6 - CAD Project of the mechanical bench, the right side is the X-ray tube side.....	51
Figure 3.7 - Trolley and supports projects for a slim stem ionization chamber. The left image shows the support mounting along the mechanical bench while the right one shows the detail of a holder indent for positioning the detector stem.....	51
Figure 3.8 - X-ray tube without additional filters on. This picture allows to see the alignment.....	52

Figure 3.9 - Self-levelling red cross line laser used to align some devices to the X-ray field centre.....	52
Figure 3.10 - Scheme of the RTC 1000 HS X-ray tube. On the right side there is the cathode and on the left the rotating anode which slanting angle is emphasized in the scheme. Here the black spot is the focal spot (IAE X-ray tubes RTC000 2019).....	53
Figure 3.11 - Photo of the RTC 1000 HS X-ray tube. On the right side there is the cathode and on the left the rotating anode (IAE X-ray tubes RTC000 2019).....	54
Figure 3.12 - X-ray tube filaments and optical projection on the anode. (Compare the cathode assembly to the scheme in Figure 1.4).	54
Figure 3.13 - X-ray unit and PTW ionization chamber placed along the mechanical bench thanks to a cart...	56
Figure 3.14 - Inner part of the monitor chamber (left): the conductive plastic has been glued to the plastic shell and the electrodes were cabled by a welding on a small Cu coating. On the right, an example of the used coaxial cable with central conductor (D), dielectric insulator (C), braided shield (B) and external insulator (A). The end of the braided shield has been twisted and welded to use it as a standard cable.....	57
Figure 3.15 - Inner view of the monitor chamber with the external Cu layer.	57
Figure 3.16 - Cabled monitor chamber with in addition the green cable ground contact. On the right, there is a scheme of the metal box which contains the end of the monitor chamber coaxial cable and allow to separate the collecting central conductor from the high voltage braided shield and direct them, through two BNC connectors, respectively to the DAQ and high voltage supply.	58
Figure 3.17 - PTW ionization chamber scheme (Appendix 10.4).	58
Figure 3.18 – PTW 1l 32002 ionization chamber for air kerma measurements.....	59
Figure 3.19 - Energy dependence of PTW chamber of type 32002 (Appendix 10.4).....	59
Figure 3.20 - Hamamatsu silicon detector. Dimensions are in mm (Appendix 10.8).	60
Figure 3.21 - CdTe planar spectrometer with BNC housing.	61
Figure 3.22 - (a) Depletion approximation, which ignores any contribution to the space charge from free electrons and holes, for an abrupt PN junction: doping levels (on the left) and resulting mobile carrier concentrations within the depletion approximation (right). (b) Charge density for the step PN junction under the depletion approximation. (c) Electric field across step PN junction for charge distribution in b. (d) Electric potential variation across PN junction for field in c-image (Papadopoulos 2014).....	61
Figure 3.23 - PN junction device structure and biasing configuration (Papadopoulos 2014).	62
Figure 3.24 - Effect of applied bias on PN junction (with similar doping levels on either side). In thermal equilibrium the Fermi level is constant across the entire structure and the built-in electric field opposes the diffusion of carriers across the junction. The applied bias is assumed to drop almost entirely across the depletion layer and thus the Fermi level becomes separated by qV_a . Forward bias reduces the built-in electric field and thus the built-in potential barrier is reduced by V_a as shown. Reverse bias on the other hand increases the built-in electric field and the built-in potential is increased by V_a	62
Figure 3.25- Long-base diode under forward bias: excess minority hole concentration vs. distance (Papadopoulos 2014).	63

Figure 3.26 - Short-base diode excess hole carrier distribution in N region under forward bias (Papadopoulos 2014).	64
Figure 3.27 - Current-Voltage reverse voltage characteristic of the Hamamatsu detector. The graph shows the very low dark current of this detector: when biased, about few nA.	65
Figure 3.28 - Experimental setup of the electrical testing workstation. Voltage generator, Keithley model 6485 picoammeter, Hewlett-Packard 4263A LCR meter and metal box for the assembly of the dut.	68
Figure 3.29 - Schematic depiction of circuit for measurement with LCR meter.	68
Figure 3.30 - Capacitance-Voltage characteristic of the Hamamatsu detector until overbiasing condition (100 V is the upper limit suggested for the working voltage range).	69
Figure 3.31 - Depletion layer thickness of the Hamamatsu detector. This experimental test shows excellent agreement with the datasheet thickness value (0.3mm – Appendix 10.8).	70
Figure 3.32 - $1/C^2$ versus reverse voltage for Hamamatsu detector.	71
Figure 3.33 - Electronic spectroscopy chain scheme. The detector is depicted as a time dependent generator with its specific capacitive and resistive contributions. The charge preamplifier shows an amplification -A since the input is the inverting input and the configuration has a negative feedback for stability reasons. The shaper is an analogic filter for nuclear spectrometry (Bessel, Butterworth etc.).	72
Figure 3.34 - Transimpedance amplifier circuit.	73
Figure 3.35 - Configuration menu for current mode measurements software.	75
Figure 3.36 - Acquisition menu for current mode measurements software.	76
Figure 3.37 - Pulse mode software panel. The oscilloscope shows a gaussian shaped pulse and the left display reports the spectrum of a 7,8 V amplitude step signal (input of the preamplifier).	77
Figure 3.38 - Examples of: input step function (top left), related gaussian shaped signals (top right), preamplifier output (bottom left) and preamplifier zoomed signal (the exponential decreasing tail is clearly visible). Amplifier and preamplifier signals refer to the same run; the input signal is about ten times fewer than the real one.	78
Figure 3.39 - External view of the experimental hall door. The device on the center signals that the X-ray tube receives the high voltage supply and is ready to be used, the red light on the right (light off) is a flashing one and indicates if the tube is on-going or not, the blue device on the right corner is the switch. The panel in the center contains the explanations of the flashing light.....	78
Figure 4.1 - Monitor ionization chamber developed within the work team.	81
Figure 4.2 - Monitor chamber signal at different applied voltage and kerma rate values.	82
Figure 4.3 - Monitor and PTW ionization chambers characterization experimental setup.	83
Figure 4.4 - Monitor chamber leakage current at different bias values.	84
Figure 5.1 - Kerma in air as a function of PTW distance from the reference point.	86
Figure 6.1 - Experimental setup for HVL measurements.	89
Figure 6.2 - Experimental setup for HVL measurements. View from the monitor chamber.	89

Figure 6.3 - Metal absorbers positioning along the mechanical bench.....	89
Figure 6.4 - Graphs for Cu HVLs determination, best fit lines and equations for N60, N80, N100 and N120 beams. When $Y = -1$, the equation gives the 1 st HVL value. For graphic consistency, the colour legend is consistent with that of the previous graph.	91
Figure 6.5 - Graphs for Al HVLs determination, best fit lines and equations for N40, N60 and N80 beams. When $Y = -1$, the equation gives the 1 st HVL value. For graphic consistency, the colour legend is consistent with that of the previous graph.	92
Figure 6.6 - Different measurement sessions for determining the N60 beam additional filtration.	93
Figure 7.1 - Gafchromic positioning. View from the tube housing. From that point of view the polyethylene trolley, the borders of the carton structure and, in the Gafchromic film reflection, the X-ray tube can be also seen.....	96
Figure 7.2 - Gafchromic film exposed to about 2.7 cGy of Kair (left) and the same figure with the overlaid PTW chamber scheme (right).....	96
Figure 7.3 - Acquisition line and plot for the vertical axis.	97
Figure 7.4 - Acquisition line and plot for the horizontal axis.	97
Figure 7.5 - Acquisition line and plot for the top right corner.....	98
Figure 7.6 - Silicon detector positioning on the polyethylene trolley.....	99
Figure 7.7 - Silicon detector positioning on the polyethylene trolley. View on the carton structure equipped with a millimetre paper sheet.	99
Figure 7.8 - Field bubble plot: the center of the bubble is the center of the detector, the dimension correspond to the intensity of the field in that point and bubbles of the same colours have the same distance from the centre (laying on the same radius).	101
Figure 7.9 - Overlap of the Gafchromic film image and the silicon detector signals bubble plot.....	102
Figure 7.10 - Comparison between signals detected with Gafchromic and silicon detectors: vertical profile.	103
Figure 7.11 - Comparison between signals detected with Gafchromic and silicon detectors: horizontal profile.	103
Figure 7.12 - Overlapping of Gafchromic image and Si measurements squares of fixed area corresponding to the real detector dimensions. Different colours refer to different distance from the center (field size 20x20 cm, 0.94 m from the tube focus, total filtration 7.5 mm Al + 0.7 mm Cu, delivered K_{air} 2.7 cGy).....	105
Figure 7.13 - Uniformity map of the radiation field (field size 20x20 cm, 0.94 m from the tube focus, total filtration 7.5 mm Al + 0.7 mm Cu, delivered K_{air} 2.7 cGy). ImageJ elaboration (Appendix 10.13) on the scanned Gafchromic film.....	106
Figure 7.14 - The uniformity of a radiation field produced by different filtration conditions (Paulo Márcio C. Oliveira 2007).	106
Figure 8.1 - Experimental setup for the spectra measurement by Si detector. Bias voltage 90 V, 2.595 m distant from the tube focus.....	108

Figure 8.2 - N40 spectrum performed by Si detector (90 V bias, 2.595 m from tube focus). The linear fit allows the best estimate of the X axis intercept in order to get the endpoint value in mV.....	109
Figure 8.3 - N60 spectrum performed by Si detector (90 V bias, 2.595 m from tube focus). The linear fit allows the best estimate of the X axis intercept in order to get the endpoint value in mV.....	109
Figure 8.4 - N60 spectrum performed by Si detector (90 V bias, 2.595 m from tube focus) with Y axis in logarithmic scale for better understanding the agreement between the linear fit and the raw spectrum.	110
Figure 8.5 - N80 spectrum performed by Si detector (90 V bias, 2.595 m from tube focus). The linear fit allows the best estimate of the X axis intercept in order to get the endpoint value in mV.....	110
Figure 8.6 - N100 spectrum performed by Si detector (90 V bias, 2.595 m from tube focus). The linear fit allows the best estimate of the X axis intercept in order to get the endpoint value in mV (log scale Y axis).	111
Figure 8.7 - N120 spectrum performed by Si detector(90 V bias, 2.595 m from tube focus). The linear fit allows the best estimate of the X axis intercept in order to get the endpoint value in mV (log scale Y axis).	111
Figure 8.8 - Calibration line using data of the Table 8-1.....	112
Figure 8.9 - N-series spectra measured by Si detector (90 V bias, threshold ~17 keV, 2.595 m from tube focus, endpoint calibration).	113
Figure 8.10 - Gaussian fit of the low energy peak in N60 spectrum by Si detector (90 V bias, 2.595 m from tube focus, endpoint calibration).....	114
Figure 8.11 - Gaussian fit of the low energy peak in N80 spectrum by Si detector (90 V bias, 2.595 m from tube focus, endpoint calibration).....	114
Figure 8.12 - Gaussian fit of the low energy peak in N100 spectrum by Si detector (90 V bias, 2.595 m from tube focus, endpoint calibration).	115
Figure 8.13 - Gaussian fit of the low energy peak in N120 spectrum by Si detector (90 V bias, 2.595 m from tube focus, endpoint calibration).	115
Figure 8.14 - CdTe calibration setup. The figure shows, from the left to the right, the positioning.....	117
Figure 8.15 - Positioning of the CdTe detector next to the ²⁴¹ Am radioactive source.	118
Figure 8.16 - Simplified decay scheme of ²⁴¹ Am (National Nuclear Data Center, NuDat 2 database 2019).	118
Figure 8.17 - Decay scheme of ⁵⁷ Co (National Nuclear Data Center, NuDat 2 database 2019).	119
Figure 8.18 - Raw spectrum for ²⁴¹ Am by CdTe detector (paragraph 3.2.7).....	119
Figure 8.19 - Raw spectrum for ⁵⁷ Co by CdTe detector (paragraph 3.2.7).....	120
Figure 8.20 - Spectrum of ²⁴¹ Am source by CdTe detector (paragraph 3.2.7). Legend reports the energy.....	121
Figure 8.21 - Spectrum of ⁵⁷ Co source by CdTe detector (paragraph 3.2.7). Legend reports the energy.....	121
Figure 8.22 - Energy calibration curve: peaks nominal energy (keV) against centroid (mV).	122
Figure 8.23 - CdTe detector (paragraph 3.2.7) ²⁴¹ Am source calibrated spectrum.....	123
Figure 8.24 - CdTe detector (paragraph 3.2.7) ⁵⁷ Co source calibrated spectrum.....	123
Figure 8.25 - Positioning of the CdTe detector and the preamplifier by aligning them to the field	125

Figure 8.26 - Experimental setup for measuring N-series spectra (aluminium layer ensures the electromagnetic shield).	125
Figure 8.27 - N-series spectra by CdTe detector (paragraph 3.2.7, 1.819 m from tube focus). All the spectra were normalized to unit area to easily visualize them in the same graph.	127
Figure 8.28 - Endpoint energies (estimates from the spectra) as a function of the measured tube potential.	128
Figure 8.29 - Plots showing the measured and modelled CdTe photopeak shape as a function of energy. At 14.4 keV (left), the photopeak is Gaussian. At 59.5 keV (middle), the photopeak exhibits a smooth asymmetric tail to lower amplitudes. At 122 keV (right), additional counts in the tail lead to a step at the anode charge collection efficiency (R. Redus 2008).	130
Figure 8.30 - Simulated monoenergetic response functions for a CdTe detector (Amptek, model XR-100T CdTe - 1 mm thickness, 9 mm ² nominal area, Be window 100 μm) at 35 keV, 90 keV and 150 keV (A. Tomal 2015).	131
Figure 8.31 - CdTe (see paragraph 3.2.7) calibration spectrum of ²⁴¹ Am radioactive source. Several distortions due to the CdTe features are highlighted with different colours. Red: photopeak with shoulder extending towards lower energies (20 keV below the incident energy). Purple: escape of characteristic K X-rays from Cd and Te (26–32 keV below the incident energy of the main peak).....	131
Figure 8.32 - Spectrum emitted from an 80 kVp X-ray tube with a tungsten (W) anode and a 15 keV filter, measured with a 1 mm thick CdTe detector. Plot showing the spectrum after processing to remove escape events. The grey trace shows the original spectrum. The green trace illustrates the escape events in the original spectrum. These are subtracted from this original spectrum, then the correct energies are computed (by adding in the energy which escaped). The blue trace shows the corrected escape events, which are then summed with the grey trace. The dark black trace shows the final result of the processing with the events in their correct channels (Amptek 2008).	132
Figure 8.33 - Measured and corrected X-ray spectra obtained with a CdTe detector (Amptek, model XR-100T CdTe - 1 mm thickness, 9 mm ² nominal area, Be window 100 μm) for (a) 50kVp and (b) 100kVp (A. Tomal 2015).	133
Figure 9.1 - The lens and its anatomical regions. Left: A classic radiation cataract imaged using a Nidek_EAS1000 Scheimpflug Slit Imaging System. Left to right are the cornea (C), anterior chamber (AC) and lens (L). The dark area in the right center is a stage 1 cataract (CAT) in the PSC/cortical region of an otherwise relatively clear lens. Right: Schematic diagram of a sagittal view of an adult human lens. The bulk of the tissue consists of fiber cells, the elongate progeny of those epithelial cells that undergo differentiation (fibrogenesis). The centrally located lens is comprised innermost of those cells that differentiate during intrauterine and early postpartum life. Later fibrogenesis compacts the early nucleus and adds to the overall nuclear mass. It is surrounded by a cortex consisting of fibers that are continuously produced and laid down during cell maturation. The most superficial fibers of the cortex are those that most recently differentiated. The capsule, a tremendously hypertrophied basal lamina, is a barrier to cells leaving or entering the tissue. After radiation injury, epithelial cells differentiate improperly and initially accrete in the superficial posterior cortex immediately subjacent to the capsule. Collectively the aberrant fibers accumulating in the back of the lens constitute the clinical entity known as posterior subcapsular (PSC) cataract. The term arose to more precisely describe, based on location, what otherwise is generically a cortical cataract (Worgul 2007).	137

Figure 9.2 – (Left) Complex cardiac procedure. Electronic C arm (X-ray tube) is highlighted in the black circle. Cardiologists are usually well protected with ceiling screen, goggles and protection under the table. Nurses usually wear only goggles, but they are exposed only for a limited time in that position (Courtesy E. Vano, Madrid). (Right) Example of a model of C arm for vascular operation (Medical 2019).....	137
Figure 9.3 - Fully coupled photon electron transport calculations results versus kerma	138
Figure 9.4 - Comparison of dose equivalents at 10 and 0.07 mm depth at 0° taken from the (ICRU report 57, 1995)report and the dose equivalent at 3 mm depth taken from (Daures J., 2009) with the absorbed dose to the eye lens in the anthropomorphic phantom for anterior-posterior (AP) irradiation taken from (ICRP publication 74, 1995). $h'(0.07)$ was plotted instead of $h_p(0.07)$ because $h_p(0.07)$ is not given above one MeV in (ICRU report 57, 1995), but is very similar to $h'(0.07)$ below one MeV (Bordy, 2015).	139
Figure 9.5 - Comparison of dose equivalents at 3 mm depth at 0° taken from (Daures J., 2009) calculated with full transport and kerma approximation with the equivalent dose to the eye lens in the anthropomorphic phantom for anterior-posterior irradiation derived from (ICRP publication 116, 2010, Bordy, 2015).	139
Figure 9.6 - Normally incident photons: comparison between the $H_T(\text{eye lens})$ (R. Behrens 2011) and $H_p(3)$ as obtained using the cylindrical phantom and the traditional 30 x 30 x 15 cm ³ slab (E. Till 1995).	140
Figure 9.7 - Laterally incident photons: comparison between the $H_T(\text{eye lens})$ (R. Behrens 2011) and $H_p(3)$ as obtained using the cylindrical phantom and the traditional 30 x 30 x 15 cm ³ slab (E. Till 1995).	141
Figure 9.8 - A detail of Figure 9.6 showing the comparison between the $H_T(\text{eye lens})$ (R. Behrens 2011).....	141
Figure 9.9 - Rotational photon exposure: comparison between the $H_T(\text{eye lens})$ (R. Behrens 2011)	141
Figure 9.10 - Four whole-body dosimeters positioned on the front surface of the ISO water.....	142
Figure 9.11 - Four head-band dosimeters positioned on the water filled cylindrical.....	142
Figure 9.12 - Linear attenuation coefficients for photo absorption and Compton scattering in silicon and other detector materials (Tadayuki Takahashi 2019).....	146
Figure 9.13 - Experimental setup for irradiating the eye lens dosimeter prototype. The dosimetric unit is placed on the surface of the water filled cylindrical head phantom according the calibration procedure (paragraph 9.3): 2.5 m distant from the tube focus (90 V bias, 1.5 V or ~ 22 keV threshold).	147
Figure 9.14 - Energy responses of the different prototypes. It is possible to see the flattening profile due to the metallic filters. The bare sensor profile shows a big variability: over response at low energies and under response at high energies. Relative standard uncertainties~ 10%.....	152
Figure 9.15 - Energy relative responses at 0° of angular incidence for every prototype. All the results fulfil the IEC 62387 limits. Relative standard uncertainties~ 10%.	153
Figure 9.16 - Measured combined energy and angular response for the best resulting eye lens dosimeter prototype (1 mm Pb 4 mm diameter hole due to the low values) calibrated on the cylinder head phantom in terms of personal dose equivalent $H_p(3)$ (relative standard uncertainties~ 10%).....	154
Figure 9.17 – Comparison between unfiltered and some filtered dosimeter prototype in the case of N40 (left) and N120 (right) spectra. The lead hardly suppresses the response at low energies (N40) and softly attenuates the response of silicon at high energies (N120), where the intrinsic response is yet weak. Considering the 4 mm diameter in the 1 mm Pb filter, the mitigation in suppression at the low energy region is clearly visible in the N40 orange curve.	155

Figure 9.18 - N120 spectrum: comparison between a filtered (1mm Pb) and bare prototype (same irradiation time, 120 s, and same distance, 2.5 m). It is possible to see the cut in the response (violet curve) at about 88 keV due to the K edge of lead (J. P. McCaffrey February 2007)..... **156**

English abstract

This PhD project is focused on the qualification of an X-ray unit for dosimetical applications.

This thesis describes all the project in three different sections.

The first part can be considered an introduction for depicting concepts and instruments used for this work. The theoretical basis of the working principle of an X-ray tube is explained in Chapter 1. Chapter 2 shows the quantities and units system on Radiation Protection. These first two chapters represent the **theoretical background** of my thesis. Chapter 3 depicts the laboratory assembled during the first part of my PhD work. The irradiation unit and the related laboratory were set up in the framework of a collaboration between INFN - Frascati National Laboratories (INFN - LNF), the Italian Space Agency (ASI) and *Consorzio di ricerca* Hypatia. The X-ray apparatus operates from 40 to 120 kV with currents up to 5 mA. Different filtrations can be implemented according to the desired beam quality. A mechanical bench allows positioning devices and samples at different distances from the anode of the X-ray tube.

The second part shows the main results obtained with different experiments and tests to **qualify** the radiation output of the X-ray tube:

- design and development of a **monitor ion-chamber** to measure the time-dependant output of the X-ray unit (Chapter 4);
- determination the X-ray tube **focus** position, which is an important reference point of the irradiation line (Chapter 5);
- experimental verification of the beam quality through **HVL** (Half Value Layer) measurements with ion-chamber for the best choice of adequate kilovolt-filtration combinations in order to achieve well-identified radiation qualities, as specified by relevant International Standards (ISO 4037). The beams from the **narrow spectrum series** (ISO 4037 N-series) were selected because their roughly mono-energetic energy distribution is well suited to study the response of devices as a function of the photon energy. The accordance between ISO values and experimental ones is excellent: the discrepancy is less than about 5% (Table 6-3, Chapter 6) .
- study on the X-ray field **uniformity** (Chapter 7), which is an important task that the X-ray beam must comply with, because it is important that all the field areas are equivalent and wherever the device under test is placed, it is exposed to the same dose. Two different measurements techniques were involved to verify the uniformity. The first is based on a passive detector, Gafchromic film, and the second employs a silicon detector operating in current mode. The total field variability is about 11% within a central region of 8 cm radius (paragraph 7.4, Chapter 7).
- **spectral measurement** of the X-ray beams using semiconductor-based photon spectrometers (Silicon and Cadmium-Telluride detector). These measurements lead a role for checking the continuum shape of bremsstrahlung spectrum and the endpoint energies

of the spectral components in addition to the quality measurements of HVLs (Chapter 8). The spectra confirm what expected from HVL measurements: using the proper kilovolt-filtration combinations (written in the Table 6-3) is possible to achieve the well-identified radiation qualities of the N-series, the narrow series of ISO 4037, useful as calibrating reference.

The activity for the last part of my PhD thesis was focused on an innovative active detector for **eye-lens dosimetry** (Chapter 9). During the last years the need of a detailed re-evaluation of the eye lens radio-sensitivity was put in evidence. Various epidemiological studies highlighted a higher incidence of cataracts than previously foreseen. For these reasons the ICRP reduced the exposure limit for workers from 150 mSv per year to 20 mSv in a year averaged over defined periods of five consecutive years, with no single year exceeding 50 mSv (ICRP 2011). Therefore, the keen interest on this topic is for the essential evaluation of the occupational eye dose and eye protection. Thanks to the physical qualification of the X-ray tube under a metrological point of view, it was possible to use this irradiation facility as test bench for the development and type testing (study on energy and angular response) of a semiconductor-based prototype of an eye-lens dosimeter developed within the work team. This innovative part of my PhD work represents a R&D study on a need for operational dosimetry.

Spanish (Castellano) abstract

Este proyecto de doctorado se centra en la evaluación de calidad de una unidad de rayos X para aplicaciones dosimétricas.

Esta tesis describe todo el proyecto en tres secciones diferentes.

La primera parte puede considerarse una introducción para presentar los conceptos e instrumentos utilizados para este trabajo. La base teórica del principio de funcionamiento de un tubo de rayos X se explica en el Capítulo 1. El Capítulo 2 muestra las magnitudes y el sistema de unidades de Protección Radiológica. Estos dos primeros capítulos representan los **antecedentes teóricos** de mi tesis. El Capítulo 3 muestra el laboratorio montado durante la primera parte de mi trabajo de doctorado. La unidad de irradiación y el laboratorio relacionado se pusieron a punto en el marco de una colaboración entre los Laboratorios Nacionales de Frascati del INFN (INFN - LNF), la Agencia Espacial Italiana (ASI) y el Consorzio di ricerca Hypatia. El aparato de rayos X funciona entre 40 y 120 kV con corrientes de hasta 5 mA. Se pueden implementar diferentes filtraciones de acuerdo con la calidad de haz deseada. Un banco mecánico permite colocar dispositivos y muestras a diferentes distancias del ánodo del tubo de rayos X.

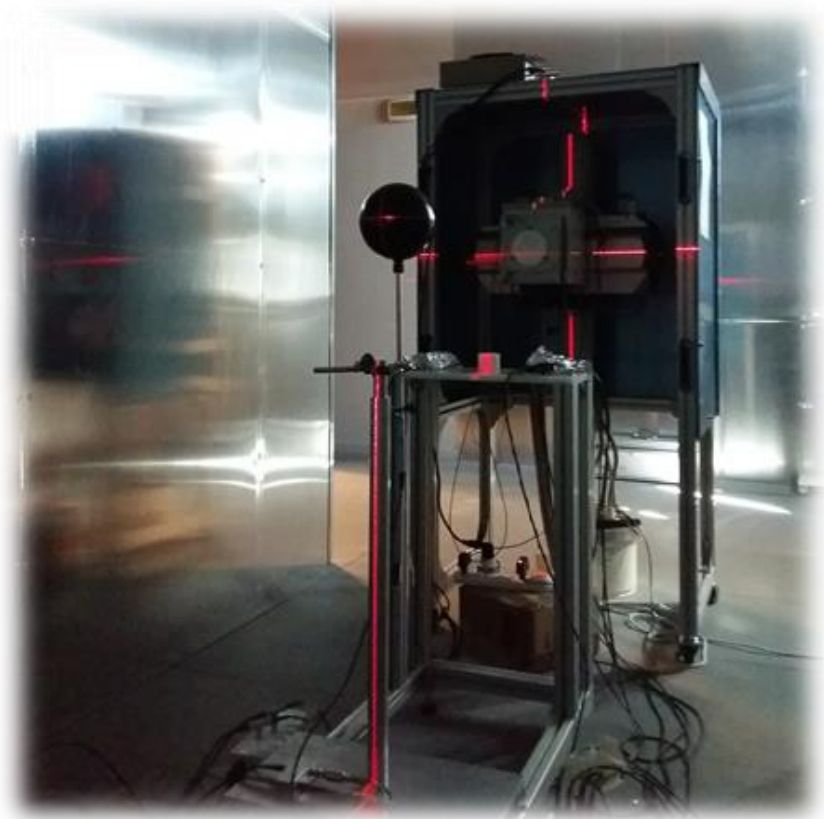
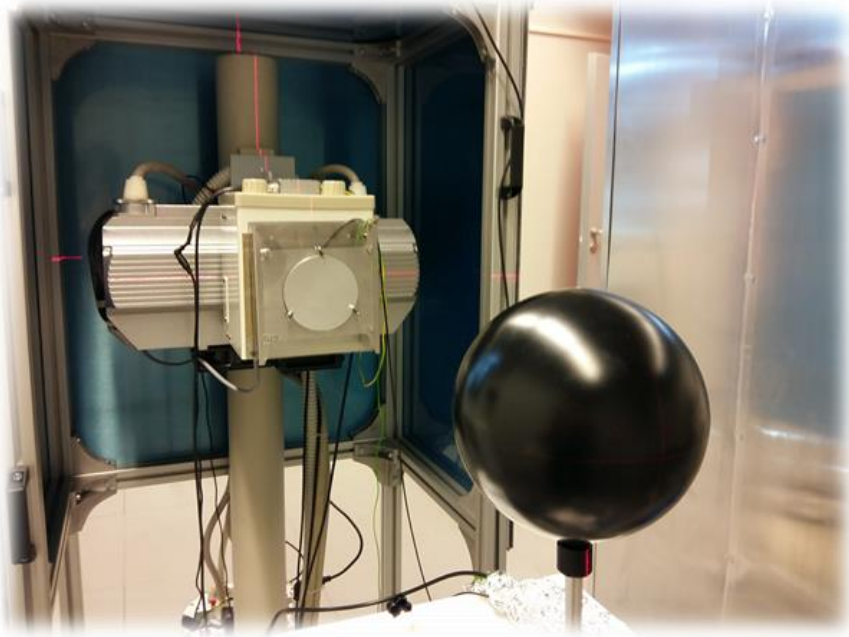
La segunda parte muestra los principales resultados obtenidos con diferentes experimentos y pruebas para **calificar** la salida de radiación del tubo de rayos X:

- diseño y desarrollo de una **cámara de ionización** para medir la salida dependiente del tiempo de la unidad de rayos X (Capítulo 4);
- determinación de la posición del **foco** del tubo de rayos X, que es un punto de referencia importante de la línea de irradiación (Capítulo 5);
- verificación experimental de la calidad del haz a través de mediciones **HVL** (Espesor de semirreducción - Half Value Layer) con la cámara de ionización para la elección de combinaciones adecuadas de kilovoltios-filtración para lograr calidades de radiación bien identificadas, según lo especificado por las Normas Internacionales relevantes (ISO 4037). Los haces de la serie de espectro estrecho (**serie ISO 4037 N**) se seleccionaron porque su distribución de energía aproximadamente monoenergética es muy adecuada para estudiar la respuesta de los dispositivos en función de la energía del fotón. La concordancia entre los valores ISO y los experimentales es excelente: la discrepancia es inferior a aproximadamente el 5% (Tabla 6-3, Capítulo 6).
- estudio sobre la **uniformidad** del campo de rayos X (Capítulo 7), que es una tarea importante que debe cumplir el haz de rayos X, ya que es importante que todas las áreas de campo sean equivalentes y que la dosis impartida al dispositivo bajo prueba sea independiente de la posición en que se coloque. Se utilizaron dos técnicas de medición diferentes para verificar la uniformidad. La primera se basa en un detector pasivo, película Gafchromica, y la segunda emplea un detector de silicio que funciona en modo corriente. La variabilidad total del campo es aproximadamente del 11% dentro de una región central de 8 cm de radio (párrafo 7.4, Capítulo 7).

- **medición espectral de los haces de rayos X** utilizando espectrómetros de fotones basados en semiconductores (detectores de silicio y de telurato de cadmio). Estas mediciones son básicas para verificar la forma del espectro continuo de radiación de frenado y las energías de punto final de las componentes espectrales, además de las mediciones de calidad de HVL (Capítulo 8). Los espectros confirman lo que se esperaba de las mediciones de HVL: utilizando las combinaciones de kilovoltios-filtración adecuadas (escritas en la Tabla 6-3) es posible lograr las calidades de radiación bien identificadas de la serie N, la serie estrecha de ISO 4037, útil como referencia de calibración

La actividad de la última parte de mi tesis doctoral se centró en un innovador detector activo para **dosimetría de cristalino** (Capítulo 9). Durante los últimos años se ha puesto de manifiesto la necesidad de una reevaluación detallada de la radiosensibilidad del cristalino. Varios estudios epidemiológicos han destacado una mayor incidencia de cataratas que la prevista previamente. Por estas razones, la ICRP redujo el límite de exposición para los trabajadores de 150 mSv por año a 20 mSv en un año promedio durante períodos definidos de cinco años consecutivos, sin que en ningún año se excedan los 50 mSv (ICRP 2011). Por lo tanto, el gran interés en este tema es la evaluación esencial de la dosis ocupacional en cristalino y la protección del ojo. Gracias a la calificación física del tubo de rayos X bajo un punto de vista metrológico, fue posible utilizar esta instalación de irradiación como banco de pruebas para el desarrollo y pruebas de tipo (estudio sobre energía y respuesta angular) de un prototipo de un dosímetro de cristalino basado en semiconductores y desarrollado dentro del equipo de trabajo. Esta parte innovadora de mi trabajo de doctorado representa un estudio de I + D sobre la necesidad de dosimetría operativa.

Part I – Introduction



1. X-RAYS PRODUCTION

1.1 X-ray tube: structure and operating principle

122 year ago

Nature, 23 January 1896

“The Newspaper reports of Prof. Rontgen’s experiments have, during the past few days, excited considerable interest. [...] Prof. Rontgen has extended the results obtained by Lenard in a manner that has impressed the popular imagination, while perhaps most important of all, he has discovered the exceedingly curious fact that bone is so much less transparent to these radiation than flesh and muscle”.

The practical sources of X-rays are radioactive isotopes, nuclear reactions such as fission and fusion, and particle accelerator but if a source is required that allows

- o to produce enough X-rays in a short time,
- o to vary the X-rays energy,
- o to provide X-rays in a reproducible way,
- o to meet standards of safety and economy of operation

only special-purpose particle accelerators known as X-ray tubes are needed.

X radiation is produced whenever a material is bombarded by high energy electrons. All X-ray tubes consist of a cathode and anode assembly, placed inside a glass envelope that has been evacuated. The cathode assembly consists of a metal with a high melting point in the form of a coil placed in shallow focusing cup. A current of a few amperes heats the filament (tungsten is mostly used), so electrons are “boiled” out of the coil (thermionic emission). These electrons are accelerated across a **high voltage** onto a target (the anode is made positive with respect to the filament). The stream of accelerated electrons is referred to as the **tube current**. X-rays are produced as the electrons interact in the target. The X-rays emerge from the target in all directions but are restricted by collimators to form a useful beam of X-rays (see Figure 1.1).

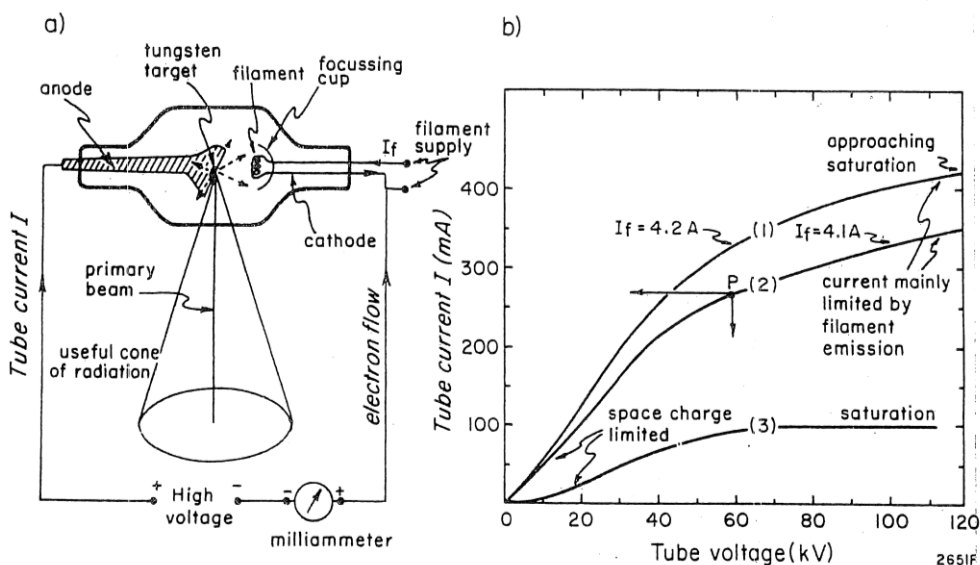


Figure 1.1 - (a) Schematic diagram of X-ray tube and circuit. (b) Tube current as a function of tube voltage. Curves 1 and 2, Siemens B150 RGS tube. Curve 3, typical data for tube operating at a lower current (Johns e Cunningham s.d.).

To understand the operation of an X-ray tube, it is important to know how the tube current depends upon the tube voltage for a given filament excitation. Figure 1.1-b shows data for a typical diagnostic X-ray tube. When a few kV are applied across the tube, the current is small due to space charge. Space charge refers to the collection of electrons which are emitted from the metal surface, after the application of tube current, at a short distance away from the metal surface. These electrons collect and form a cloud of negative charge around the metal surface. This space charge repels and limits the further emission of electrons from the surface and is referred to as the space charge effect (Radiopaedia 2019). The effect is most noticeable at lower kV. As the kV is increased, the effects of the space charge are gradually overcome and the current increases until most of the electrons liberated in the filament are pulled to the anode. At still higher voltages the region of saturation is reached where all the liberated electrons are pulled to the anode. To achieve stability in the operation of an X-ray tube, the current used to excite the filament and the high voltage applied across the tube must be carefully stabilized and controlled.

In a typical medical X-ray tube, the accelerating voltage is set at 30-150 kV so that the electrons acquire 30-150 keV of kinetic energy just before they hit the target anode. Typically electron currents will be in the range 10-100 mA and thus the electrical power consumed by the tube will be about 10 kW. When the electrons interact with the target are brought to rest within a few mm in the anode. By far the largest part of the electron beam energy is converted into **heat** and this is deposited within a few mm of the surface of the target. Only about 1% of the available electron energy is actually converted into useful X-ray radiation. Without special precautions, the electron beam would rapidly melt the surface of the target.

To solve this important problem for the tube designer

- the electron beam is shaped into a long thin rectangle oriented radially with respect to the anode disc and
- the anode is made to rotate at high speed (2000-3000 RPM) underneath the beam (see Figure 1.2).

Both of these ensure that the beam energy is spread over as large an area of target anode as possible. Even then the anode will get very hot, so high melting point metals such as tungsten rhenium alloy (90:10) bonded to a molybdenum disc are used as targets. Finally there is a sensor system that detects the raise of the anode temperature and shuts the tube down in case of emergency until the **cooling system** (circulating water, oil, just radiative cooling) has decreased the temperature to start again.

These cautions allow a better electron bombardment resistance and a much longer useful life. With use, all tubes deteriorate because of pitting due to the electron bombardment. A pitted anode (see Figure 1.2) affects the electric field across the tube and so alter the size of the focal spot, the volume of target within electrons are absorbed and X-ray are produced (Hendee e Ritenour 2002, Fourth edition).

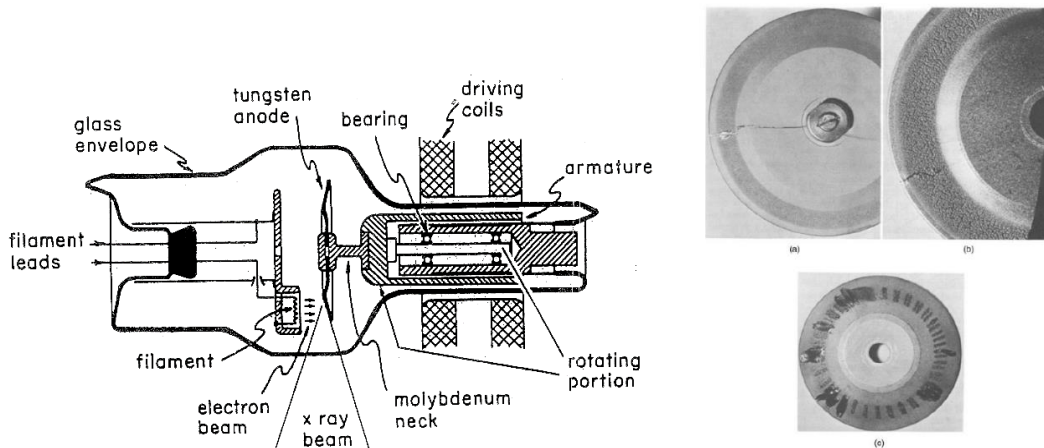


Figure 1.2 - (On the left) Rotating anode tube, adapted from diagram by Philips. (On the right) Rotating targets damaged by excessive loading or improper rotation of the target. A: target cracked by lack of rotation. B: target damaged by slow rotation and excessive loading. C: target damaged by slow rotation (Johns e Cunningham s.d.).

High resolution in X-ray radiography demands the smallest possible X-ray source diameter. Although the electron beam is generally spread out along a line, this is oriented edge on with respect to the exit window: see Figure 1.3. Thus X-rays emerge from a small area, limited by the thinner, vertical dimension of the electron beam in one direction and the shallow angle of the target in the other. This is called the **focus** of the X-ray tube.

For radiographs of highest clarity, electrons should be absorbed within a small focal spot. To achieve a small focal spot, the electrons should be emitted from a small or “fine” filament. Radiographic clarity is often reduced by voluntary or involuntary motion of the patient. This effect can be decreased by using X-ray exposures of high intensity and short duration. However, these high-intensity exposures may require an electron emission rate that exceeds the capacity of a small filament. Consequently many X-ray tubes have two filaments. The smaller, fine filament is used when radiographs with high detail are desired and short, high-intensity exposures are not necessary. If high-intensity exposures are needed to limit the blurring effects of motion, the larger, coarse filament is used. The cathode assembly of a **dual-focus X-ray tube** is illustrated in Figure 1.4.

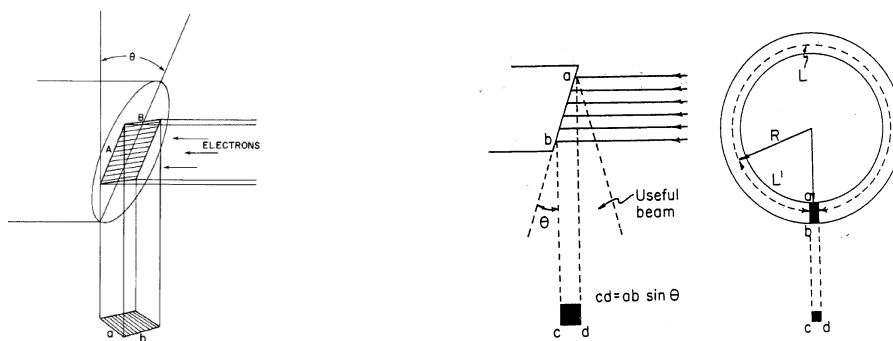


Figure 1.3 - Illustration of the line-focus principle, which reduces the apparent size of the focal spot (J. T. Bushberg 2012).

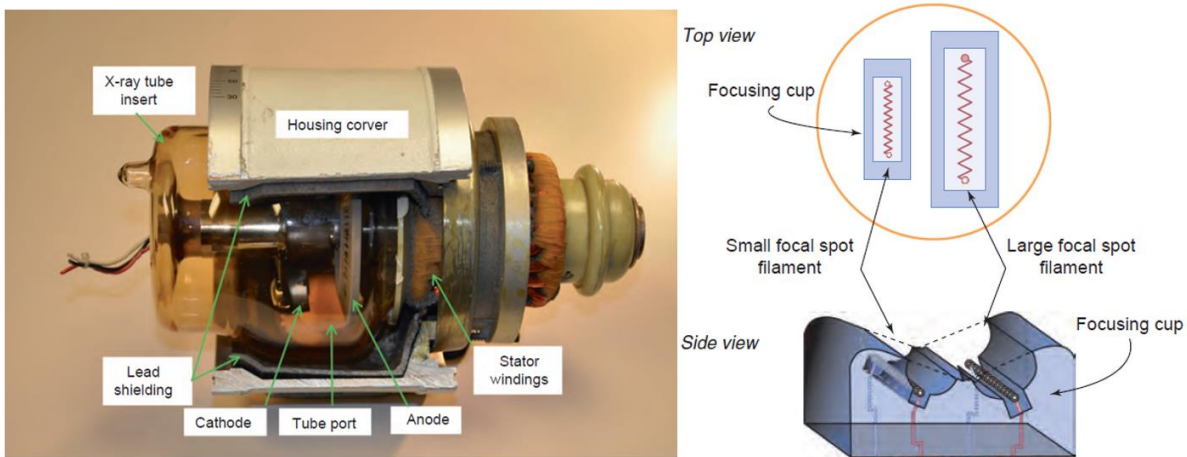


Figure 1.4 - On the left: a dual-focus X-ray tube with a rotating anode. Picture of an X-ray tube insert and partially cut-away housing, shows the various components of the X-ray tube. On the right: cathode assembly of a dual-focus X-ray tube. The small filament provides a smaller focal spot and a radiograph with greater detail, provided that the patient does not move. The larger filament is used for high-intensity exposures of short duration (J. T. Bushberg 2012).

In order to produce an adequate focal spot size a structure, called focusing cup, is needed. The cup is at the same potential as the cathode and it provides a series of parallel field lines when the anode bias is on. Figure 1.5 shows the difference in electron trajectories if the focusing cup is at the same voltage of the cathode or if it has a negative values. With negative biased focusing cup, electrons are forced to follow a path which is very close to the beam axis and produce a smaller focal spot.

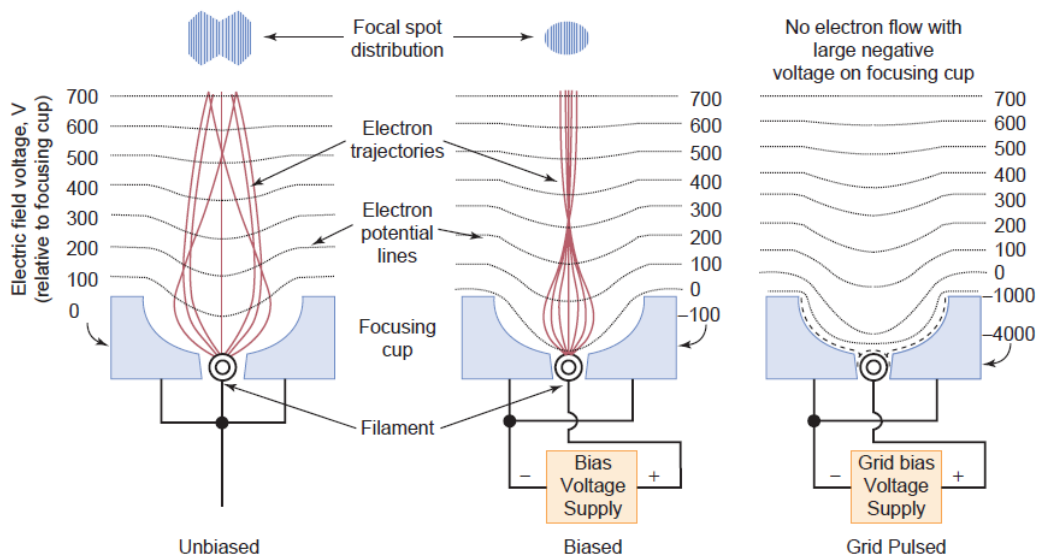


Figure 1.5 - The focusing cup shapes the electron distribution when it is at the same voltage as the filament (left). Isolation of the focusing cup from the filament and application of a negative bias voltage (-100 V) reduces electron distribution further by increasing the repelling electric fields surrounding the filament and modifying the electron trajectories (middle). At the top are typical electron distributions incident on the target anode (the focal spot) for the unbiased and biased focusing cups. Application of -4000 V on an as a grid biased or grid pulsed tube (right) (J. T. Bushberg 2012).

Collimators adjust the size and shape of the X-ray field emerging from the tube port. The collimator assembly typically is attached to the tube housing at the tube port with a swivel joint. Two pairs of

adjustable parallel-opposed lead shutters define a rectangular X-ray field (see Figure 1.6). In the collimator housing, a beam of light reflected by a mirror of low X-ray attenuation mimics the X-ray beam. Thus, the collimation of the X-ray field is identified by the collimator's shadows.

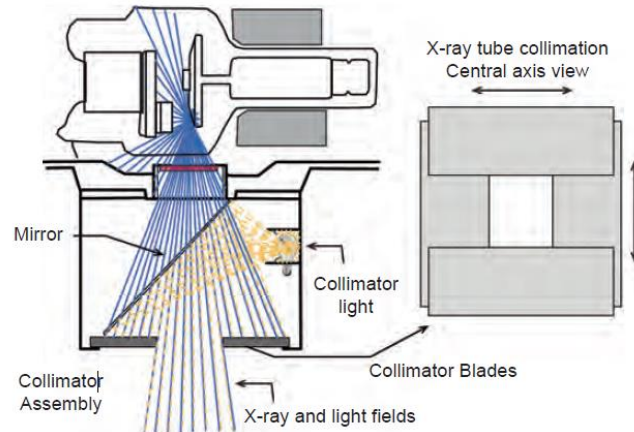


Figure 1.6 - The X-ray tube collimator assembly is attached to the housing at the tube port, typically on a collar that allows it to be rotated. A light source, positioned at a virtual focal spot location, illuminates the field from a 45° angle mirror. Lead collimator blades define both the X-ray and light fields (J. T. Bushberg 2012).

1.2 X-ray tube spectra

The spectrum of X-ray photon energies emerging from the target anode – see Figure 1.7 – illustrates the two involved mechanisms of X-ray generation. The broad “hump” results from X-ray produced by a continuum of changes in electron velocity as the electron makes a series of glancing encounters with the target atoms. At each encounter the electron velocity is changed, it therefore decelerates and emits an amount of electromagnetic energy whose frequency depends on the degree of deceleration. This is the **bremstrahlung** or “breaking radiation” process. The maximum possible photon energy emerging from the tube is exactly equal to the incident electron kinetic energy. This photon is emitted if the electron is brought to rest in just one encounter (see Figure 1.8). The peak of the spectrum corresponds to the most probable magnitude of electron deceleration. The energy at which the peak occurs varies with applied high voltage. Thus the mean photon energy in a ray beam is governed by the applied voltage (Guy 2000). The spikes, or peaks, on this continuous spectrum (white radiation) are called **characteristic radiation** since their position depends upon the atomic number of the target.

In summary the useful beam of an X-ray tube is composed of photons with an energy distribution that depends on several factors.

- Bremsstrahlung X-rays are produced with a range of energies even if electrons of a single energy bombard the target.
- X-rays released as characteristic radiation have energies independent of those of the bombarding electrons, except for the fact that the electrons energy must be higher of a certain limit, which is the threshold energy for characteristic X-ray emission.
- The energy of the bombarding electrons varies with tube voltage, which fluctuates rapidly in some X-ray tubes.

- X-rays are produced at a range of depths in the target of the X-ray tube. These X-rays travel through different thicknesses of target and may lose energy through one or more interactions.

Changes in other variables such as filtration, target material, peak tube voltage, current, and exposure time all may affect the range and intensity of X-ray energies in the useful beam. The distribution of photon energies produced by a typical X-ray tube, referred to as an emission spectrum, is shown in Figure 1.7.

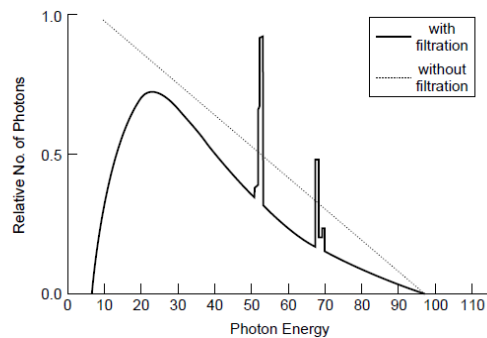


Figure 1.7 - Emission spectrum for a tungsten target X-ray tube operated at 100 kVp. K-characteristic X-ray emission occurs for tungsten whenever the tube voltage exceeds 69 keV, the K-shell binding energy for tungsten. The dotted line represents the theoretical bremsstrahlung emission from a tungsten target. The solid line represents the spectrum after self-, inherent, and added filtration. The area under the spectrum represents the total number of X-rays (J. T. Bushberg 2012).

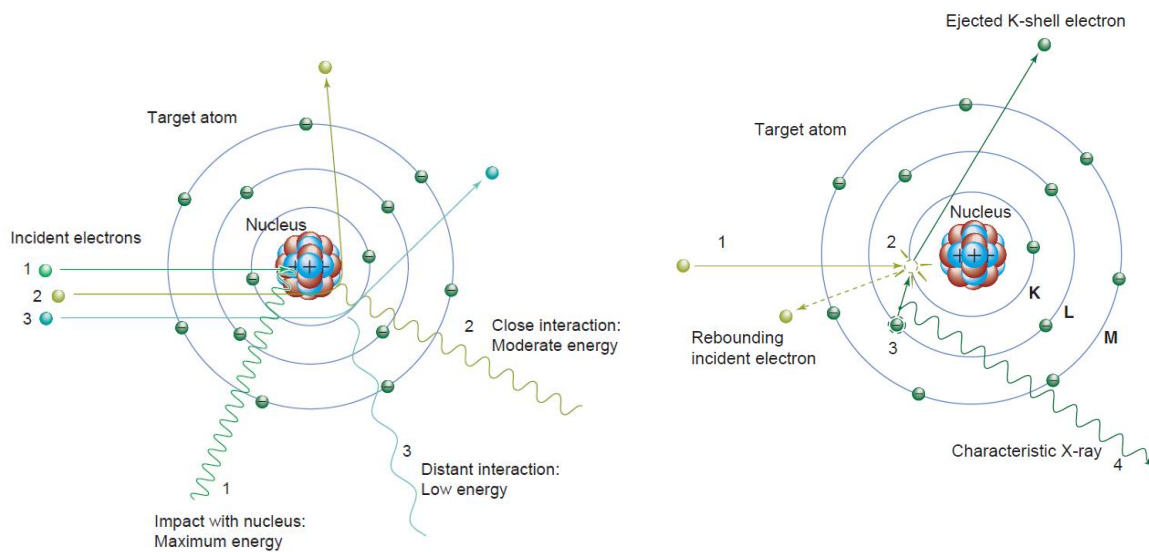


Figure 1.8 - (On the left) Bremsstrahlung radiation arises from energetic electron interactions with an atomic nucleus of the target material. In a “close” approach, the positive nucleus attracts the negative electron, causing deceleration and redirection, resulting in a loss of kinetic energy that is converted to an X-ray. The X-ray energy depends on the interaction distance between the electron and the nucleus; it decreases as the distance increases. (On the right) Generation of a characteristic X-ray in a target atom occurs in the following sequence: (1) the incident electron interacts with the K-shell electron via a repulsive electrical force. (2) The K-shell electron is removed (only if the energy of the incident electron is greater than the K-shell binding energy), leaving a vacancy in the K-shell. (3) An electron from the adjacent L-shell (or possibly a different shell) fills the vacancy. (4) A K_{α} characteristic X-ray photon is emitted with energy equal to the difference between the binding energies of the two shells. In this case, a 59.3 keV photon is emitted (J. T. Bushberg 2012).

1.2.1 Characteristic radiation

A more detailed energy level diagram is required to understand the production of characteristic radiation. Once the K electron is ejected, the space may be filled with an electron from the L, M or N shells. When the electron moves in this way, a transition has taken place. For example, when an electron in tungsten moves from the L_{III} to the K shell, energy is radiated and the amount is the difference between the corresponding energy levels, i.e. 69.525 keV – 10.204 keV = 59.321 keV (see Figure 1.9). This is a K-L_{III} transition and the photon emitted is called the K_{α1} line. K radiation denotes characteristic radiation for electron transitions to the K shell, and likewise, L radiation for transitions to the L shell. The origin of the electron filling the vacancy is indicated by suffixes (**α**, **β**, **γ**, etc.), where **α** stands for a transition from the adjacent outer shell, **β** from the next outer shell, etc. K_α radiation results from L to K shell transitions; K_β radiation from M to K shell transitions, etc. Energies are further split owing to the energy levels in a shell, indicated with a numerical suffix. Further, each vacancy in an outer shell following from such a transition gives rise to the emission of corresponding characteristic radiation causing a cascade of photons. Quantum mechanical reasoning shows that many of the transitions between the different shells are forbidden and only those that follow certain selection rules are allowed. A few of the important emission lines from tungsten and molybdenum are given in Table 1-1 (Johns e Cunningham s.d.).

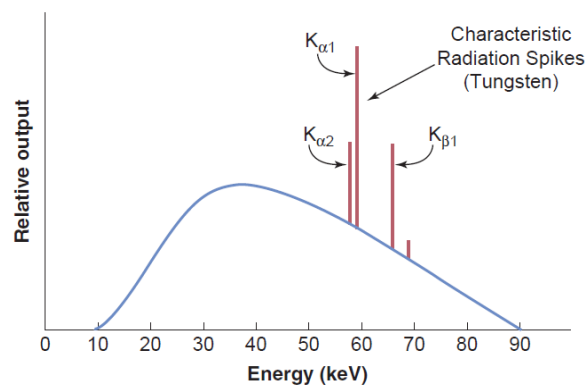


Figure 1.9 - The filtered spectrum of bremsstrahlung and characteristic radiation from a tungsten target with a potential difference of 90 kV illustrates specific characteristic radiation energies from K_α and K_β transition (J. T. Bushberg 2012).

Shell Transition	Tungsten (W)	Molybdenum (Mo)	Rhodium (Rh)
K _{α1}	59.32	17.48	20.22
K _{α2}	57.98	17.37	20.07
K _{β1}	67.24	19.61	22.72

Table 1-1 - K- shell characteristic X-ray energies (keV) of common X-ray tube target materials. Note: only prominent transitions are listed. The subscripts 1 and 2 represent energy levels that exist within each shell (J. T. Bushberg 2012).

The discrete lines of the characteristic spectrum are usually not of great importance either in diagnosis or therapy because they contribute only a small fraction of the energy in the total spectrum.

It could be useful to consider the equation 1.0 to describe the trend of the spectral line energy as a function of atomic number, Z. Moseley was the first to investigate and find the relationship between the atomic number of an element and the energy of its spectral lines (Dalba a.a. 1999-2000).

$$E(Z) = k_j (Z - \sigma_j)^2 \quad (1.0)$$

Where k_j and σ_j are different constants for each characteristic line. σ_j is a screen constant: it corrects the effect of orbital electrons that reduce the nuclear charge Z.

In terms of wavelength, the previous equation becomes equation 1.1.

$$\lambda \propto \frac{1}{Z^2} \quad (1.1)$$

1.2.2 Filtration

An X-ray beam traverses several attenuating materials before it reaches the patient, including the glass envelope of the X-ray tube, the oil surrounding the tube, and the exit window in the tube housing. These attenuators are referred to collectively as the **inherent filtration** of the X-ray tube. The aluminium equivalent for each component of inherent filtration is the thickness of aluminium that would reduce the exposure rate by an amount equal to that provided by the component. The inherent filtration of most X-rays tubes is about 1 mm Al.

The low-energy X-rays are attenuated to a greater extent than those of high energy.

After passing through a material, an X-ray beam has a higher average energy per photon even though the total number of photons in the beam has been reduced, because more low-energy photons than high-energy photons have been removed from the beam.

The inherent filtration of an X-ray tube “hardens” the X-ray beam. Additional hardening may be achieved by purposefully adding filters of various composition to the beam. The total filtration in the X-ray beam is the sum of the inherent and added filtration. Usually, additional hardening is desirable because the filter removes low-energy X-rays that, if left in the beam, would increase the radiation dose to the patient without contributing substantially to image formation. The effect of the added aluminium is to decrease the total number of photons but increase the average energy of photons in the beam. These changes are reflected in a decrease in the overall height of the emission spectrum and a shift of the peak of the spectrum toward higher energy.

1.2.3 The angular distribution

In a practical X-ray tube the polar distribution is as indicated in Figure 1.10. The maximum yield is usually 5° to 10° to the cathode side of the line 0° and falls slowly as the is increased beyond 10°. The distribution shown in Figure 1.10 is typical of a practical diagnostic tube with a target angle at 16°. The reduced intensity on the anode side is called the **heel effect**. The beam near the anode, although of reduced intensity, is more penetrating because of self-filtration in the target.

The conversion of the electron beam into X-rays doesn't simply occur at the surface of the target material but deep within it. Because X-rays are produced deep in the target material, they must traverse back out of it before they can proceed to the target field. More target material needs to be traversed at emission angles that are perpendicular to the electron beam (closer to the anode) than

at those more parallel to it (closer to the cathode). This increase in material leads to more resorption of the X-rays by the target material resulting in fewer X-rays reaching the field at angles perpendicular to the electron beam. It also means that the X-rays emitted to angles closer to the incident beam travel through less target material and fewer are resorbed. The end result is that the field intensity towards the cathode is more than that towards the anode (Radiopaedia 2019). This is used in mammography by aligning the cathode over the chest wall end (thicker area to penetrate, higher energy beam) and the anode over the nipple end (thinner area to penetrate, lower energy beam, Figure 1.11).

Many factors can affect the heel effect:

- anode angle: by increasing the angle, the amount of target material perpendicular to the anode is decreased resulting in less resorption of X-rays produced,
- target-to-film distance: increase in distance reduces heel effect by allowing more divergence of the beam which produces a more uniform image,
- field size: the field will be more uniform at the centre (i.e. smaller field size) due to the collimator absorbing the peripheral variations,
- positioning: by aligning higher attenuating material towards the cathode and lower attenuating material towards the anode the resulting field is more uniform (Radiopaedia 2019).

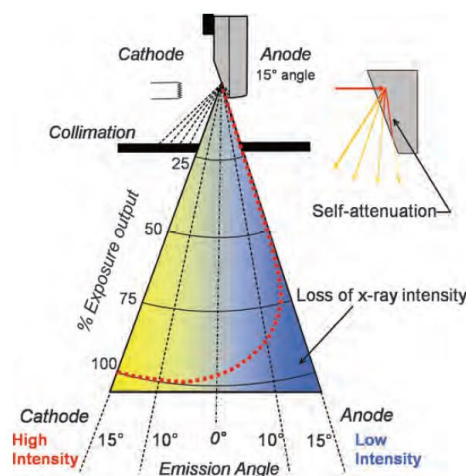


Figure 1.10 - The heel effect is a loss of intensity on the anode side of the X-ray field of view. It is caused by attenuation of the X-ray beam by the anode. Upper right is an expanded view that shows electrons interacting at depth within the anode and the resultant “self attenuation” of produced X-rays that have a trajectory towards the anode side of the field (J. T. Bushberg 2012).

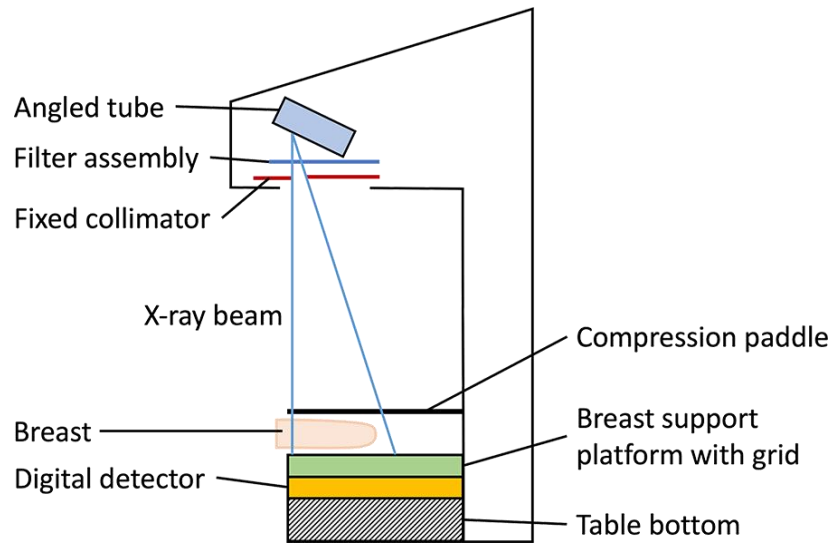


Figure 1.11 - Heel effect is usually exploited in mammography where there is need to penetrate different tissue thicknesses (Radiology C. - Mammography 2019).

2. RADIATION PROTECTION QUANTITIES

The aim of radiological protection is to control the exposure to ionising radiation for preventing acute damage and for limiting the risk of long term effects in humans to acceptable levels.

International Commission on Radiation Protection (ICRP) defined in its publication 60 (ICRP publication 60 1991), a radiation protection system that has been implemented in almost all national regulations and which contemplates three main type of quantities to reach three different objectives.

- The **primary quantities** allow the characterisation of the radiation fields and their interactions with matter thank to physical and measurable quantities.
- The **protection (or limiting) quantities** are used to quantify the extent of exposure of the human body to ionising radiation from both whole- and partial-body irradiation. The main uses of the protection quantities are the optimisation of protection and setting of control criteria: limits, constraints and reference levels.
- The **operational quantities** are used in practical measurement, since limiting quantities can not be applied directly since they are not directly measurable.

All these quantities are related with each other and define a clear hierarchy, as it can be seen in Figure 2.1, being the effective dose the limiting quantity in terms of which dose limits for workers and population are defined, playing then a central role in radiological protection.

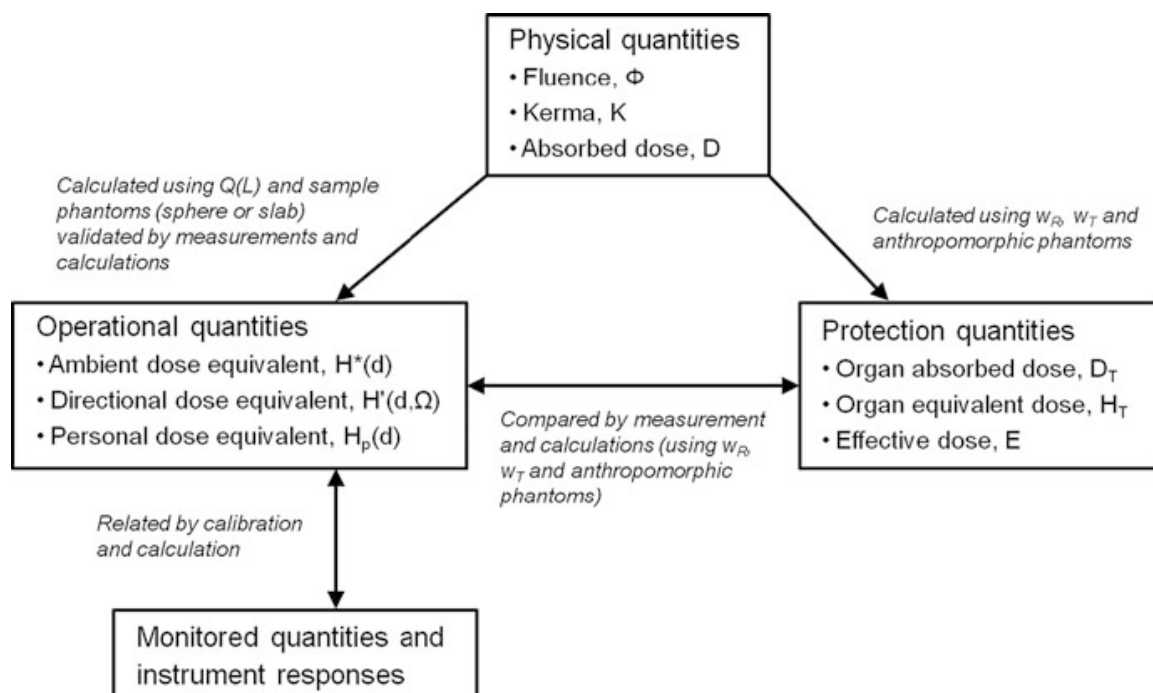


Figure 2.1 - Relationship between physical protection and operational quantities (IAEA 2000).

2.1 Dosimetry

Radiation interacts with matter in a series of processes in which particle energy is converted and finally deposited in matter. The fundamental primary quantities that describe these processes are

presented below considering the conversion and the deposition of energy. All units and quantities system refer to ICRU 85 2011. Some basic definitions are needed to show the quantities that are usually used to describe photon beams: fluence, energy fluence, fluence rate and energy fluence rate.

Fluence

From ICRU 85: “the fluence, ϕ , is the quotient of dN by da , where dN is the number of particles incident on a sphere of cross-sectional area da .”

$$\phi = \frac{dN}{da} \quad (2.0)$$

Unit: m^{-2} .

Energy fluence

From ICRU 85: “the energy fluence, ψ , is the quotient of dR by da , where dR is the radiant energy¹ incident on a sphere of cross-sectional area da .”

$$\psi = \frac{dR}{da} \quad (2.1)$$

Unit: $J m^{-2}$.

The distributions, ϕ_E and ψ_E of the fluence and energy fluence with respect to energy are by the following equations.

$$\phi_E = \frac{d\phi}{dE} \quad (2.2)$$

$$\psi_E = \frac{d\psi}{dE} \quad (2.3)$$

Where $d\phi$ is the fluence of particles of energy between E and $E+dE$, and $d\psi$ is their energy fluence. The relationship between the two distribution is given by equation 2.4.

$$\psi_E = E \phi_E \quad (2.4)$$

Fluence rate

From ICRU 85: “the fluence rate is the quotient of $d\phi$ by dt , where $d\phi$ is the increment of the fluence in the time interval dt .”

$$\dot{\phi} = \frac{d\phi}{dt} \quad (2.5)$$

Unit: $m^{-2} s^{-1}$.

¹ From ICRU 85: “the radiant energy is the energy, excluding rest energy, of the particles that are emitted, transferred or received”. Unit: J.

Energy-fluence rate

From ICRU 85: “the energy-fluence rate is the quotient of $d\psi$ by dt , where $d\psi$ is the increment of the energy fluence in the time interval dt .”

$$\dot{\psi} = \frac{d\psi}{dt} \quad (2.6)$$

Unit: W m^{-2} .

2.1.1 Conversion of energy

Kerma (kinetic energy released in matter)

The term conversion of energy refers to the transfer of energy from indirectly ionizing particles to secondary ionizing particles. The quantity kerma pertains to the kinetic energy of the charged particles liberated by uncharged particles; the energy expended to overcome the binding energies, usually a relatively small component, is, by definition, not included. Kerma involves the energy of outgoing charged particles as a result of interactions by incoming uncharged particles.

From ICRU 85: “the kerma, K , for ionizing uncharged particles, is the quotient of dE_{tr} by dm , where dE_{tr} is the mean sum of the initial kinetic energies of all the charged particles liberated in a mass dm of a material by the uncharged particles incident on dm ”.

$$K = \frac{dE_{tr}}{dm} \quad (2.7)$$

The SI unit of kerma is J kg^{-1} and its special name is Gray (Gy).

The quantity dE_{tr} includes the kinetic energy of the charged particles emitted in the decay of excited atoms/molecules or in nuclear de-excitation or disintegration.

Consider now the mass energy-transfer coefficient of a material, for indirectly ionising particles of a given type and energy, defined as in equation 2.8, that is the mean energy transferred to kinetic energy of charged particles by interactions of the uncharged particles of incident radiant energy¹ E in traversing a distance dl in the material of density ρ . The binding energies of the liberated charged particles are not to be included.

$$\frac{\mu_{tr}}{\rho} = \frac{1}{\rho dl} \frac{dE_{tr}}{E} \quad (2.8)$$

A fraction g of kinetic energy transferred to charged particles can be lost on average in radiative processes (i.e. bremsstrahlung, in-flight annihilation and fluorescence radiations) as the charged particles slow to rest in the material, and this fraction g is specific to the material. The product of μ_{tr}/ρ for a material and $(1-g)$ is called the mass energy-absorption coefficient, μ_{en}/ρ , of the material for uncharged particles.

$$\frac{\mu_{en}}{\rho} = \frac{\mu_{tr}}{\rho} (1 - g) \quad (2.9)$$

In dosimetric calculations, the kerma, K , is usually expressed in terms of the distribution, Φ_E , of the uncharged particle fluence with respect to energy (see page 16 – note 1) as in equation 2.10.

$$K = \int \Phi_E E \frac{\mu_{tr}}{\rho} dE = \int \Psi_E \frac{\mu_{tr}}{\rho} dE \quad (2.10)$$

Where μ_{tr}/ρ is the mass energy-transfer coefficient of the material for uncharged particles of energy E .

A quantity related to the kerma, named collision kerma, can be used when radiative losses are not negligible. In dosimetric calculations, the collision kerma, K_{col} , can be expressed in terms of the distribution, Φ_E , of the uncharged particle fluence with respect to energy as in equation 1.4, where \bar{g} is the mean value of g averaged over the distribution of the kerma with respect to the electron energy.

$$K_{col} = \int \Phi_E E \frac{\mu_{en}}{\rho} dE = \int \Psi_E \frac{\mu_{tr}}{\rho} (1 - g) dE = K(1 - \bar{g}) \quad (2.11)$$

Some important remarks about kerma are (D.R. Dance 2014):

- kerma may be defined in any material, so it is important that the material is declared when a value of kerma is presented;
- kerma is defined for indirectly ionizing radiation – uncharged particles such as photons and neutrons – and is related to the first step of transfer energy from these particles to matter, in which uncharged particles transmit kinetic energy to secondary charged particles.
- the kinetic energy transferred to the secondary particles is not necessarily spent in the volume where they were liberated. The kerma definition is constrained to the energy the secondary particles receive at the moment of liberation;
- for photons in the diagnostic energy range (up to 150 keV) interacting in low Z material, the differences between the energy absorption and energy transfer coefficients are negligible, as the fraction of the electron energy converted to bremsstrahlung x -ray is very small. For these conditions, the radiative kerma is negligible and the collision kerma is numerically equal to the kerma.,

Kerma rate

From ICRU 85: “the kerma rate, \dot{K} , is the quotient of dK by dt , where dK is the increment of kerma in the time interval dt ”.

$$\dot{K} = \frac{dK}{dt} \quad (2.12)$$

The SI unit of kerma is $J\ kg^{-1}\ s^{-1}$ and its special name is $Gy\ s^{-1}$.

Exposure

From ICRU 85: “the exposure, X , is the quotient of dq by dm , where dq is the absolute value of the mean total charge of the ions of one sign produced when all the electrons and positrons liberated or created by photons incident on a mass dm of dry air are completely stopped in dry air”.

$$X = \frac{dq}{dm} \quad (2.13)$$

The SI unit of exposure is C kg⁻¹.

The ionization produced by electrons emitted in atomic/molecular relaxation processes is included in dq . The ionization due to photons emitted by radiative processes (i.e. bremsstrahlung and fluorescence radiations) is not included in dq . Except for this difference, significant at high energies, the exposure, as defined above, is the ionization analogue of the dry-air collision kerma. For photons of the order of 1 MeV or below, for which the value of g is small, the exposure can be further approximated as in equation 2.14, where K_{air} is the dry-air kerma for primary photons, \bar{g} is the mean value of g averaged over the distribution of the kerma with respect to the electron energy, e is the elementary charge and W is the mean energy expended in dry air per ion pair formed.

$$X \approx \frac{e}{W} K_{air} (1 - \bar{g}) = \frac{e}{W} K_{col,air} \quad (2.14)$$

Exposure rate

From ICRU 85: “the kerma rate, \dot{X} , is the quotient of dX by dt , where dX is the increment of kerma in the time interval dt ”.

$$\dot{X} = \frac{dX}{dt} \quad (2.15)$$

The SI unit of kerma is C kg⁻¹s⁻¹.

2.1.2 Deposition of energy

Energy deposit

From ICRU 85: “the energy deposit, \mathcal{E}_i , is the energy deposited in a single interaction, i , thus

$$\mathcal{E}_i = \mathcal{E}_{in} - \mathcal{E}_{out} + Q \quad (2.16)$$

where \mathcal{E}_{in} is the energy of the incident ionizing particle (excluding rest energy), \mathcal{E}_{out} is the sum of the energies of all charged and uncharged ionizing particles leaving the interaction (excluding rest energy), and Q is the change in the rest energies of the nucleus and of all elementary particles involved in the interaction ($Q>0$: decrease of rest energy; $Q<0$: increase of rest energy)”.

The SI unit of kerma is J. This quantity may also be expressed in eV. Note that \mathcal{E}_i is a stochastic quantity. For the energies encountered in diagnostic radiology, Q is negligible (D.R. Dance 2014).

Energy imparted

From ICRU 85: “the energy imparted, \mathcal{E} , to the matter in a given volume is the sum of all energy deposits in the volume, thus

$$\mathcal{E} = \sum_i \mathcal{E}_i \quad (2.17)$$

where the summation is performed over all energy deposits, \mathcal{E}_i , in that volume”.

The SI unit of kerma is J. This quantity may also be expressed in eV.

Note that \mathcal{E} is a stochastic quantity.

Absorbed dose

From ICRU 85: “the absorbed dose, D , is the quotient of $d\bar{\mathcal{E}}$ by dm , where $d\bar{\mathcal{E}}$ is the mean energy imparted by ionizing radiation to matter of mass dm ”.

$$D = \frac{d\bar{\mathcal{E}}}{dm} \quad (2.18)$$

The SI unit of kerma is J kg^{-1} and its special name is Gray (Gy).

Absorbed dose rate

From ICRU 85: “the absorbed dose rate, \dot{D} , is the quotient of dD by dt , where dD is the increment of absorbed in the time interval dt ”.

$$\dot{D} = \frac{dD}{dt} \quad (2.19)$$

The SI unit of absorbed dose rate is $\text{J kg}^{-1} \text{s}^{-1}$ and its special name is Gy s^{-1} .

2.1.3 Relation between dosimetric primary quantities

Kerma and dose (charged particle equilibrium)

Generally, the transfer of energy (kerma) from the photon beam to charged particles at a particular location does not lead to the absorption of energy by the medium (absorbed dose) at the same location. This is due to the non-zero (finite) range of the secondary electrons released through photon interactions.

Since radiative photons mostly escape from the volume of interest, one relates absorbed dose usually to collision kerma. In general, however, the ratio of dose and collision kerma is often denoted as in equation 2.20.

$$\beta = \frac{D}{K_{col}} \quad (2.20)$$

If radiative photons escape the volume of interest, an assumption is made that $\beta \approx 1$.

The relationship between collision kerma and absorbed dose under build-up conditions is illustrated in Figure 2.2: under conditions of charged particle equilibrium (CPE) in part (a) and under conditions of transient charged particle equilibrium (TCPE) in part (b).

As an energy photon beam penetrates the medium, collision kerma is maximal at the surface of the irradiated material because photon fluence is greatest at the surface. Initially, the charged particle fluence, and hence the absorbed dose, increases as a function of depth until the depth of dose maximum z_{\max} is attained.

If there were no photon attenuation or scattering in the medium, but yet production of electrons, a hypothetical situation, as illustrated in Figure 2.2(a), would occur: the build-up region (with $\beta < 1$) is followed by a region of complete CPE where, i.e., $\beta = 1$.

As the photon interactions occur, electrons are liberated, contributing to the growth of the energy imparted, according to the growth of the ionization in the material. Thus, there is a build-up region for the dose, at small depths in the medium, as shown in Figure 2.2. The build-up region has dimensions (z_{\max}) similar to the range of the charged particles in the medium. For high energy photons, this region can extend to 1 or 2 cm, and this effect is responsible for the known effect of skin sparing in external radiotherapy. For diagnostic photon beams, the energies are lower, and the electron ranges are too small to produce this effect: the maximum dose is reached within the skin (D.R. Dance 2014).

In the more realistic situation, however, due to photon attenuation and scattering in the medium, a region of TCPE occurs (Figure 2.2(b)) where there exists an essentially constant relation between collision kerma and absorbed dose. Beyond the maximum, the absorbed dose is larger than the collision kerma, as the energy imparted is a result of charges liberated by photon fluences slightly greater than the fluence in the volume of interest. This relation is practically constant since (except for low energy photon beams): the average energy of the generated electrons and hence their range does not change appreciably with depth in the medium (J.P. Seuntjens n.d.). Usually, the approximation $\beta \approx 1$ can be used for diagnostic radiology and low Z materials (D.R. Dance 2014).

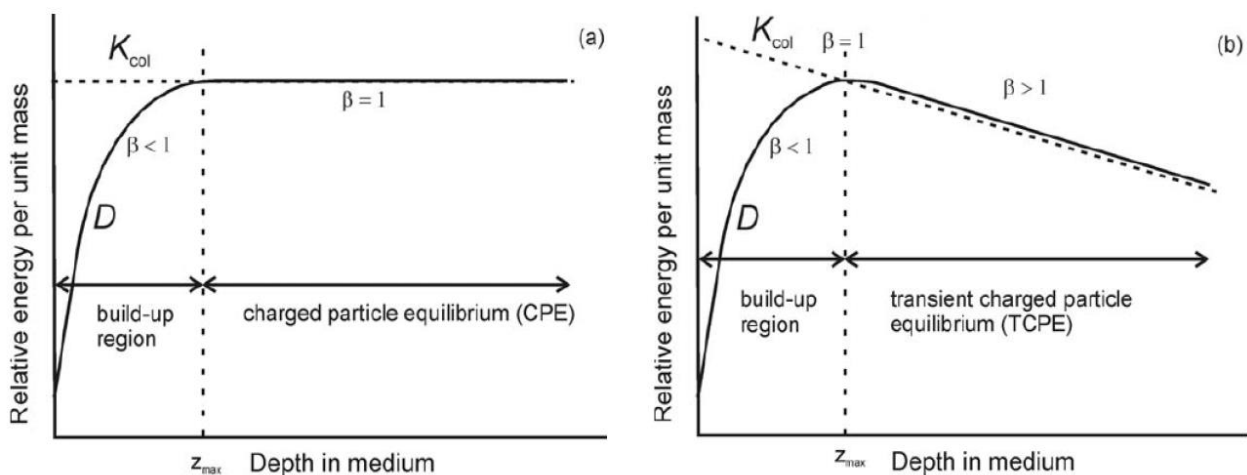


Figure 2.2 - Collision kerma and absorbed dose as a function of depth in a medium, irradiated by a high-energy photon beam for (a) the hypothetical case of no photon attenuation or scattering and for (b) the realistic case (J.P. Seuntjens n.d.).

2.2 Limiting quantities

The absorbed dose can be averaged over larger volumes, like tissues and organs, considering also the radiation type. Nevertheless, this quantity is unable to estimate, by definition, the radiation risk due to induced stochastic health effects. For this reason, additional quantities were defined to take into account variations in the biological effectiveness of radiations as well as the different sensitivities of organs and tissues of the human body to each ionising radiation.

The procedure for the assessment of effective dose adopted by the International Commission on Radiological Protection (ICRP) is to use absorbed dose as the fundamental physical quantity, to average it over specified organs and tissues, to apply suitably chosen weighting factors to take account of differences in biological effectiveness of different radiations to give the quantity equivalent dose, and to consider differences in sensitivities of organs and tissues to stochastic health effects (ICRP 103 2007).

2.2.1 Equivalent dose and radiation weighting factors

The protection quantities are used to specify exposure limits to ensure that the occurrence of stochastic health effects is kept below unacceptable levels and that tissue reactions are avoided. The definition of the protection quantities is based on the average absorbed dose, $D_{T,R}$ in the volume of a specified organ or tissue T (see Table 2-2), due to radiation of type R (see Table 2-1). The radiation R is given by the type and energy of radiation either incident on the body or emitted by radionuclides residing within it. The protection quantity equivalent dose in an organ or tissue, H_T , is then defined as in the following equation.

$$H_T = \sum_R w_R D_{T,R} \quad (2.21)$$

Where w_R is the radiation weighting factor for radiation R. The sum is performed over all types of radiations involved. The unit of equivalent dose is Sievert (Sv). The recommended radiation weighting factors for different radiation type are given in ICRP 103 and shown in Table 2-1. In the case of neutrons, Figure 2.3 shows the continuous function of neutron energy defined in ICRP 103.

Recommended radiation weighting factors.	
Radiation type	Radiation weighting factor, w_R
Photons	1
Electrons and muons	1
Protons and charged pions	2
Alpha particles, fission fragments, heavy ions	20
Neutrons	A continuous function of neutron energy

All values relate to the radiation incident on the body or, for internal radiation sources, emitted from the incorporated radionuclide(s).

Table 2-1 - Radiation weighting factors from ICRP 103.

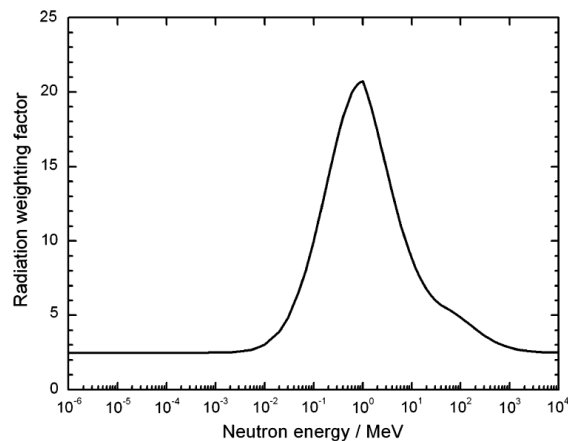


Figure 2.3 - Radiation weighting factor for neutrons versus neutron energy (ICRP 103 2007).

2.2.2 Effective dose and tissue weighting factors

The relationship between equivalent dose and the probability of stochastic effects is found to vary also with the organ or tissue irradiated. For this purpose, ICRP Publication 60 (ICRP publication 60 1991) introduced the notion of effective dose, E , which is defined by weighted sum of tissue equivalent doses as in the following equation.

$$E = \sum_T w_T H_T = \sum_T w_T \sum_R w_R D_{T,R} \quad (2.22)$$

Where w_T is the tissue weighting factor for tissue T and R , $\sum w_T = 1$. The sum is performed over all organs and tissues of the human body considered to be sensitive to the induction of stochastic effects. These w_T values are chosen to represent the contributions of individual organs and tissues to overall radiation detriment from stochastic effects. The unit of effective dose is Sievert (Sv). The recommended tissue weighting factors for different organs and tissues are given in ICRP 103 and shown in Table 2-2.

Recommended tissue weighting factors.

Tissue	w_T	$\sum w_T$
Bone-marrow (red), Colon, Lung, Stomach,	0.12	0.72
Breast, Remainder tissues*		
Gonads	0.08	0.08
Bladder, Oesophagus, Liver, Thyroid	0.04	0.16
Bone surface, Brain, Salivary glands, Skin	0.01	0.04
	Total	1.00

* Remainder tissues: Adrenals, Extrathoracic (ET) region, Gall bladder, Heart, Kidneys, Lymphatic nodes, Muscle, Oral mucosa, Pancreas, Prostate (♂), Small intestine, Spleen, Thy-mus, Uterus/cervix (♀).

Table 2-2 - Tissue weighting factors from ICRP 103.

2.3 Operational quantities

The body-related protection quantities (equivalent dose and effective dose) are not measurable in practice and therefore cannot be used directly as quantities in radiation monitoring. Operational quantities are, therefore, used for the assessment of effective dose or equivalent doses in tissues or organs. Operational quantities are aimed at providing an estimate or upper limit for the value of the protection quantities related to an exposure, or potential exposure of persons under most irradiation conditions. They are often used in practical regulations or guidance.

Specific operational dose equivalent quantities are defined for radiation monitoring in situations of external exposure (area or individual monitoring). In routine monitoring, the values of these dose-equivalent quantities are taken as sufficiently precise assessments of effective dose or skin dose, respectively, especially if their values are below the protection limits.

Operational dose quantities are used for monitoring external exposures because:

- point quantities are needed for area monitoring;
- instruments for radiation monitoring need to be calibrated in terms of a physical quantity for which calibration standards exist.

It is worth noting that the operational quantities, referring to a certain point, are additive quantities: this is the main improvement with respect to units system before ICRU 51 1993 (“maximum dose equivalent” etc.)

The quantity dose equivalent, H , is defined as in the following equation.

$$H = Q D \quad (2.23)$$

Where D is the absorbed dose at the point of interest in tissue and Q the corresponding quality factor at this point, the value of which is determined by the type and energy of charged particles passing a small volume element at this point. It is well known that the biological effectiveness of a radiation is correlated with the ionisation density along the track of charged particles in tissue. Therefore, Q is defined as a function of the unrestricted linear energy transfer, L_∞ (often denoted as L or LET), of charged particles in water. The quality factor function $Q(L)$ was given in Publication 60 (see equation 2.24, ICRP publication 60 1991).

$$Q(L) = \begin{cases} 1 & L < 10 \text{ keV}/\mu\text{m} \\ 0.32L - 2.2 & 10 \leq L < 100 \text{ keV}/\mu\text{m} \\ 300/\sqrt{L} & L > 100 \text{ keV}/\mu\text{m} \end{cases} \quad (2.24)$$

The function is the outcome of judgements taking account of results of radiobiological investigations on cellular and molecular systems as well as on the results of animal experiments.

The quality factor Q at a point in tissue is then given by the following equation.

$$Q = \frac{1}{D} \int_{L=0}^{\infty} Q(L) D_L dL \quad (2.25)$$

Where $D_L = dD/dL$ is the distribution of D in L for the charged particles contributing to absorbed dose at the point of interest.

Different operational dose quantities are required for different tasks in radiological protection. These include area monitoring for controlling the radiation in workplaces and for defining controlled or restricted areas, and individual monitoring for the control and limitation of individual exposures. While measurements with an area monitor are preferably performed free in air, personal dosimeters are worn on the body. As a consequence, in a given situation, the radiation field 'seen' by an area monitor free in air differs from that 'seen' by a personal dosimeter worn on the body where the radiation field is strongly influenced by the backscatter and absorption of radiation in the body. The use of different operational dose quantities reflects these differences.

2.3.1 Operational quantities for area monitoring

For a complete understanding of the next definitions, two concepts have to be clarified.

ICRU sphere phantom

For all types of external radiation, the operational quantities for area monitoring are defined on the basis of a dose equivalent value at a point in a simple phantom, the ICRU sphere. It is a sphere of tissue-equivalent material (30 cm in diameter, ICRU (soft) tissue with density: 1 g cm^{-3} , and mass composition: 76.2% oxygen, 11.1% carbon, 10.1% hydrogen, and 2.6% nitrogen). For radiation monitoring, in most cases it adequately approximates the human body as regards the scattering and attenuation of the radiation fields under consideration.

Aligned and expanded radiation field

The operational quantities for area monitoring defined in the ICRU sphere should retain their character of a point quantity and the property of additivity. This is achieved by introducing the terms 'expanded' and 'aligned' radiation field in the definition of these quantities.

An expanded radiation field (Figure 2.4 and Figure 2.5), defined as a hypothetical field, is a radiation field in which the spectral and the angular fluence have the same value in all points of a sufficiently large volume equal to the value in the actual field at the point of interest. The expansion of the radiation field ensures that the whole ICRU sphere is thought to be exposed to a homogeneous radiation field with the same fluence, energy distribution and direction distribution as in the point of interest of the real radiation field.

If all radiation is aligned in the expanded radiation field so that it is opposed to a radius vector X specified for the ICRU sphere, the aligned and expanded radiation field is obtained (Figure 2.4 and Figure 2.5). In this hypothetical radiation field, the ICRU sphere is homogeneously irradiated from one direction, and the fluence of the field is the integral of the angular differential fluence at the point of interest in the real radiation field over all directions. In the expanded and aligned radiation field, the value of the dose equivalent at any point in the ICRU sphere is independent of the direction distribution of the radiation in the real radiation field. Conversion coefficients relating radiation field quantities to the operational quantities are usually calculated assuming a vacuum outside of the phantom considered.

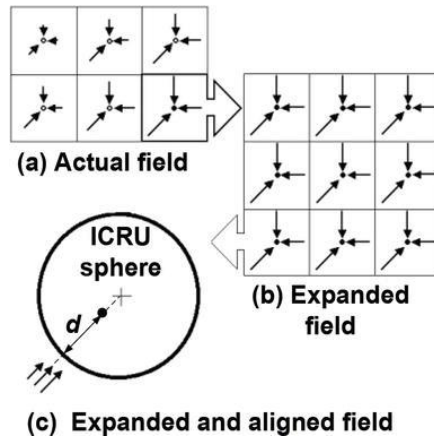


Figure 2.4 - Actual, expanded and aligned radiation field (Kutkov 2018).

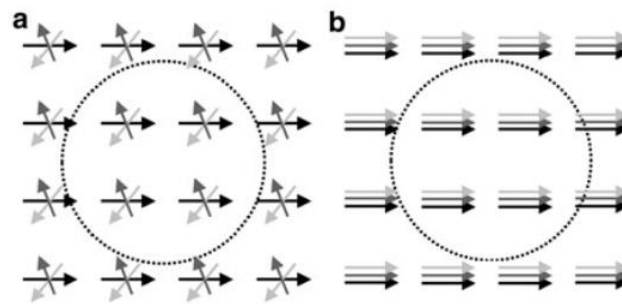


Figure 2.5 - Diagram of an expanded (a) and an oriented (b) radiation field (Kutkov 2018).

Two operational quantities are considered for area monitoring to assess effective dose. The ambient dose equivalent, $H^*(10)$, which is appropriate for strongly penetrating radiation (photons above 12 keV, neutrons) and the directional dose equivalent, $H'(d, \Omega)$, only suitable for weakly penetrating radiation (α or β particles).

The ambient dose equivalent, $H^*(10)$, at a point in a radiation field, is the dose equivalent that would be produced by the corresponding expanded and aligned field in the ICRU sphere at a depth of 10 mm on the radius vector opposing the direction of the aligned field.

The directional dose equivalent, $H'(d, \Omega)$, at a point in a radiation field, is the dose equivalent that would be produced by the corresponding expanded field in the ICRU sphere at a depth, d , on a radius in a specified direction X . For low-penetrating radiation it is $d = 0.07$ mm, and $H'(d, X)$ is then written $H'(0.07, X)$.

2.3.2 Operational quantities for individual monitoring

Individual monitoring of external exposure is usually performed with personal dosimeters worn on the body, and the operational quantity defined for this application takes this situation into account. The true value of the operational quantity is determined by the irradiation situation near the point where the dosimeter is worn. The operational quantity for individual monitoring is the personal dose equivalent, $H_p(d)$.

The personal dose equivalent, $H_p(d)$, is the dose equivalent in soft tissue at an appropriate depth, d , below a specified point on the human body. The specified point is usually given by the position where the individual dosimeter is worn. For the assessment of effective dose a depth $d = 10$ mm is recommended, and for assessing equivalent dose to the skin, and to the hands and feet, a depth $d = 0.07$ mm. In special cases of monitoring the dose to the lens of the eye, it was proposed that a depth $d = 3$ mm would be appropriate.

The operational quantities for individual monitoring meet several criteria. They are equally defined for all types of radiation, additive with respect to various directions of radiation incidence, take into account the backscattering from the body and can be approximately measured with a dosimeter worn on the body. An operational quantity for individual monitoring should allow the effective dose to be assessed or should provide a conservative estimate under nearly all irradiation conditions. This, however, requires that the personal dosimeter be worn at a position on the body which is representative with respect to the exposure. For a dosimeter position in front of the trunk, the quantity $H_p(10)$ mostly furnishes a conservative estimate of E even in cases of lateral or isotropic radiation incidence on the body. In cases of exposure from the back only, however, a dosimeter worn at the front side and correctly measuring $H_p(10)$, will not appropriately assess E . Also in cases of partial body exposures the reading of a personal dosimeter may not provide a representative value for the assessment of effective dose. It is, therefore, an additional requirement in individual dosimetry that the personal dosimeter must be worn at a position on the body which is representative of body exposure. For a dosimeter position in front of the trunk, however, the quantity $H_p(10)$ mostly furnishes a conservative estimate of E even in cases of lateral or isotropic radiation incidence on the body (Dietze 2019).

A further requirement for an operational quantity is that it allow dosimeters to be calibrated under reference conditions in terms of that quantity. The personal dose equivalent is defined in the individual human body and it is obvious that individual dosimeters cannot be calibrated in front of a real human body. For a calibration procedure, the human body must therefore be replaced by an appropriate phantom. Some standard phantoms have been defined by ISO for this purpose and the definition of $H_p(10)$, $H_p(0.07)$ and $H_p(3)$ is extended to define positions and doses not only in the human body but also in the proper phantoms of ICRU tissue. In reference radiation fields used for calibration, the values of the quantities in these phantoms are defined as the true values of the corresponding H_p -quantities (Dietze 2019).

2.4 Calibration principle

Calibration can be defined as a set of operations performed under specified conditions to establish the relationship between values indicated by a measuring instrument or system and the corresponding known true values of a quantity to be measured. In the field of radiation protection, the measuring instruments are usually area survey meters or personal dose and dose rate meters. The calibration of personal dosimeters or area survey meters used for radiation protection purposes is mostly a three step process (Dietze 2019).

First, the value of a physical quantity such as air kerma or particle fluence for which primary standards usually exist, is determined by a reference instrument at a reference point in the radiation field used for calibration.

Second, the value of the appropriate radiation protection quantity is determined by application of a conversion coefficient relating the physical quantity to the radiation protection quantity. Conversion coefficients used to determine operational quantities for neutrons and photons were evaluated by international committees and finally accepted for general use by international agreements.

Third, the device being calibrated is placed at this reference point to determine the response of the instrument to the radiation protection quantity, e. g. the personal, ambient or directional dose equivalent.

For example, the personal dosimeter is fixed to the front face of the phantom so that the reference direction of the dosimeter coincides with the normal to the front face of the phantom. The reference point of the dosimeter is placed at the point of test. When angular studies are performed, the dosimeter, together with the phantom, is rotated about an axis passing through the reference point.

If several dosimeters are irradiated simultaneously, they should be fixed to the front face of the phantom in a circular pattern around the centre of the front face so that no sensitive element of a dosimeter is positioned outside a circle 15 cm in diameter (Dietze 2019).

The calibration methods described in this part closely follow the recommendations of the International Organization for Standardization (ISO) dealing with reference radiations (e.g. ISO 4037-1 2016). These methods are applicable only to the determination of dose equivalents from external radiation sources.

2.5 New ICRU approach on operational quantities

The operational quantities in current use were defined in the 1980s (ICRU 39 1985, ICRU report 43 1988), which have been introduced into practice in many countries under radiological protection directives and regulations over the past 30 years. Nevertheless, the existing system has some limitations and needs further improvement to consider changes in the field of application of the protection quantities and operational quantities (ICRP 103 2007, ICRP publication 116 2010, ICRU 84 2010).

ICRU Report Committee 26 (A. Endo 2015) investigated a set of alternative definitions for the operational quantities. The major change to the currently favoured set of quantities is redefinition of the operational quantities, from being based on doses at specific point in the ICRU sphere and soft tissue, to being based on particle fluence and conversion coefficients for effective dose and absorbed dose to the lens of the eye and local skin.

The current protection quantities and operational quantities are now related to basic physical quantities which are generally used in radiation metrology and radiation dosimetry, and are obtained through primary standards at national standards laboratories. Reference conversion coefficients from the physical radiation field quantities, fluence and air kinetic energy per unit mass (kerma), to the protection and operational quantities are calculated using the definitions of the quantities. For the operational quantities, conversion coefficients are used for the calibration of radiological protection dosimeters. The existing quantities system has some limitations (A. Endo 2015).

- There is the fundamental problem that the ICRU 4-element tissue (density of 1 g cm^{-3} , composition by mass of 76.2% oxygen, 11.1% carbon, 10.1% hydrogen and 2.6% nitrogen) cannot be fabricated. Therefore, there are problems with a few aspects of strict metrology.
- The dose equivalent is defined as the product of Q and D at a point in tissue. This specific definition can never be realised experimentally and can, hence, only be calculated based on knowledge of the radiation field of secondary charged particles at the point of interest.
- The values of conversion coefficients for the operational quantities given in Publication 74 (ICRP publication 74 1995) and ICRU Report 57 (ICRU report 57 1995) were calculated in some cases using the kerma approximation method for energies where this approximation is not appropriate. For superficial organs (e.g. skin, breast, and testes), the kerma approximation leads to overestimations of absorbed dose of up to a factor of two at a photon energy of 10 MeV. For the superficial organs, the kerma approximation is only valid below $\sim 1 \text{ MeV}$ (see Figure 2.6 and Figure 2.7).

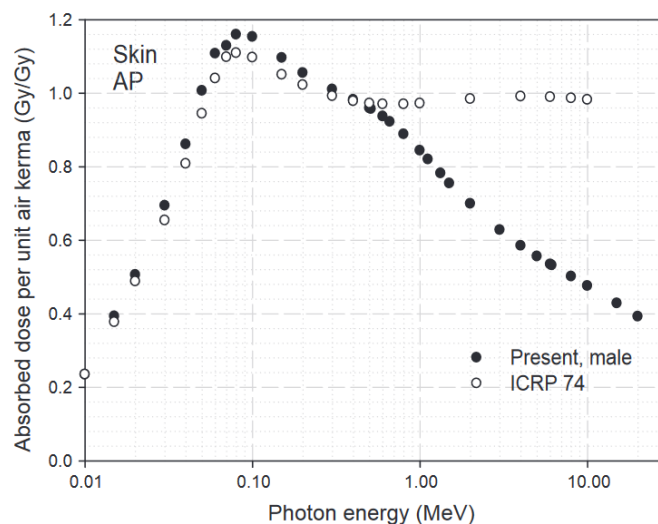


Figure 2.6 - Comparison of skin absorbed dose conversion coefficients for the male phantom for antero-posterior geometry as calculated for ICRP Publication 116 (ICRP publication 116 2010) and those of ICRP Publication 74 (ICRP publication 74 1995).

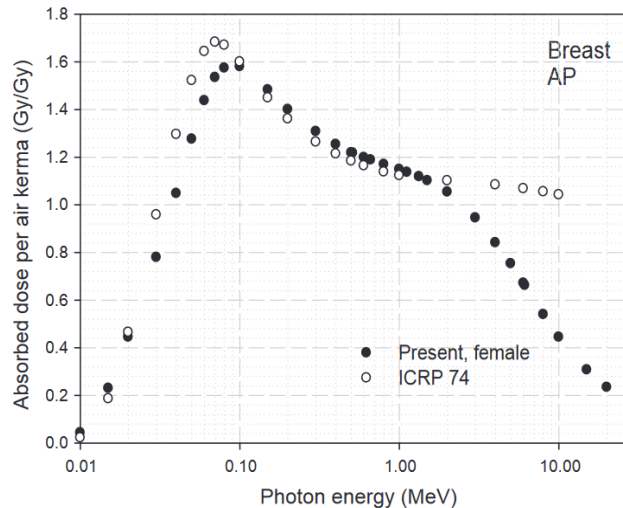


Figure 2.7 - Comparison of the breast absorbed dose conversion coefficients of the female phantom for antero-posterior geometry as calculated for ICRP Publication 116 (ICRP publication 116 2010) and those of ICRP Publication 74 (ICRP 74 1996).

- The operational quantities are not always close estimates of the protection quantities in higher energy fields, and the effective dose is underestimated.
- Based on recent epidemiological studies, ICRP has recommended lowering the occupational equivalent dose limit to the lens of the eye (ICRP 118 2012). There is now strong interest in better modelling of the lens of the eye (R. Behrens 2011) for the assessment of dose to the lens of the eye and in terms of determining the operational quantity, $H_p(3)$ (A. Endo 2015).

Therefore, as a favoured approach, ICRU Report Committee 26 proposes to define the operational quantities based on the protection quantities. The approach is justified because the reference values of the conversion coefficients for the protection quantities (ICRU 84 2010) are available. This concept can help avoid the use of different phantoms and different weighting factors for radiation quality between the protection quantities and the operational quantities, and simplifies the system of radiation monitoring and dose assessment.

Equivalent dose to the lens of the eye and local skin has been used to specify limits to prevent tissue reactions. The equivalent dose is the product of absorbed dose and w_R , which is only defined for stochastic effects. Therefore, the operational quantities for the lens of the eye and local skin could be set more appropriately in terms of absorbed dose.

Calibration phantoms for personal dosimeters remain unchanged, and there are a few minor changes to be made to the dosimetry of the International Organisation for Standardisation reference fields and calibration procedures.

Therefore, this new set of operational quantities was defined using the values of conversion coefficients from particle fluence to effective dose and absorbed dose to the lens of the eye and local skin.

3 THE X-RAY IRRADIATION FACILITY: description of the experimental setup

This chapter describes the experimental setup used for the measurements taken for the metrological qualification of the X-ray unit placed in the irradiation facility assembled during this PhD work. The laboratory structure is presented as first, then there is the description of the detectors that were used during the characterization measurements, a brief processing electronic explanation is reported and finally the acquisition system is described.

3.1 Description of the laboratory

The first part of the PhD project was focused on installing and assembling the machine. Together with the technician of the Burgatti enterprise, that provided this customized X-ray irradiation unit, at the beginning my activity was based on the preparation and the setting up of the X-ray unit with its high voltage generator. In the following photographs (see Figure 3.1) it is possible to see the work in progress in the irradiation room, where the X-ray tube, its generator and the voltage divider to precisely monitor the high voltage supply were arranged.

The X-ray tube is not a conventional commercial machine, but it is a customized machine (improved heat transfer for long irradiation – scopy mode) modified to be used for research work, like dosimetrical and metrological application.



Figure 3.1 - Work in progress in the irradiation room: assembling and setting up the X-ray irradiation unit.

The facility is located at the Key Enabling Technologies Laboratory (KET-Lab) c/o Agenzia Spaziale Italiana (ASI) di Via del Politecnico snc, Roma. All the measurements have been made in this context.

The rooms available in the laboratory are made up of two rooms (see Figure 3.2):

- **the irradiation room**, where the suitably shielded irradiation unit is placed together with the mechanical bench for the positioning of the instrumentation under test,
- **the control room**, where, in addition to managing and monitoring the various operating parameters to control the X-ray tube, it is possible to find a free space for the experiment preparation or for the post processing.

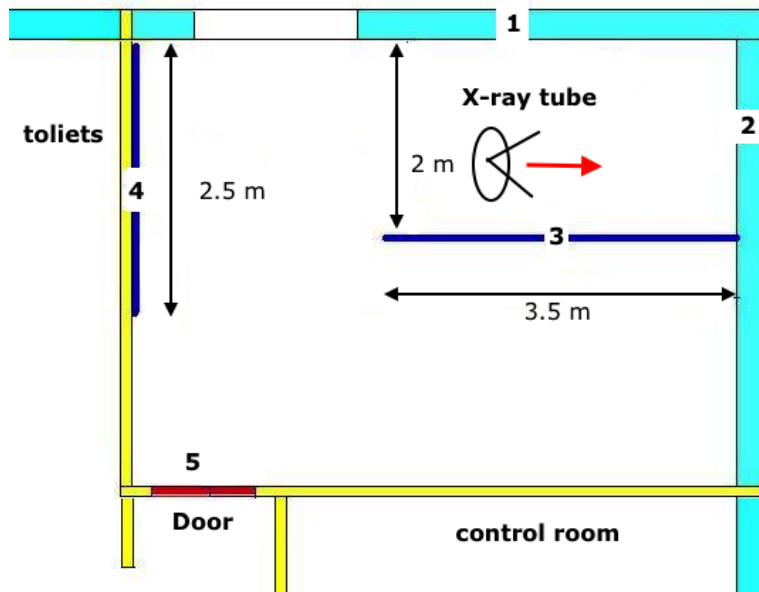


Figure 3.2 - Control room and experimental hall schematic view from above. The light blue walls are the external walls of the ASI building; the yellow ones are the walls that delimit the rooms and the blue ones are lead walls placed for staff radioprotection. The numbers are the walls identification names.

The control room has a workstation equipped with the X-ray tube control console, a PC station, a monitor linked to the experimental hall control video camera and a device for inserting a key, which enables the use of the X-ray tube. The command panel allows to set up the kilovolt, the tube current and the time for an irradiation. Next to this there is the PC for the data acquisition (Figure 3.3).



Figure 3.3 - Photograph of the control room (on the top), control console (bottom right) and device for the X-ray tube ignition (bottom left). On the latter, it has been placed a passive dosimeter for the necessary radioprotection tests.

The experimental hall lodges the X-ray tube and all the devices used to perform the measurements described in the following chapters:

- X-ray tube RTC1000 HS, serial number 735019;
- X-ray tube assembly C100XT, serial number X0995;
- Endeavour generator R306.35 (50 HF R);
- voltage divider GiCi 2000 (H917);
- collimator;
- pressure sensor Motorola's MPXAZ4115A;
- temperature sensor Innovative Sensor Technology's TSic 301/306;
- Bosh self-levelling cross-line laser;
- aluminium (Al), copper (Cu) and tin (Sn) absorbers;
- laser meter;
- mechanical bench (self-designed);
- monitor ionization chamber (self-designed and self-constructed);
- ionization chamber for air kerma measurements PTW type TW32002, serial number 000591;
- cadmium telluride (CdTe) Eurorad spectrometer S1.1.1U, serial number 1100-25A;
- Hamamatsu S3590-09 silicon detector;
- Gafchromic films XR-QA2;
- data AcQuisition (DAQ) National Instruments NI USB-6216 BNC and NI USB-6366;
- high voltage power supply CAEN;
- low voltage power supply (12 V and 6 V battery);
- processing electronics associated with the detector.

3.2 The irradiation room

3.2.1 The irradiation line

Referring to Figure 3.2, looking the room from the door, the X-ray tube is placed close to the lead wall n. 3 and has the 2,5 m long mechanical bench on its front. The X-ray tube has further lead shielding on the back, left and right sides, to screen the room from the residual X-rays emerging from the tube assembly. In Figure 3.4 a complete view of the experimental hall is shown.

In front of the tube port there is a medical collimator provided with a projection lamp and a shutter. This is a "beam direction" device along with an arrangement of mirrors and light are used in such a way that the light and X-ray fields match each other (remember Figure 1.6).

The shutter is made up of four lead jaws which absorb the photons, thus focus the radiation accordingly to the area of interest. They allow different projections of X-ray fields by modifying its rectangular shape from few mm to about 20 cm long sides.

On the top of the collimator, there is an electronic circuit that allows to measure environmental pressure and temperature for kerma corrections (equation 3.1).

At the tube port, a support was provided for positioning a monitor ionization chamber in direct contact with the collimator. In front of the detector and thanks to this support there is also the possibility of placing filters (aluminium, copper or tin disks) needed to obtain an energy distribution of the beams as close as possible to that specified in the International Organization for Standardization (ISO) 4037 (see 1.2.2 Filtration, see Figure 3.5).

In Figure 3.5, it is possible to see the "reference point" for all measurements of device under test (DUT) distance: this point lies on the filter support surface in contact with collimator. In order to set precisely the distance along the irradiation line it can be used a laser meter (see Figure 3.5).

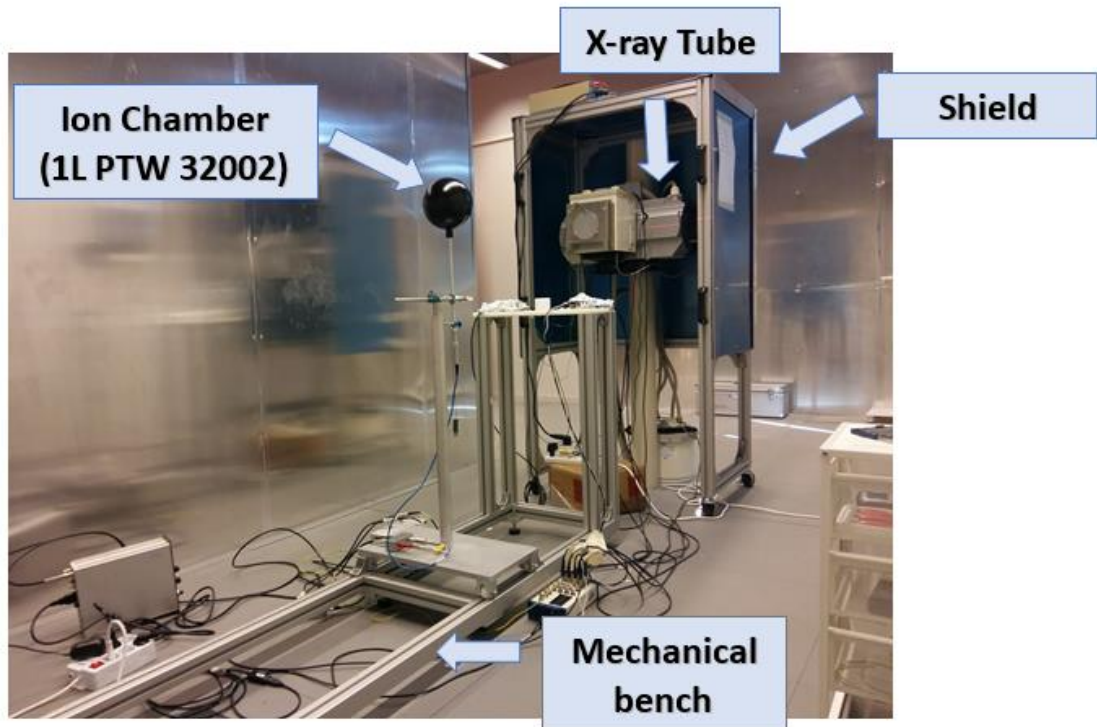


Figure 3.4 - Complete vision of the experimental hall. X-ray tube with the additional lead shielding (blue walls in Figure 3.2), collimator, monitor chamber support, metal filters, mechanical bench, a cart with PTW chamber, NI DAQ.

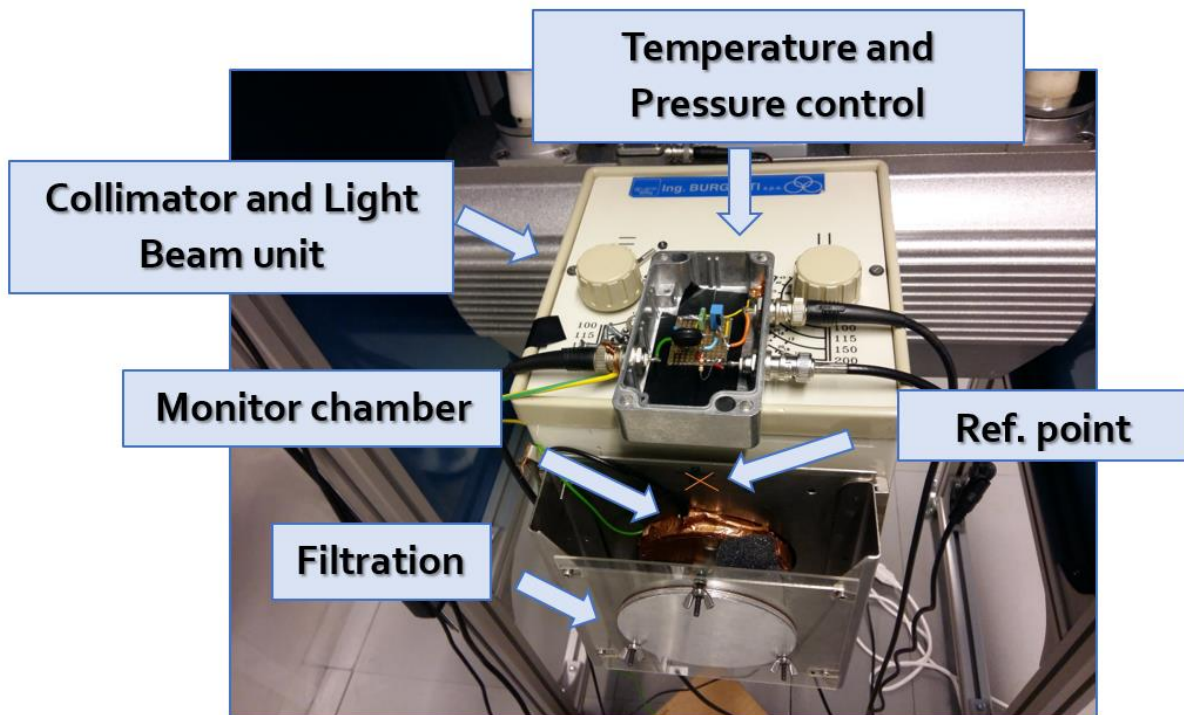


Figure 3.5 - The collimator and support for the monitor ionization chamber.

3.2.2 The mechanical bench and the alignment system

The mechanical bench was designed so that the devices to be irradiated are best placed during the various tests (see Figure 3.6). It is positioned in front of the X-ray tube and consists of two aluminium rails of about 2,5 m long length and some aluminium or polyethylene carts that, by sliding on the rails, allow the positioning of the devices at the desired distance from the X-ray tube.

The trolley, which can be fastened to the rails by means of special locks, consists of a telescopic rod ending on a platform provided with a specific support for fastening the device to be used (see Figure 3.7).

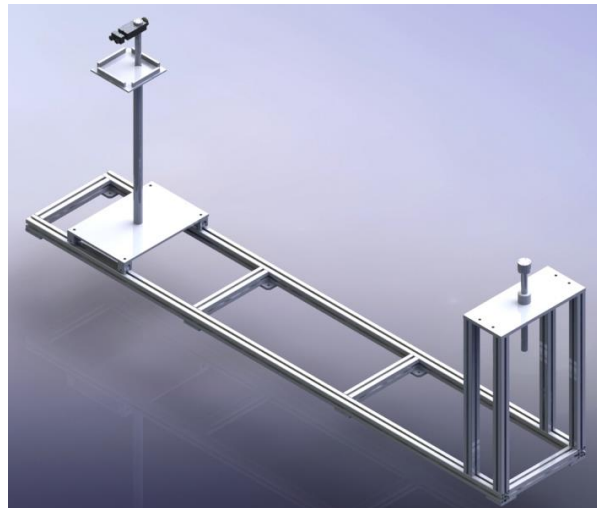


Figure 3.6 - CAD Project of the mechanical bench, the right side is the X-ray tube side.

The described mechanical bench fixes the relative horizontal position between the X-ray tube field and detector centres: the two centres are perfectly aligned. The cart telescopic rod is the device that enables the user to vertically align this two centres.

This alignment is achieved thanks to the collimator lamp and to a self-levelling cross line laser put in front of the tube exit window on wall n. 2 of Figure 3.2. The lamp in the beam collimator unit projects a forward light cone that illuminates the field, whose centre is indicated by the insertion of an opaque cross on the X-ray tube window. On the other side the laser enlightens a red cross; the centres of these two crosses perfectly match (see Figure 3.8).



Figure 3.7 - Trolley and supports projects for a slim stem ionization chamber. The left image shows the support mounting along the mechanical bench while the right one shows the detail of a holder indent for positioning the detector stem.

Thanks to this system it is possible to check that the device under test placed along the irradiation line is centred within the beam and that is uniformly illuminated (see Figure 3.9).

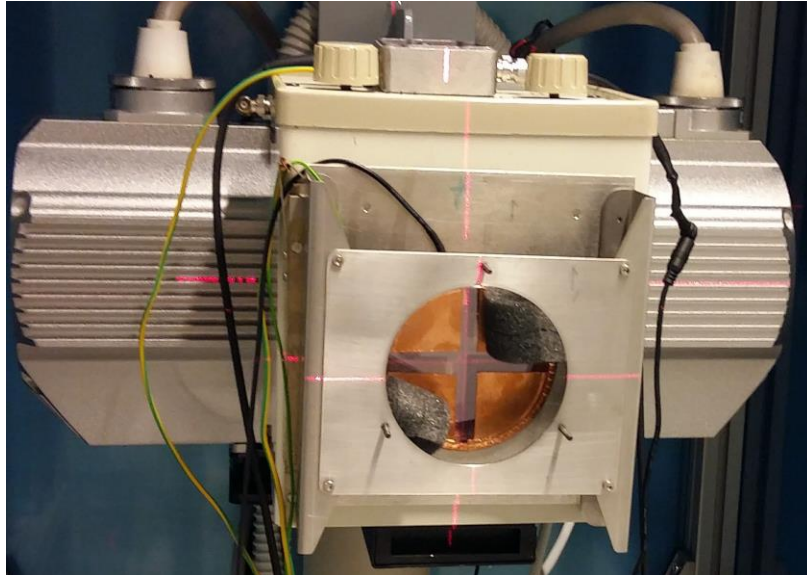


Figure 3.8 - X-ray tube without additional filters on. This picture allows to see the alignment between the laser red cross and the centre of the X-ray field. Here the opaque cross of the exit window is not visible due to the presence of monitor ionization chamber which is placed in front of it.



Figure 3.9 - Self-levelling red cross line laser used to align some devices to the X-ray field centre.

3.2.3 The RTC1000 HS X-ray tube

The X-ray unit is made up of a rotating anode RTC1000 HS X-ray tube, an X-ray tube assembly (C100XT) and the R306.35 (50 HF R) Endeavour generator.

The X-ray tube is a RT-TZM-C rotating anode one with two focal spots (0.6 and 1.2 mm), anode diameter of 110 mm and slanting angle 13° (Figure 3.10, Figure 3.11). The inherent filtration is equivalent to 0.7 mm Al and the maximum filament current is 5.4 A (see Appendix 10.1).

The anode is a graphite backed X-ray target that consist of a thin tungsten-rhenium alloy layer with 5 or 10% rhenium, behind which a TZM body is fixed onto a layer of high purity graphite. The TZM is an alloy of molybdenum and small amounts of carbides like 0.50% titanium, 0.08% zirconium and 0.02% carbon. This alloy was preferred to pure molybdenum because it exhibits good thermal conductivity and has higher recrystallization temperature, higher strength, hardness and good ductility at room and elevated temperatures. See Appendix 10.2 for its chemical and physical characteristics. The TZM body imparts outstanding dimensional stability under severe heating, whilst the graphite layer provides a much higher heat capacity and a higher heat emission capacity. Because they can be subjected to high thermal stresses, the graphite backed X-ray targets are particularly suitable for X-ray tubes in medical applications.

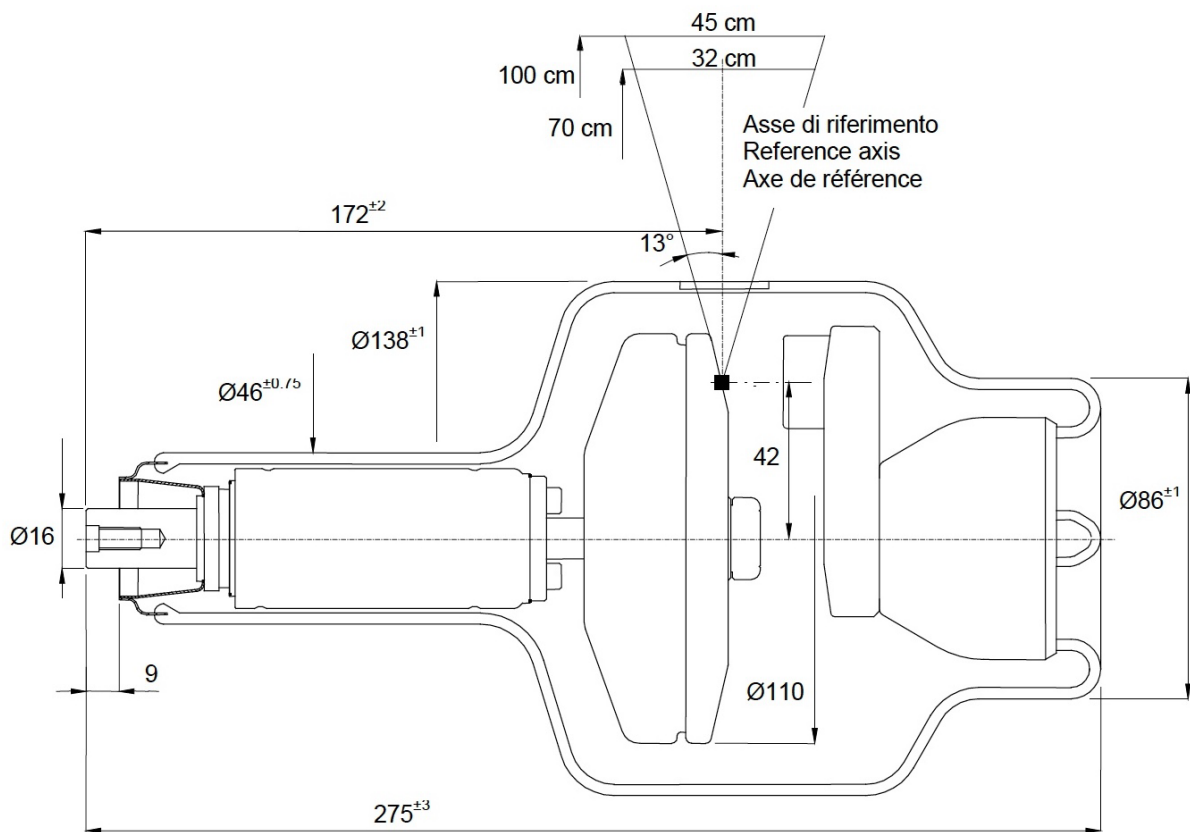


Figure 3.10 - Scheme of the RTC 1000 HS X-ray tube. On the right side there is the cathode and on the left the rotating anode which slanting angle is emphasized in the scheme. Here the black spot is the focal spot (IAE X-ray tubes RTC000 2019).

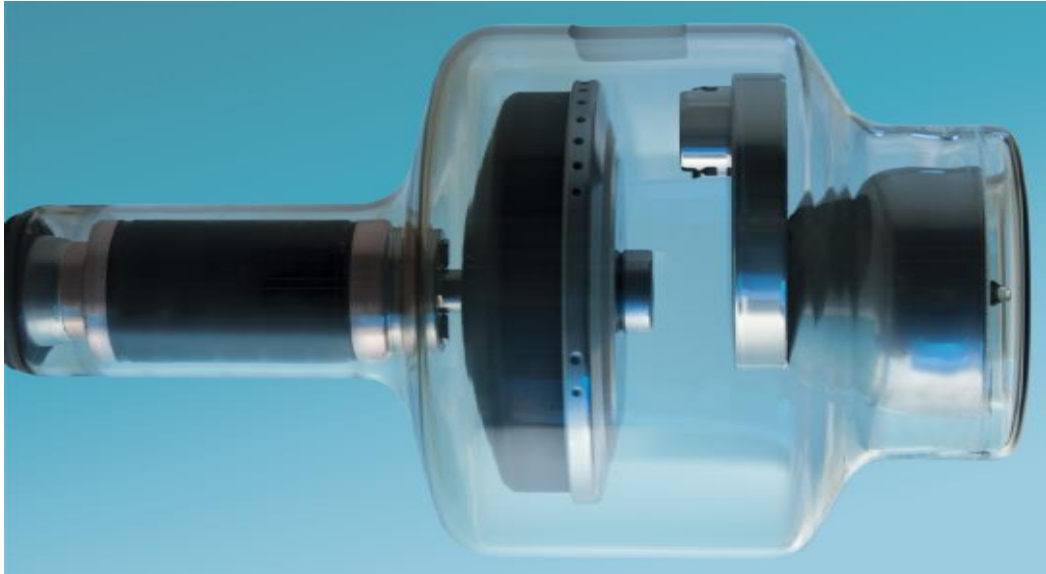


Figure 3.11 - Photo of the RTC 1000 HS X-ray tube. On the right side there is the cathode and on the left the rotating anode (IAE X-ray tubes RTC000 2019).

Appendix 10.1 reports the anode heating and cooling curves and cathode emission characteristic graphs which define the performances of the radiation unit.

Figure 3.12 shows the two filaments and their optical projection on the anode.



Figure 3.12 - X-ray tube filaments and optical projection on the anode. (Compare the cathode assembly to the scheme in Figure 1.4).

The X-ray tube is housed in a lead lined aluminium body. This assembly is under vacuum and it is filled with a specially processed insulating oil for heat dissipation and it is provided with a specific internal circulation system to improve temperature uniformity.

The minimum total filtration is equivalent to 1.5 mm Al.

The housing cooling is performed by two internal pumps and two additional external fans. The pumps are always on during tube operation and cooling, while fans are switched on above about 43°C. In Appendix 10.3 the differences between the thermally switched and continuously operating fans cooling times are visible.

The assembly is equipped with three thermostats that act as thermal safety in case the temperature exceeds certain pre-set values that would damage the machine: two bimetallic thermal switch and a microswitch (see Appendix 10.3). Two of them must be connected to the system safety circuits and in case of failure functioning operates the third thermal security which is connected to the stator and switches off at 80°C.

3.2.4 The high voltage generator

The power generator is a R306.35 (50 HFR) Endeavour one which works at 50/60 Hz of nominal frequency with supply voltage of 400 V and a three-phase wave form; the maximum power absorbed is 63 kW. The generator is provided with a C306.36 control desk, which allows to set the tube current and the kVp from the control room (see Figure 3.3). The only possible values are from 40 to 120 nominal kV (real about 42 – 117) with 1 kV step and tube currents of 0.5 - 1 - 2 - 3 - 4 and 5 mA.

In the irradiation room there are two important additional devices: a voltage divider and some metal absorbers.

The voltage divider is used to measure the tube kV value when it is in operation.

This GiCi 2000 (H917) Voltage Divider (Appendix 10.14) is designed to measure high voltage continuous values with accuracy better than 1%. The low-voltage output signal is proportional to the (high voltage) input signal and is recorded by the used data processing software (see paragraph 3.2.9). The two signals can be in the ratio 10000: 1 or 1000: 1, so that 40 kV (or 1 kV) of input voltage corresponds to a 4 V output voltage.

The metal absorbers are placed next to the tube exit window (see Figure 3.5).

Commonly used materials as a filter are Al, Cu, Sn and Pb in combinations of different thicknesses. Following the X-rays path, the various filter materials must be placed in descending order of Z to let the low Z filter absorb the X-ray fluorescence emitted by the upstream filters. Table 3-1 shows the energy of the K shell fluorescence photons for the previously mentioned materials. Because of the high-energy value of emitted photons, lead and tin cannot be used without additional filtration, while aluminium is a good candidate for performing the final filter function.

Figure 3.12 shows all the mentioned components of the X-ray unit and the positioning of the PTW ionization chamber, used for air kerma measurements.

Material	$E_{K-shell}$ (keV)
Al	1,5
Cu	9
Sn	29
Pb	85

Table 3-1 - The K shell fluorescence photons energies of the filter materials.

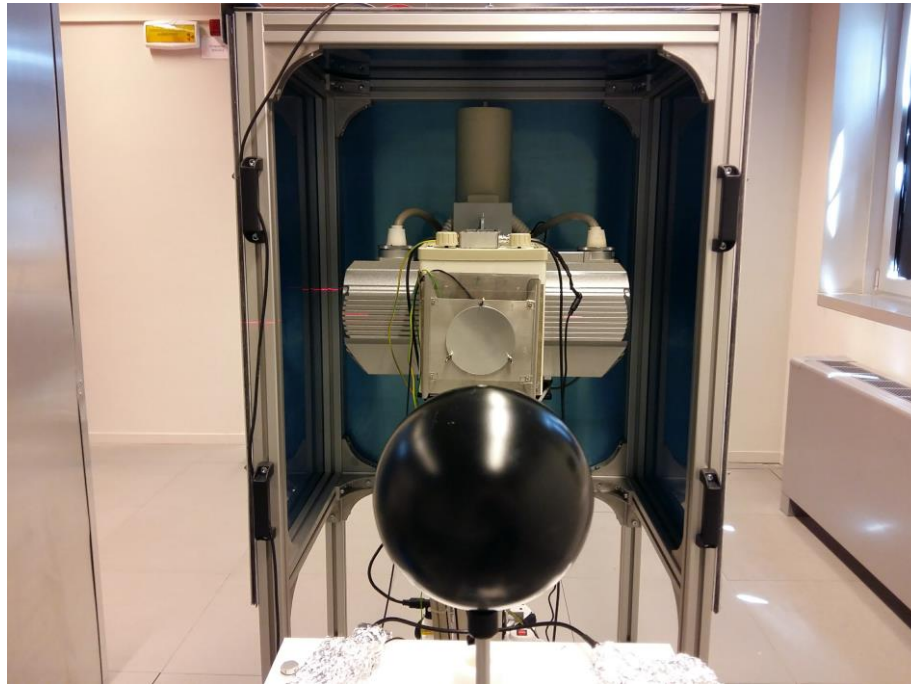


Figure 3.13 - X-ray unit and PTW ionization chamber placed along the mechanical bench thanks to a cart.

3.2.5 Monitor ionization chamber

The monitor chamber is a parallel plate disc ionization chamber. The design and the fabrication of this device was one of the main activities of the first part of PhD project. This ionization chamber is placed at the tube port to monitor the tube radiation output before this is modified by the additional filtration. Thus, this detector must comply with some requirements:

- be as “transparent” as possible for X-rays in order to not modify or attenuate unintentionally the radiation, so the walls have to be as thin as possible;
- the sensitive area has to be greater than the field size: the chamber dimensions have to contain all the X-ray beam;
- collect the signal with high repeatability, as a consequence its operating point must be very stable depending on the voltage variation applied to the electrodes, i.e. to be independent on radiation qualities and tube current.

These fundamental characteristics allow to monitor the X-ray tube and to study the accuracy of its output obtained under the same conditions.

The size of this ionization chamber was chosen depending on the above requirements and on the need to be placed between the tube exit window and the additional filtration. The wall thickness is as small as possible to avoid the low energy X-ray attenuation, thus 1 mm plastic wall was chosen.

The distance between the two electrodes equals 1 cm and the single electrode area is 50 cm². The body of the chamber is made in transparent plastic and the inner face was made conductive thanks to a thin conductive and transparent plastic foil. Both the electrodes were cabled using a coaxial cable. The central conductor was welded to one electrode (the cathode) and the other one was linked to the braided shield. The wires have been welded on a small area of a Cu layer, which ensures a better grip and prevents the plastic from melting due to the tin welder heat. Those

welding have been surrounded by an insulating glue to cover all possible tin spikes leaved from the welder which can eventually cause discharges between the electrodes (see Figure 3.14).

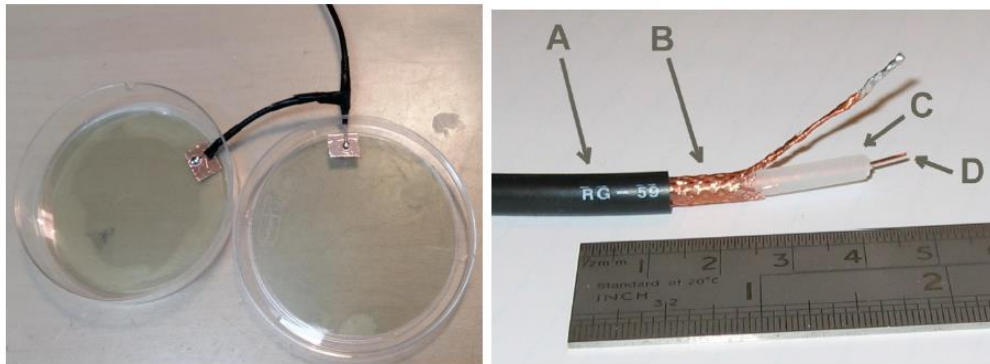


Figure 3.14 - Inner part of the monitor chamber (left): the conductive plastic has been glued to the plastic shell and the electrodes were cabled by a welding on a small Cu coating. On the right, an example of the used coaxial cable with central conductor (D), dielectric insulator (C), braided shield (B) and external insulator (A). The end of the braided shield has been twisted and welded to use it as a standard cable.

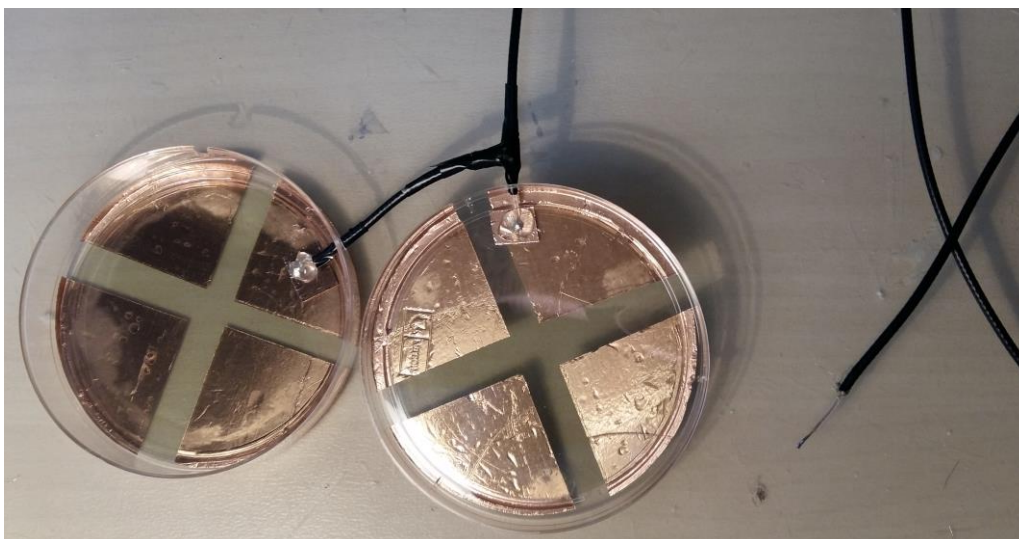


Figure 3.15 - Inner view of the monitor chamber with the external Cu layer.

The anode receives the voltage supply (CAEN model) which produces an electric field inside the monitor chamber; the cathode collects the signal from the charge movement, due to the electric field between anode and cathode, inside the ionization chamber volume.

To ensure electromagnetic shielding of the entire sensitive volume, copper conductive tape was applied to all external walls, except for the central area where a cross was left free. In this way and thank to the use of transparent conductive plastic, it is possible the use of the collimator lamp, even when the monitor chamber is inserted.

The ground contact of the external part is ensured by a thin cable, the green one of Figure 3.16, which links the Cu external layer to the box where signal is redirected to the processing electronics and high voltage is provided to the central conductor of the coaxial cable (see Figure 3.16). By means of this green cable, the other part of the monitor ionization chamber is at the same potential of the box, which in turns is linked, by BNC cable to the DAQ: all the devices have the same ground

potential. This is a good choice in order to avoid interference and to minimize the electronic noise. The mounting phase of the monitor ionization chamber is shown in Figure 3.14 and Figure 3.15.

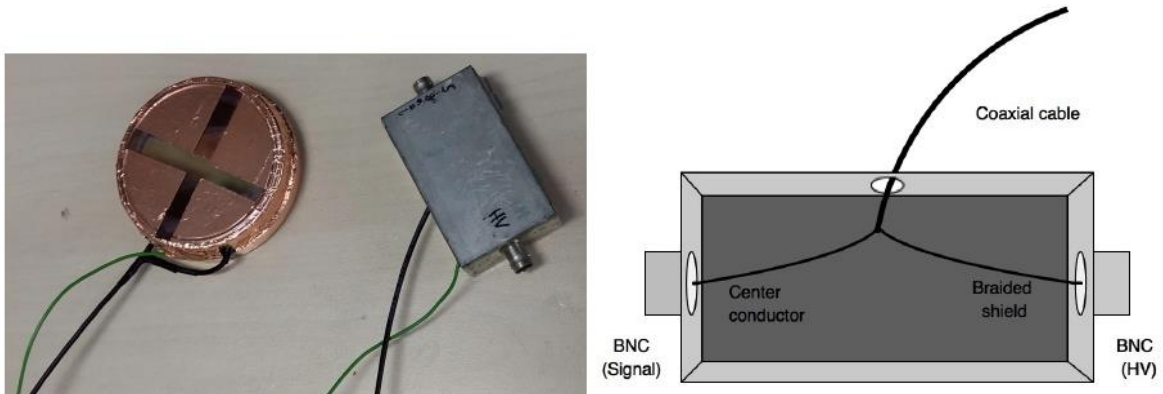


Figure 3.16 - Cabled monitor chamber with in addition the green cable ground contact. On the right, there is a scheme of the metal box which contains the end of the monitor chamber coaxial cable and allow to separate the collecting central conductor from the high voltage braided shield and direct them, through two BNC connectors, respectively to the DAQ and high voltage supply.

In order to define the operating point of the monitor chamber, a voltage scan was made for every possible tube current value (see chapter 4). The operating point was chosen to be 400 V.

3.2.6 PTW ionization chamber

PTW chamber is a 1 litre volume spherical chamber, type 32002 of PTW-Freiburg (Figure 3.18) and it is the ionization chamber used in this work for air kerma measurements.

It is a vented ionization chamber exploitable for the measurement of dose or dose rate in the measuring quantities photon equivalent dose, kerma and exposure, even if this detector is calibrated in terms of air kerma and it is only used for air kerma and air kerma rate measurements. The measuring range is 25 keV up to 50 MeV.

It is a 14 cm diameter ionization chamber with 3 mm polyoxymethylene (POM) (CH_2O)N walls and polystyrene (PS) graphite coated electrodes. Both electrodes are spherical; the inner one has a diameter of 5 cm and the external is 14 cm.

The stem is 26 cm long and has on one side a red line; this line should point towards the source during its usage. The reference point for kerma measurements is the chamber centre (see Figure 3.17).

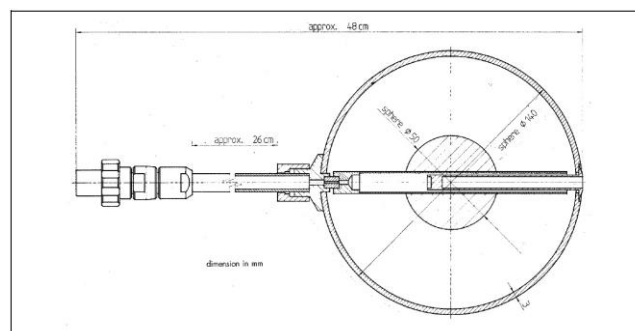


Figure 3.17 - PTW ionization chamber scheme (Appendix 10.4).

The chamber is fully guarded: the guard ring has the same potential as the measuring electrode. In this way it is possible to minimize the leakage current of the instrument for better performances.

This chamber operates at a high voltage supply between 100 and 500 V and shows a very flat response for incoming photons of energy between 50 keV and about 120 keV. If the response to ^{60}Co source is taken as reference, the maximum variation is 4% (see Figure 3.19) and Appendix 10.4 for further information).

This ionization chamber was calibrated in air kerma with a ^{60}Co beam using +400 V as bias voltage and the calibration factor is $2.44 \cdot 10^4 \text{ Gy/C}$. This value allows to convert the detector signal (in Volt) into an air kerma value and was used in some measurements (see Appendix 10.5).

As this detector is a vented ionization chamber, the sensitive volume has the same temperature and pressure of the environment and the signal has to be corrected for air density applying this formula:

$$C_{T,P} = (P_{ref} * T) / (P * T_{ref}) \quad (3.1)$$

where T and P are respectively temperature in measuring volume and pressure at that point, T_0 and P_0 are reference temperature (293,15 K) and pressure (101.325 kPa).



Figure 3.18 – PTW 11 32002 ionization chamber for air kerma measurements.

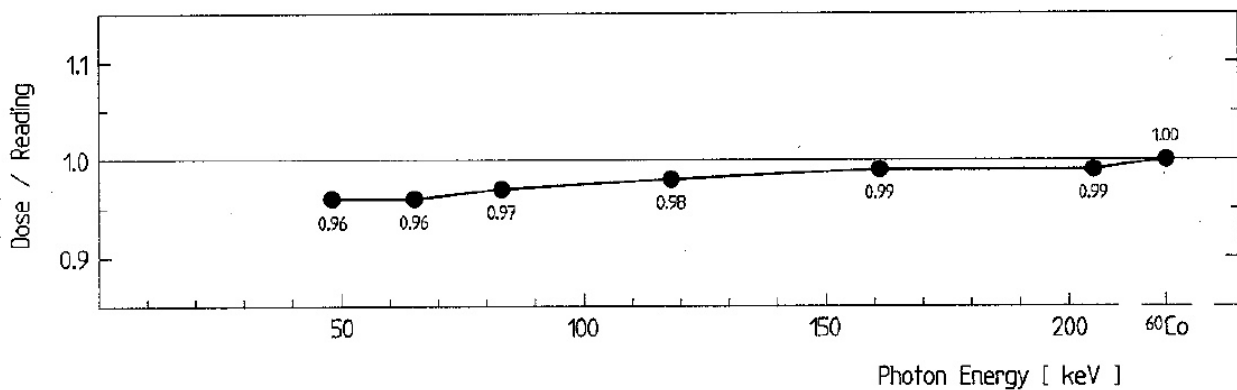


Figure 3.19 - Energy dependence of PTW chamber of type 32002 (Appendix 10.4).

In order to obtain this correction factor, an electronic circuit for environmental temperature and pressure measurements has been realized.

This circuit was placed on the top of the collimator in order to stay near the ionization chamber and to avoid sensors irradiation.

The pressure sensor is a piezoresistive silicon sensor. It provides an output voltage signal proportional to the applied pressure with an accuracy $< 1.5\%$ VFSS (voltage full scale span) from 0 to 85°C. The measurable pressure range is from 15 to 115 kPa and it is temperature compensated from -40° to 125°C (see Appendix 10.6) for further information).

The temperature sensor is a fully calibrated silicon sensor. The widest measuring range is from -50° to 150°C and has an accuracy of 0.3 K in a range of 80 K, typically from 10° to 90°C (see Appendix 10.7) for further information).

3.2.7 Semiconductor detectors: Si detector and CdTe spectrometer

Two different semiconductor detectors were used in experimental measurements: Si and CdTe detectors. The first was used in current mode to study the field uniformity and, as spectrometer (pulsed mode), together with the second (pulsed mode) for beams spectra acquisition.

The silicon detector used is the S3590-09 Hamamatsu (Appendix 10.8) large active area Si PIN photodiode (see Figure 3.20). Its active area is $10 \times 10 \text{ mm}^2$ and the full depletion layer is 0.3 mm thick. It was chosen for its low capacitance and its high purity substrate (see paragraph 3.2.7.1 and 3.2.7.2). It can operate to maximum 100 V of reverse bias voltage at temperatures between -20° and 60°C. For a satisfactory explanation of the main features of this silicon detector (used for various application during this work), the next paragraphs (3.2.7.1 and 3.2.7.2) shows its complete electrical characterization.

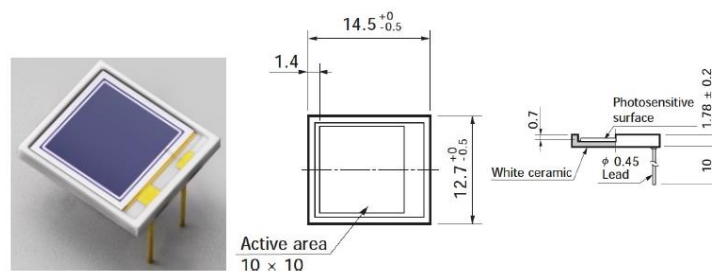


Figure 3.20 - Hamamatsu silicon detector. Dimensions are in mm (Appendix 10.8).

The CdTe detector used in this work is a 1 mm^3 sensible volume spectrometer. The sensitive thickness is 1 mm and the area $1.33 \times 1.33 \text{ mm}^2$ (see Appendix 10.9).

The device is the S1.1.1U Eurorad detector (serial number 1100-25A, see Figure 3.21). This planar spectrometer was chosen for his high performances at room temperature: low noise, good energy resolution and high detection efficiency. The detector is housed in an aluminium enclosure which includes a BNC termination, to link it up to a charge preamplifier and the processing electronics. The CdTe is characterized by a very high energy resolution, high efficiency and wide energy domain (from few keV to 1 MeV). It has a very good radio-resistance and needs a bias voltage of 100 V.

This detector was used in association with the Eurorad low noise preamplifier (PR 16-H type and 1502 serial number). This preamplifier has a sensitivity of 6.6 V/pC and needs ± 12 V power supply (for further electrical specifications see Appendix 10.10).



Figure 3.21 - CdTe planar spectrometer with BNC housing.

3.2.7.1 Electrical characterization of the Hamamatsu detector s3590-09: I-V characteristic

Under the hypothesis of an abrupt junction and uniform doping in the two regions, considering a PN junction, with p and n respective majority carriers concentrations in P zone and in N zone (Figure 3.22), the built-in voltage (V_{bi}) works against these concentrations: in thermal equilibrium diffusion is counterbalanced by drift (Figure 3.22).

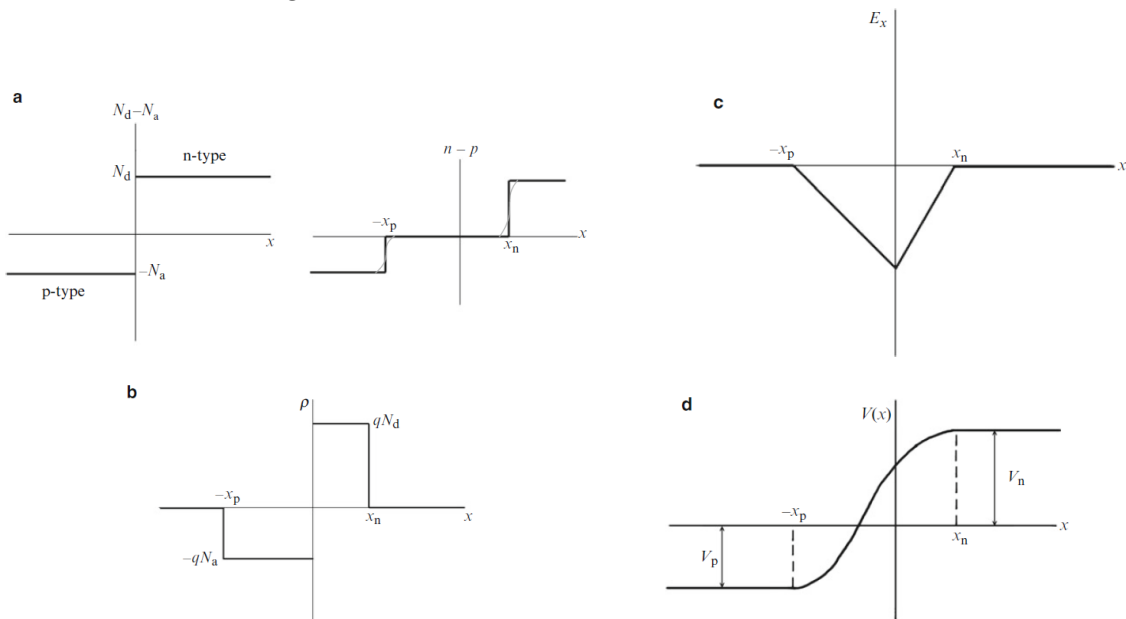


Figure 3.22 - (a) Depletion approximation, which ignores any contribution to the space charge from free electrons and holes, for an abrupt PN junction: doping levels (on the left) and resulting mobile carrier concentrations within the depletion approximation (right). (b) Charge density for the step PN junction under the depletion approximation. (c) Electric field across step PN junction for charge distribution in b. (d) Electric potential variation across PN junction for field in c-image (Papadopoulos 2014).

With a forward bias, the voltage across the junction decreases from the equilibrium value V_{bi} by the externally applied voltage (figure 3.23 and figure 3.24). The majority carriers diffuse in zone where their concentrations are minor, therefore minority concentrations increase at the edges of the

space-charge region. The nonequilibrium concentration can be expressed as a function of thermal equilibrium concentration and of exponential trend with applied voltage, V_a .

$$(3.2) \quad n_p(x_p) = n_{p0} \left[e^{q \frac{V_a}{k_B T}} - 1 \right] \quad p_n(x_n) = p_{n0} \left[e^{q \frac{V_a}{k_B T}} - 1 \right] \quad (3.3)$$

Where n_{p0} is the electron density at the edge of the neutral P zone in the thermal equilibrium case, which is equal to the electron density inside the neutral P region in the nonequilibrium case (n_p) far away from the edge (similarly for p_{n0} and p_n); considering Boltzmann's constant, k_B ², and q fundamental charge³, $\frac{q}{k_B T}$ is also defined as thermal voltage (V_t).

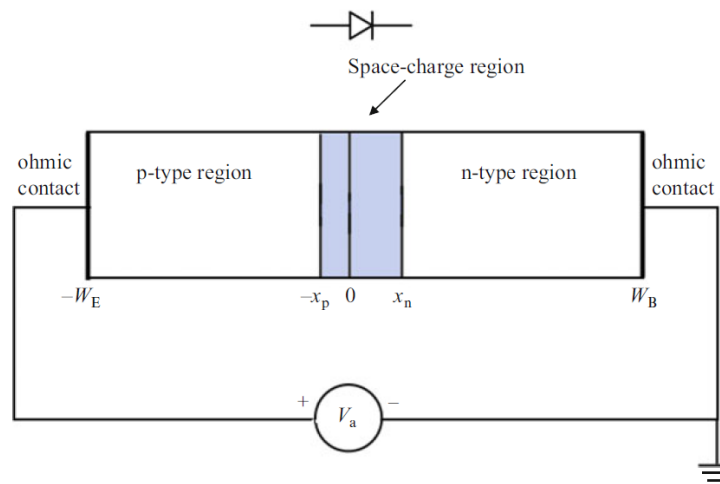


Figure 3.23 - PN junction device structure and biasing configuration (Papadopoulos 2014).

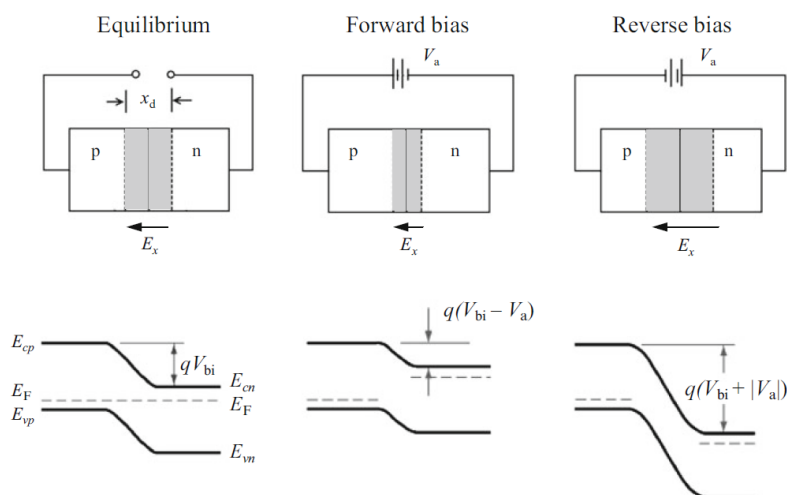


Figure 3.24 - Effect of applied bias on PN junction (with similar doping levels on either side). In thermal equilibrium the Fermi level is constant across the entire structure and the built-in electric field opposes the diffusion of carriers across the

² Boltzmann's constant, $k_B = 1,3087 \cdot 10^{-23} \text{ J/K}$.

³ Fundamental charge, $q = 1,602176 \cdot 10^{-19} \text{ C}$.

junction. The applied bias is assumed to drop almost entirely across the depletion layer and thus the Fermi level becomes separated by qV_a . Forward bias reduces the built-in electric field and thus the built-in potential barrier is reduced by V_a as shown. Reverse bias on the other hand increases the built-in electric field and the built-in potential is increased by V_a .

As minority diffusion currents are proportional to the deviation of the minority carrier concentrations from their equilibrium values at the boundary, that in turn has an exponential dependence on voltage, the same happens to the total diode current (Lutz 1999). This can be expressed by Shockley equation 3.4.

$$J = J_s \left(e^{\frac{qV_a}{k_B T}} - 1 \right) \quad (3.4)$$

J_s , reverse bias saturation current density, can be calculated by solving the time independent continuity equation for minority carriers with the boundary condition of zero minority carrier concentration at the edge towards the space-charge region. Therefore, at the edges of the space-charge region there is a zone where minority carrier concentration profiles are not in equilibrium: strong recombination occurs and the diode current is related to this phenomenon. The explanation is referred to long-base diode. “Long-base” means sufficient dimension of the silicon wafer allows recombination: read expressions below (3.4 and 3.5), remembering symbols in figure 3.23.

$$\text{for holes: } x_B = W_B - x_n \gg L_p \quad (3.5)$$

$$\text{for electrons: } x_E = W_E - x_p \gg L_n \quad (3.6)$$

Where L is called diffusion length and represents the average distance a minority carrier travels before recombining.

Considering for instance the hole current, this is therefore greatest at $x = x_n$, the edge of the space-charge region, and decreases away from the junction because the hole concentration gradient decreases as carriers are lost by recombination (analogous treatment for electrons): see Figure 3.25.

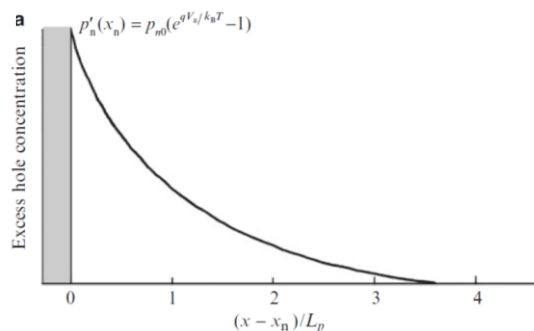


Figure 3.25- Long-base diode under forward bias: excess minority hole concentration vs. distance (Papadopoulos 2014).

If dimensions are very small, very little recombination occurs in the bulk of n- and p-type regions, therefore exponential trend is interrupted and the concentration is forced to zero at the contact

with neutral zone, because recombination is complete at the contact surface. This situation is described as short-base diode.

$$\text{for holes: } x_B = W_B - x_n \ll L_p \quad (3.7)$$

$$\text{for holes: } x_B = W_B - x_n \ll L_p \quad (3.8)$$

In this case, almost all the injected minority carriers recombine at the ohmic contacts at either end of the diode structure and thus the excess minority carrier distribution can be approximated as being essentially linear (Figure 3.26).

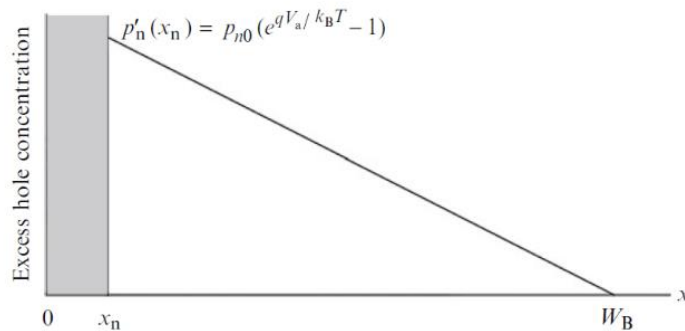


Figure 3.26 - Short-base diode excess hole carrier distribution in N region under forward bias (Papadopoulos 2014).

From I-V forward characteristic, the reverse bias saturation current can be read at the intercept with current axis. In long base diode, I_s depends on $\frac{qn_i^2 D}{N_D L}$, where q is the fundamental charge, L is the diffusion length, D is the diffusion constant, N_D is the donor concentration and n_i is the intrinsic carrier density. While in short base diode, I_s depends on $\frac{qn_i^2 D}{N_D x}$, where x is the width of the p- or n-type region in the short-base diode case.

This is the difference between the current through the short-base and long-base diode: the characteristic length associated with each geometry – the minority carrier diffusion length in the long-base diode case and the width of the p- or n-type region in the short-base diode case. For devices of this work, x is the wafer thickness.

Hamamatsu detector under characterisation can be considered short base diode for high purity of silicon, so there is great lifetime τ , that is equivalent to previous assumption of no recombination.

Keithley model 6485 picoammeter (Figure 3.28) are the instruments used to read the current from the devices under characterisation. The graph in Figure 3.27 shows the very low dark current of this detector: when biased, about few nA. This generally provides good results about the noise performance for this detector.

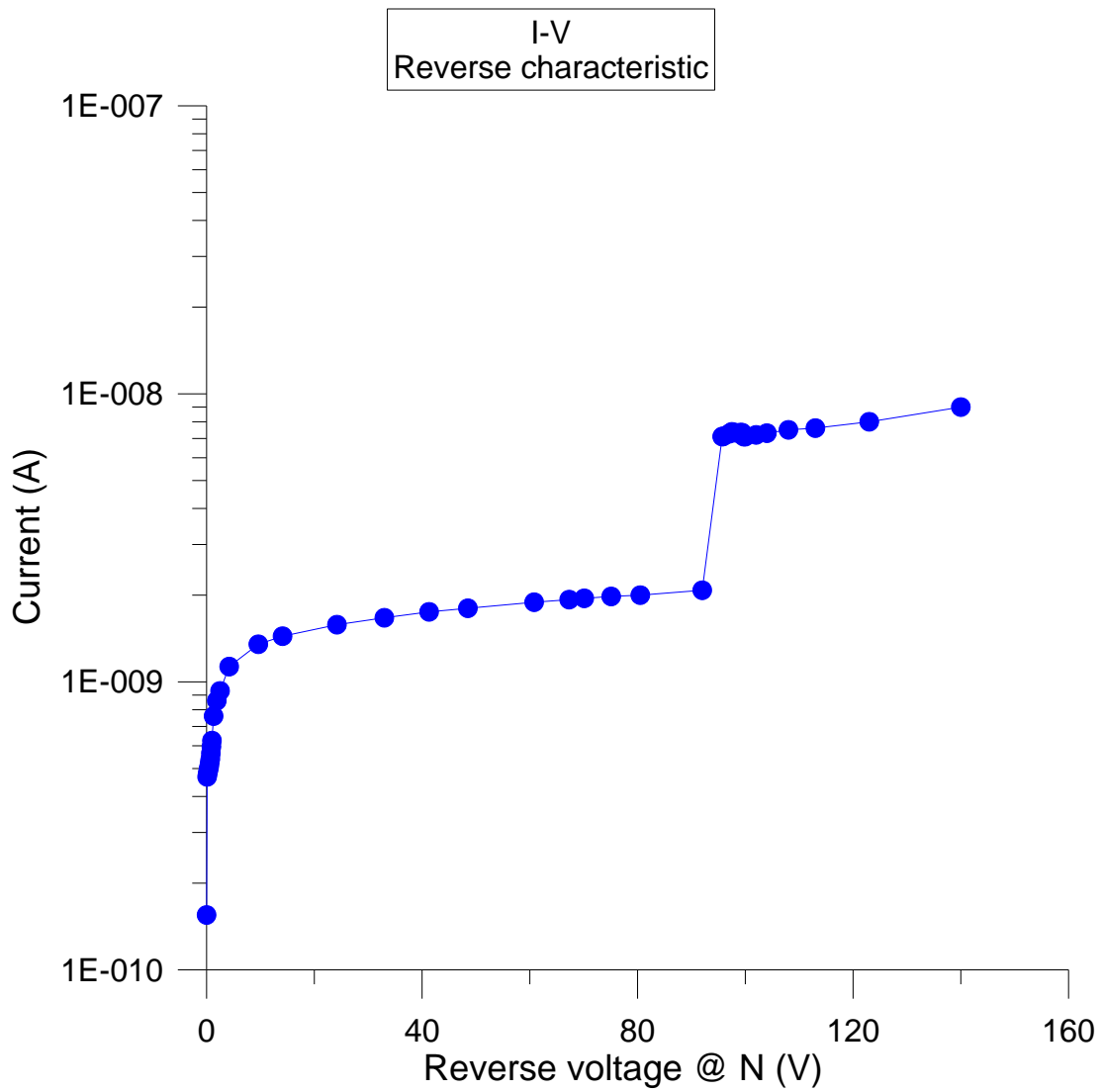


Figure 3.27 - Current-Voltage reverse voltage characteristic of the Hamamatsu detector. The graph shows the very low dark current of this detector: when biased, about few nA.

3.2.7.2 Electrical characterization of the Hamamatsu detector s3590-09: C-V characteristic

The fixed charges inside depletion layer will contribute what is known as the depletion or junction capacitance, C_j , which characterizes the expansion or contraction of majority carrier distributions near the edges of the depletion region in response to a time-varying bias. The space charge per unit area on either side of the metallurgical junction is given by equation 3.9, which can be used to find the small-signal capacitance C_j (per unit area) of the junction (equation 3.10). Consider $V_a < 0$ for the reverse bias condition in all equations of this paragraph.

$$Q = qN_d x_n = qN_a x_p \quad (3.9)$$

$$C_j = \left| \frac{dQ}{dV_a} \right| = qN_d \frac{dx_n}{dV_a} = qN_a \frac{dx_p}{dV_a} \quad (3.10)$$

Considering $x_p = (N_d/N_a)x_n$ and $x_d = x_n + x_p$ equation 3.11 gives us an expression for x_d in terms of the applied voltage, which can be used to calculate C_j .

$$x_d = x_n(1 + N_d/N_a) = \left[\frac{2\varepsilon_s}{q} \left(\frac{1}{N_a} + \frac{1}{N_d} \right) (V_{bi} - V_a) \right]^{1/2} \quad (3.11)$$

Taking the derivative with respect to applied voltage and rearranging terms, equation 3.12 is obtained.

$$\frac{dx_n}{dV_a} = \frac{1}{N_d} \left[\frac{\varepsilon_s}{2q(1/N_a + 1/N_d)(V_{bi} - V_a)} \right]^{1/2} \quad (3.12)$$

Therefore junction capacitance is expressed in equation 3.13.

$$C_j = \left[\frac{q\varepsilon_s}{2(1/N_a + 1/N_d)(V_{bi} - V_a)} \right]^{1/2} = \frac{\varepsilon_s}{x_d} \quad (3.13)$$

Thus for V_a much greater than V_{bi} (considering the absolute values), the capacitance of a PN step junction (always under assumptions of the depletion approximation; see paragraph 3.2.7.1) varies approximately inversely with the square root of the reverse bias.

Capacitance-voltage measurements are often used to measure the doping profile of semiconductors. Considering an arbitrary (one-dimensional) doping profile and restricting explanation to an extremely asymmetric junction with very high p-doping on a low-doped n-substrate, equation 3.14 is obtained by solving equation 3.13 for the total voltage across the junction.

$$(V_{bi} - V_a) = \frac{q\epsilon_s N_d}{2C_j^2} \quad (3.14)$$

Assuming N_d constant, the form of equation 3.14 indicates that a plot of the square of the reciprocal of the small-signal capacitance versus the reverse bias voltage should be a straight line. The slope of the straight line can be used to obtain the doping in the semiconductor. Measurements of the small-signal capacitance are useful even in cases where the semiconductor doping varies with distance. For a given dc reverse bias, the space-charge layer is of width x_d . A small increase in the magnitude of V_a causes a small increase in space-charge density Q , given by equation 3.15 (where $N = N_d - N_a$ is the net dopant density).

$$Q = q \int_0^{x_d} N(x) dx \quad (3.15)$$

Consequently, an increment in voltage dV_a results in an increment in Q of value

$$dQ = qN(x_d)dx = -C_j dV_a \quad (3.16)$$

or

$$N(x_d) = -\frac{C_j}{q \left(\frac{dx}{dV_a} \right)} \quad (3.17)$$

Where x_d is the depletion-region width that corresponds to the applied dc voltage V_a at which the small-signal capacitance C is to be measured. Manipulating equation 3.16, equation 3.18 is obtained, that can be placed in a more useful form, like in equation 3.19.

$$N(x_d) = \frac{C_j^3}{q\epsilon_s \left(\frac{dC_j}{dV_a} \right)} \quad (3.18)$$

$$N(x_d) = -\frac{2}{q\epsilon_s [d(1/C^2)/dV_a]} \quad (3.19)$$

The slope of a plot $1/C^2$ versus reverse bias voltage directly indicates the doping concentration at the edge of the space-charge layer. This slope, when divided into $(2q\epsilon_s)$, gives directly $N(x_d)$.

With Hewlett-Packard 4263A LCR meter (of the laboratory, it is possible to measure the capacitance of the dut varying the applied voltage. The basic idea for this type of measurement is the injection of a test signal in the biased device. The test signal is a sine with his specific frequency and amplitude, that has to be negligible in respect of bias voltage to respect the condition for "small signal": while dut is biased, so the working point is fixed, the sinusoidal signal injected in the dut allows the

instrument reads current in phase and in quadrature (Figure 3.29). From these components and setting up equivalent circuits (series or parallel), instrument calculates circuitual parameters. Change frequency (100Hz – 100kHz) is useful to measure small or big capacitance.



Figure 3.28 - Experimental setup of the electrical testing workstation. Voltage generator, Keithley model 6485 picoammeter, Hewlett-Packard 4263A LCR meter and metal box for the assembly of the dut.

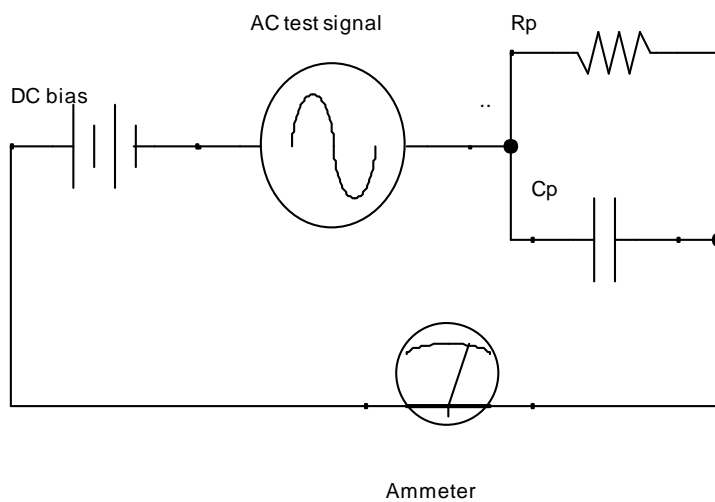


Figure 3.29 - Schematic depiction of circuit for measurement with LCR meter.

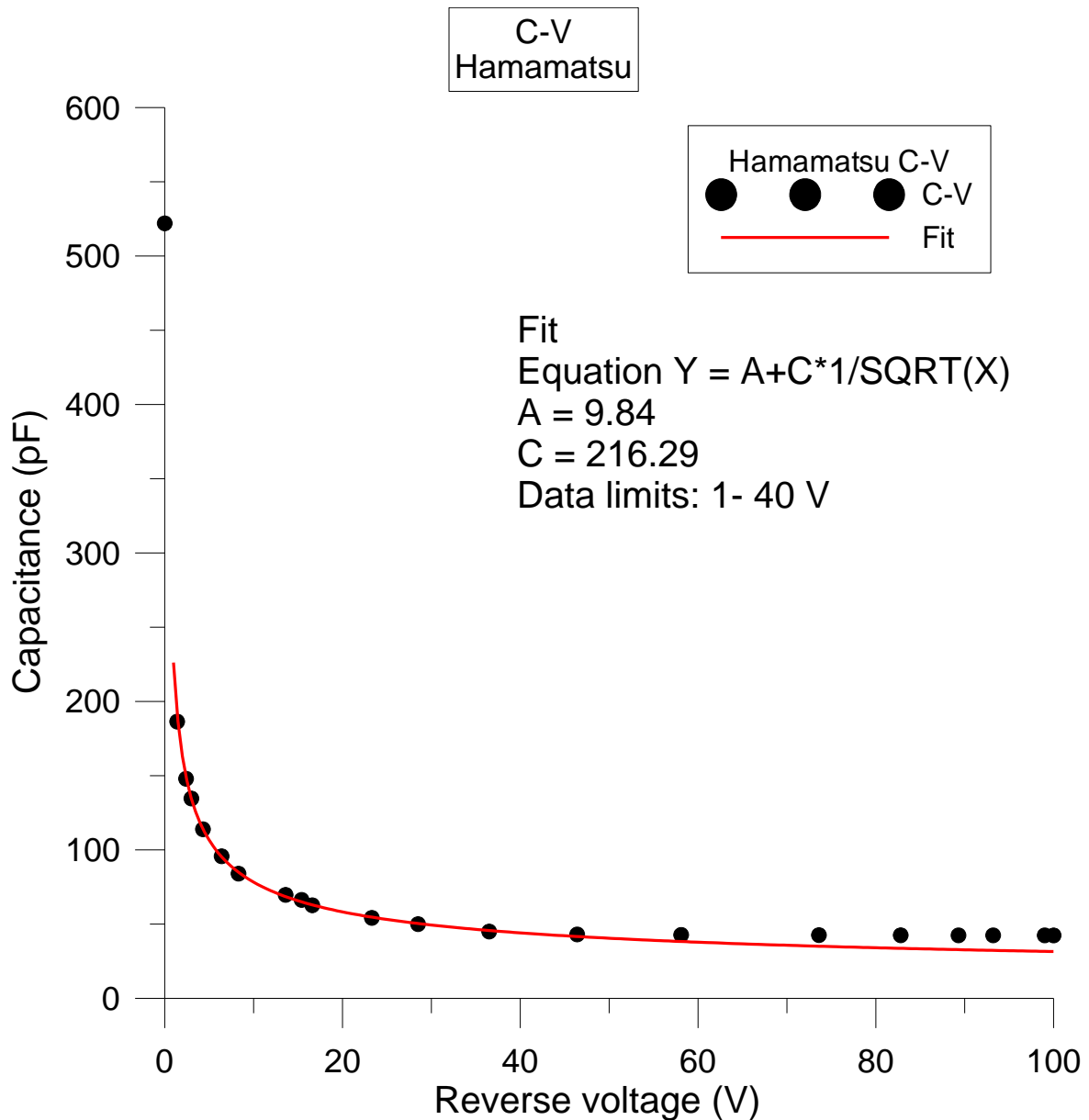


Figure 3.30 - Capacitance-Voltage characteristic of the Hamamatsu detector until overbiasing condition (100 V is the upper limit suggested for the working voltage range).

In figure 3.30, C-V characteristic of Hamamatsu detector is shown. Equation 3.20 describes the fit applied to data. From fit parameter it is possible to extract important information.

$$Y = A + \frac{C}{\sqrt{X + B}} \quad (3.20)$$

Parameter A consists in the value of parasitic capacitance that alters junction capacitance measurement. Parasitic capacitance value is considered independent from voltage. This was initially supposed, then verified with specific measurement for check possible trend for parasitic capacitance of measurement system⁴.

⁴ The estimate dependence in the range 0 – 500 V is 0.01 fF/V.

Parameter B is the built-in voltage. This parameter describes correctly the value of V_{bi} only when the fit is applied in a range that start at low voltage values. At high voltage values, this B can be neglected.

Remembering equation 3.13 (where Parameter $N_d \gg N_a$), parameter C contains information about dopant concentration, N_a .

$$A = C_{par} [pF]$$

$$B = V_{bi} [V]$$

To find voltage value at which device is completely depleted, to increase voltage is necessary.

In C-V plot, the region where capacitance doesn't change with voltage indicates that complete depletion is reached. Other methods, like calculating and graphing the depletion layer versus voltage or $1/C^2$ plot, are useful to find in a more precisely way voltage of depletion.

Measuring capacitance, then correcting measured value with parasitic capacitance estimated from fit applied to C-V characteristic, and inverting equation 3.13, it is possible calculate the thickness of depletion layer at different voltage values.

From applied fits, parasitic capacitance value of about 10 pF was estimated. Subtracting this value from capacitance values measured, plot in Figure 3.31 is obtained.

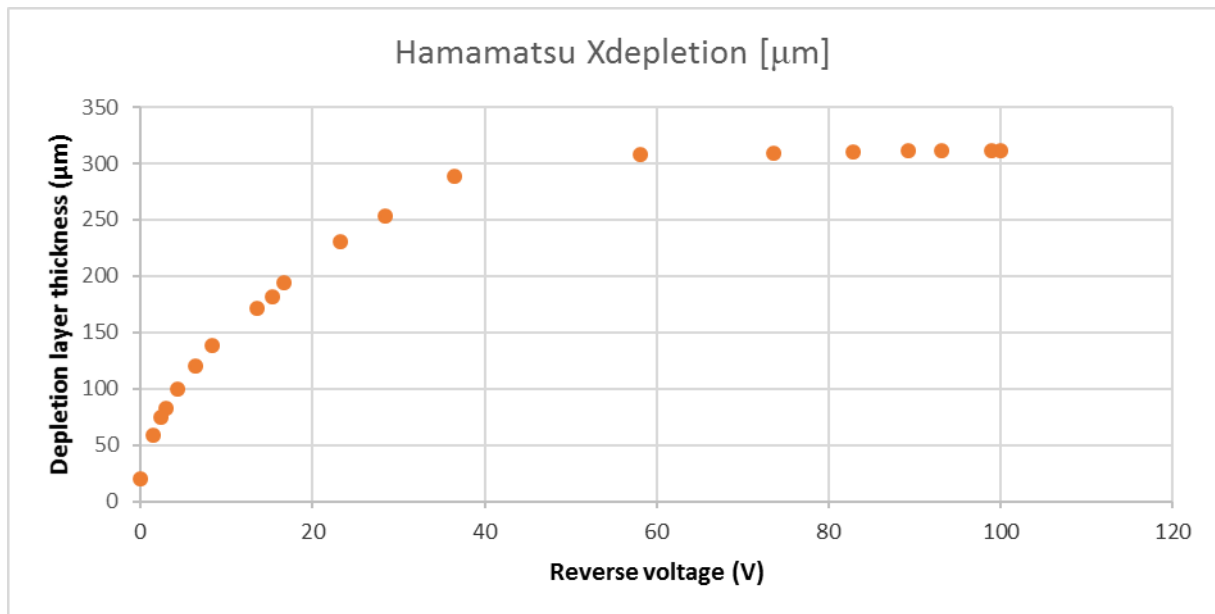


Figure 3.31 - Depletion layer thickness of the Hamamatsu detector. This experimental test shows excellent agreement with the datasheet thickness value (0.3mm – Appendix 10.8).

The region where X_d -V and C-V plots are flattened indicates depletion condition is reached. For better determination of depletion voltage, plot of the square of the reciprocal of the capacitance versus the reverse bias voltage is useful. Until depletion voltage its trend is straight line, then it is flat (Figure 3.32). Like explained before in this paragraph, capacitance-voltage measurements are often used to measure the doping profile of semiconductors. The slope of the straight line of $1/C^2$ plot can be used to obtain the doping in the semiconductor (Figure 3.32).

To extract donor concentration as function of distance, equation 3.19 was used.

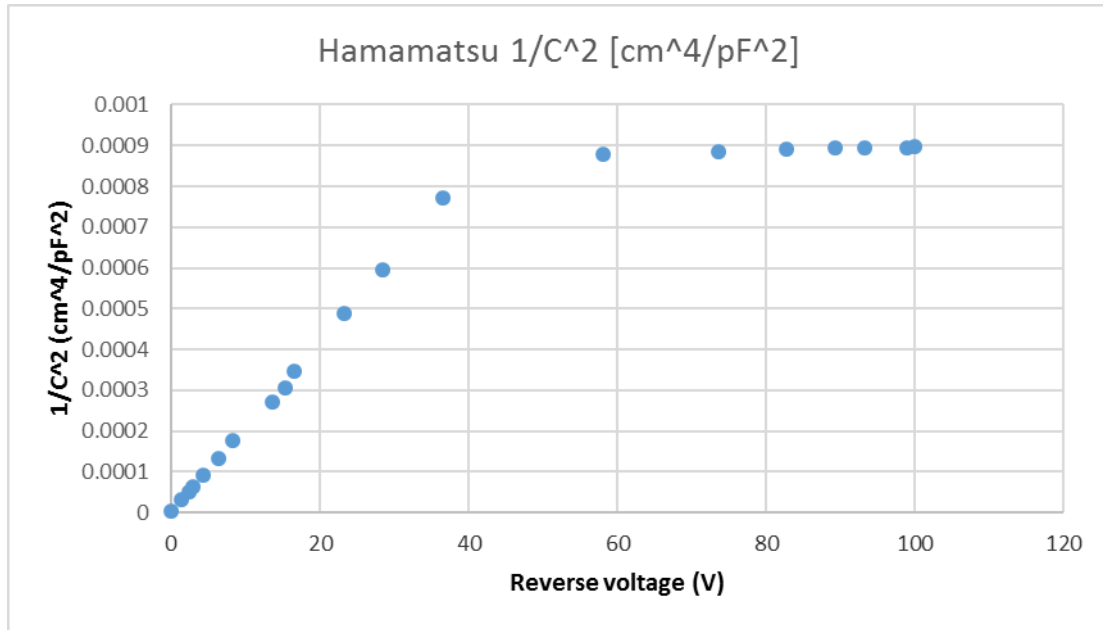


Figure 3.32 - $1/C^2$ versus reverse voltage for Hamamatsu detector.

Full depletion voltage for devices about 300 μm thick is about 50 V. This low voltage value is an advantage on field trials and, with practical overbias voltage, it allows to decrease time of the charge collection and to improve its efficiency.

Regarding to the doping profile, it is possible to verify and to compute that the donor is rather constant with depth and it results about $7 \cdot 10^{11} \text{ cm}^{-3}$. This parameter can be considered a proof of the high purity substrate of this silicon detector.

3.2.8 The processing electronics

The useful information, that has to be extracted from a detector, is the charge generated in the interaction of the incident radiation with the instrument sensitive volume. The motion of the generated pairs induces an electrical signal that can be read by a signal chain for pulse height spectrometry (pulse mode) or with some electronics, which can measure the generated low ionization currents - pA, fA - (current mode).

In **pulse mode** the measuring system is made up of a front-end part realized with a charge sensitive preamplifier which integrates the collected charge by means of the operational amplifier feedback capacitance at the inverting input (see Figure 3.33: -A amplification in Charge Preamp). The step signal, with low exponential decreasing tail (ruled by the time constant $\tau = R_f C_f$), is then processed by the shaping amplifier which allows to obtain a pseudo-gaussian signal as the spectrometry chain output and increase the signal to noise ratio.

This is the analog part of the electronic system. After that the signal is sampled and converted into a digital one by a DAQ, it is acquired and then stored in a PC.

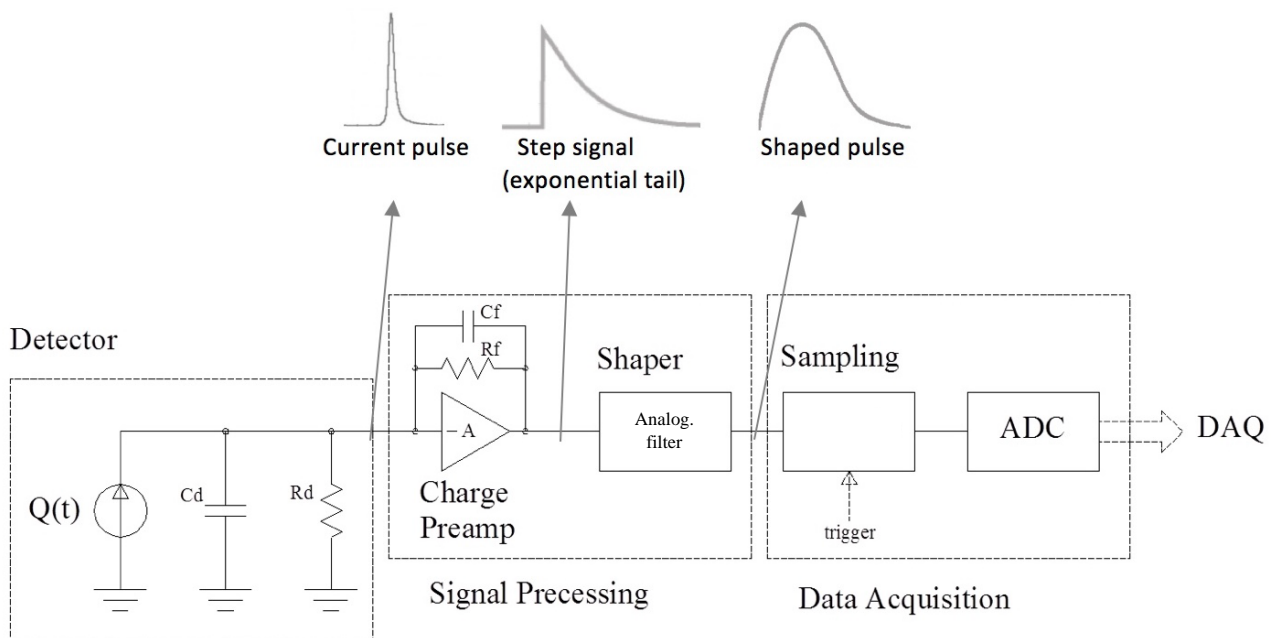


Figure 3.33 - Electronic spectroscopy chain scheme. The detector is depicted as a time dependent generator with its specific capacitive and resistive contributions. The charge preamplifier shows an amplification $-A$ since the input is the inverting input and the configuration has a negative feedback for stability reasons. The shaper is an analogic filter for nuclear spectrometry (Bessel, Butterworth etc.).

In **current mode**, there is the need of using a technique for measuring very low current values. The use of a transimpedance amplifier (TIA) has this function.

The TIA consist of an inverting operational amplifier configuration, realized connecting a suitable resistor (hundreds $M\Omega$ - few $G\Omega$) across the amplifier from the output terminal back to the inverting input terminal (see Figure 3.34). This negative feedback is obtained by an external resistor called R_f and it produces a very stable system. The positive non-inverting input is connected to a ground or zero voltage terminal, as shown in Figure 3.34. The effect of the high gain closed loop feedback circuit results in producing a virtual ground summing point. Thus, inverting and non-inverting inputs are at the same potential and the current is forced to pass in the feedback resistor. As a

result, no current flows in the inverting input terminal. The potential difference across R_f is the processed detector signal.

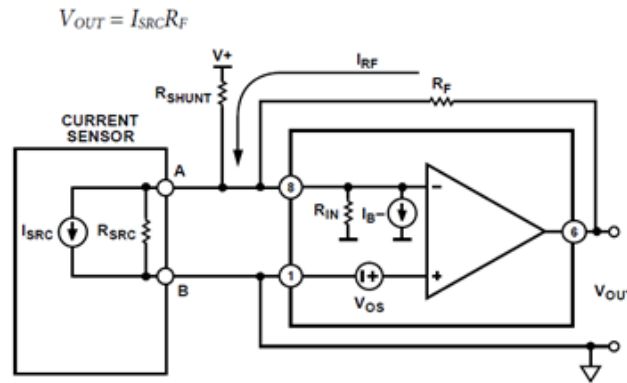


Figure 3.34 - Transimpedance amplifier circuit.

The proper processing electronics was associated with each of the devices described above in order to always have a detector connected with the same specific electronics: the system detector-electronics is considered as a unique device. This association was made to perform as maximum as possible reproducible measurements and the details are given in the following.

Monitor chamber operates at a value of voltage supply of 400 V provided by CAEN high voltage power supply. The step signal is analyzed by a current mode electronics which feedback resistor and capacitance values are 20 M Ω and 10 nF; it is powered by a ± 5 DC voltage generator (Traco power). The signal is sampled by NI USB-6216 BNC DAQ and analyzed by the current measurements software.

PTW chamber is supplied by CAEN high voltage power supply (400 V) and is connected to an electronic system similar to the monitor chamber. For this detector, a low noise operational amplifier has been used, which was powered by the same ± 5 V DC voltage generator as the monitor chamber; the feedback resistor and capacitance are $R_f = 5$ G Ω (unc. 10%) and $C_f = 10$ pF. The signal is sampled by NI USB-6216 BNC DAQ and analyzed by the current measurements software.

Also, the Si detector has been used in current mode with a transimpedance circuit with $R_f = 5$ G Ω and $C_f = 10$ pF, ± 5 V DC voltage generator, NI USB-6216 BNC DAQ and current measurements software.

The CdTe detector works at 100 V of voltage bias which was supplied by ORTEC - 556 high voltage power supply. The electronic system is a spectrometry chain, which comprehends the Eurorad preamplifier 16H 1502 and an amplifier stage obtained with a CREMAT CR 160 + CR-200 1 μ s (gain stage 1 and 2 on) supplied by a ± 12 DC voltage generator (Appendix 10.11 and 10.12). The DAQ used is NI USB-6366 (pulse mode measurements) read by the pulse mode software. For silicon the spectrometry chain is the same with the exception of the chosen CR-200 shaping time, that was 500 ns for faster shaped pulsed. In the next chapters the mounting of the experimental setup is shown for every measurement session.

3.2.9 The acquisition system

After the signal is processed by the electronic system, it is sampled, digitalized and analyzed by a computer: this is achieved by a LabVIEW software.

Based on the type of measurements, two different DAQ have been used:

- NI USB- 6216 BNC for current mode measurements and
- NI USB-6366 for pulse mode measurements.

The two different techniques require two different softwares. In the following sections will be described the DAQ and the software that is used. Both LabVIEW softwares were specifically designed for those kinds of measurements.

Current measurement

The NI USB-6216 BNC is an USB powered DAQ which is optimized to obtain high accuracy for sampling rates of 400 kS/s maximum. It is equipped with:

- 8 differential BNC analog inputs, 16 bits, 400 kS/s;
- 2 BNC analog outputs at 16 bits, 250 kS/s;
- 4 programmable inputs (between ± 0.2 - ± 10 V);
- digital triggering;
- 32-bit;
- 80 MHz counter/timers and 60 V, CAT isolation.

The sampled signal is sent to the control room PC which elaborates and stores it. Current mode software has several tasks:

- sets the run condition;
- manages the X-ray tube turning it on and off;
- visualizes the detectors signals as an oscilloscope;
- computes some defined quantities;
- stores the important data in a text file for post analysis.

This software has two main menus: the configuration (see Figure 3.35) and the acquisition one (see Figure 3.36). In both, the yellow boxes require some parameter from the user and the white ones displays preset values or the results of some measurements.

The top left part of the configuration menu allows to set the channels used by the DAQ (physical channels), the maximum and minimum signal range and the run configuration.

A run is composed by an initial part, where the X-ray tube is not delivering dose, then the beam on phase and the X-ray beam turning off. As the transition between on and off phases is not sudden, there is the need of defining a transit time in which acquired data aren't used for further analysis. Referring to Figure 3.35 the initial and final part of the run are used to compute the baseline (here 7 s); after the first baseline calculation there are 2 s after which, the software sends the signal to power on the beam (these seconds are fundamental: otherwise the baseline calculation will be distort by tube ignition); the first transit time (here 5s) helps to define the starting time for recording

the signals, this time period ends with the beam turning off (the seconds between the two orange lines correspond to the beam on time); then there is a second transitory time and another baseline calculation.

The last settable parameter is the number of averages per second (here 4) and corresponds to the number of averages that the software performs, in a second, as passing the sampled data in a digital filter. At last, on the right side of the run figure there is a short guide to beam settings (in Italian language).

At the top right corner, there is a part in which DAQ input channels from different devices are stored: this section allows to know from which DAQ channel comes the signal of a specific device. Starting from channel 0 to 5 the software receives the signal from the monitor chamber, the DUT, pressure sensor, temperature sensor, X-ray tube voltage divider, X-ray tube temperature sensor.

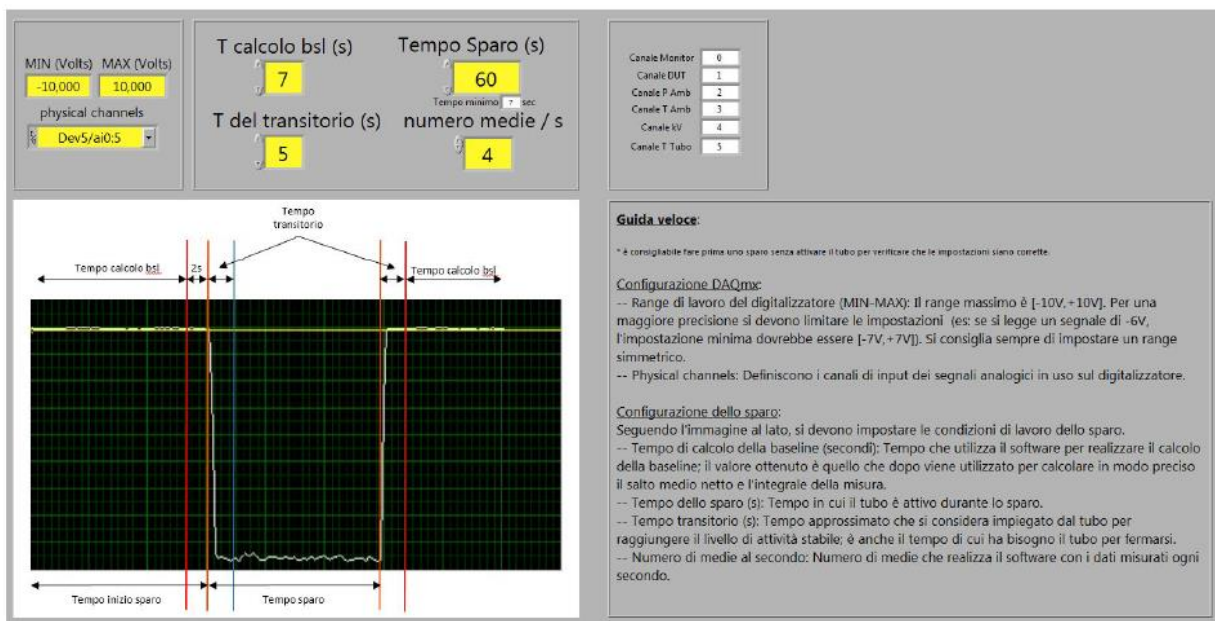


Figure 3.35 - Configuration menu for current mode measurements software.

The acquisition menu of Figure 3. has several parts which allows to control the devices functioning. On the left side of the panel there is the visualization of the monitor chamber, the device under test (DUT) and the ratio DUT/MON (monitor) signals. The first two oscilloscopes display in real time the monitor chamber and DUT detected values. The right side of the panel has the progress bar which shows the run progress. The top right corner shows the real-time value of X-ray tube voltage and its temperature. All the other outputs are the mean values computed after the entire run.

Those values are: tube voltage, room pressure and temperature, tube temperature, temperature and pressure correction factor (from equation 3.1), monitor chamber and DUT baselines, signal and integral with relative uncertainties, DUT/MON ratio. The signal is the net signal value: raw signal to which the baseline has been removed and is a flat stable value (typical for current mode measurements). The integral is the net signal multiplied for the beam on time and is linked to the air kerma. The DUT/MON has been included because allows to disengage from any fluctuations due to the non-uniform delivery of X-ray tube, as these must be recorded by both detectors. This quantity is proportional to the air kerma.

The red button allows to immediately interrupt the beam and the green one reports if the X-ray tube is used during the run.

When the run is finished, data are saved in a dedicated folder. Files are classified by the current data and hour. For every run five different files are stored: the pictures of the three displays, the "integrals" file (output values summary) and the "signal" file (time, monitor signal, DUT signal and measured kV at fixed time intervals).

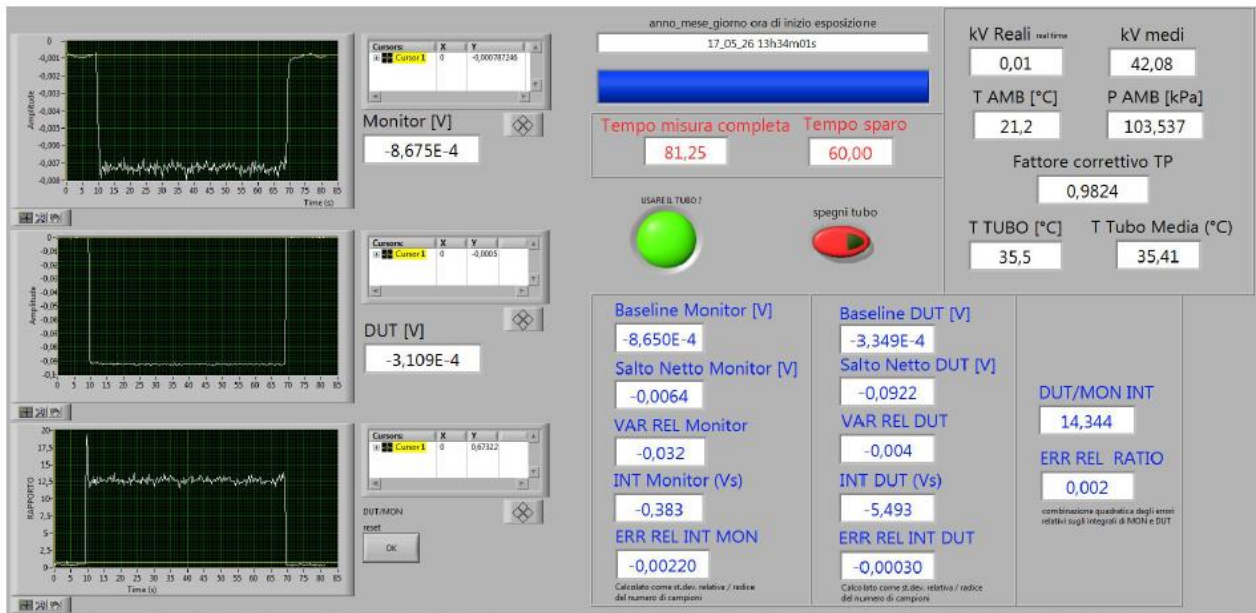


Figure 3.36 - Acquisition menu for current mode measurements software.

Pulse mode measurements

The DAQ used is a NI USB-6366. It is composed of:

- 8 differential input channels with 16 bit resolution and maximum sample rate of 2.00 MS/s, a trigger;
- 2 output channels;
- 4 counter-timers.

This device needs appropriate power supply by its power cord, is connected to a PC by USB and is used in pulse measurements for its high sampling rate: a greater number of samples per second is needed in very short signals.

For pulse mode measurements, the software is completely different from the previous one because it reflects the need of displaying the signal and eventually perform a spectrum.

Referring to the figure Figure 3.37, on the top there is the path in which the run information and spectra are stored, the recording time and the interval of data backup. The black button, if pressed, starts the spectrum acquisition. The right side is composed by two displays (an oscilloscope and a spectrum visualizer) and a part which reports all the needed information. The two displays are available for 0 and 1 DAQ channels and can be selected by means of a flag on the top of the oscilloscope. The bottom part has the values for minimum and maximum detectable signal values (from left to right); counts per seconds (cps) net, cps under the region of interest (ROI) and total

counts for both channels; minimum and maximum voltage values for the spectrum (channel 0 and 1); number of bins in which the spectrum x-axis is divided; the ROI Sx (low voltage cut-off which delimits the ROI); the threshold that discriminates if a signal is an interesting event or not.

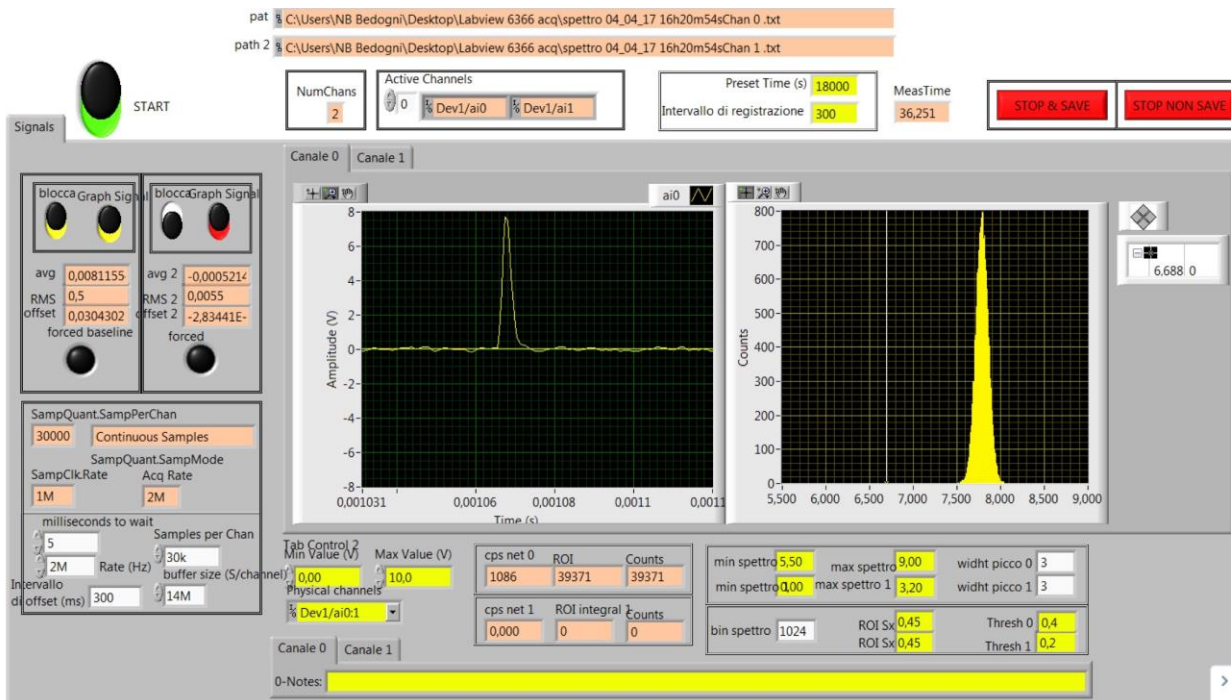


Figure 3.37 - Pulse mode software panel. The oscilloscope shows a gaussian shaped pulse and the left display reports the spectrum of a 7,8 V amplitude step signal (input of the preamplifier).

The left side of the panel shows some buttons to block the desired image on the oscilloscope; the instantaneous value of average and RMS signal value (very useful tool in absence of events because the RMS allows to calculate the threshold value); number of samples per channel and sample rate. If the user wants to interrupt the measure before its end, one of the two red button can be pressed choosing if data have to be saved or not.

The saving procedure is similar to the current mode case: files are identified by saving data and hour and for every run there is the production of six files, three for each channel. The spectrum image, the "integrals file" with run setup and the "spectrum file" which contains the data that let reconstruct the stored spectra (numbers of counts for each channel). Usually the channel zero is connected to the shaping amplifier (output of the processing chain) and the first channel to the preamplifier output. Figure 3.37 shows some examples of input, amplifier and preamplifier signals.

The following figure shows typical gaussian shaped signals exiting form the amplifier (the shape could not be appreciated due the time scale used, but they are the same to the one of Figure 3.38); the red signals are the step signals with exponential decay: the recorded shape is very similar to the theoretical one.

At last it has to be told that this software can not operate by itself on the control room workstation because it is not equipped with the X-ray tube control. So, the current software has to be put in background to give the beam on signal to the X-ray tube.

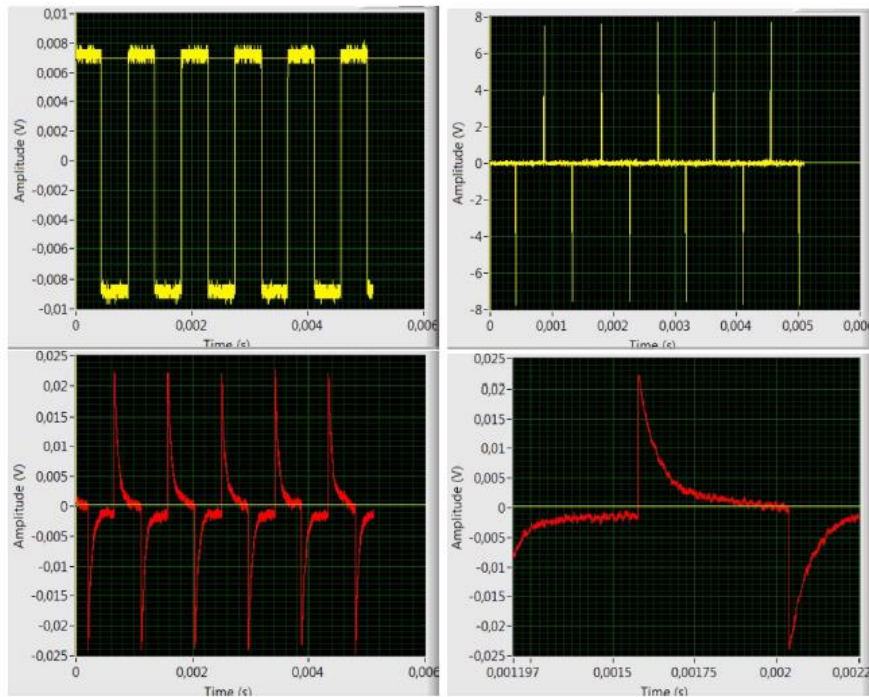


Figure 3.38 - Examples of: input step function (top left), related gaussian shaped signals (top right), preamplifier output (bottom left) and preamplifier zoomed signal (the exponential decreasing tail is clearly visible). Amplifier and preamplifier signals refer to the same run; the input signal is about ten times fewer that the real one.

3.3 Radiological safety system

To ward off the presence of people inside the experimental hall while the tube is on-going there are several security systems. First of all there is a video camera which allows to monitor the whole experimental setup form the control room; above the front door of the experimental hall, inside and outside the room, there is a flashing light signal that indicates if the X-ray tube is in use or not; a switch put next to the external light signal which inhibits the X-rays delivering if the door is open: even if the X-ray tube receives the input of delivering X-rays, this order would be ignored (see Figure 3.39).

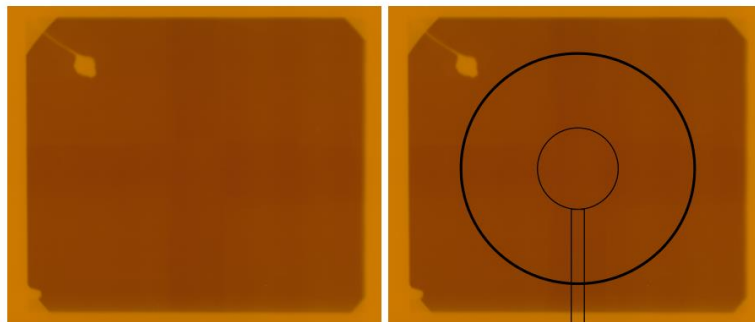
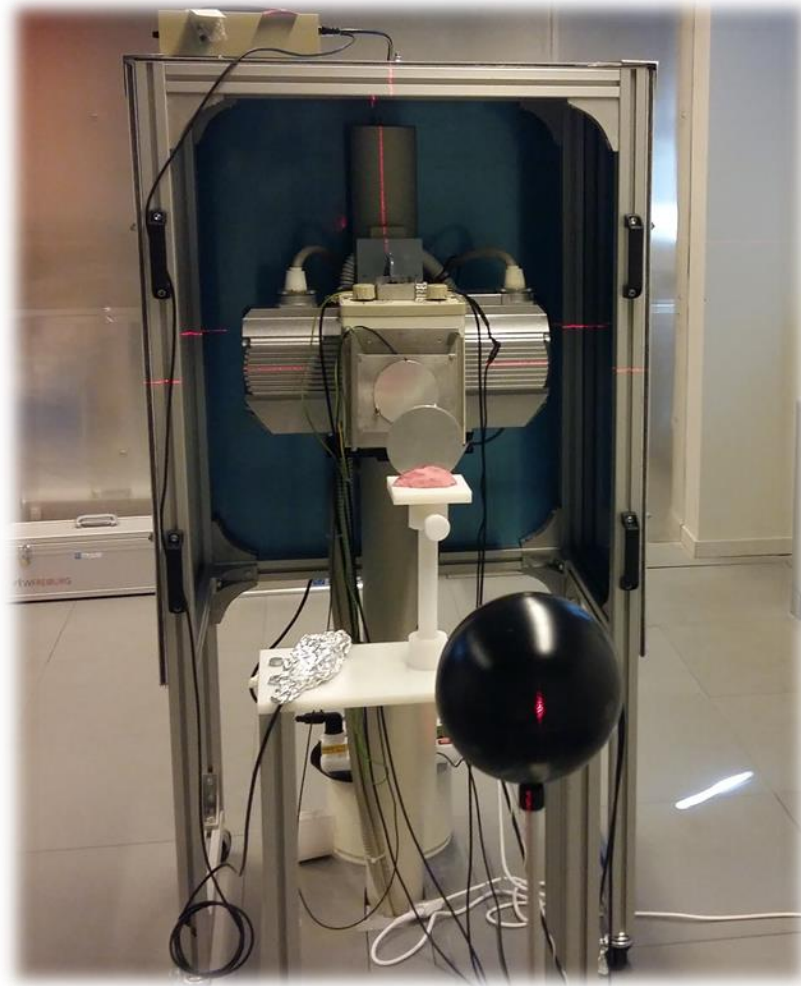


Figure 3.39 - External view of the experimental hall door. The device on the center signals that the X-ray tube receives the high voltage supply and is ready to be used, the red light on the right (light off) is a flashing one and indicates if the tube is on-going or not, the blue device on the right corner is the switch. The panel in the center contains the explanations of the flashing light.

It is possible to use the device in safety thanks to several precautions including the design of the shielding walls based on a project dose of 0.1 mSv/y. Looking at Figure 3.2, the walls no. 1 and n. 2 are in reinforced concrete with a thickness greater than 40 cm; there is a wall-to-ceiling 3 mm lead shield (n.3) and a 2 mm lead layer (4) mounted on the communication wall with the bathrooms; the floor and the ceiling are at least 30 cm thick and were made of reinforced concrete.

In order to verify that the annual dose limit is not exceeded, some thermoluminescence environmental dosimeters were installed in adjoining rooms; they are provided by a regular dosimetry service, with a periodicity of no longer than three months.

Part II – The complete qualification and characterisation of the X-ray irradiation unit



4 MONITOR ION CHAMBER

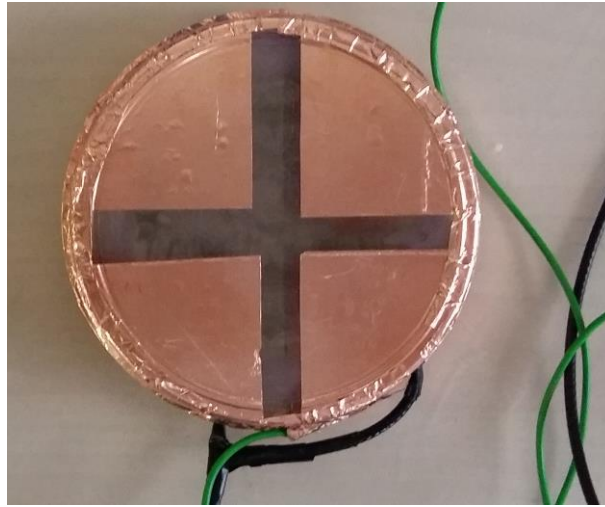


Figure 4.1 - Monitor ionization chamber developed within the work team.

The first requirement for the monitor chamber (Figure 4.1), developed within the work team (more details about the design in 3.2.5 paragraph), was to know the operating point for the monitor chamber which controls the X-ray tube output.

To determine the bias voltage needed to have a stable and reproducible output signal, for every possible tube current value, a voltage scan was made. The tables in the Appendix 10.15 contain, for every applied voltage value the average of kV measured by the voltage divider, the baseline, the recorded signal and the integral for both the monitor and PTW chambers, the ratio between the integrals (PTW/MON) and kerma in air, calculated using the following equation.

$$K_{air} = \frac{\Delta V}{R_f} * F_{cal} * F_{T,P} \quad (4.1)$$

Where ΔV is the PTW integral ($V*s$), R_f is the feedback resistor of the electronics, $F_{cal} = 2,448 \cdot 10^4$ Gy/C is the detector calibration factor and $F_{T,P}$ is the temperature and pressure correction factor ($C_{T,P}$ equation 3.1).

Baseline (bsl), integral and signals values are reported as displayed by the acquisition software, and have a negative sign, because ionization chambers processing electronics is provided with an inverting operational amplifier configuration. The absolute values were used for calculating PTW/MON, K_{air} and K rate (i.e. kerma in air rate). Every value was estimated with an uncertainty lower than 0.1%, which is not explicitly written.

From all those tables, it is possible to verify that, given a value of preset current, K rate has a unique value. Considering that tube current is not a measurable variable due to the lack of a feedback control and that can vary from day to day, the measurements will be classified in the following in terms of K rate. For every tube current, the chosen K rate value is the average of all the computed ones and the associated uncertainty is the standard deviation.

To determine the operation point of the monitor chamber, the average values of signals were calculated and reported in Table 4-1. Finally, using the average values, the plot of Figure 4.2 was drawn.

Bias (V)	Monitor signal (V)					
	0.21 ± 0.02 μGy/s	0.566 ± 0.008 μGy/s	1.278 ± 0.008 μGy/s	1.79 ± 0.02 μGy/s	2.46 ± 0.015 μGy/s	3.20 ± 0.02 μGy/s
50	0.017	0.044	0.089	0.122	0.157	0.193
70	0.017	0.047	0.099	0.138	0.183	0.229
90	0.017	0.048	0.104	0.147	0.196	0.250
100	0.018	0.049	0.106	0.150	0.201	0.252
200	0.018	0.049	0.110	0.159	0.218	0.280
300	0.018	0.049	0.111	0.161	0.221	0.286
400	0.018	0.049	0.111	0.161	0.222	0.289
500	0.018	0.049	0.111	0.162	0.223	0.291
600	0.018	0.049	0.111	0.162	0.223	0.292
700	0.018	0.049	0.111	0.163	0.223	0.292
800	0.018	0.049	0.111	0.163	0.223	0.293
900	0.018	0.049	0.111	0.164	0.224	0.293

Table 4-1 - Averaged values of Monitor signals for different applied voltage and kerma in air rate.

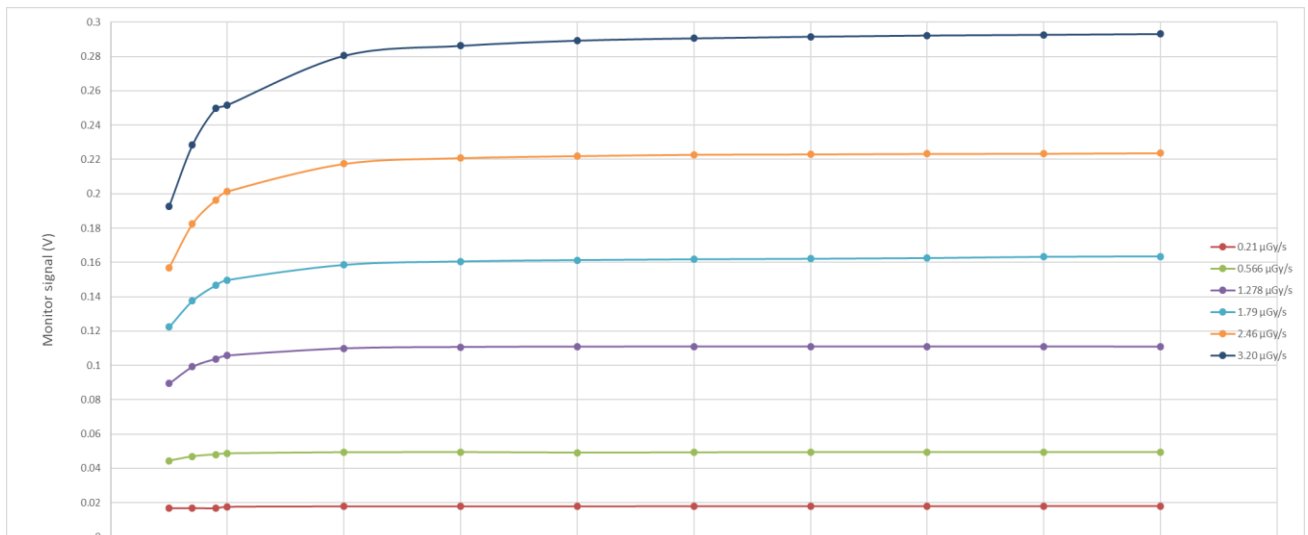


Figure 4.2 - Monitor chamber signal at different applied voltage and kerma rate values.

The graph of Figure 4.2 emphasizes the signal stability above a monitor chamber operating bias of 400 V. The six different curves have all the same shape but this is not clearly visible because of the need of representing all the curves in the same graph. A rise initial part followed by a plateau region shows that with the increasing voltage, a major percentage of electronic charges is collected thanks to the more intense electrical field, which can separate efficiently the charges. When the charge collection is complete, the plateau region is reached. The level of the plateau depends on the generated ionization, so it is important studying the monitor chamber output for different anodic current values, i.e. for different air kerma rates.

400 V was chosen as working point because it is the value for which the monitor signal stabilizes for every air kerma rate value and because applying a higher voltage could be in contrast with the insulation of electrodes welding. Above 400 V bias voltage the signal stability is reached for the different air kerma rates.

During those set of measurements, the PTW chamber was placed at 951 mm from the reference point and the tube operated at the reference condition named "F60 beam". This beam quality was obtained by applying 60 kV between anode and cathode and an additional filtration of 4 mm of Al and 0.6 mm of Cu. The runs setup was: 13 s for the baseline calculation, 5 s of transition time, 60 s of X-ray supply and 4 average/s.

The measuring setup is the one of Figure 4.3. PTW chamber was placed at a chosen distance from the tube, thanks to a mobile trolley and its locking system. It was positioned in front of the tube exit, aligning the tube and the detector centres. The figure also shows the electronics associated, the DAQ and the high voltage supply.

All measurements in Appendix 10.15 were done with a monitor chamber bias of 400 V.

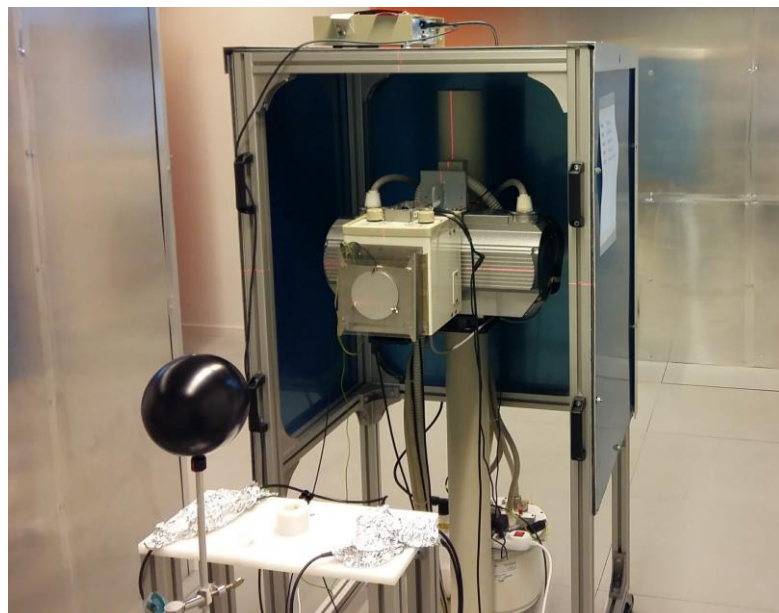


Figure 4.3 - Monitor and PTW ionization chambers characterization experimental setup.

Using the values of tables in Appendix 10.15 the monitor chamber leakage current was studied. For every applied bias, baseline averaged values were computed and used in a graph which shows the dependence of the detector leakage current as a function of the applied voltage (see Figure 4.4).

The leakage current was estimated as:

$$I_{leak} = \frac{V_{bsl}}{R_{feedback}} \quad (4.2)$$

where V_{bsl} is the output signal of the chamber (baseline) and $R_{feedback}$ is 20 M Ω .

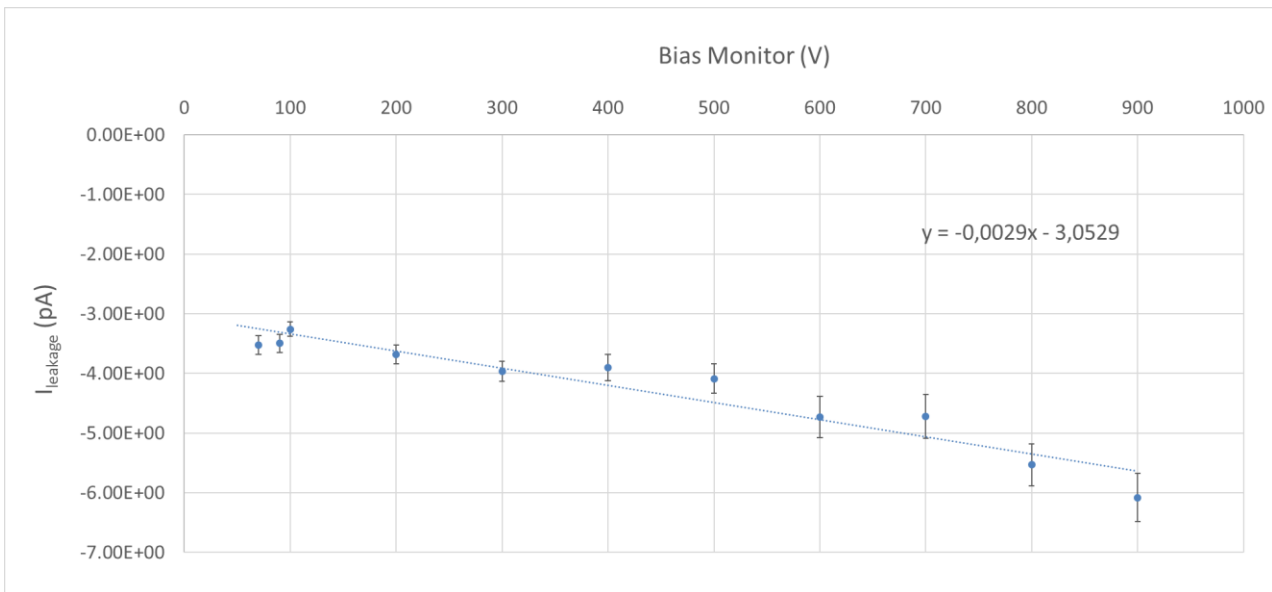


Figure 4.4 - Monitor chamber leakage current at different bias values.

As expected, the absolute value of the leakage current increases with the applied voltage as the detector constituents are subjected to more intense electric field is cause for the current increase. Nevertheless, the slope of the curve is roughly zero; this means that leakage current variations are not so large.

5 FOCUS REGRESSION

X-ray tube focus determination is useful to get K_{air}/MON trend as a function of the distance of PTW from the tube. In addition, given some reference values of K_{air}/MON and knowing this law, it is possible to make interpolations between two given values and thus obtain the desired tube output monitor quantity value.

In order to determine the X-ray tube focus position inside the lead tube enclosure, the variation of kerma in air with respect to PTW position from the reference point was studied.

The experimental setup configuration is always the one described above, but the PTW chamber was set free to be moved along the irradiation line.

The different runs were performed with the tube at 60 kV with a current of 0,5 mA without using additional filtration, 13 s for baseline calculation, 5 s of transit time, 4 means/s and 60 s of X-ray beam on.

The choice not to use additional filtration lies in the fact that the focus determination is an extrapolation made in a point where the beam has not yet been modified by the possibly present additional filtration: there is the need to have an uniform beam in the entire beam line (from the focus to PTW chamber).

Data referring to this topic are listed in Table 5-1.

Distan. (m)	kV	Monitor			PTW			PTW/MON	Corr. Fact.	K_{air} (μGy)	Mean	Unc.
		bsl (V)	Integral (Vs)	Net signal (V)	bsl (V)	Integral (Vs)	Net signal (V)					
0.605	60.55	-1.15 E-04	-1.078	-0.0180	-7.204 E-05	-121.401	-2.0308	112.662	0.983	584.21	576	8
0.605	60.55	-9.31 E-05	-1.048	-0.0178	-7.716 E-05	-118.224	-2.0076	112.770	0.982	568.52		
0.884	60.56	-9.99 E-05	-1.045	-0.0177	-8.486 E-05	-69.946	-1.1879	66.942	0.981	336.13	342	6
0.884	60.55	-1.04 E-04	-1.081	-0.0181	-2.715 E-05	-72.328	-1.2120	66.939	0.982	347.90		
0.954	60.54	-1.07 E-04	-1.077	-0.018	-8.501 E-05	-64.384	-1.0879	59.781	0.982	309.52	312	3
0.954	60.55	-1.24 E-04	-1.095	-0.0183	-7.920 E-05	-65.416	-1.0915	59.757	0.982	314.69		
1.267	60.51	-1.21 E-04	-1.067	-0.0181	-7.90 E-05	-40.815	-0.6928	38.245	0.982	196.12	199	3
1.267	60.56	-1.18 E-04	-1.097	-0.0183	-6.06 E-05	-41.927	-0.6996	38.236	0.982	201.71		
1.576	60.55	-1.00 E-04	-1.093	-0.0183	-5.11 E-05	-29.203	-0.4893	26.706	0.982	140.28	140	2
1.576	60.57	-1.05 E-04	-1.096	-0.0184	-1.37 E-05	-29.243	-0.4900	26.690	0.982	140.60		
1.835	60.56	-1.12 E-04	-1.100	-0.0184	-7.04 E-05	-22.581	-0.3767	20.534	0.982	108.54	108.51	0.04
1.835	60.56	-1.10 E-04	-1.101	-0.0184	-4.64 E-05	-22.574	-0.3767	20.511	0.981	108.47		
2.115	60.55	-9.91 E-05	-1.096	-0.0184	-3.33 E-05	-17.439	-0.2922	15.922	0.981	83.78	83.79	0.06
2.115	60.56	-9.03 E-05	-1.097	-0.0184	1.89 E-05	-17.45	-0.2924	15.901	0.981	83.81		

Table 5-1 - Monitor and PTW chamber signals as the distance of the PTW from the reference point varies. The column "uncertainty" lists the standard uncertainty associated with the mean values.

Data of Figure 5.1 lie along a curve that reflects the kerma trend according to the inverse square law. Those data was fitted with a best fit curve of the following equation.

$$K_{air} = \frac{A}{(x + F)^2} \quad (5.1)$$

Where A is a normalization constant, x the PTW distance from the reference point and F the focus to reference point distance.

Using this function and setting A and F as free parameter it has been possible to determine the equation of the best fit curve, whose results are shown in the legend of Figure 5.1.

The focus most probable value is $F = 0,341$ m. To calculate the associated uncertainty, the best fit curve was used with every K_{air} value of Table 5-1.

This procedure allowed to extrapolate seven focus best fit values, whose standard deviation corresponds to the uncertainty of the focus most probable value which results in:

$$F = 0.341 \pm 0.005 \text{ m} \quad (5.2)$$

From this moment on, all PTW distances values will refer to the distance from the X-ray tube focus.

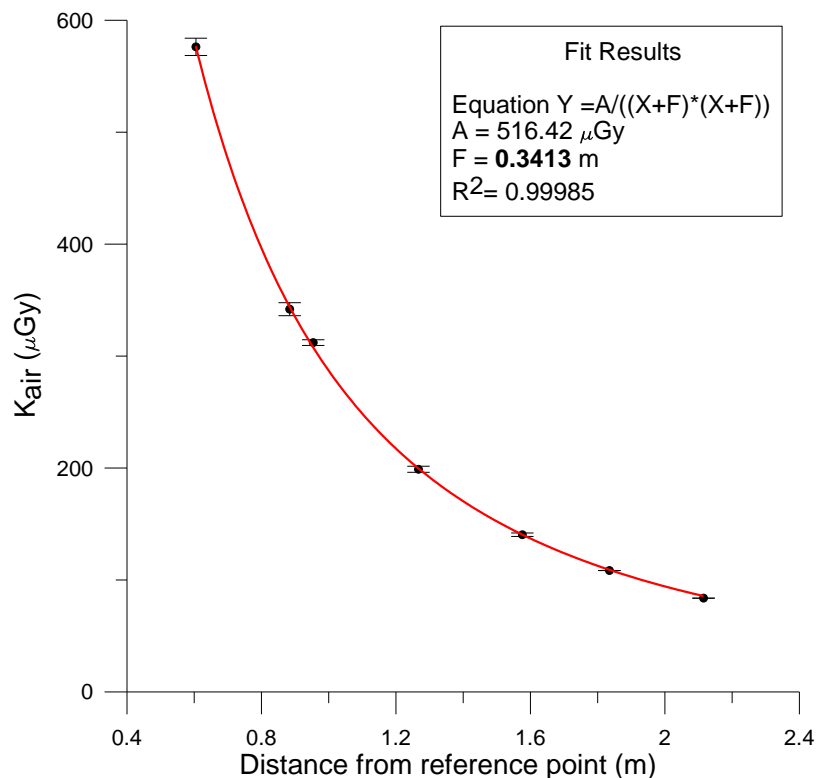


Figure 5.1 - Kerma in air as a function of PTW distance from the reference point.

6 HALF VALUES LAYERS EVALUATION

The half value layer (HVL) is the “thickness of a specified material which attenuates the beam of radiation to an extent such that the total air kerma rate is reduced to half of its original value” (ISO 4037-1 2016). In this chapter the taken measurements to evaluate the first HVL values of the beams in use are shown.

To esteem half value layers (HVLs) there is the need of placing some metal absorbers that attenuate the beam between the X-ray tube focus and the device under test (DUT). By varying the thickness of these absorbers, it is possible to evaluate the beam HVL.

HVLs determination is a powerful test to evaluate if the beams in use are consistent with ISO ones or not. Indeed, as there is no spectrometry standard procedure to evaluate the energy composition of the beam (ISO 4037-1 2016), HVL determination allows to verify it in an indirect way.

Because of all the materials between the anode and the tube exit window, the X-ray tube inherent filtration was not known with high precision, so an iterative procedure for determining the additional filtration in order to reproduce the N-series beams was used (see the last part of this chapter for an example).

The objective was reaching the proper choice of kiloVolt / filtration combinations to achieve well-identified radiation qualities, as specified by relevant international Standards. These are the quasi monochromatic spectra of the N series, the narrow series of ISO 4037, useful as calibrating reference: radiation beams with narrow energy spectrum, recommended for the study of the dependence of the dosimeter response on the energy of the incident radiation (ISO 4037-1 2016).

6.1 HVL evaluation procedure

What it was done, was to use the HVLs determination procedure backwards. For every beam quality the aim was to obtain the ISO HVL value by different measurement session. Each session was performed with a specific value of additional filtration and recording one run for every metal absorber thickness used. Among those sessions, it was chosen the one with the discrepancy between experimental and theoretical first HVLs values less than 5%. Limited to the laboratory availability of metal absorbers, the evaluation was done both with aluminium and with copper.

To perform this measurements ISO good geometry recommendations were followed as much as possible (ISO 4037):

- I. the metal absorbers shall have a purity of at least 99.98 %;
- II. if a monitor ionization chamber is used during the measurement, it shall be placed between the two sets of beam collimator and be followed by the metal absorbers in such a manner that it does not respond to radiation backscattered from the absorbers;
- III. the HVLs shall be determined using an ionization chamber with a small dependence of the response to total air kerma (rate) over the energy range of interest, e.g., in line with clause 4.3 of ISO 4037-2. Corrections shall be applied for any variation in detector response with changes in the photon spectrum as the thickness of the metal absorber is increased;
- IV. the measurements shall be made in a manner such that negligible scattered radiation from the absorbers reaches the detector, since such radiation would increase the measured HVL;

- V. the metal absorbers shall be located equidistant from the X-ray tube focus and from the detector. The diameter of the beam at the detector location shall be just sufficient to irradiate it completely and uniformly;
- VI. the diameter of the detector shall be less than 3 cm. The distance between the metal absorbers and the detector shall be at least ten times the diameter of the beam at the detector;
- VII. plot the attenuation curve:

$$f(D) = \log_e(ID) \tag{6.1}$$

where ID is the value of the total air kerma rate which is transmitted through a filter having a thickness D ;

- VIII. from the attenuation curve, determine the HVL.

The HVLs shall be determined according to the previous indications. As it was not possible to fulfil all the recommendations at the same time, measurements were made at first with the PTW chamber.

6.2 PTW HVLs measurements

Using PTW ionization chambers, some points of the previous list are automatically fulfilled while others need special arrangements to be respected.

The monitor ionization chamber could not be placed between two collimators because in the laboratory there was no structures to place a second collimator, but however it doesn't respond to backscattered radiation because the recorded signal with and without the presence of metal absorbers is unchanged (Table 6-1 and Table 6-2). Point III is automatically fulfilled by using PTW chamber (Appendix 10.4). A wider explication should be made about points IV, V and VI.

As the ISO HVLs are given at a distance from the X-ray source of 1.0 m and 2.5 m and the results don't vary significantly with the distance, the PTW chamber was placed at 1.40 m and the additional filtration at 0.74 m from the tube focus. Since the condition of point VI could not be satisfied with PTW chamber because of its big dimensions, the choice of those distances are related to the possibility of placing two different devices along the irradiation line maintaining the indications of point V. Nevertheless the PTW chamber was set at more than the distance between focus and absorbers in order to avoid scattered radiation from metal absorbers.

The used beam is narrower than usual to make it the exact size to just cover the PTW chamber.

The attenuation curve was drawn as

$$\log_2(K/K_0) \tag{6.2}$$

where K is K_{air} with a defined thickness of metal absorbers and K_0 the one without them. Using air kerma instead of air kerma rate doesn't affect the results because every run has the same duration. This procedure was chosen with respect to the ISO one for its simplicity and graphic immediacy. When the curve reaches $Y = -1$, the corresponding X value is the HVL. Every run was performed with 5 s for baseline calculation, 5 s of transit time, 60 s of beam on and 4 means/s. The tube current was set at 1 mA so as to not overheat it.

Figure 6.1, Figure 6.2 and Figure 6.3 show the mounting of the experimental setup.

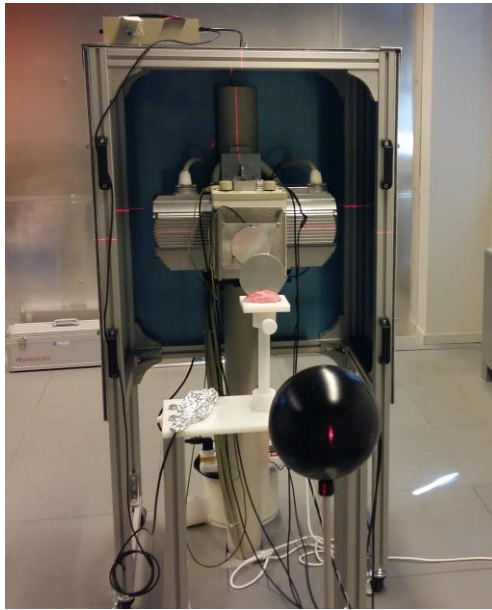


Figure 6.1 - Experimental setup for HVL measurements.

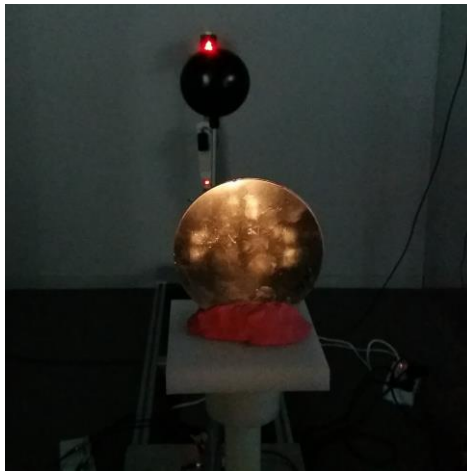


Figure 6.2 - Experimental setup for HVL measurements. View from the monitor chamber.

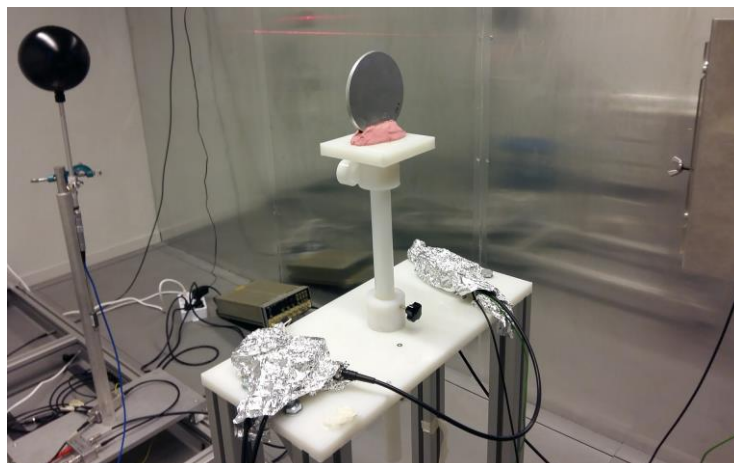


Figure 6.3 - Metal absorbers positioning along the mechanical bench.

Those figures show how the metal absorbers were put along the irradiation line, more or less at the centre between tube focus and PTW chamber. The Figure 6.2 enhances the X-ray field reflection on the metal absorber. It had a cross shape due to the interposition of the monitor ionization chamber between the tube exit window and the support for placing the additional filtration. HVLs have been reckoned both with Al and Cu absorbers. Data are listed in Table 6-1 and Table 6-2 and plotted in Figure 6.4 and Figure 6.5.

		Cu thickness	Integral MON	Integral PTW	Corr. Fact.	K_{air}	log₂ (K/K₀)
	kV	(mm)	(Vs)	(Vs)		(μGy)	
N60	60.32	0.00	0.776	7.353	0.978	35.21	
	60.32	0.10	0.778	5.342	0.978	25.59	-0.461
	60.32	0.20	0.758	3.887	0.978	18.62	-0.919
	60.32	0.25	0.786	3.589	0.979	17.19	-1.034
	60.3	0.26	0.774	3.415	0.979	16.37	-1.105
	60.32	0.30	0.776	3.007	0.978	14.40	-1.290
	60.32	0.40	0.776	2.269	0.979	10.87	-1.696
	60.32	0.50	0.785	1.792	0.978	8.58	-2.036
N80	80.29	0.00	1.316	3.158	0.978	15.13	
	80.30	0.25	1.336	2.383	0.979	11.43	-0.400
	80.30	0.50	1.330	1.735	0.980	8.32	-0.857
	80.31	0.75	1.337	1.324	0.980	6.35	-1.247
N100	100.24	0.00	1.921	1.222	0.980	5.86	
	100.24	0.50	1.913	0.891	0.980	4.28	-0.455
	100.24	0.75	1.917	0.768	0.980	3.69	-0.669
	100.24	1.00	1.912	0.654	0.981	3.14	-0.900
	100.23	1.25	1.932	0.572	0.981	2.75	-1.093
N120	117.82	0.00	3.097	1.197	0.982	5.76	
	117.83	0.25	3.099	1.082	0.983	5.21	-0.145
	117.82	0.50	3.089	0.968	0.983	4.66	-0.306
	117.82	0.75	3.095	0.881	0.983	4.24	-0.441
	117.83	1.00	3.097	0.793	0.982	3.81	-0.594
	117.83	1.25	3.098	0.719	0.982	3.46	-0.735
	117.83	1.50	3.088	0.650	0.983	3.13	-0.880

Table 6-1 - Cu first 1stHVLs.

		Al thickness	Integral MON	Integral PTW	Corr. Fact.	K _{air}	log ₂ (K/K ₀)
	kV	(mm)	(Vs)	(Vs)		(uGy)	
N40	42.08	0	0.376	15.202	0.983	73.16	
	42.08	2	0.380	8.951	0.983	43.08	-0.764
	42.07	3	0.382	6.970	0.983	33.54	-1.125
	42.08	4	0.383	5.493	0.982	26.42	-1.469
N60	60.32	0	0.776	7.353	0.978	35.21	
	60.32	4	0.776	4.560	0.978	21.84	-0.689
	60.32	5	0.772	4.055	0.978	19.42	-0.859
	60.32	6	0.775	3.625	0.978	17.36	-1.020
	60.32	7	0.767	3.209	0.978	15.37	-1.196
N80	80.29	0	1.316	3.158	0.978	15.13	
	80.31	7	1.327	1.973	0.979	9.46	-0.672
	80.29	8	1.326	1.843	0.979	8.84	-0.771
	80.31	9	1.318	1.717	0.979	8.23	-0.873
	80.29	10	1.320	1.606	0.979	7.70	-0.969

Table 6-2 - Al 1stHVLs.

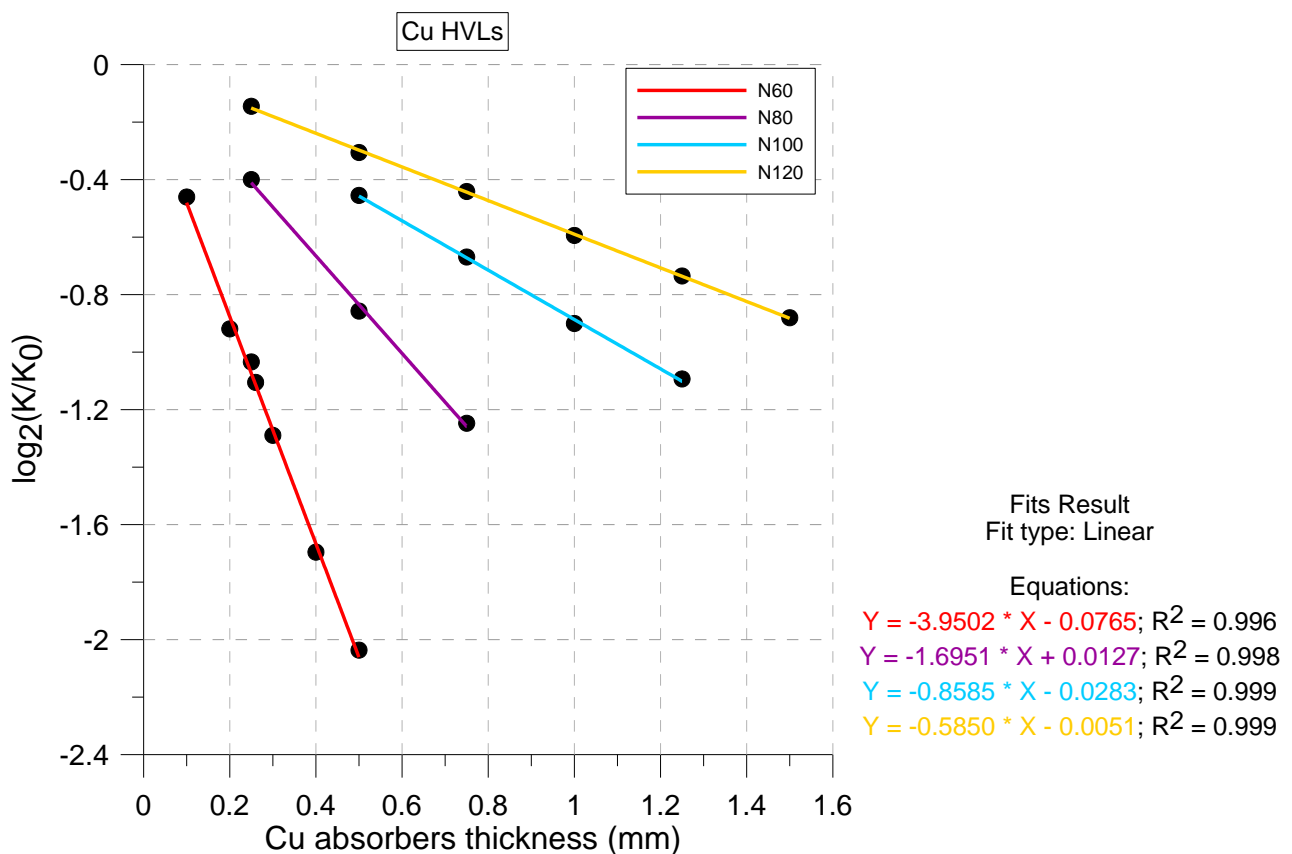


Figure 6.4 - Graphs for Cu HVLs determination, best fit lines and equations for N60, N80, N100 and N120 beams. When Y = -1, the equation gives the 1stHVL value. For graphic consistency, the colour legend is consistent with that of the previous graph.

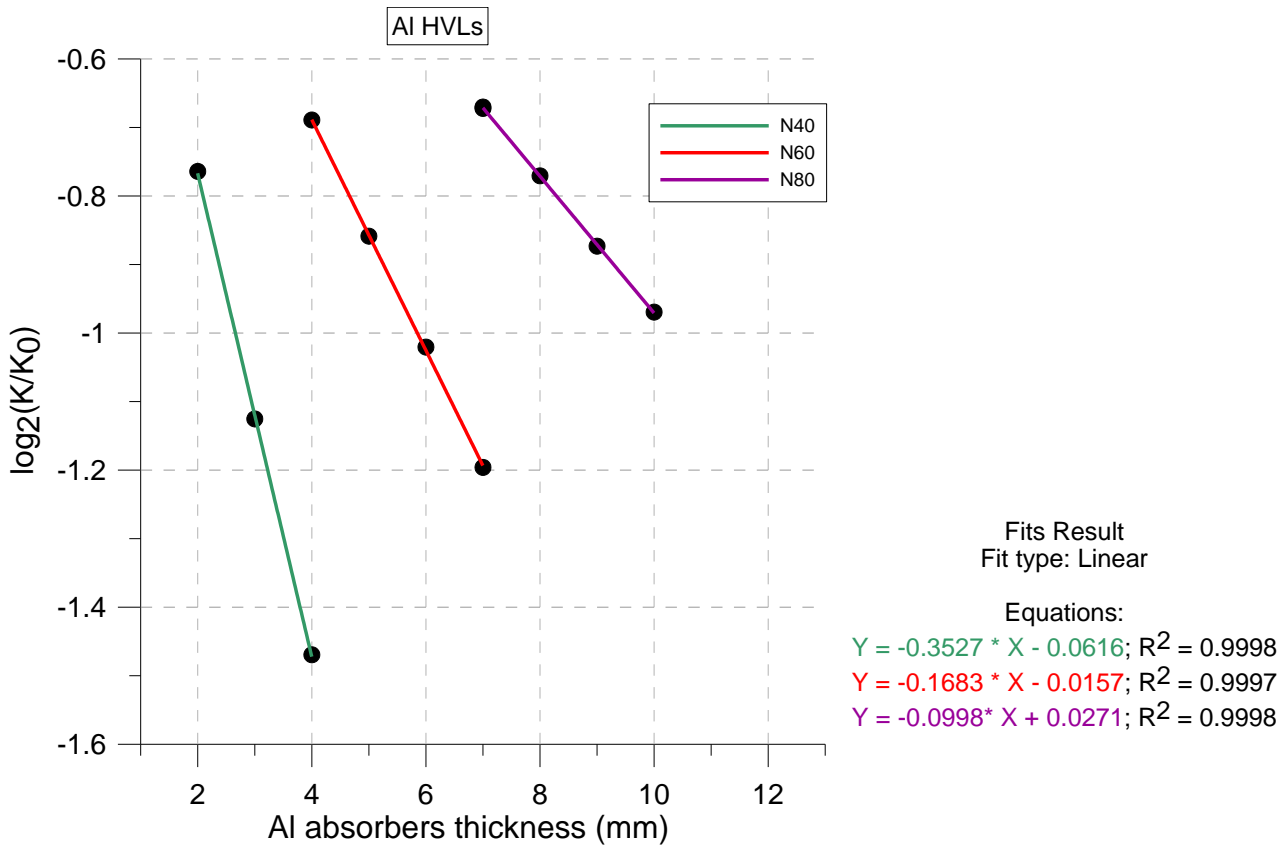


Figure 6.5 - Graphs for Al HVLs determination, best fit lines and equations for N40, N60 and N80 beams. When $Y = -1$, the equation gives the 1stHVL value. For graphic consistency, the colour legend is consistent with that of the previous graph.

Figure 6.4 and Figure 6.5 show, for every beam quality, the plotted data and the corresponding best fit equation, in which R^2 is very high in all cases. From those equations it was possible to go back to the first HVL values, which are listed in Table 6-3.

The uncertainty associated with experimental HVLs is not reported since, for every beam quality, the high value of R^2 means good accordance between data and best fit curves. Furthermore, as the PTW and monitor chamber integrals have an uncertainty of not more than the 1%, the uncertainty of equation (6.2) is not more than 4%, thus, the maximum uncertainty associated with the HVLs extrapolation by best fit curves could not be more than 4%. As shown, the accordance between theory and experiment is very good even if all the requirements were not met.

Beam features			Theoretical HVL		Experimental HVL		Discrepancy (%)	
Beam	kV	Additional filtration	mm Al	mm Cu	mm Al	mm Cu	Al	Cu
N40	42.08	inher + 0,5 mm Al + 0,1 mm Cu	2.72	0.085	2.66		-2.2%	
N60	60.32	inher + 0,5 mm Al + 0,5 mm Cu	5.87	0.234	5.848	0.2330	-0.37%	-0.44%
N80	80.30	inher + 0,5 mm Al + 1,8 mm Cu	9.79	0.578	10.29	0.5973	5.1%	3.3%
N100	100.24	inher + 0,5 mm Al + 4,8 mm Cu		1.09		1.1319		3.8%
N120	117.83	inher + 0,5 mm Al + 4,9 mm Cu + 1 mm Sn		1.67		1.7007		1.8%

Table 6-3 - 1st HVLs experimental results. The sign of the discrepancy reflects a greater or a fewer experimental value with respect to theory (ISO 4037-1 2016). Inherent filtration: 3.5 mm Al + 0.1 mm Cu.

6.3 Example of the procedure for determining the additional filtration

As instance, it is reported the complete procedure for determining the N60 beam additional filtration to reproduce the ISO 4037 HVL .

Three different measurements session have been performed by using, for every session, a different additional filtration; 0.5 mm Cu + 0.2 mm Al, 0.5 mm Cu + 4 mm Al and 0.5 mm Cu + 0.5 mm Al respectively.

Figure 6.6 shows the difference in fitting curve for data pertaining to those sessions.

As can be seen there is no big change in the slope of the best fit curves, but the difference in the y-intercept causes a variation in the resulting HVL.

By adding aluminium foils as additional filtration the computed HVL are respectively 6.34 mm, 6.26 mm and 5.85 mm of aluminium resulting in a discrepancy with respect to the theoretical value of 7.98%, 6.58% and -0.37%.

This is why the last filtration (0.5 mm Cu + 0.5 mm Al) was chosen for being the N60 beam additional filtration.

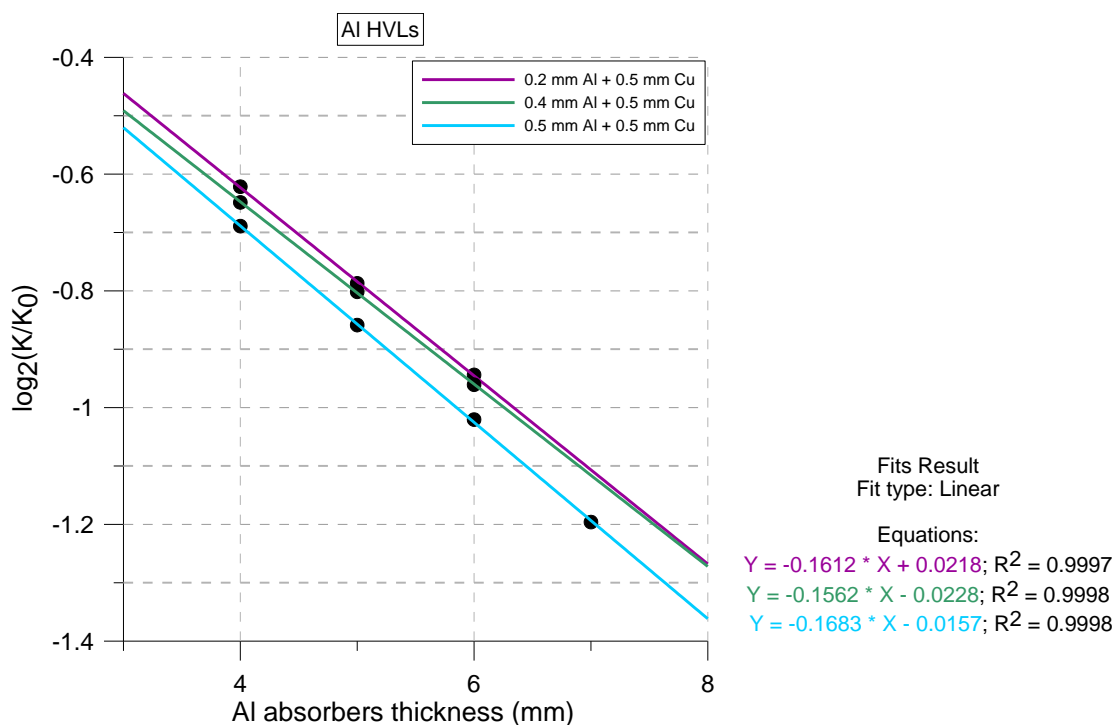


Figure 6.6 - Different measurement sessions for determining the N60 beam additional filtration.

6.4 2ndHVL and homogeneity coefficient

In order to complete the study of the radiation beams quality, the experimental method for determination of X-ray spectral composition by attenuation analysis usually shows also the second HVLs values and the homogeneity coefficient, *h*, as figure of merit.

This homogeneity coefficient is defined as the ration of the first HVL value to the second one for each beam.

$$h = \frac{1^{st} \text{ HVL}}{2^{nd} \text{ HVL}} \quad (6.3)$$

In absence of the needed metallic layers to experimentally reach the y-intercept -2 in the graphs of Figure 6.4 and Figure 6.5 (exception made for N60 Cu HVL: see Figure 6.4), an extrapolation to the second HVL values was made by using the trusted fit equations (R^2 is very high for all cases). For strong filtrations the spectral composition of the beam is constant, i.e. the beam is attenuated in number of photons but the spectrum does not significantly change, so a simple exponential describes well the situation.

Beam	m fit (mm ⁻¹)	q fit	II HVL (mm)	ISO II HVL (mm)	Δ% II HVL	h	h ISO
N60	-3.9502	-0.0765	0.253	0.263	3.74	0.92	0.89
N80	-1.6951	0.0127	0.590	0.622	5.16	1.01	0.93
N100	-0.8585	-0.0283	1.165	1.15	1.29	0.97	0.95
N120	-0.585	-0.0051	1.709	1.73	1.19	0.99	0.97

Table 6-4 - Using the fit parameters of Figure 6.4, the extrapolation to the second HVL values was made for Cu HVL. The extrapolated results are compared to the values reported in ISO 4037 (ISO 4037-1 2016). Note: the value for N60 beam has to be considered like experimental result because the corresponding line in Figure 6.4 crosses $y = -2$.

Table 6-4 shows the resulting 2ndHVLs values together with the homogeneity factor, *h*. The accordance between values from literature (ISO 4037-1 2016) and experiment is very good: the discrepancy is less than about 5%. This further proves that with the choice of proper kilovolt / filtration combinations (Table 6-3) is possible to achieve well-identified radiation qualities, as specified by relevant international Standards.

7 FIELD UNIFORMITY MEASUREMENTS

This chapter has the purpose of investigating the uniformity of the X-ray field used during the measurements presented in this PhD project.

The X-ray field uniformity is an important task that the X-ray beam must comply with, because it ensures that all the field areas are equivalent and thus that, wherever the device under test is placed, it is exposed to the same dose. Every radiation field has a divergence with respect to its centre which is the theoretical point of maximum beam intensity. This effect is due to the dimensions and electrons distribution within the X-ray tube electronic focus. All this can affect the field uniformity, in addition to the heel effect, discussed in paragraph 1.2.3.

To determine the magnitude of the variations in beam intensity within the field, two different measurements techniques were involved. The first is based on a passive detector - Gafchromic XR-QA2 - and the second one involved a silicon detector - Hamamatsu 1 cm² sensitive area - operating in current mode.

The Gafchromic XR-QA film is designed specifically as a quality assurance (QA) tool for radiology and dosimetry. Its major advantage is that it provides a high-resolution image with no chemical processing: it is enough to digitize the image through a scanner.

The film is sensitive to dose ranges between 0.1 and 20 cGy, it is not sensitive to visible light and can therefore be handled in room light. The active layer of this detector has a thickness of 25 μm and both surfaces are covered by a 97 μm thick substrate. Heavy elements ($Z_{\text{eff}} = 7.14$), composing the active layer, interact with low energy photons, mainly via photoelectric effect. The working principle of the film is the polymerization induced by ionizing radiation within the active layer that changes its reflectance turning darker the film. The film darkening is dependent on the radiation exposure received and this occurs instantaneously: the reaction immediately creates a polymer dye complex within the film active layer.

Within this measurement, a unique film to detect the whole field at the same time was used.

The Gafchromic was chosen to study the field uniformity because different beam intensities correspond to different blackening levels so, by elaborating the scan image of the film, it is possible to deduce an intensity map. Overall, thanks to a scanner and a dedicated software, it is possible to know if the tube delivers uniformly X-rays or not.

The silicon detector, used in current mode, allowed to measure the field uniformity with a spatial resolution of 1 cm² (corresponding about to the detector area) thus measurements in different field positions were made. Every measurement were taken to study the intensity of the X-ray beam in that point because the signal produced by the interactions with the detector, and thus the detected signal (Volt), is tightly connected to the fluence and dose rate of the X-ray beam, therefore generally to its intensity.

For both Gafchromic and silicon detector, the placement along the mechanical bench was made thanks to a polyethylene trolley and a carton structure (equipped with a millimetre paper sheet) to reduce, as best as possible, the scattering from the surfaces next to the device. All measurements were performed with a filtered beam (60 kV) where the additional filtration was made of 4 mm Al + 0.6 mm Cu, in addition to the inherent one of 3.5 mm Al + 0.1 mm Cu.

7.1 Gafchromic measurements

The Gafchromic film was placed at 0.94 m (Figure 7.1) from the X-ray tube focus and was exposed to a K_{air} of about 2.7 cGy correspondent to 2.68 h of tube beam on. Several runs at 5 mA were made in order to reach the desired air kerma without overheating the tube. The dimensions of the field were about 20 x 20 cm.

The Gafchromic image was digitalized through a "Canon Canonscan 9000F Mark II" scanner and thanks to the "ImageJ" software it was possible to choose a pixel line of the film along which to study the blackening variations profile. This kind of analysis was the first elaboration type of the scan image involving just the axis pixel lines (Figure 7.3 and Figure 7.4). Other special elaborations of the image were made: see next paragraphs. As explained above, the difference in blackening along the film is due to the difference in delivered dose from the X-ray tube. So, by analyzing the results, it is possible to know if the tube delivers uniformly X-rays along the whole field.

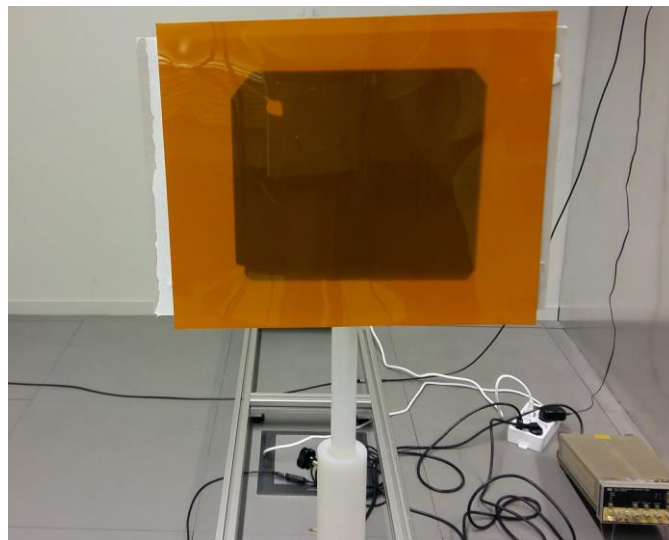


Figure 7.1 - Gafchromic positioning. View from the tube housing. From that point of view the polyethylene trolley, the borders of the carton structure and, in the Gafchromic film reflection, the X-ray tube can be also seen.

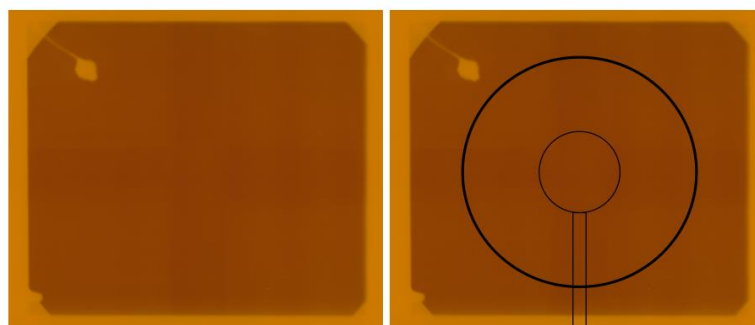


Figure 7.2 - Gafchromic film exposed to about 2.7 cGy of K_{air} (left) and the same figure with the overlaid PTW chamber scheme (right).

Figure 7.2 shows the digitalized image of the Gafchromic film. Observing the top left corner, it is visible a narrow region where almost no dose was detected; this is the field area corresponding to monitor chamber welding which allows to collect the signal from the chamber plate and direct it to the processing electronics (par. 3.2.5). Other features are evident in the same picture:

- as the field is bordered by a lead shutter, almost no penumbra is expected, nevertheless all the corners display a visible shadow area due to the shutter shape;
- in the centre of the field appears a darker cross-shaped zone corresponding to the monitor chamber part which is not covered by the copper coating (par. 3.2.5).

On the right side part of Figure 7.2 the overlap of the PTW chamber schematic profile allows to see which part of the field is really used to made air kerma measurements: no penumbra is included. In this work, two profiles were studied with "ImageJ": the horizontal and vertical one which pass through the field centre, corresponding to the monitor chamber centre.

Figure 7.3 and Figure 7.4 report the two greyscale profiles showing at the same time which line was considered. Profiles were reported as they are drawn by "ImageJ": intensity in greyscale against pixels (the pixel named as zero is the point to the left or to the top, where the line starts). The lower the grey number, the higher the dose detected in that point. This reflects the 256 shades of greyscale which associates the lowest value to the darkest shade (the black corresponds to zero) and the white as 256.

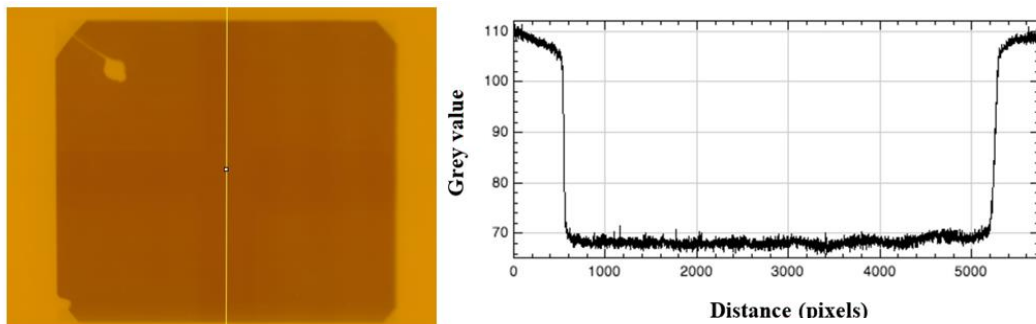


Figure 7.3 - Acquisition line and plot for the vertical axis.

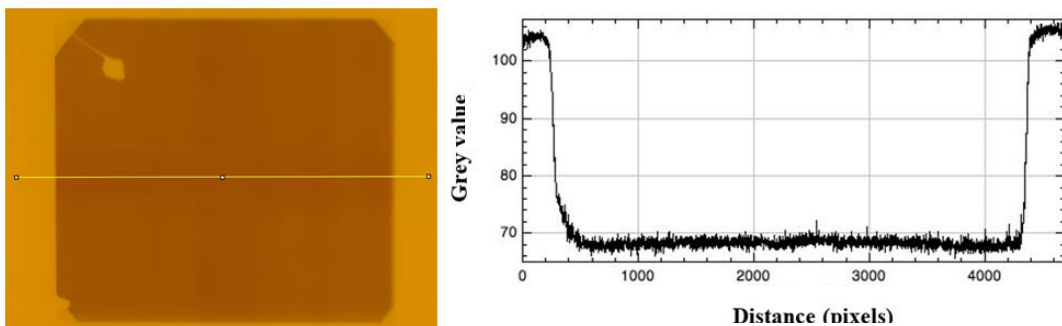


Figure 7.4 - Acquisition line and plot for the horizontal axis.

Both figures show a high field uniformity:

- (68.3 ± 0.7) grey colour considering pixels from 500 to 4100 of the vertical line,
- (68.3 ± 0.8) grey colour considering pixels from 800 to 5000 of the horizontal one.

Another interesting check about uniformity was the shadow area width: to make this, the horizontal line was chosen. The aim of this investigation was to find out how wide is the area that received a dose between 90% and 10% of the one delivered in the centre of the film.

The result is that the horizontal dimension of the shadow area is (0.65 ± 0.05) cm wide, which corresponds to the 3,35% of the horizontal field amplitude. This value is almost the same along all the points of the border line, exception made for the corners where a bigger light grey area is clearly visible (see Figure 7.5).

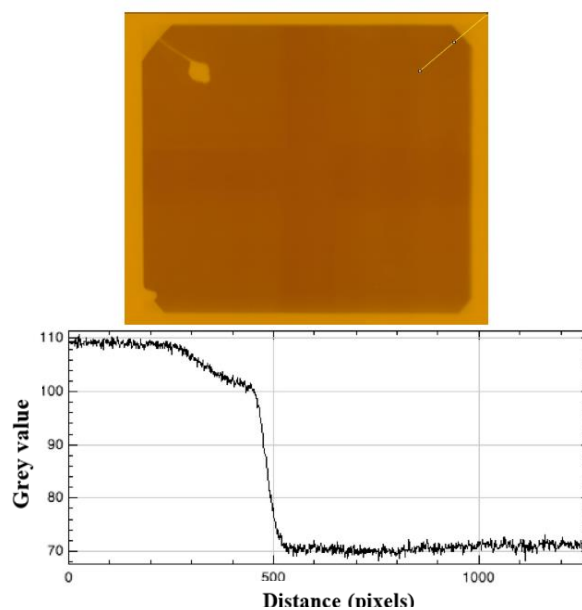


Figure 7.5 - Acquisition line and plot for the top right corner.

Analysing this plot, the penumbra was found compatible with the one written above: (0.70 ± 0.05) cm. So the penumbra has always the same width along the field border but the intensity is differently distributed. Overall, if we consider the space (in cm) where is performed the attenuation from 90% to 50% of the central value, we have (0.58 ± 0.05) cm for the corner and a value compatible with zero for the horizontal line. So, due to the shutter shape, the corners borders are defined with less precision.

7.2 Silicon detector measurements

The field uniformity was also studied by means of the Hamamatsu detector which was put on the carton structure equipped with a millimetre paper sheet in order to set precisely the different position where measurements had to be done. The detector was used in current mode and unbiased. The detector surface was set to 0.94 m from the tube focus, the same distance at which was exposed the Gafchromic film. Aligning the holder with the laser and considering the centre of the monitor chamber as the centre of the field, were taken measurements at different values of distance from the centre (Figure 7.6, Figure 7.7).

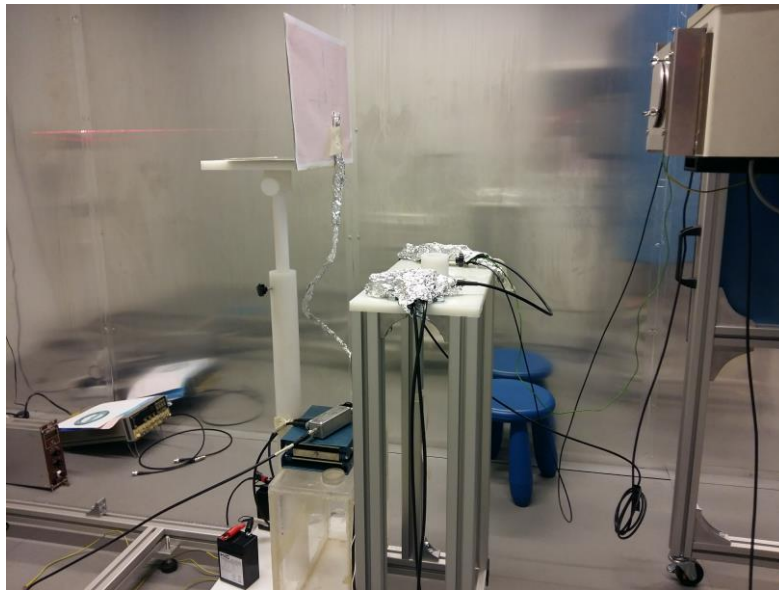


Figure 7.6 - Silicon detector positioning on the polyethylene trolley.

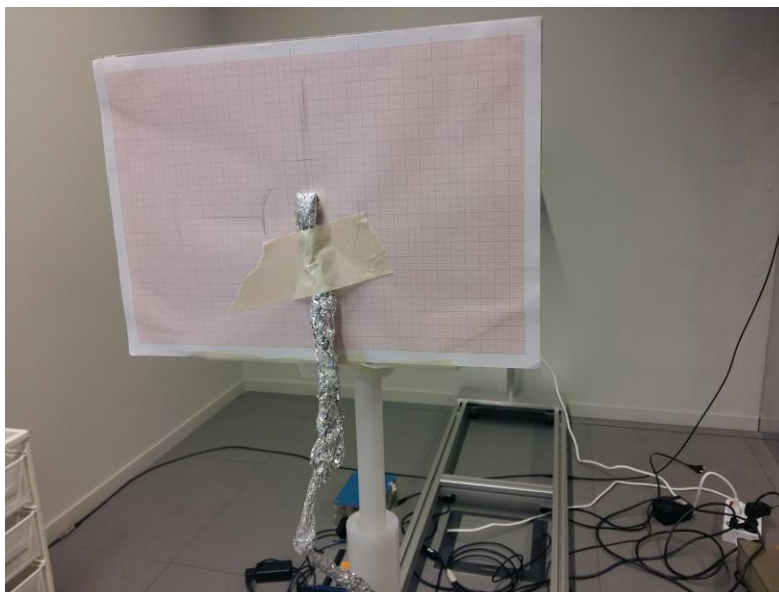


Figure 7.7 - Silicon detector positioning on the polyethylene trolley. View on the carton structure equipped with a millimetre paper sheet.

Table 7-1 lists, for every position, monitor chamber and silicon detector signal values, the integral and their ratio.

Position	Monitor		Silicon detector		Si/MON
	Signal (V)	Integral (Vs)	Signal (V)	Integral (Vs)	
center	-0.0452	-2.66	0.883	51.70	19.44
center	-0.0472	-2.83	0.923	55.25	19.54
R1	-0.0470	-2.76	0.833	49.02	17.74
R1	-0.0478	-2.85	0.845	50.38	17.68
R1	-0.0462	-2.72	0.812	47.80	17.58
R1	-0.0475	-2.84	0.834	49.93	17.56
R1	-0.0481	-2.88	0.851	51.00	17.70
R1	-0.0484	-2.88	0.855	50.98	17.68
R1	-0.0485	-2.89	0.838	49.96	17.29
R1	-0.0486	-2.90	0.839	50.03	17.27
R2	-0.0487	-2.90	0.918	54.74	18.85
R2	-0.0488	-2.92	0.921	55.06	18.85
R2	-0.0489	-2.92	0.869	51.74	17.75
R2	-0.0490	-2.92	0.867	51.73	17.71
R2	-0.0490	-2.93	0.916	54.87	18.71
R2	-0.0491	-2.93	0.916	54.65	18.68
R2	-0.0489	-2.91	0.891	53.12	18.23
R2	-0.0490	-2.92	0.892	53.21	18.22
R3	-0.0491	-2.93	0.039	2.34	0.80
R3	-0.0492	-2.94	0.039	2.33	0.79
R4	-0.0492	-2.93	0.373	22.26	7.59
R4	-0.0492	-2.95	0.372	22.28	7.56
R5	-0.0492	-2.95	0.021	1.26	0.43
R5	-0.0491	-2.93	0.021	1.26	0.43
R3	-0.0491	-2.93	0.040	2.40	0.82
R3	-0.0491	-2.94	0.040	2.41	0.82
R3	-0.0491	-2.93	0.488	29.10	9.93
R4	-0.0491	-2.93	0.486	28.27	9.65
R5	-0.0491	-2.93	0.024	1.43	0.49
R5	-0.0491	-2.93	0.024	1.42	0.49
R3	-0.0491	-2.95	0.028	1.67	0.57
R3	-0.0491	-2.96	0.028	1.67	0.56
R3	-0.0493	-2.94	0.031	1.85	0.63
R6	-0.0493	-2.94	0.847	50.74	17.26
R7	-0.0493	-2.94	0.092	5.52	1.88
R8	-0.0494	-2.95	0.016	0.98	0.33

Table 7-1 - Signals registered from the monitor chamber and the silicon detector for each position. Uncertainties are not reported since they are fewer or equal to 1%.

All those values were averaged in order to depict a graph which displays the field uniformity by means of a bubble plot (see Figure 7.8) where x and y axis run from the minimum to the maximum horizontal or vertical position chosen on the millimetre paper, the origin corresponds to the field centre and the bubble dimension stands for the percentage of the detected signal respect to the central value. The graph of Figure 7.8 contains data of Table 7-2 to show the results about field uniformity.

R	Position			Si/MON mean	%
	R (cm)	X (cm)	Y (cm)		
center	0.00	0.00 ± 0.05	0.00 ± 0.05	19.49 ± 0.07	100%
R1	4.00	4.00 ± 0.05	3.00 ± 0.05	17.71 ± 0.04	91%
R1	4.00	4.00 ± 0.05	-3.00 ± 0.05	17.57 ± 0.01	90%
R1	4.00	-3.50 ± 0.05	-3.00 ± 0.05	17.69 ± 0.02	91%
R1	4.00	-3.50 ± 0.05	3.00 ± 0.05	17.28 ± 0.01	89%
R2	7.00	0.00 ± 0.05	6.70 ± 0.05	18.85 ± 0.01	97%
R2	7.00	0.00 ± 0.05	-7.00 ± 0.05	17.73 ± 0.03	91%
R2	7.00	8.50 ± 0.05	0.00 ± 0.05	18.70 ± 0.02	96%
R2	7.00	-8.00 ± 0.05	0.00 ± 0.05	18.22 ± 0.01	94%
R3	11.00	0.00 ± 0.05	11.00 ± 0.05	0.80 ± 0.01	4%
R4	9.50	0.00 ± 0.05	9.50 ± 0.05	7.57 ± 0.03	39%
R3	11.00	12.00 ± 0.05	0.00 ± 0.05	0.82 ± 0.01	4%
R4	9.50	10.50 ± 0.05	0.00 ± 0.05	9.79 ± 0.20	50%
R5	13.25	14.50 ± 0.05	0.00 ± 0.05	0.49 ± 0.01	2%
R3	11.00	-12.00 ± 0.05	0.00 ± 0.05	0.56 ± 0.01	3%
R3	11.00	0.00 ± 0.05	-11.00 ± 0.05	0.63 ± 0.01	3%
R6	8.00	7.50 ± 0.05	3.50 ± 0.05	17.26 ± 0.17	89%
R7	12.00	-9.50 ± 0.05	7.00 ± 0.05	1.88 ± 0.02	10%
R8	15.00	-15.00 ± 0.05	0.00 ± 0.05	0.33 ± 0.01	2%

Table 7-2 - Averaged value for Si/MON signal. For each measurement it was also reported the position of the detector with respect to the field center.

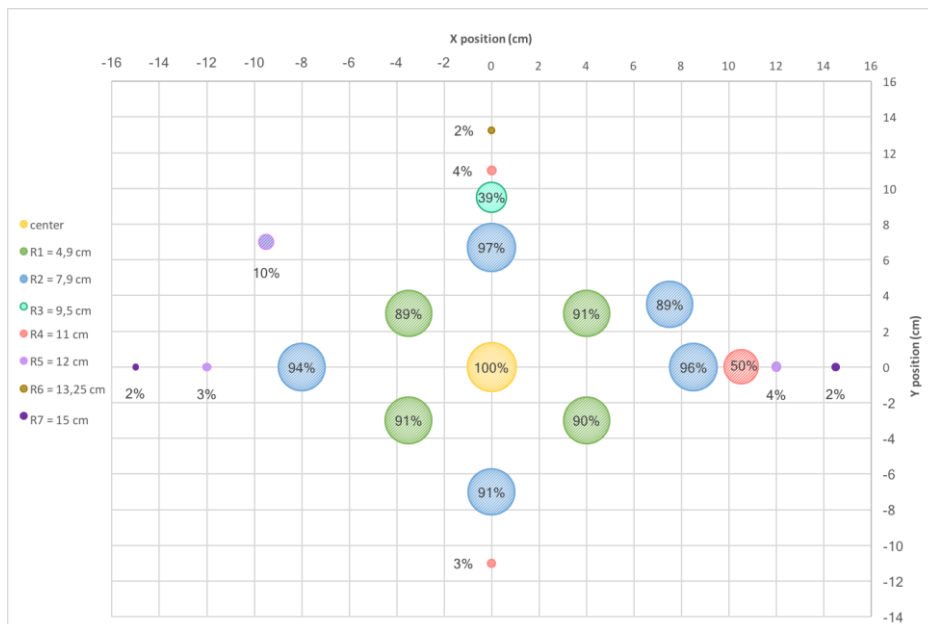


Figure 7.8 - Field bubble plot: the center of the bubble is the center of the detector, the dimension correspond to the intensity of the field in that point and bubbles of the same colours have the same distance from the centre (laying on the same radius).

From the plot of Figure 7.8 is clear that, for every radius, the recorded values are in good agreement. We can also see that the field is symmetric with respect to the origin, feature that had allowed to focus the measurements on the top of the chart. Nevertheless, within a radius of 8 cm, the field has a uniformity of 11%. This is the same region occupied by the PTW chamber when it is placed along the mechanical bench.

7.3 Silicon and Gafchromic comparison

In order to compare the two results, first a graphic overlapping of Gafchromic image and the bubble plot was made (see Figure 7.9) to visually associate the field intensity with the position with respect to the centre.

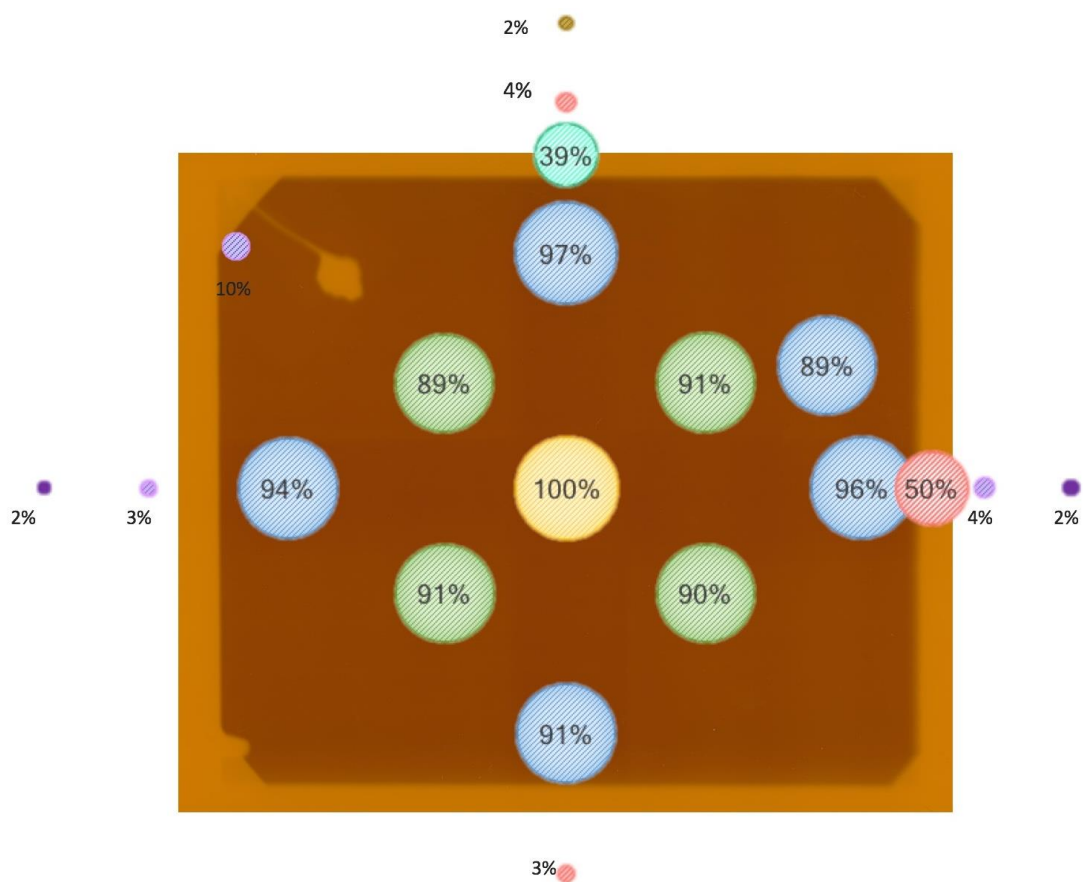


Figure 7.9 - Overlap of the Gafchromic film image and the silicon detector signals bubble plot.

Secondly, histograms of Figure 7.3 and Figure 7.4 were compared with Si detector integral normalized to the monitor chamber one (Si/MON) to prove that the results obtained in the two measurements sessions match.

Making this comparison, it is necessary to convert the Gafchromic histograms x and y axes respectively in distance from the centre (cm) and intensity (arbitrary units normalized to Si/MON values).

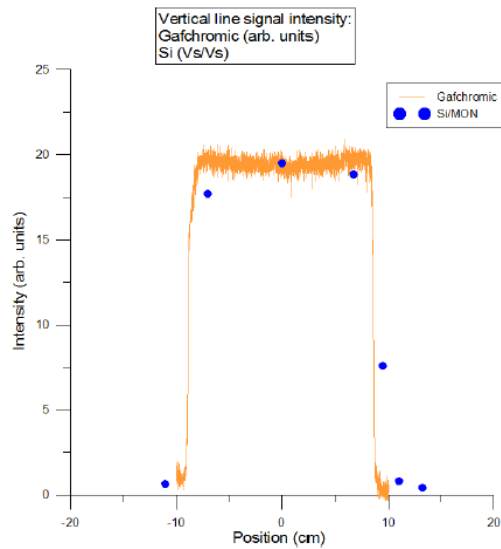


Figure 7.10 - Comparison between signals detected with Gafchromic and silicon detectors: vertical profile.

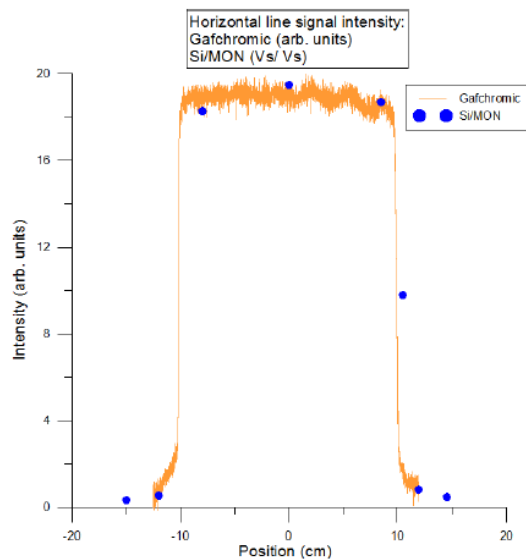


Figure 7.11 - Comparison between signals detected with Gafchromic and silicon detectors: horizontal profile.

Figure 7.10 and Figure 7.11 prove that measurements with silicon detectors and Gafchromic agree. The outstanding difference is that Gafchromic is not very good at evaluating the peripheral field. For this purpose, it is mandatory to deliver a much larger dose with the weakness of achieving the saturation in the field centre.

So, with the proof that the two measures are almost equivalent, is possible to evaluate the peripheral region with the silicon detector only, which was previously done.

7.4 Concluding remarks about X-ray field uniformity

The studied axes across the centre show good results considering the greyscale variability along the pixel lines studied by ImageJ profiles.

The shadow area (90%-10%), considering the horizontal profile, correspond to a region wide (0.65 ± 0.05) cm, which is equal to 3.35% of horizontal width (field size 20x20 cm).

The total field variability is about 11% within a central region of 8 cm radius. This area corresponds to the most important region where the air kerma measurements are usually taken by PTW chamber.

The two different measurement techniques - Gafchromic and Si detector - agree as can be observed in Figure 7.10 and Figure 7.11 and in the following elaborations (Figure 7.12 and Figure 7.13). The global variability (11%) is confirmed also in these plots.

Figure 7.12 is similar to the overlapping of Gafchromic image and bubble plot (Figure 7.9) except for the dimension of the bubbles, which were replaced by squares of fixed area corresponding to the real detector dimensions.

The intensity map of Figure 7.13 was built by a customized ImageJ macro (Appendix 10.13). To explain in an easy way the procedure involved by the script, the workflow is here described by the following list.

- The input Gafchromic scanned image (RGB) is transformed into 8 bit image (256 grey values).
- The script divides the image into a grid of user defined spacing producing 85 x 100 (vertical x horizontal) squared sub-images.
- The mean grey value is computed for each sub-image by means of a statistical analysis. All the mean values are subsequently stored in an array (the first sub-image is the top left corner).
- A new image with all black pixels is created with the same dimensions as the input one.
- Starting from the top left part, the black image is coloured referring to the mean values in the array. Each array value is assigned to a portion of this picture as big as the sub-images. The array elements order is preserved.
- The assigned colours are chosen in order to obtain a pseudo-colour image. This image shows different coloured regions corresponding to different percentage values of the maximum field intensity.

It is clear that some structures are evident in the map of Figure 7.13. The more radiation transparent cross-shaped area is a consequence of the special design of monitor ion chamber. The copper tape acts like an additional filtration in the four quarters of the field resulting in the attenuation of about 10% respect to central region (the cross).

The top left area, where the monitor chamber welding causes an important perturbation of the field, is a region to keep in mind to avoid different exposures. This is important when working with the constraint to irradiate all the devices under test with the same intensity.

The heel effect is not significant in this situation because of the previous described perturbations (welding point and cross area), but also for the chosen filtration for these measurements. Among some factors affecting the heel effect (for example the target etc. – see paragraph 1.2.3) and

consequently the field uniformity, the filtration is an important choice. It is possible to observe that the increasing of the filtration equipment generates the uniformization of the radiation field, increasing its useful area (Figure 7.14, (Paulo Márcio C. Oliveira 2007)). This happens due to the great amount of low energy photons in high intensity radiation fields, which are now attenuated or absorbed. It demonstrates the importance of realizing instruments calibrations only under special conditions by using the proper filtration (Paulo Márcio C. Oliveira 2007).

The obtained results about the field uniformity were taken with not exactly the same filtration of the N-series spectra, that will be explained in the next chapter, but the situation is equivalent to a “strong filtered” beam. So, the uniformity results can be still valid for the N-series spectra, which are a special kind of hard filtered spectra.

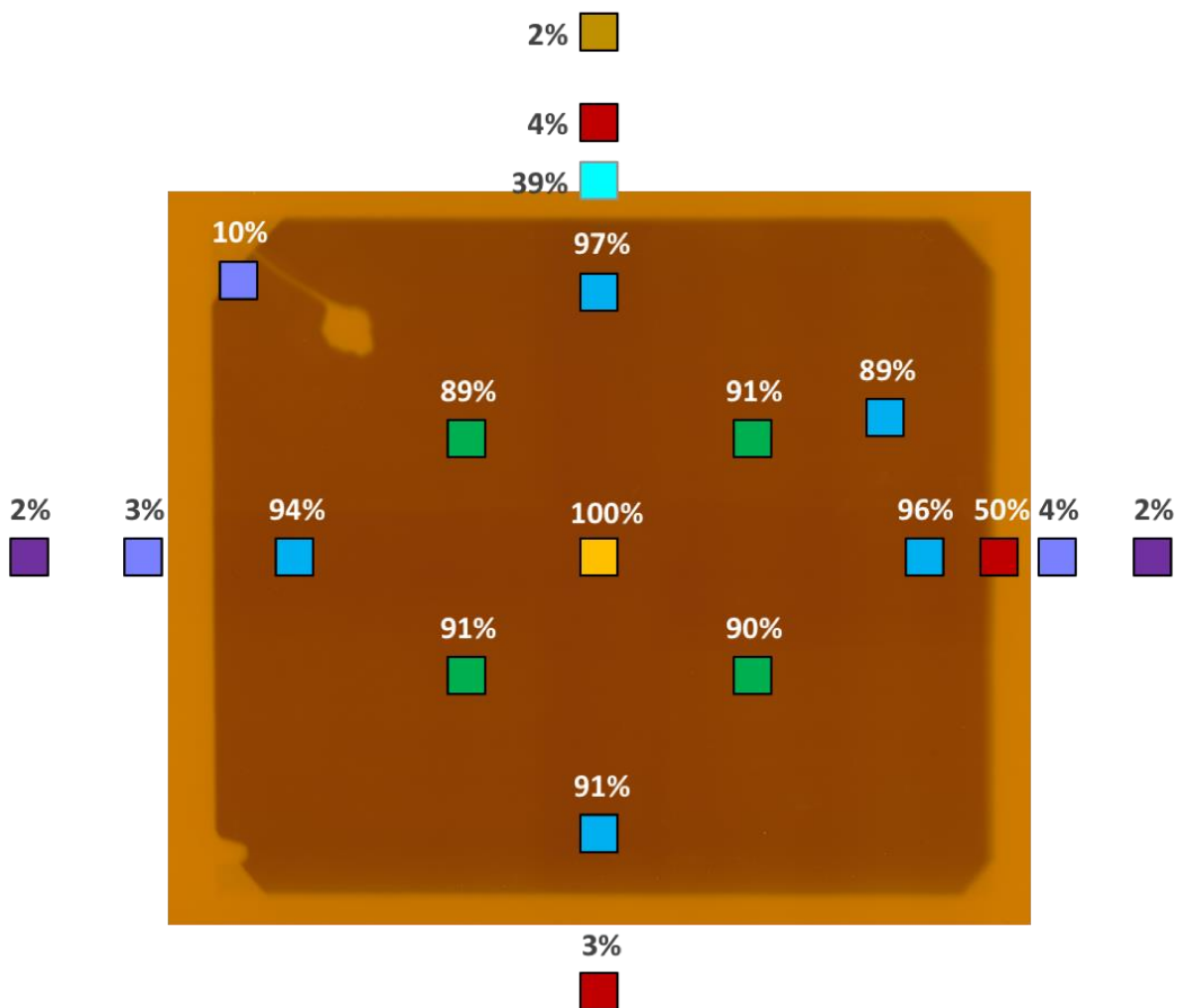


Figure 7.12 - Overlapping of Gafchromic image and Si measurements squares of fixed area corresponding to the real detector dimensions. Different colours refer to different distance from the center (field size 20x20 cm, 0.94 m from the tube focus, total filtration 7.5 mm Al + 0.7 mm Cu, delivered K_{air} 2.7 cGy).

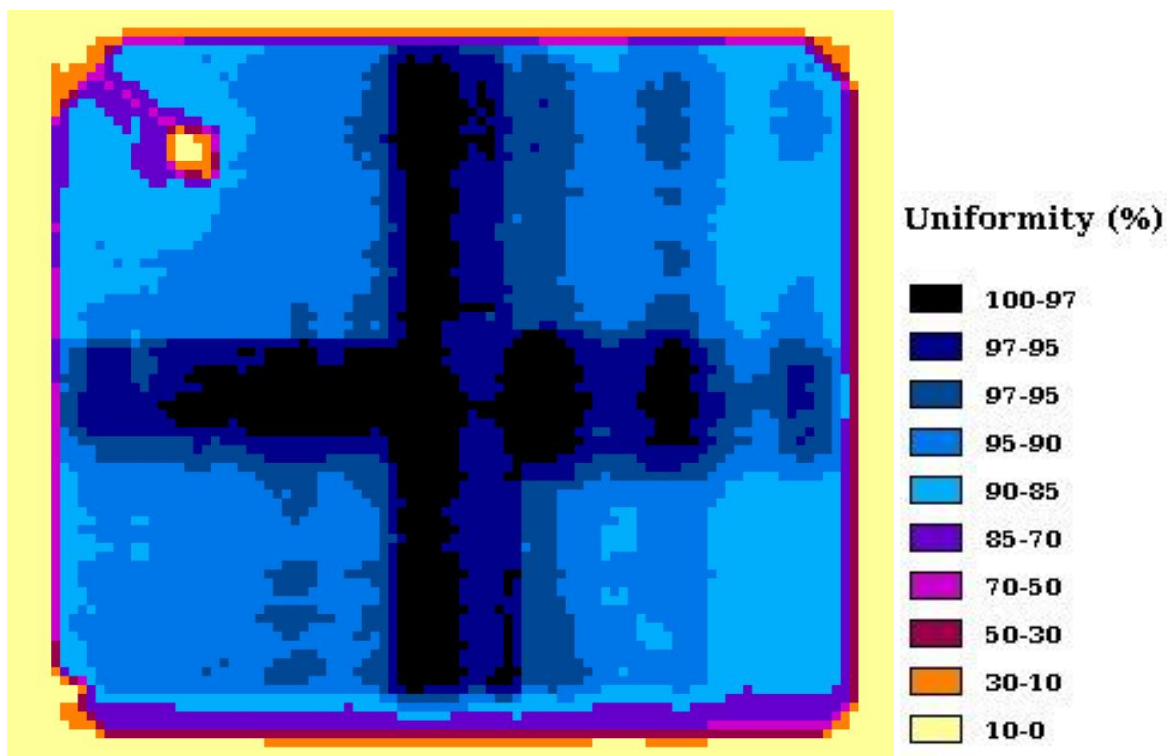


Figure 7.13 - Uniformity map of the radiation field (field size 20x20 cm, 0.94 m from the tube focus, total filtration 7.5 mm Al + 0.7 mm Cu, delivered K_{air} 2.7 cGy). ImageJ elaboration (Appendix 10.13) on the scanned Gafchromic film.

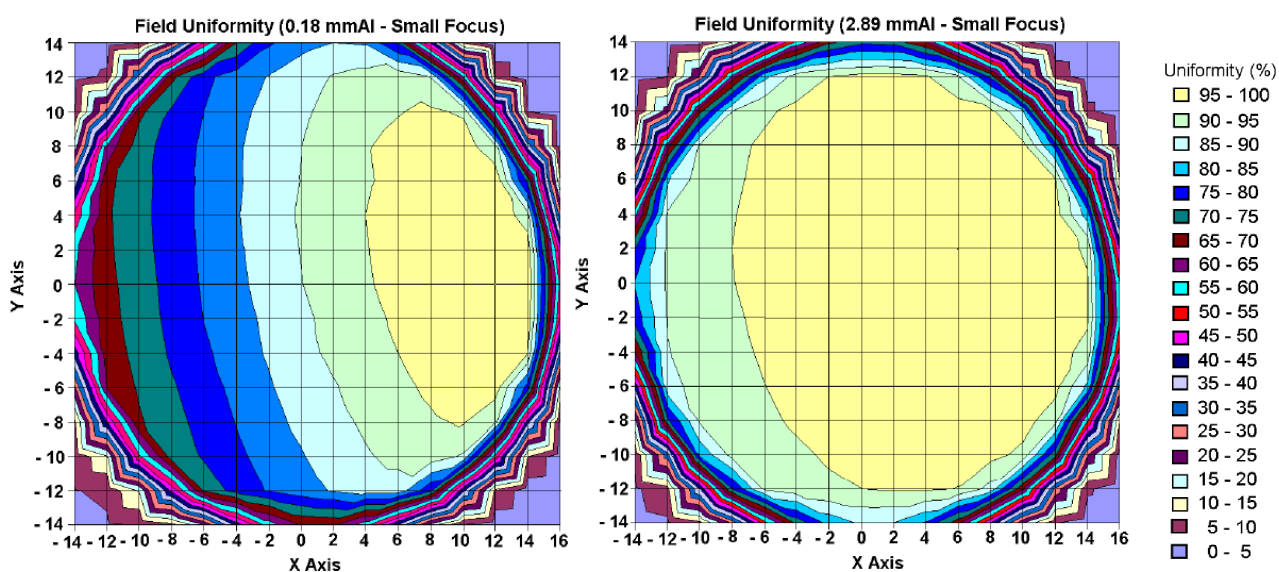


Figure 7.14 - The uniformity of a radiation field produced by different filtration conditions (Paulo Márcio C. Oliveira 2007).

8 N-SERIES SPECTRAL MEASUREMENTS

Silicon based detectors have traditionally been the choice for quantitative X-ray spectroscopy despite of silicon limited sensitivity at energies above 30 keV (see Figure 9.12). Since CdTe detectors has a much higher stopping power, they are a viable attractive alternative for this application providing adequate energy resolution for distinguishing peaks of interest (R. Redus 2008).

Nevertheless, experimental determination of X-ray spectra is a complex task, due to the spectral distortion due to the inherent detector efficiency, escape of secondary radiation, incomplete charge collection and carrier trapping effects (E. P. Di Castro 1984, Matsumoto 2000, A. Tomal 2015).

Thus, a common approach to accurate spectra determination is based on proper correction of the measured pulse-height distribution for the energy response function of the detector effects. In order to correct the spectra, it is usually suggested a procedure, named stripping method (Matsumoto 2000, R. Redus 2008, A. Tomal 2015).

The stripping procedure requires complex simulations of the detector response (monoenergetic responses) considering the interaction of photon with the crystal (related to the number of electron-hole pairs created), a deep knowledge of the crystal geometry and surroundings materials (dead layer, contacts), the carrier transport (carrier trapping effects and incomplete charge collection) and the finite energy resolution (A. Tomal 2015). This clearly exceeds the objectives of this PhD work, where the measurements by Si and CdTe lead a role for having a reasonable idea (continuum shape of bremsstrahlung spectrum, endpoint energies) of the spectral components in addition to the quality measurements of HVLs, but these spectra obviously does not claim to be so accurate for the fulfilment of the constraints for performing quality assurance and control of radiographic systems. (for more detailed see paragraph 9.7).

In this chapter some measurements performed by Hamamatsu silicon (Si) detector - 10 x 10 mm² sensitive area - and cadmium telluride (CdTe) detector - 1 mm³ of volume, 1 mm of sensitive thickness and 1.33 x 1.33 mm² area - will be presented.

The calibration system is reported: for calibrating the Si detector the known endpoint energies were used, as the peak structure of radioactive sources spectra for CdTe. Then X-ray spectral measurements of the quasi monocromatic spectra of the N series (the narrow series of ISO 4037-1 2016 useful as calibrating reference: see chapter 6).

8.1 Silicon detector calibration

Referring to the description made in 3.2.7, 3.2.8 and 3.2.9 about the electronics and main features of the detectors, the result of the measurements performed by Hamamatsu silicon detector, used in pulse mode, with a bias voltage value of 90 V (threshold 1.2 V), at 2.595 m distant from the tube focus (Figure 8.1) are shown in the following paragraphs.

When a particle interacts within the Si detector, which was used in pulse mode, the produced output signal is voltage gaussian shaped pulse whose amplitude is proportional to the energy released by the particle in the detector active volume (which, in some cases, coincides with the incident particle energy). The energy calibration of the detector is necessary to trace back from the voltage signal to the released energy.

To perform the spectrum, the acquisition software samples the signal form the detector but, to realize the spectrum, it only uses those signals whose amplitude is above a pre-set threshold.

The exploitable maximum-minimum range pulse amplitude corresponds to the one where the spectrum is drawn. The acquisition program divides this interval into 1024 histogram bins to be filled so every bin corresponds to a range of signals amplitude.

To fill the histogram bins each signal (named as a count) has to be associated with its amplitude in volt. Thus, every pulse above threshold is fitted with a parabolic curve and its amplitude is computed. The resulting spectrum is a graph with counts number versus signal amplitude so that, on the x axis, signals are classified and assigned to the corresponding bin as a function of their amplitude, which is, of course, proportional to the incident radiation energy.

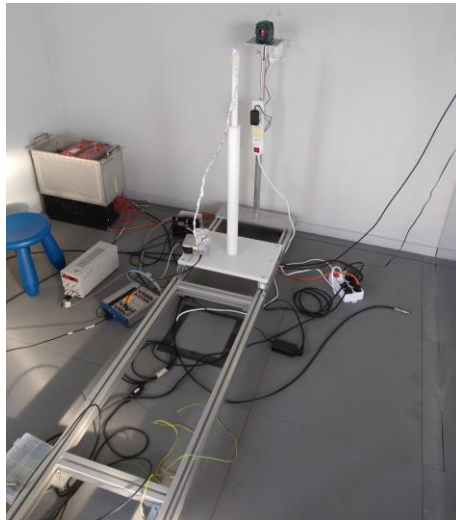


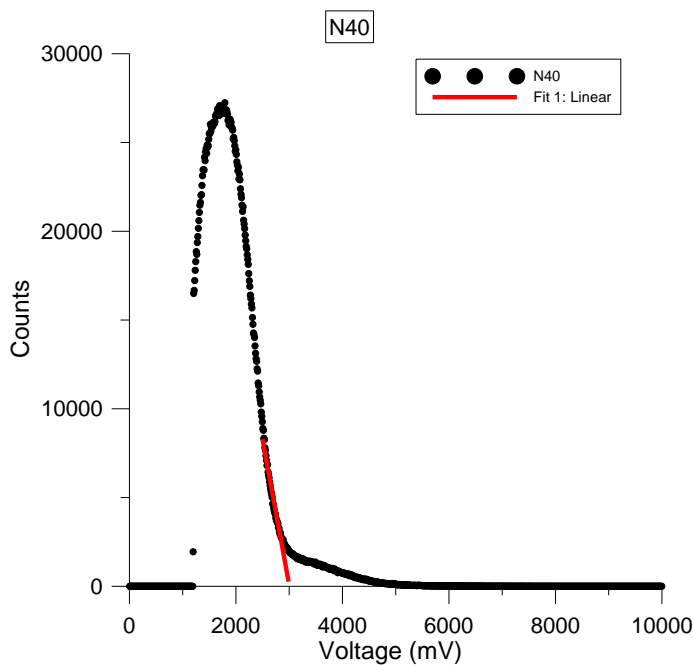
Figure 8.1 - Experimental setup for the spectra measurement by Si detector. Bias voltage 90 V, 2.595 m distant from the tube focus.

To bring the performed spectra by Si detector into energy, the endpoint energies of the same spectra were used. These values are the upper limit of the energies in the X-ray beam for a physical reason (paragraph 1.2), so that it is possible to use these points to build a calibration line.

The values expressed in energy are well known thanks to the precise control on the kV applied to the tube. Thanks to the voltage divider (Appendix 10.14) measurements (paragraph 3.2.4), the acquisition software gives as output a trusted mean value after the end of each run.

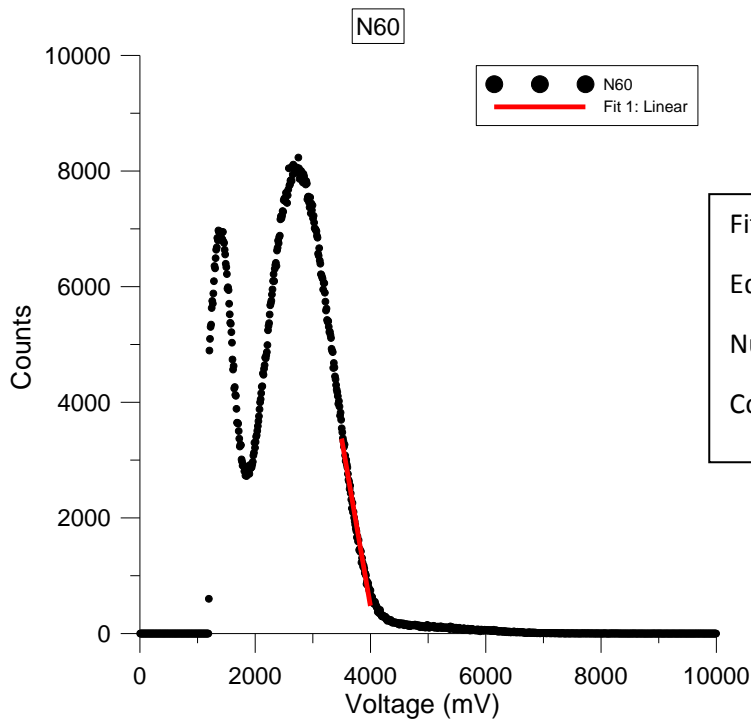
The endpoint energies correspond almost exactly to the applied kV; it should be noted that N40 and N120 were performed using a nominal applied voltage of 40 and 120 keV, which correspond to about 42 and 117 keV measured by the voltage divider. For a more precise estimate of the endpoint values, the numbers recorded during the measurements by means of the voltage divider are listed in Table 8-1.

Despite the necessary precautions (max distance, 0.5 mA as tube current, shaping time $\tau = 500$ ns), the experimental setup for these measurements did not guarantee that the upper limit of the spectra could not be affected by few pile-up events. To get the best estimate of the endpoint value expressed in mV, some fits were applied to the raw spectra in order to study the proper X axis intercept (from Figure 8.2 to Figure 8.7). After calculating the equations of these fit lines, it was possible to get the endpoint in mV from the different spectra.



Fit N40: Linear
 Equation $Y = -16.382 * X + 49242$
 Number of data points used = 41
 Coef. of determination, R-squared = 0.967

Figure 8.2 - N40 spectrum performed by Si detector (90 V bias, 2.595 m from tube focus). The linear fit allows the best estimate of the X axis intercept in order to get the endpoint value in mV.



Fit N60: Linear
 Equation $Y = -5.788 * X + 23628$
 Number of data points used = 52
 Coef. of determination, R-squared = 0.983

Figure 8.3 - N60 spectrum performed by Si detector (90 V bias, 2.595 m from tube focus). The linear fit allows the best estimate of the X axis intercept in order to get the endpoint value in mV.

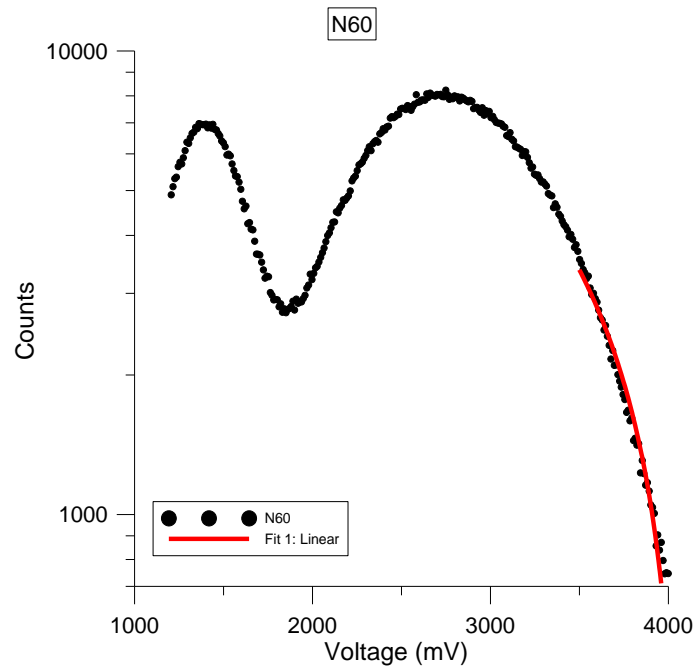


Figure 8.4 - N60 spectrum performed by Si detector (90 V bias, 2.595 m from tube focus) with Y axis in logarithmic scale for better understanding the agreement between the linear fit and the raw spectrum.

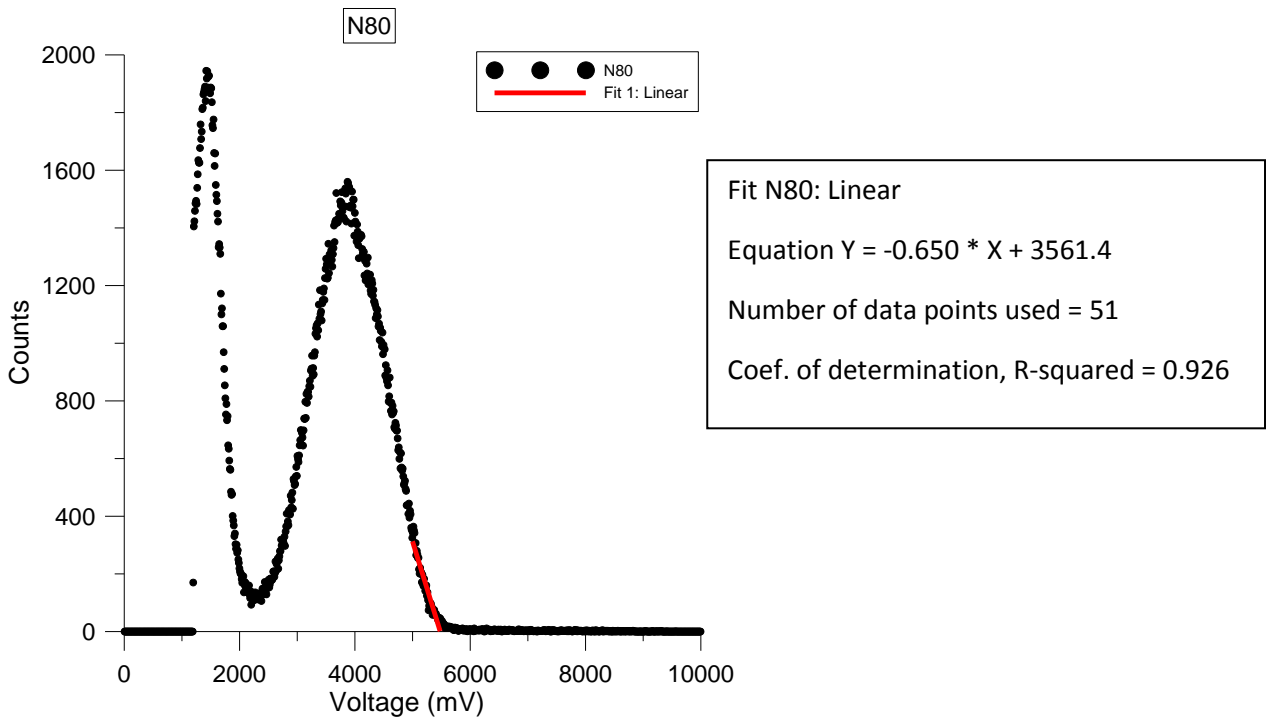


Figure 8.5 - N80 spectrum performed by Si detector (90 V bias, 2.595 m from tube focus). The linear fit allows the best estimate of the X axis intercept in order to get the endpoint value in mV.

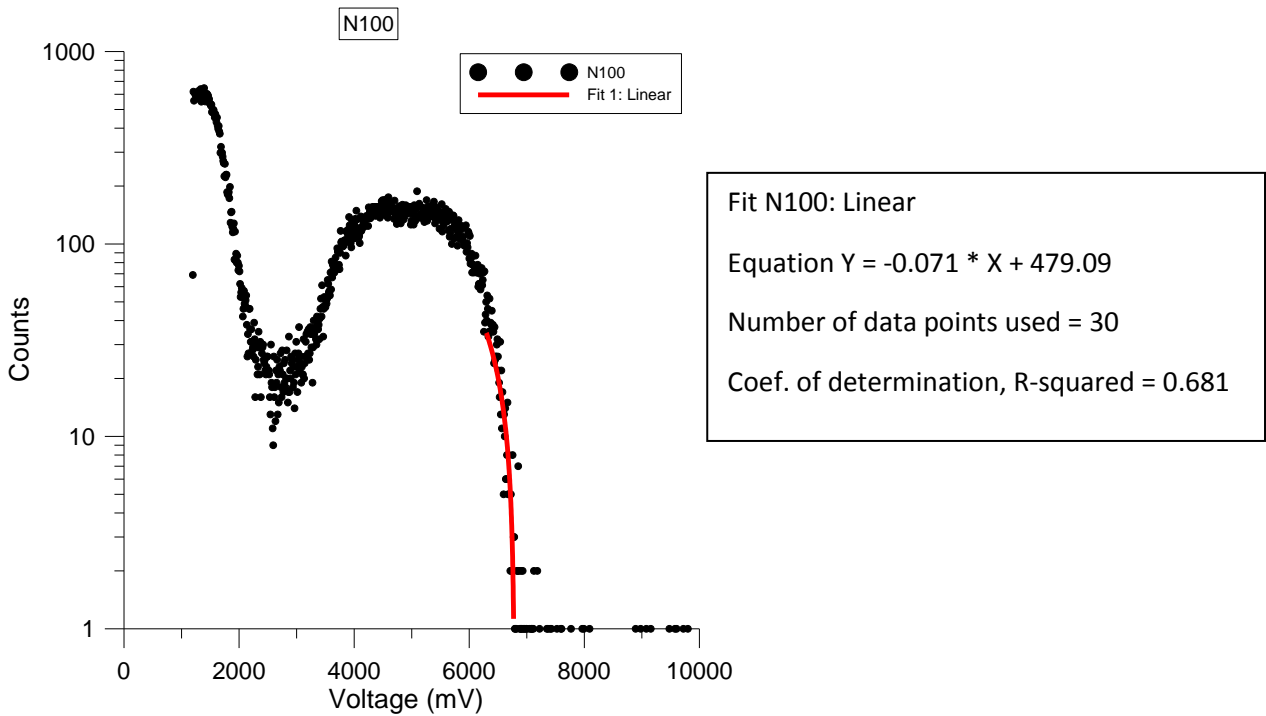


Figure 8.6 - N100 spectrum performed by Si detector (90 V bias, 2.595 m from tube focus). The linear fit allows the best estimate of the X axis intercept in order to get the endpoint value in mV (log scale Y axis).

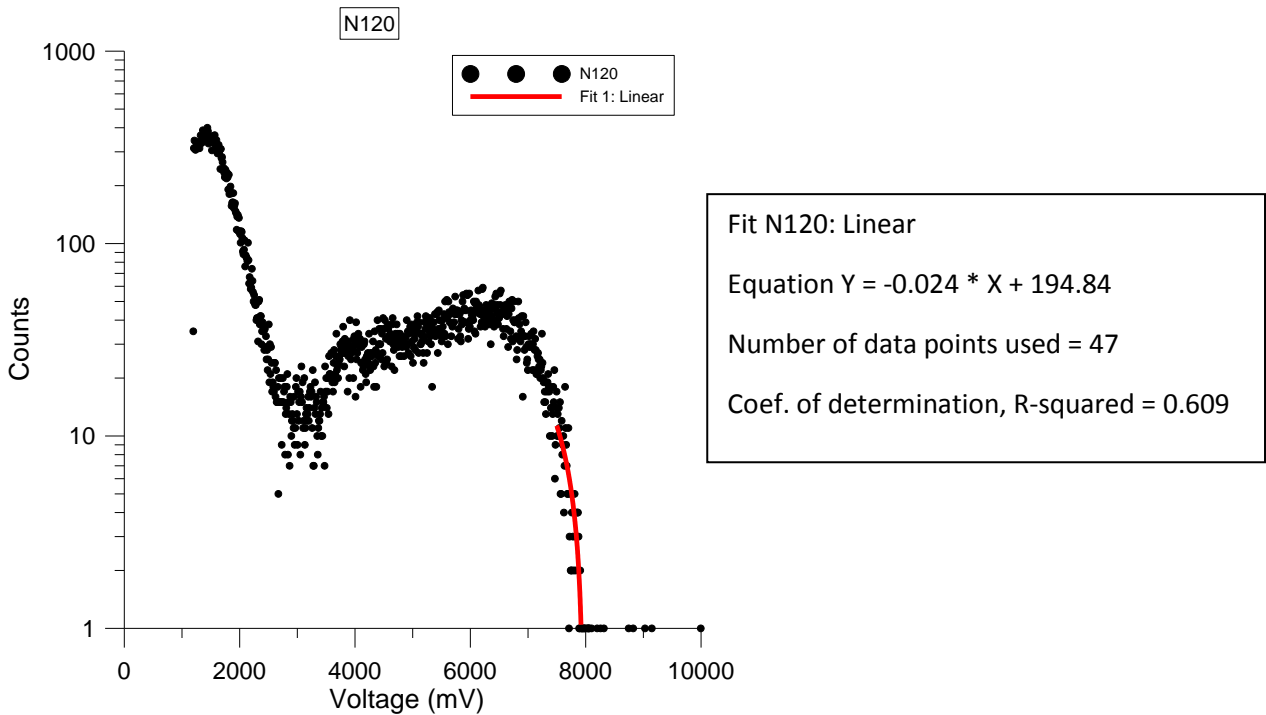


Figure 8.7 - N120 spectrum performed by Si detector (90 V bias, 2.595 m from tube focus). The linear fit allows the best estimate of the X axis intercept in order to get the endpoint value in mV (log scale Y axis).

Table 8-1 summarizes the parameters of the previous different fit equations. Thanks to the well known endpoint energy values, it was possible to get the calibration line of Figure 8.8.

Beam	m (mV ⁻¹)	q	X intercept (mV)	Endpoint (keV)
N40	-16.382	49242	3005.9	42.75
N60	-5.788	23628	4082.2	60.49
N80	-0.65	3561.4	5479.1	80.2
N100	-0.071	479.09	6747.7	99.99
N120	-0.024	194.84	8118.3	117.24

Table 8-1 - Parameters of the previous fit equations for a proper estimate of the endpoint values in mV. The list of the measured applied kV by voltage divider was taking into account to know precisely the endpoint energy values of the different measurements (last column "Endpoint (keV)").

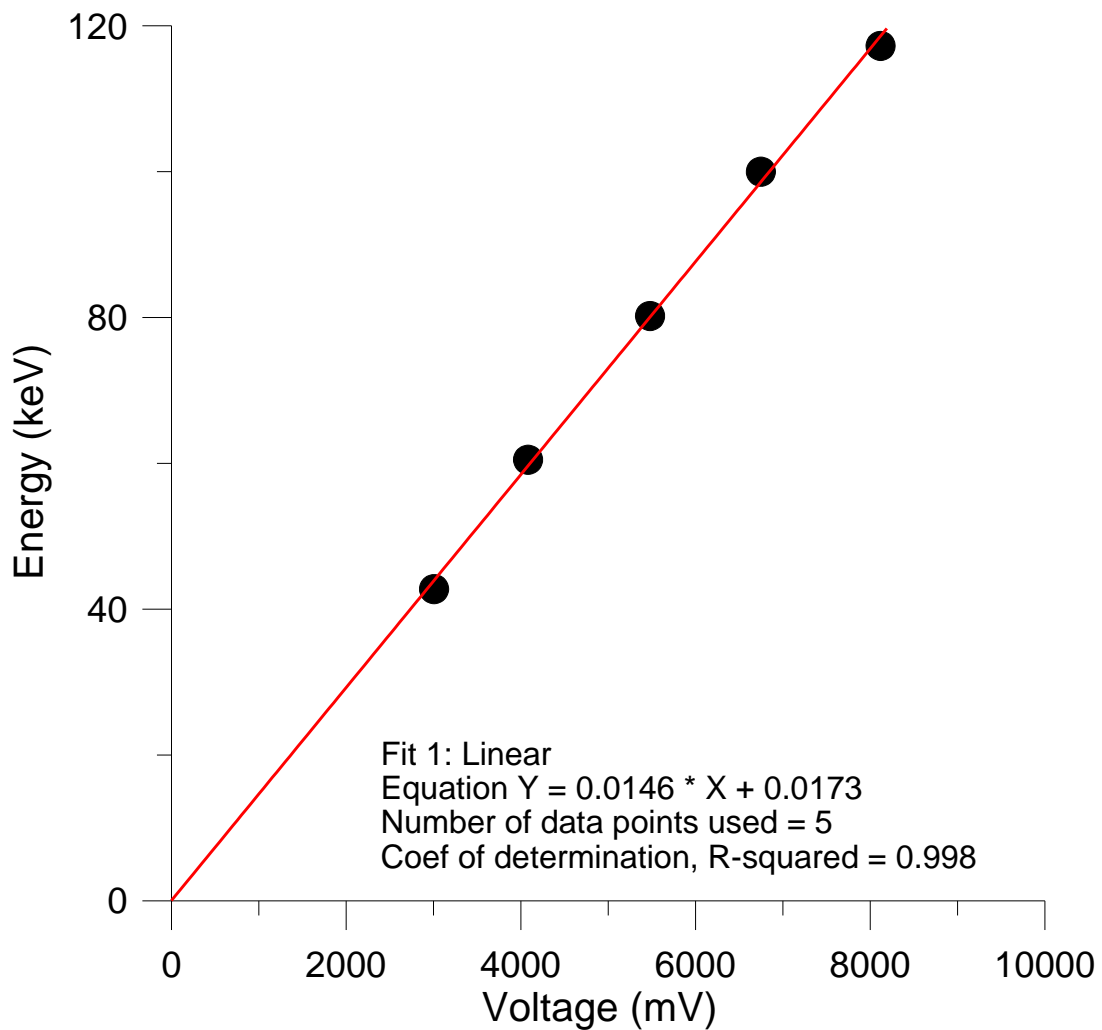


Figure 8.8 - Calibration line using data of the Table 8-1.

8.2 Si N-series experimental spectra

Using the calibration equation of Figure 8.8, it was possible to transform the previous raw graphs in the energy spectra performed by Si detector. Figure 8.9 shows all the N-series spectra taken by Si detector.

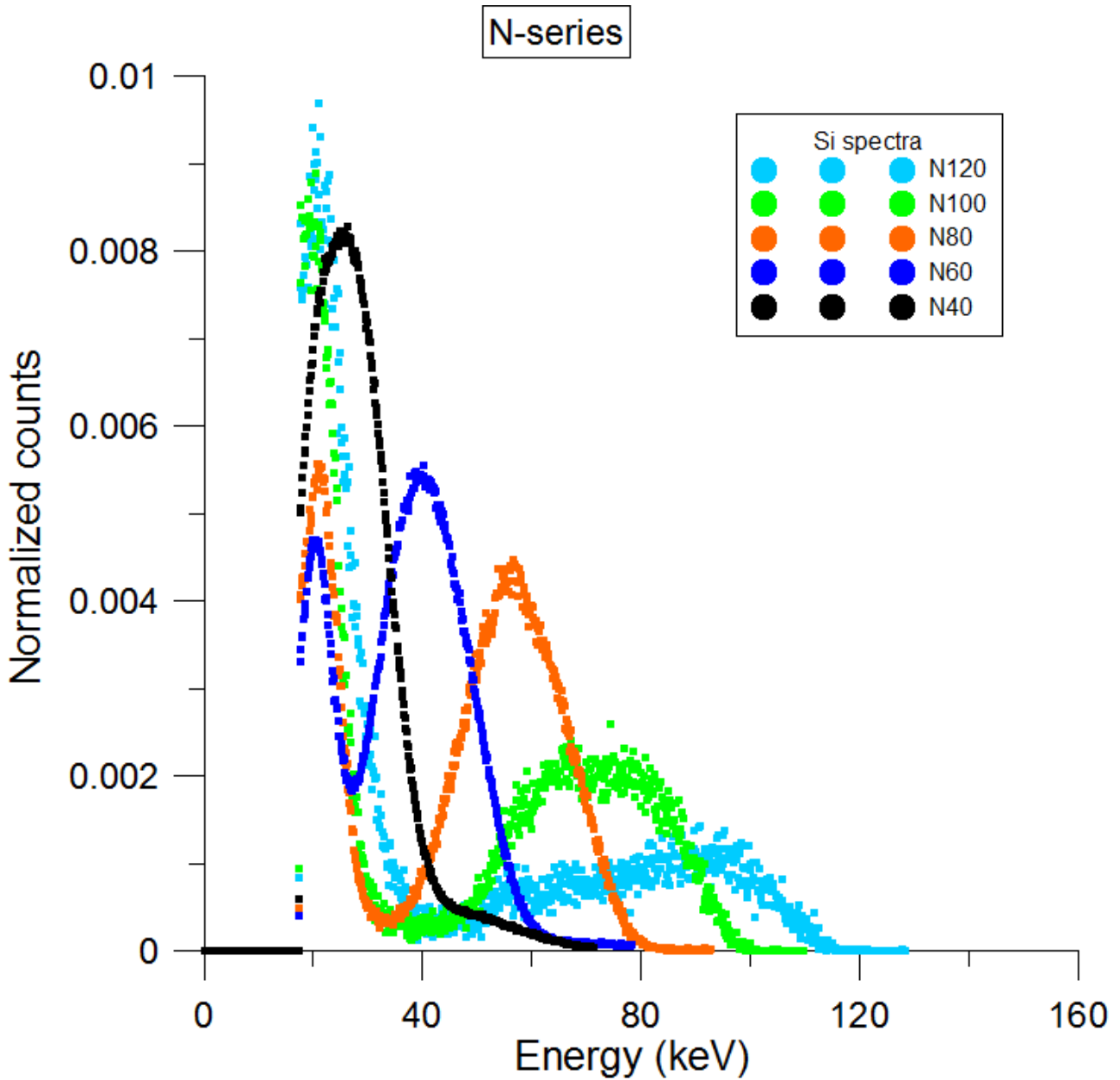
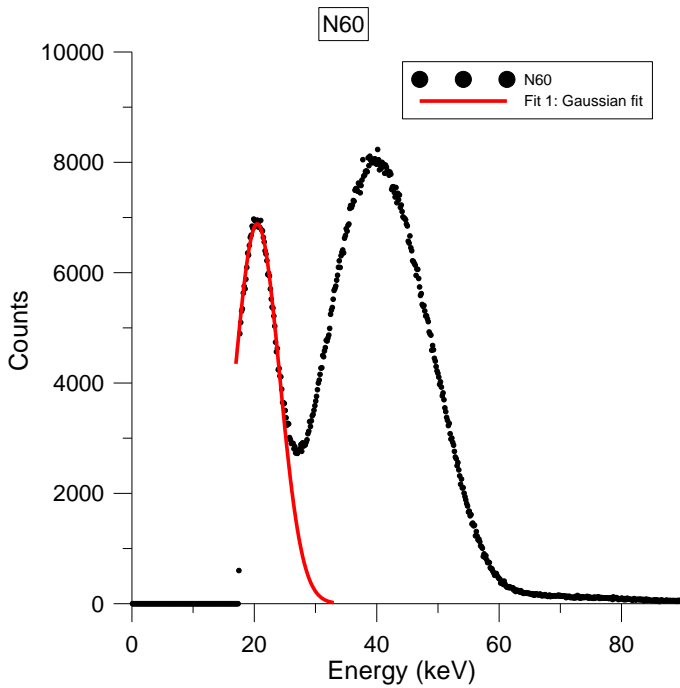


Figure 8.9 - N-series spectra measured by Si detector (90 V bias, threshold ~17 keV, 2.595 m from tube focus, endpoint calibration).

Observing the low energy part of these spectra, it is clear that a peak is placed in that region. In order to investigate the origin of this component, the energy calibration helped to link this peak to a certain energy value. Fitting this structure with a gaussian function and extrapolating the centroid, it was possible to estimate the corresponding energy value. The different gaussian fits, together with their numerical results, are shown in the following figures for the different spectra (except of N40 because of the low energy position of all the spectrum, which is superimposed the secondary peak).



Fit 1: Gaussian fit

$$Equation Y = A * \exp(-(x-m)^2 / (2*s*s))$$

A = 6881.97

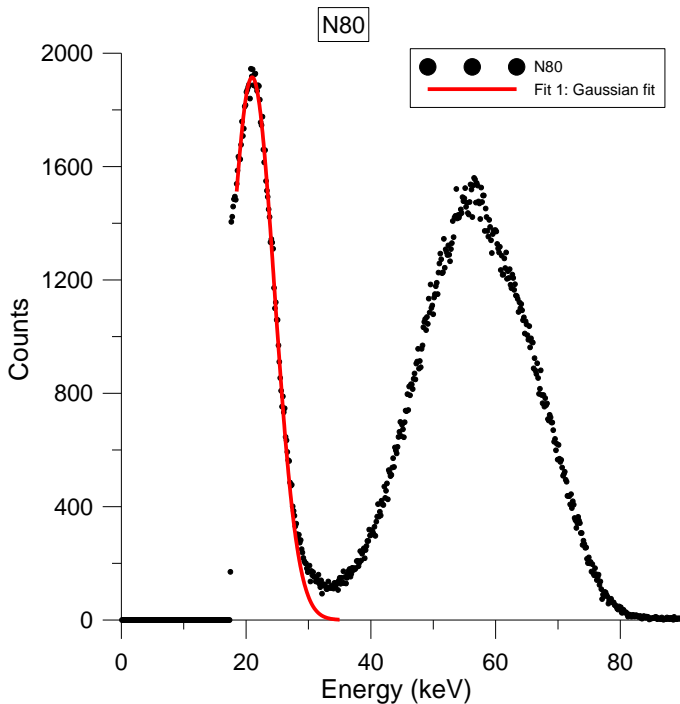
m = 20.48

s = 3.63

Number of data points used = 49

Coef. of determination, R-squared = 0.99

Figure 8.10 - Gaussian fit of the low energy peak in N60 spectrum by Si detector (90 V bias, 2.595 m from tube focus, endpoint calibration).



Fit 1: Gaussian fit

$$Equation Y = A * \exp(-(x-m)^2 / (2*s*s))$$

A = 1914.97

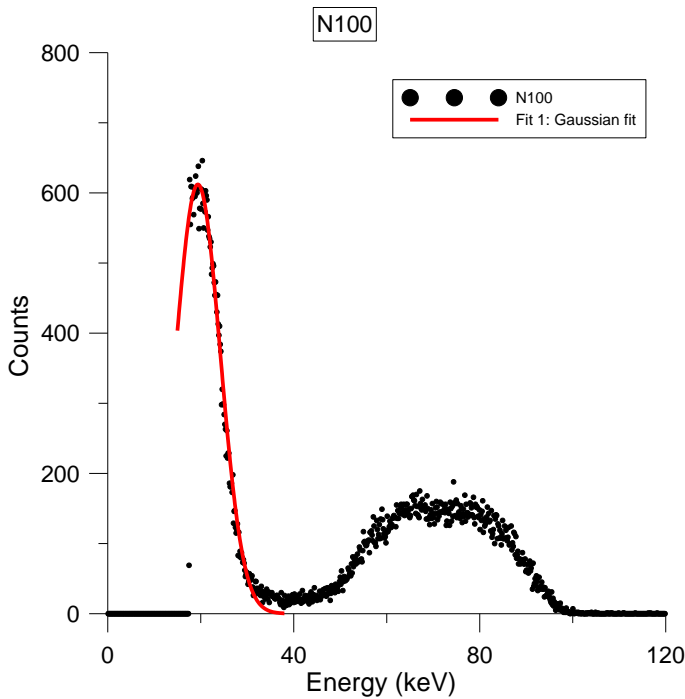
m = 20.97

s = 3.60

Number of data points used = 45

Coef. of determination, R-squared = 0.98

Figure 8.11 - Gaussian fit of the low energy peak in N80 spectrum by Si detector (90 V bias, 2.595 m from tube focus, endpoint calibration).



Fit 1: Gaussian fit

Equation $Y = A \cdot \exp\left(-\frac{(x-m)^2}{2 \cdot s^2}\right)$

A = 612.01

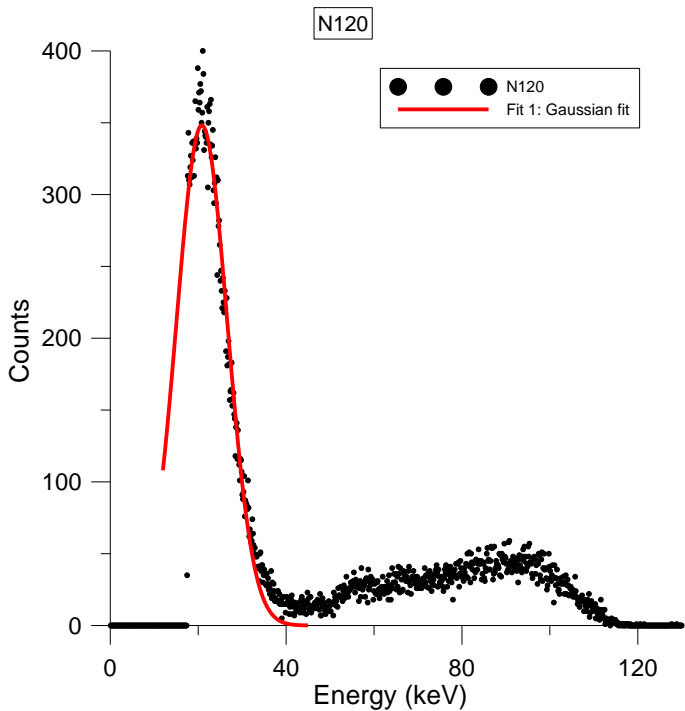
m = 19.40

s = 4.82

Number of data points used = 52

Coef. of determination, R-squared = 0.94

Figure 8.12 - Gaussian fit of the low energy peak in N100 spectrum by Si detector (90 V bias, 2.595 m from tube focus, endpoint calibration).



Fit 1: Gaussian fit

Equation $Y = A \cdot \exp\left(-\frac{(x-m)^2}{2 \cdot s^2}\right)$

A = 348.18

m = 20.85

s = 5.78

Number of data points used = 194

Coef. of determination, R-squared = 0.96

Figure 8.13 - Gaussian fit of the low energy peak in N120 spectrum by Si detector (90 V bias, 2.595 m from tube focus, endpoint calibration).

In Table 8-2 the numerical results obtained by the fits are summarized for each spectrum. The peak at low energy in the spectra can be due to the characteristic radiation spikes from the anode, mainly made of a molybdenum alloy (TZM, paragraph 0). The comparison with the energies of the spikes from K_{α} and K_{β} transitions (Table 8-3, (S. B. Gudennavar 2013)) corroborates this origin.

Spectrum	Energy fit (keV)	Mean (keV)	Dev stand. σ (keV)	Mean σ (keV)
N120	20.85	20.42	3.63	4.46
N100	19.40		3.6	
N80	20.97		4.82	
N60	20.48		5.78	

Table 8-2 - Numerical results obtained by gaussian fits listed for each previous spectrum.

Mo K shell	Energy peak (keV)	$I(K_{\beta})/I(K_{\alpha})$	Weighted peak energy (keV)
K_{α}	17.42	0.184	17.76
K_{β}	19.6		

Table 8-3 - Characteristic radiation energies of molybdenum (S. B. Gudennavar 2013).

Considering the mean value of the fitted peaks (20.42 keV) and the associated uncertainty ($\sigma = 4.46$ keV), it is worth to note that these values can be compared with the energies of the characteristic radiation of Mo, listed in Table 8-3, but the threshold of 1.2 V (equivalent to ~ 17 keV) depresses the contribution of the K_{α} . Therefore, in this situation, the expected peak energy is shifted towards higher values respect to the weighted peak energy (Table 8-3).

8.3 CdTe calibration

Like for Si detector (explanation in paragraph 8.1), the energy calibration of the CdTe detector is also necessary to go back from the voltage signal to the released energy.

As the output signal depends both on the detector and on the processing electronics, the calibration has to be performed using the whole experimental setup that will be used during the measurements of interest. Usually, energy calibrations are made by means of radioactive sources with different well-known emitted radiation energies (e.g. γ emitters). Knowing the radiation energies and measuring the associated output pulses amplitude, it is possible to draw a plot of radiation energy as a function of pulse amplitude thus, the best fit curve is the calibration equation which allows to go back from a given pulse amplitude to the radiation energy. In this work, two radioactive sources of known decay schemes were used: ^{241}Am and ^{57}Co .

The CdTe calibration setup is shown in Figure 8.14 and Figure 8.15.

The radioactive source was placed as near as possible in front of the detector. Signals coming from the source were recorded and stored by the acquisition software.



Figure 8.14 - CdTe calibration setup. The figure shows, from the left to the right, the positioning of the radioactive source, the CdTe detector, the preamplifier and the processing electronics (which was covered by an aluminium layer to ensure the electromagnetic shield) and then the voltage supply for detector biasing.



Figure 8.15 - Positioning of the CdTe detector next to the ^{241}Am radioactive source.

The raw spectra (x axis in Volt), together with the decay schemes, are shown in Figure 8.16, Figure 8.17, Figure 8.18 and Figure 8.19. For ^{241}Am the scheme portrays only the most probable channels of decay.

Known the decay schemes of the two sources, it was possible to get the mean values of the known structures as the full energy peak or the escape peak of Cd and Te (see paragraph 8.5).

Fitting those structures with a gaussian function and extrapolating the peak channel, the calibration line was drawn. This line depicts the signal amplitude as a function of the energy released by radiation in the detector (see Figure 8.22).

For this study, all the known structures of the ^{241}Am and ^{57}Co spectra were fitted with a gaussian function and included in the calibration. Thus, the curve validity goes from about 10 keV to about 120 keV; this range perfectly matches the ISO 4037 narrow series energy range.

Table 8-4 lists all the energies, the mean values and the sigma of the accounted peaks.

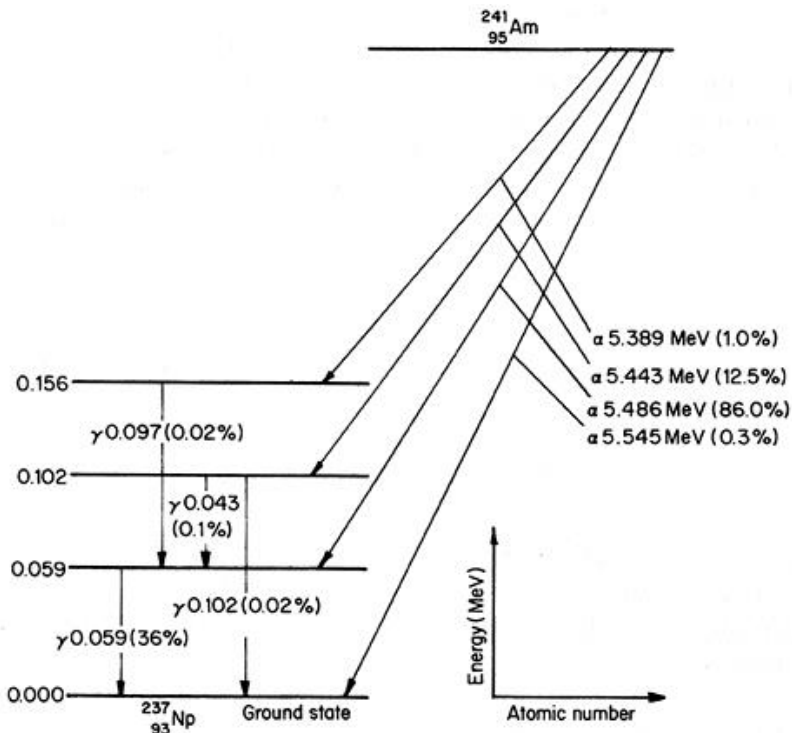


Figure 8.16 - Simplified decay scheme of ^{241}Am (National Nuclear Data Center, NuDat 2 database 2019).

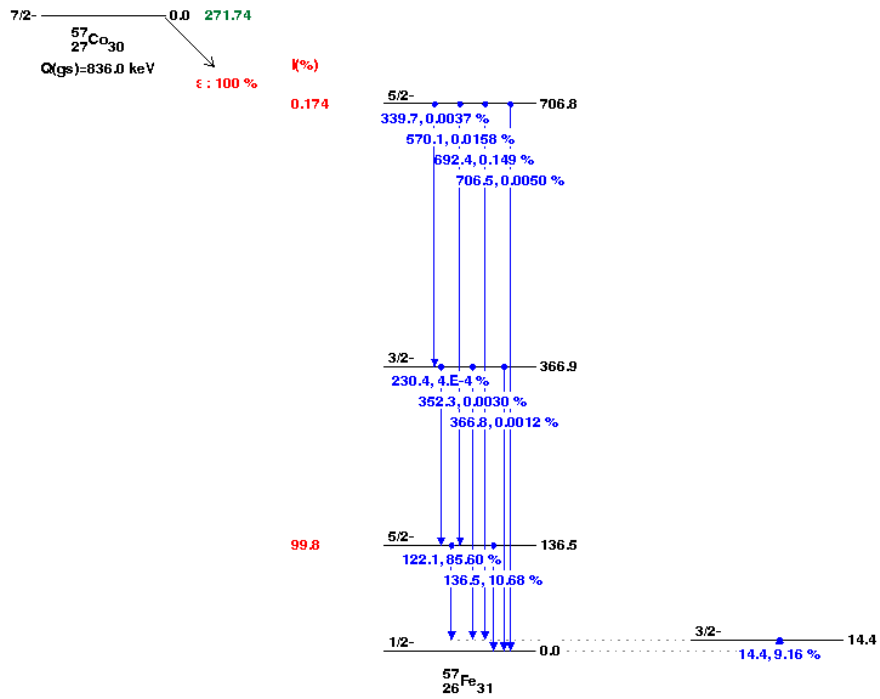


Figure 8.17 - Decay scheme of ^{57}Co (National Nuclear Data Center, NuDat 2 database 2019).

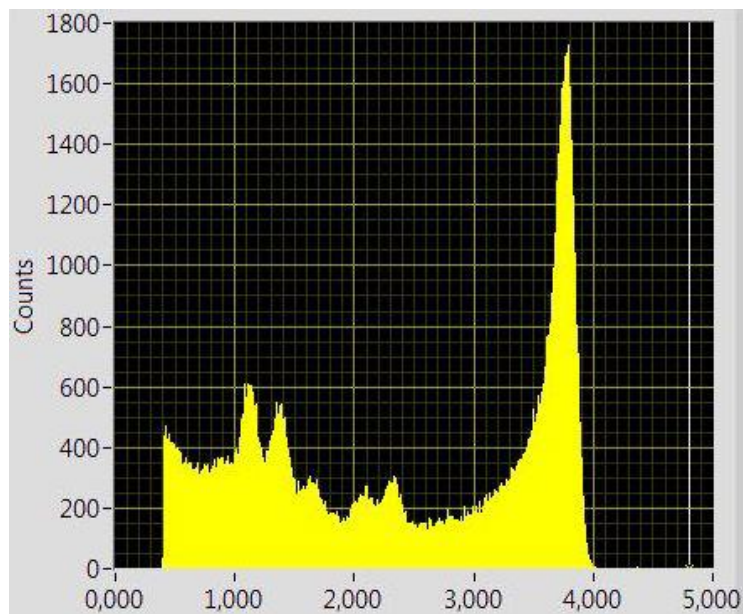


Figure 8.18 - Raw spectrum for ^{241}Am by CdTe detector (paragraph 3.2.7).

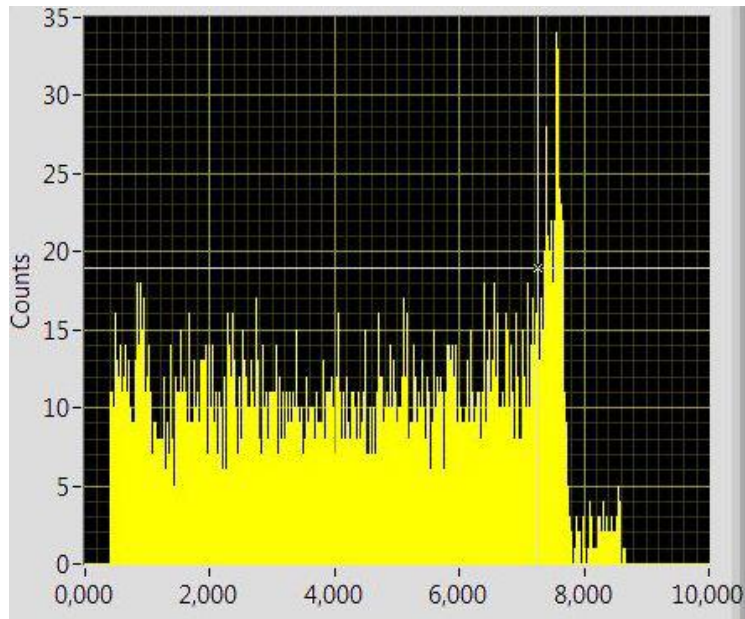


Figure 8.19 - Raw spectrum for ^{57}Co by CdTe detector (paragraph 3.2.7).

Source	Peak	E (keV)	m (mV)	σ (mV)
^{241}Am	L_{α}	13.95	1117.1	102.1
	L_{β}	17.74	1365.3	116.9
	L_{γ}	20.8	1627.5	179.4
	Te escape peak	30.9	2099	202
	Cd escape peak	36.3	2309.4	123.9
	Photo-peak (b.r. 37%)	59.5	3769.4	74.4
^{57}Co	Photo-peak (b.r. 85.6%)	122.06	7569	89

Table 8-4 - Type of peak, nominal energy, mean and sigma for the peaks observed in the ^{241}Am and ^{57}Co spectra by CdTe detector (paragraph 3.2.7), (Grodzins L. 2002, National Nuclear Data Center, NuDat 2 database 2019, Sordo 2009)⁵.

Figure 8.20 and Figure 8.21 shows ^{241}Am and ^{57}Co spectra together with the performed fit whose parameters were used to draw the calibration curve. Using all the information extracted by these figures (Figure 8.20 and Figure 8.21), it was possible to plot the energy calibration curve of Figure 8.22.

⁵ Regarding the name of **L peak**: K radiation denotes characteristic radiation for electron transitions to the K shell, and likewise, L radiation for transitions to the L shell. The origin of the electron filling the vacancy is indicated by suffixes (α , β , γ , etc.), where α stands for a transition from the adjacent outer shell, β from the next outer shell, etc. K_{α} radiation results from L to K shell transitions; K_{β} radiation from M to K shell transitions, etc. Energies are further split owing to the energy levels in a shell, indicated with a numerical suffix. Further, each vacancy in an outer shell following from such a transition gives rise to the emission of corresponding characteristic radiation causing a cascade of photons. Regarding the **escape peaks**, more detailed explanation is given in paragraph 8.5.

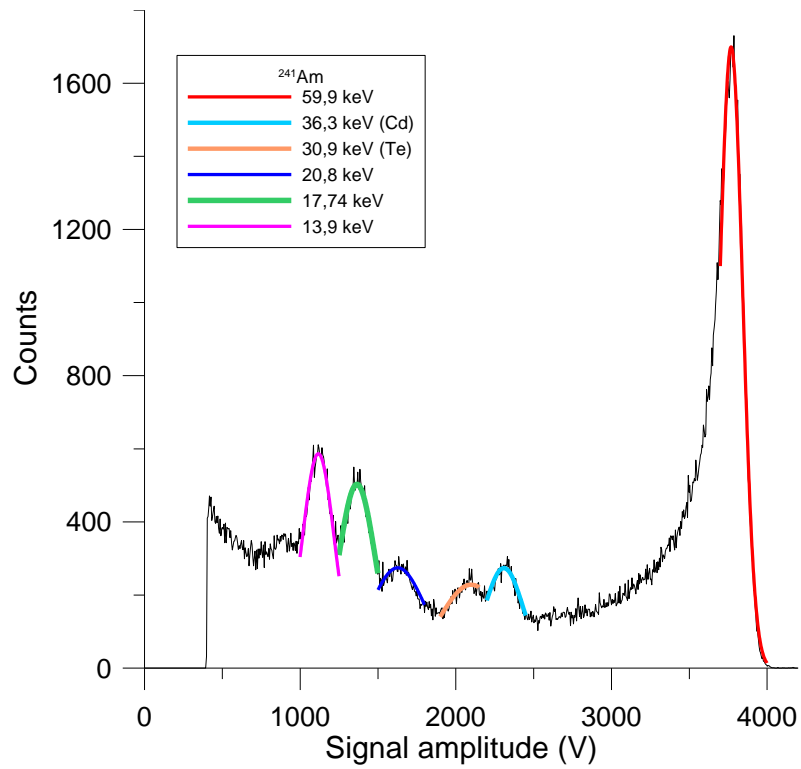


Figure 8.20 - Spectrum of ^{241}Am source by CdTe detector (paragraph 3.2.7). Legend reports the energy values of emitted photons which form the different peaks fitted with gaussian curves drawn in colours.

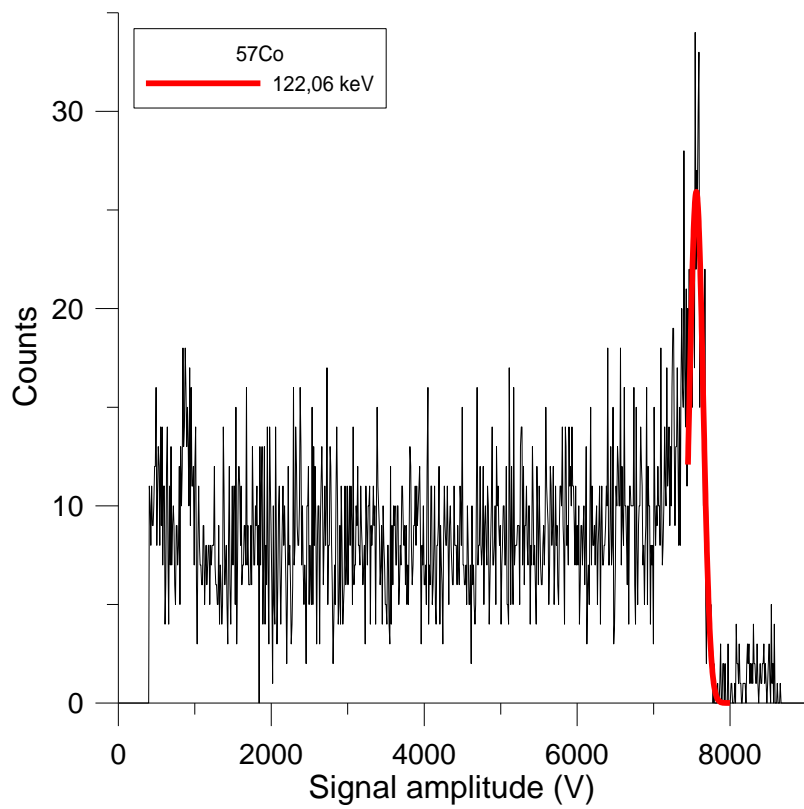


Figure 8.21 - Spectrum of ^{57}Co source by CdTe detector (paragraph 3.2.7). Legend reports the energy values of emitted photons which form the peak fitted with gaussian curves drawn in red.

The calibration equation is (8.1).

$$E \text{ (keV)} = 0.0168 * x \text{ (mV)} - 4.695 \quad (8.1)$$

with E the energy (keV) and x the pulse amplitude (mV). Equation (8.1) allows to link every recorded signal to a specific value of the energy released in the detector. In the follows the calibrated spectra (Figure 8.23, Figure 8.24) are depicted and the energy peaks centroids extrapolated by gaussian fits are listed.

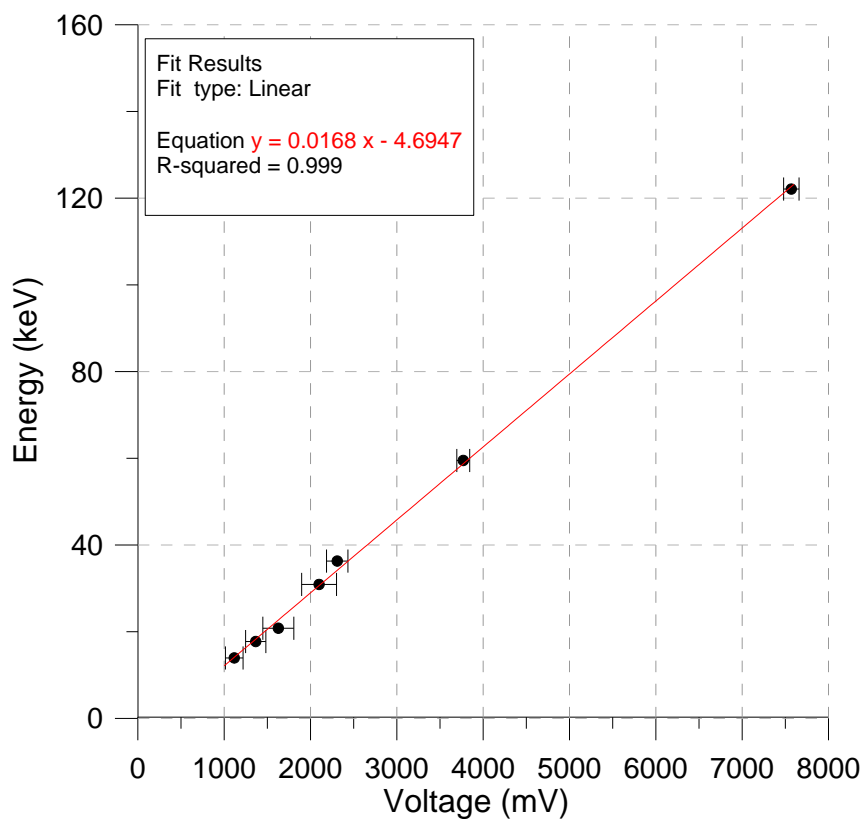


Figure 8.22 - Energy calibration curve: peaks nominal energy (keV) against centroid (mV). Uncertainties are the standard deviations obtained by gaussian fits.

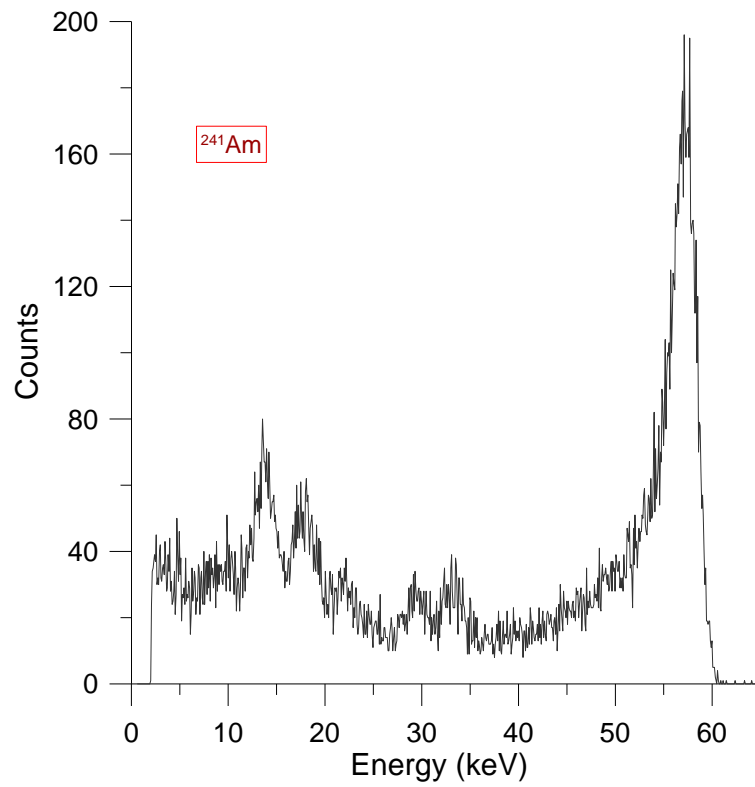


Figure 8.23 - CdTe detector (paragraph 3.2.7) ^{241}Am source calibrated spectrum.

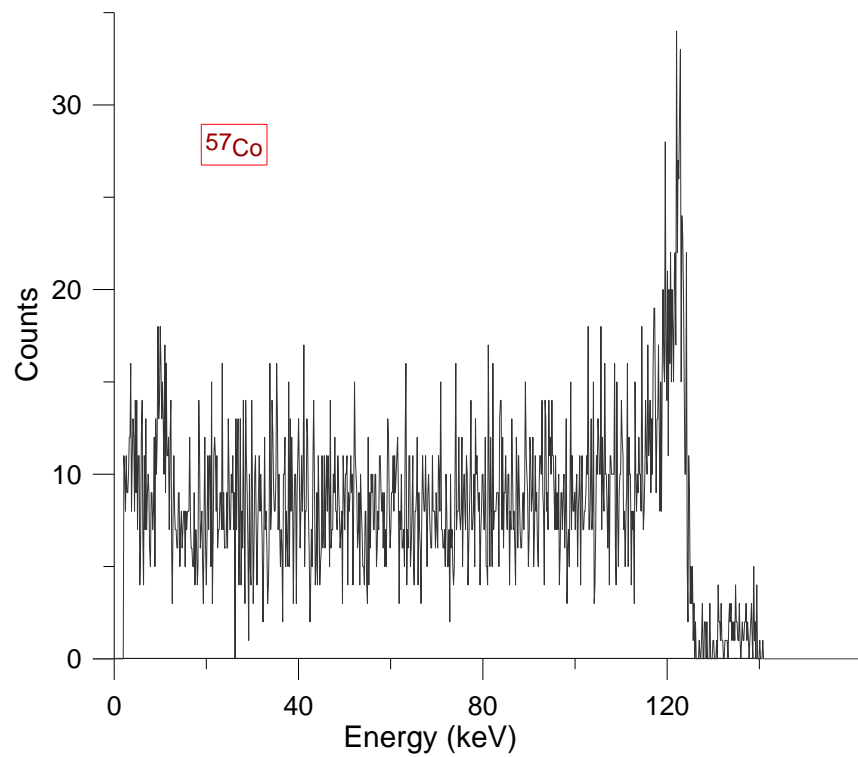


Figure 8.24 - CdTe detector (paragraph 3.2.7) ^{57}Co source calibrated spectrum.

To check the detector performances, the FWHM was determined pursuing two different ways: the first accounts for the sigma values given in Table 8-5 and uses the known equation (8.2).

$$FWHM \sim 2,35 * \sigma \quad (8.2)$$

The second method is based on the extreme values of the peak at the half maximum height, using the calibration curve to transform them in energy values and finally, the difference between them is the required FWHM. With this in mind, using the mean values is possible to get the detector energy resolution by means the full width at half maximum respectively as FWHM = 3.76 keV and FWHM = 3.4 keV. Both results are in accordance with the theoretical value of FWHM < 6 keV given by the manufacturer (see Appendix 10.9).

Source	Peak	E (keV)	m (keV)
²⁴¹ Am	L _σ	13.95	13.74 ± 1.5
	L _β	17.74	17.79 ± 1.8
	L _γ	20.8	21.43 ± 2.8
	Te escape peak	30.9	29.53 ± 1.5
	Cd escape peak	36.3	33.17 ± 2.0
	Photo-peak (b.r. 37%)	59.5	57.15 ± 1.2
⁵⁷ Co	Photo-peak (b.r. 85.6%)	122.06	121.99 ± 1.6

Table 8-5 - Type of peak, nominal energy, mean and sigma for the peaks observed in the ²⁴¹Am and ⁵⁷Co calibrated spectra (Grodzins L. 2002, National Nuclear Data Center, NuDat 2 database 2019, Sordo 2009).

8.4 CdTe N-series experimental spectra

In order to study the beams produced by the X-ray tube, a spectral measurement for every beam of the N-series was obtained. All those measurements were made with the CdTe detector (paragraph 3.2.7) external surface at a distance of 1.819 m from the tube focus and 0.5 mA for the tube current to avoid pulses pile-up.

The experimental setup is shown in Figure 8.25 and Figure 8.26. From those figures, it is possible to see that the detector was aligned with the field center thanks to the self-leveling laser and that, because of how it is built, the Eurorad preamplifier could not be put outside the beam line.

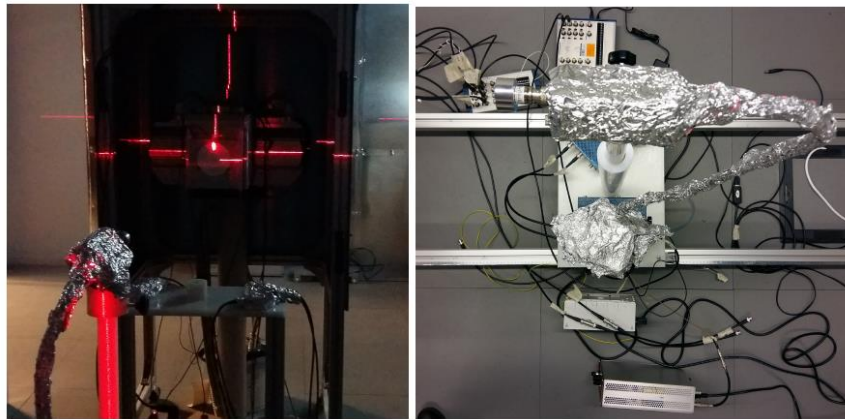


Figure 8.25 - Positioning of the CdTe detector and the preamplifier by aligning them to the field center (aluminium layer ensures the electromagnetic shield).

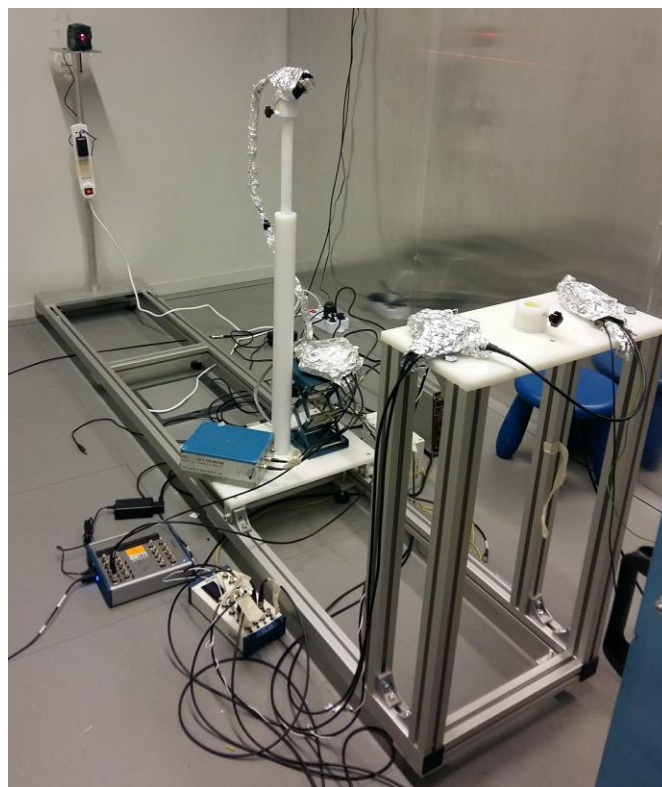


Figure 8.26 - Experimental setup for measuring N-series spectra (aluminium layer ensures the electromagnetic shield).

The different beam configurations that was used are listed in Table 8-6; for every spectrum the signal threshold was set to 0.4 V according to the fact that the threshold is about six times the RMS value of the system noise.

Increasing the tube potential, it has been necessary to increase measurement time because the spectrum shape, at high values of applied voltage, is smoother.

Figure 8.27 shows the graph of the different runs described in Table 8-6. For visualization needs, for every spectrum, counts in the single channels were normalized to the total area. Using data pictured in Figure 8.27, the end-point energies of the spectra were evaluated and reported in Table 8-7.

Endpoint energies were extrapolated by means of a linear trend fit curve (like for Si detector in paragraph 8.1). Figure 8.28 shows the linear trend of E_{end} with respect of the tube potential. This graph confirms what expected: endpoint energies, as a function of measured kV, are on the bisector of the first quadrant. The slope of the curve is likely 1 and the very low y-intercept value corroborates the accuracy of the fits.

The endpoint energies correspond almost exactly to the applied kV; it should be noted that N40 and N120 were performed using a nominal applied voltage of 40 and 120 keV, which correspond to 42 and 117 keV measured by the voltage divider.

Beam	Nom. kV	Mean measured kV	Tube current (mA)	Run time (s)	Max spec. (V)	Min spec. (V)	Threshold (V)	Counts (tot)	Cps
N40	40	42.57	0.5	120	6	0	0.4	1.03 E+06	8.59 E+03
N60	59	60.46	0.5	120	6	0	0.4	1.31 E+06	10.92 E+03
N80	81	80.43	0.5	120	6	0	0.4	0.72 E+06	6.64 E+03
N80	81	80.43	1	120	6	0	0.4	2.02 E+06	1.68 E+04
N100	102	100.32	1	120	9	0	0.4	0.24 E+06	1.96 E+03
N120	120	117.83	1	120	9	0	0.4	0.40 E+06	3.36 E+03

Table 8-6 - N-series spectrum configurations: beam type, applied and measured kV, tube current, running time, minimum and maximum amplitude, threshold to perform the spectrum; experimental results: counts and cps of the total spectrum.

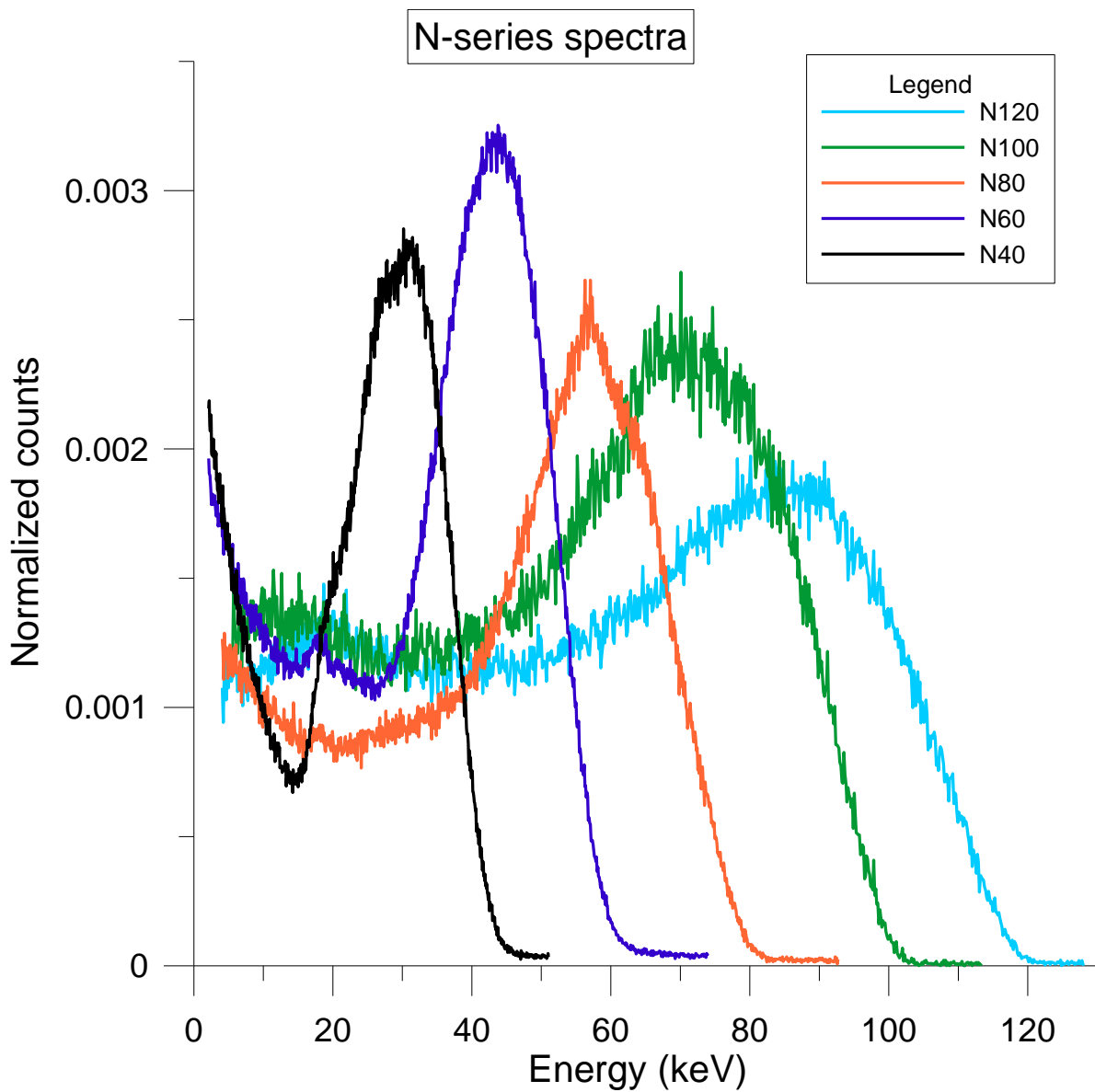


Figure 8.27 - N-series spectra by CdTe detector (paragraph 3.2.7, 1.819 m from tube focus). All the spectra were normalized to unit area to easily visualize them in the same graph.

Beam	Meas. Endpoint (keV)	Estim. Endpoint (keV)
N 40	42.57	43
N 60	60.46	60
N 80	80.43	80
N 100	100.32	100
N 120	117.83	117

Table 8-7 - Comparison between the expected endpoint energy values (thanks to the voltage divider measurements) and their estimate values from the different spectra.

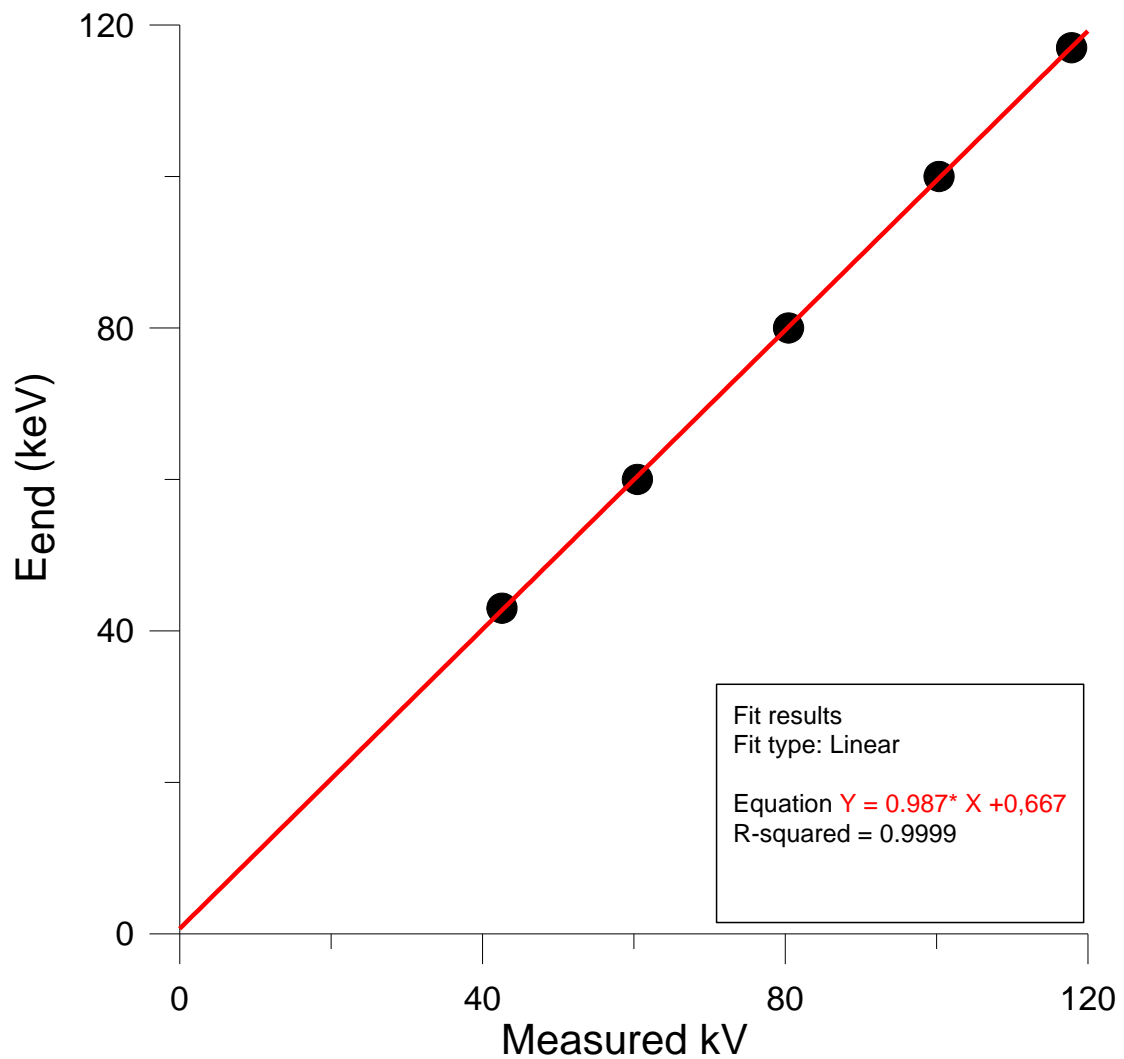


Figure 8.28 - Endpoint energies (estimates from the spectra) as a function of the measured tube potential.

8.5 Concluding remarks about spectral measurements

X-ray measured spectra by use of semiconductor detectors are generally distorted by the response of the detector. For this reason, to perform quality assurance (QA) and a quality control (QC) of radiographic system in diagnostic technologies, the well-known experimental method for determination of X-ray spectral composition is attenuation analysis (ISO 4037-1 2016). In practical situations, the information about the energy of a polyenergetic X-ray beam is provided by simplified beam quality parameters (i.e half-value layers etc.), which characterize the beam in terms of its ability to penetrate a given material. Despite these quality parameters can be easily determined using an ionization chamber and specific filters, they are not useful to provide the more complete representation of the detailed information about the distribution of photons with the quantity and quality of the beam. To experimentally determine the photon energy distribution of the radiation field produced by X-ray tubes, direct X-ray spectroscopy uses high resolutions semiconductor detectors. Nevertheless, experimental determination of X-ray spectra is a complex task, due to the spectral distortion due to the inherent detector efficiency, escape of secondary radiation, incomplete charge collection and carrier trapping effects (E. P. Di Castro 1984, Matsumoto 2000, A. Tomal 2015).

The high purity germanium (HP-Ge) semiconductor detector is widely known for measuring photon energy spectra with excellent energy resolution, but the constraint of cooling by liquid nitrogen makes all the equipment large and hard to move.

Silicon detectors have traditionally been the choice for quantitative X-ray spectroscopy despite of their limited sensitivity at energies above 30 keV (see Figure 9.12). Since CdTe detectors has a much higher stopping power, they are a viable attractive alternative for this application providing adequate energy resolution for distinguishing peaks of interest (R. Redus 2008).

However, the response function of a CdTe detector has some important difference from that of Si detector and these differences must be understood and quantified to achieve accurate results.

CdTe is a wide bandgap compound semiconductor. Its bandgap of 1.44 eV (Si: 3.62 eV) reduces leakage current and makes near room temperature operation feasible. Its constituents have atomic numbers of 48 and 52 (Si: Z=14) and it has a density of 6.2 g/cm³ (Si: $\rho = 2.33$ g/cm³), so it has much better stopping power than Si (R. Redus 2008). One of the most evident features in the CdTe response above 50 keV is **hole tailing**. Figure 2 shows several CdTe photopeak shapes (measured and modelled) as a function of energy (R. Redus 2008). The 122 keV photopeak in Figure 8.29 is clearly not gaussian but it has a shoulder extending towards lower energies. Hole tailing arises from the short lifetime of the holes due to the density of trapping sites in the crystal. This short life time leads to an incomplete collection especially for the charge created far away from the semiconductor cathode. The defect density and thus hole lifetime are intrinsic properties of the CdTe and, although much research has gone into improved crystal fabrication, the defect density remains high enough to be important (Shah 1995).

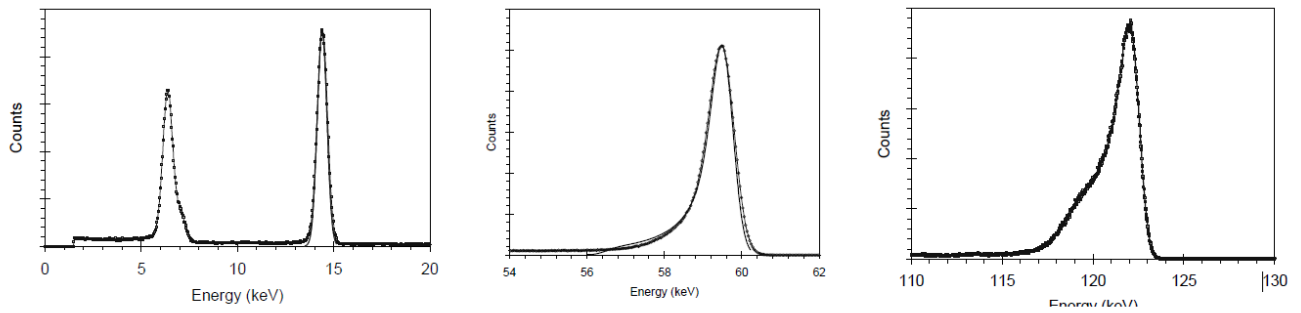


Figure 8.29 - Plots showing the measured and modelled CdTe photopeak shape as a function of energy. At 14.4 keV (left), the photopeak is Gaussian. At 59.5 keV (middle), the photopeak exhibits a smooth asymmetric tail to lower amplitudes. At 122 keV (right), additional counts in the tail lead to a step at the anode charge collection efficiency (R. Redus 2008).

At 14.4 keV interactions all occur near the semiconductor cathode so there is no variation in charge collection efficiency. At 59.5 keV, enough photons interact near the anode to cause a visible asymmetry in the peak, but the counts fall off smoothly, with no visible step. At 122 keV, the attenuation length is much longer than the detector size so interactions occur uniformly throughout. Many photons occur near the anode, leading to a more significant tail and to a clearly visible step termination to the tail at the charge collection efficiency of the anode (R. Redus 2008). For this reason, the peak centroid is shifted by the asymmetry due to the hole tailing leading to an **apparent nonlinearity**. To avoid this problem, the correct technique is to use the peak channel rather than the centroid.

Another important feature, that affects the CdTe X-rays spectra, is represented by the **escape peaks**. The escape peaks have a much more pronounced effect in CdTe than in Si detectors. The physical process is the same: secondary X-rays produced in the detector by the interaction with Cd or Te escape the detector and thus reduce the measured energy. Three intrinsic properties of Cd and Te make them more prominent. First, in Si only 5% of the atoms decay with emission of an X-ray, while in Cd and Te the yield is near 85% (Markowicz 2002), so far more X-rays are produced. Second, in Si only the K_{α} peak is usually visible. In CdTe, both the Cd and the Te produce both K_{α} and K_{β} peaks, so each primary photopeak can produce four escape peaks. Third, in Si the characteristic X-rays have low energy, 1.74 keV, so they only exit the detector for interactions near the surface. In CdTe, the characteristic energies are higher (about 20-30 keV for the Cd and Te K_{α} and K_{β}). They have longer range so are important at higher energies (R. Redus 2008).

Thus, a common approach to accurate spectra determination is based on proper correction of the measured pulse-height distribution for the energy response function of the detector effects. In order to correct the spectra, it is usually suggested a procedure, named **stripping method** (Matsumoto 2000, R. Redus 2008, A. Tomal 2015). Figure 8.30 shows the distortions of a CdTe detector response 35 keV, 90 keV and 150 keV like example of **monoenergetic functions**.

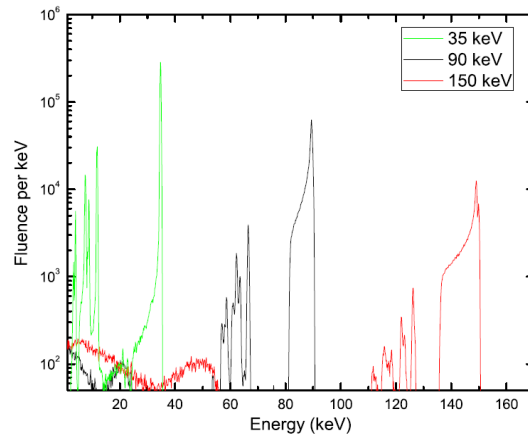


Figure 8.30 - Simulated monoenergetic response functions for a CdTe detector (Amptek, model XR-100T CdTe - 1 mm thickness, 9 mm² nominal area, Be window 100 μm) at 35 keV, 90 keV and 150 keV (A. Tomal 2015).

It can be observed that the height of the main peaks decreases when the energy increases, indicating that the distortions due to the transmission of primary X-rays are greater for high energies, which is explained by the lower attenuation of the radiation with higher energy. With the energy increase, the tail and flat-shelf contributions to the total response also increase due to the hole trapping effect. This effect reduces the height of the main peak and distorts the spectra toward the energies below the main peak, adding counts at energies up to approximately 20 keV below the incident energy. Besides, the escape of characteristic K X-rays from Cd and Te is also an important contribution to the response function of this detector, since it distorts the spectra towards the region of energies below the main peak (Miyajima 2002), i.e., around 26–32 keV below the incident energy. However, the contribution of the escape of characteristic radiation decreases when the energy increases (A. Tomal 2015).

After this short explanation of the main distortions in CdTe spectra, it is worth to look again at ²⁴¹Am spectrum performed in this work for the calibration of the CdTe detector (Figure 8.31, paragraph 3.2.7) used for spectral measurements of the N-series spectra.

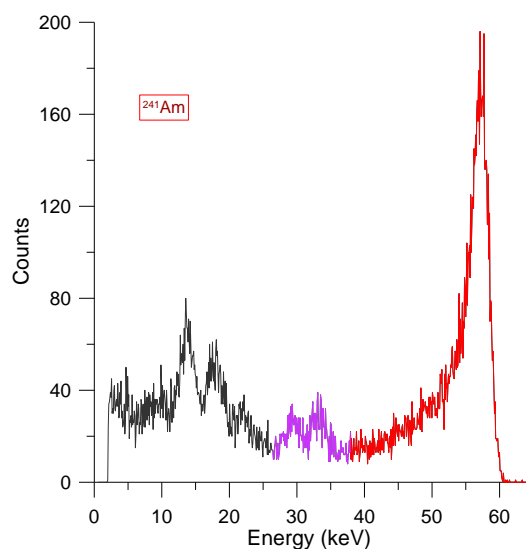


Figure 8.31 - CdTe (see paragraph 3.2.7) calibration spectrum of ²⁴¹Am radioactive source. Several distortions due to the CdTe features are highlighted with different colours.

Red: photopeak with shoulder extending towards lower energies (20 keV below the incident energy).

Purple: escape of characteristic K X-rays from Cd and Te (26–32 keV below the incident energy of the main peak).

The agreement with the features of the previous explanation is excellent:

- the hole trapping effect distorts the spectra toward the energies below the main peak, adding counts at energies up to approximately 20 keV below the incident energy,
- the escape of characteristic K X-rays from Cd and Te distorts the spectra towards the region of energies around 26–32 keV below the incident energy of the main peak.

For the same reasons, the N-series spectra taken by CdTe detectors (Figure 8.27) show that background continuum, that includes many physical process (counts at low energies due to Cd and Te characteristic X-ray escape, Compton scattering etc., Figure 8.32). A correction procedure should be applied in order to remove this contribution and the distortions (like it is made in Figure 8.32 and Figure 8.33, A. Tomal 2015), but the stripping method requires complex simulations of the detector response (monoenergetic responses) considering the interaction of photon with the crystal (related to the number of electron-hole pairs created), a deep knowledge of the crystal geometry and surroundings materials (dead layer, contacts), the carrier transport (carrier trapping effects and incomplete charge collection) and the finite energy resolution (A. Tomal 2015). This clearly exceeds the objectives of this PhD work, where the measurements by Si and CdTe lead a role for having a reasonable idea (continuum shape of bremsstrahlung spectrum, endpoint energies) of the spectral components in addition to the quality measurements of HVLs, but these spectra obviously does not claim to be so accurate for the fulfilment of the constraints for performing quality assurance and control of radiographic systems.

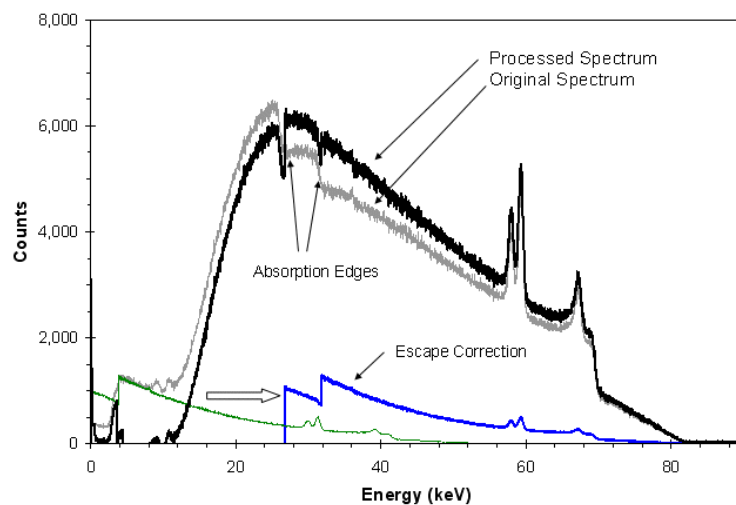


Figure 8.32 - Spectrum emitted from an 80 kVp X-ray tube with a tungsten (W) anode and a 15 keV filter, measured with a 1 mm thick CdTe detector. Plot showing the spectrum after processing to remove escape events. The grey trace shows the original spectrum. The green trace illustrates the escape events in the original spectrum. These are subtracted from this original spectrum, then the correct energies are computed (by adding in the energy which escaped). The blue trace shows the corrected escape events, which are then summed with the grey trace. The dark black trace shows the final result of the processing with the events in their correct channels (Amptek 2008).

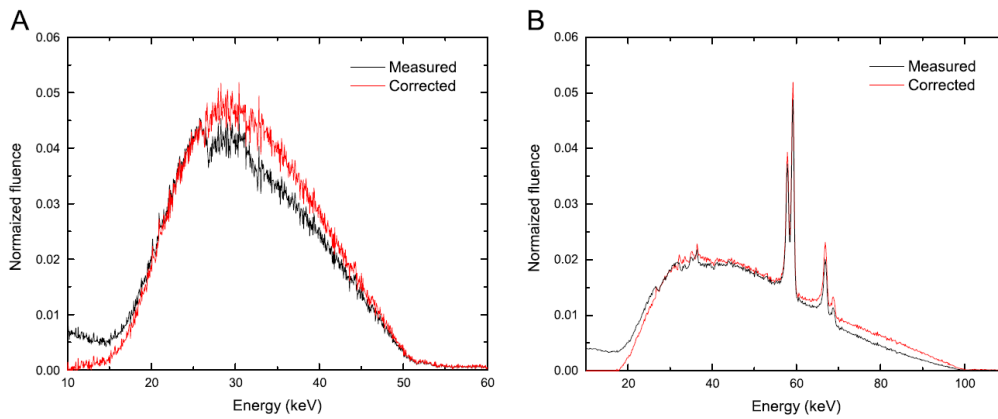


Figure 8.33 - Measured and corrected X-ray spectra obtained with a CdTe detector (Amptek, model XR-100T CdTe - 1 mm thickness, 9 mm² nominal area, Be window 100 μ m) for (a) 50kVp and (b) 100kVp (A. Tomal 2015).

Finally, it is worth to note that also the Si spectra (Figure 8.9) should be elaborated in order to have the corrected fluence distribution in energy. Anyway, the measured spectra allow to see a component of the beam (Mo anode contribution), exactly in the energy region where the CdTe shows the greater distortion because of the superimposed continuum. This spectral component is physically coherent with the beam from the anode of this specific tube. The characteristic radiation of Mo (from Figure 8.10 to 8.13) can be recognised in that peak. In addition, the bremsstrahlung continuum is clearly distinguishable.

Part III – R&D on a need for operational dosimetry



9.1 Introduction: why is the eye lens dose monitoring important?

In the last years the need of a detailed re-evaluation of the eye lens radio-sensitivity was put in evidence. Various epidemiological studies highlighted a higher incidence of cataracts than previously foreseen.

Cataract is the loss of transparency of the lens of the eye. When opacities occur, the light is scattered inside the eye and cannot normally pass and focus on the retina. Therefore, vision is reduced and the image is perceived to be blurred. The cataract slowly progresses to cause vision loss and may eventually lead to blindness. Luckily, this disease is quite easy to treat. Old age and metabolic conditions, like diabetes, are the typical factors associated with the onset of cataract. It is known that cataract can also be radiation induced (ICRP 85 2000).

In the previous ICRP approach, cataract induction is classified as a tissue reaction with a definite threshold (ICRP 103 2007). This threshold was set between 0.5 and 2 Gy for acute exposures, and 5-6 Gy for prolonged exposures. There is a latency period that can last many years. This amount of time, required for a cataract to develop, depends on the rate at which damaged epithelial cells undergo aberrant differentiation (fibrogenesis) and accumulate in the posterior subcapsular (PSC, see Figure 9.1) region of the lens cortex (Worgul 2007).

The annual dose limit for the eye lens for occupationally exposed workers was set to 150 mSv per year (European Commission 1996). Eye lens doses have received a lot of attention during the last years because of several epidemiological studies on specific groups of workers, especially on astronauts (L. T. J. Chylack 2009), interventional cardiology and radiology (IC/IR) workers (Vano 2010, Junk 2008), radiological technologists (Chodick 2008), Chernobyl clean-up workers, the so-called “liquidators” (Worgul 2007), interventionalists and survivors of the atomic bombs (Ciraj-Belac 2010, K. Neriishi 2007). These studies clearly show that the threshold dose for cataract induction is lower than previously assumed, even lower than 0.8 Gy. More recent studies put in evidence an excess of cataracts at lower doses than 0.5 Gy, whilst other studies did not provide any significant proof of the existence of a threshold dose (Nakashima 2006, Worgul 2007, Chodick 2008).

For these reasons the ICRP reduced the exposure limit for workers from 150 mSv per year to 20 mSv in a year averaged over defined periods of five consecutive years, with no single year exceeding 50 mSv (ICRP 2011). These recommendations are introduced in the European directive 2013/59 (EURATOM 2013, Table 9-1). Therefore, the keen interest on this topic is for the essential evaluation of the occupational eye dose and eye protection.

Dose quantity	Limit in 2017 (Real Decreto 783/2001 2001)	Limit after February 2018 (Implementation Directive 2013/59)
E	100 mSv in a consecutive five-year period subject to a maximum E of 50 mSv in any single year.	20 mSv in any single year. In special situations, a higher E up to 50 mSv may be authorised.
H _{lens}	150 mSv/year	20 mSv per year, averaged over 5 years, with no single year exceeding 50 mSv.
H _{skin}	500 mSv/year This limit shall apply to the dose averaged over 1 cm ² .	500 mSv/year This limit shall apply to the dose averaged over 1 cm ² .
H _{extremities}	500 mSv/year	500 mSv/year

Table 9-1 - Comparison of Spanish dose limits for occupational exposure between 2016 and after the implementation of the 2013/59 Directive EURATOM (EURATOM 2013).

In particular the occupation exposure for interventional radiology and interventional cardiology staff is a critical issue for medical workers. Interventional cardiology is a diagnostic or therapeutic technique in which cardiac chambers or coronary vessels are accessed by inserting catheters through blood vessels. Visualization and guidance of the devices inserted into the patient plus acquisition of additional high-quality images are done using X-ray imaging (fluoroscopy and radiography). Due to its advantages over surgery (low invasiveness, risk, cost etc.) the frequency of this technique has increased (Thom 2006, Togni 2004), so has the workload per physician (Vañó 1998). The specific character of IC procedures results in inevitable occupational exposure of the medical staff to ionizing radiation scattered from the patient (Figure 9.2). Significant radiation doses are received especially by unshielded body parts, primarily legs, arms, hands and eyes of the staff (Kim 2008, K. M. Kim 2009, Martin 2009, Vanhavere 2008).

A better than now eye lens dose monitoring is therefore necessary in order to have an appropriate assessment of extent of exposure for the lens of the eye to ionizing radiation. As expected, implementation of the limit reduction in European legislation implies a greater focus on individual supervisory control and emphasis on the role of protection tool on occupational exposure at some workplaces. Consequently, optimization of calibration procedures and measurement techniques for this specific tissue (eye lens) is needed. Furthermore, an urgent need to educate radiation exposed professionals is suggested, in order to reduce the likelihood of radio-induced cataracts.

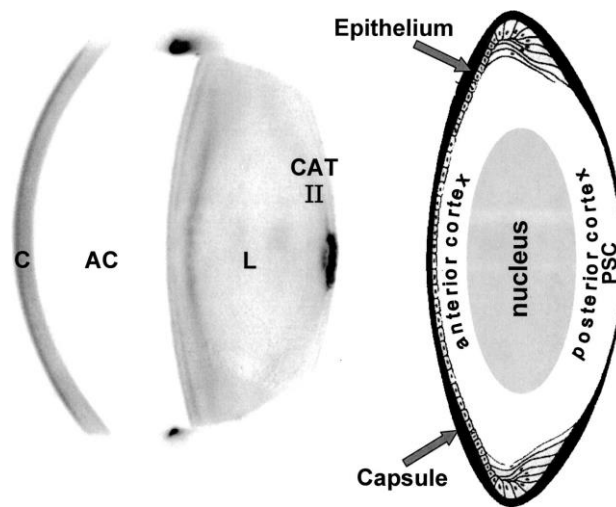


Figure 9.1 - The lens and its anatomical regions. Left: A classic radiation cataract imaged using a Nidek_EAS1000 Scheimpflug Slit Imaging System. Left to right are the cornea (C), anterior chamber (AC) and lens (L). The dark area in the right center is a stage 1 cataract (CAT) in the PSC/cortical region of an otherwise relatively clear lens. Right: Schematic diagram of a sagittal view of an adult human lens. The bulk of the tissue consists of fiber cells, the elongate progeny of those epithelial cells that undergo differentiation (fibrogenesis). The centrally located lens is comprised innermost of those cells that differentiate during intrauterine and early postpartum life. Later fibrogenesis compacts the early nucleus and adds to the overall nuclear mass. It is surrounded by a cortex consisting of fibers that are continuously produced and laid down during cell maturation. The most superficial fibers of the cortex are those that most recently differentiated. The capsule, a tremendously hypertrophied basal lamina, is a barrier to cells leaving or entering the tissue. After radiation injury, epithelial cells differentiate improperly and initially accrete in the superficial posterior cortex immediately adjacent to the capsule. Collectively the aberrant fibers accumulating in the back of the lens constitute the clinical entity known as posterior subcapsular (PSC) cataract. The term arose to more precisely describe, based on location, what otherwise is generically a cortical cataract (Worgul 2007).



Figure 9.2 - (Left) Complex cardiac procedure. Electronic C arm (X-ray tube) is highlighted in the black circle. Cardiologists are usually well protected with ceiling screen, goggles and protection under the table. Nurses usually wear only goggles, but they are exposed only for a limited time in that position (Courtesy E. Vano, Madrid). (Right) Example of a model of C arm for vascular operation (Medical 2019).

9.2 Choice of the operational quantity to monitor eye lens exposures

The personal dose equivalent at 3 mm depth, $H_p(3)$, was defined in ICRU Reports 43 and 47 (ICRU report 43 1988, ICRU report 47 1992) but no conversion coefficient, $h_p(3)$, was officially agreed. The ORAMED project, for one of its tasks, proposed a new definition of the personal dose equivalent $H_p(3)$ (Daures J., 2011, Daures J. 2009, Gualdrini G., 2011). A new phantom was proposed, as previously done for the finger and the wrist. This new cylindrical phantom is made of tissue-equivalent ICRU material and has a height and diameter equal to 20 cm: simple shape and size, which are close to the dimensions of an adult head. Conversion coefficients $h_p(3)$ were calculated (Daures J., 2009, Mariotti F., 2009, Gualdrini G., 2013) through Monte Carlo calculations (see Figure 9.3).

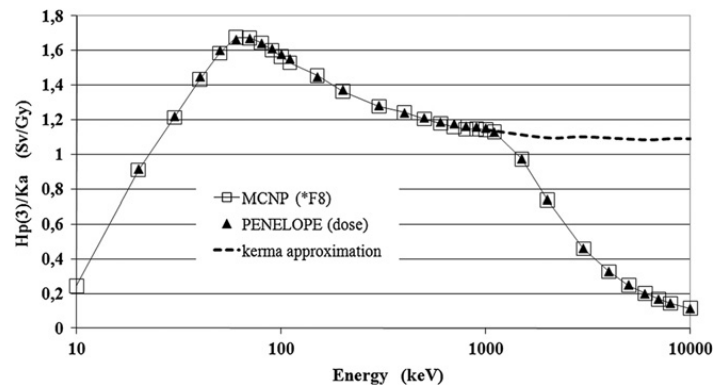


Figure 9.3 - Fully coupled photon electron transport calculations results versus kerma approximation for evaluating $H_p(3,0^\circ)/K_a$ (Gualdrini G., 2011).

Considering that the operational quantities are used as estimators of the protection quantities (chapter 2), in order to choose the most suitable quantity to estimate H_{lens} , in Figure 9.4 and Figure 9.5 the operational quantities are compared. More precisely, the conversion coefficients, h , from air kerma toward the operational and protection quantities are compared.

For better understanding the comparison in Figure 9.4 and Figure 9.5 and the following comments, consider that the conversion coefficients for operational quantities and protection quantities were calculated using the kerma approximation in (ICRP publication 74, 1995) and in (ICRU report 57, 1995). This is equivalent to consider that the energy is absorbed in the vicinity of the interaction.

The values of protection quantities are now calculated without the kerma approximation in (ICRP publication 116, 2010), taking into account the follow-up of the secondary particles produced after interaction of the photons.

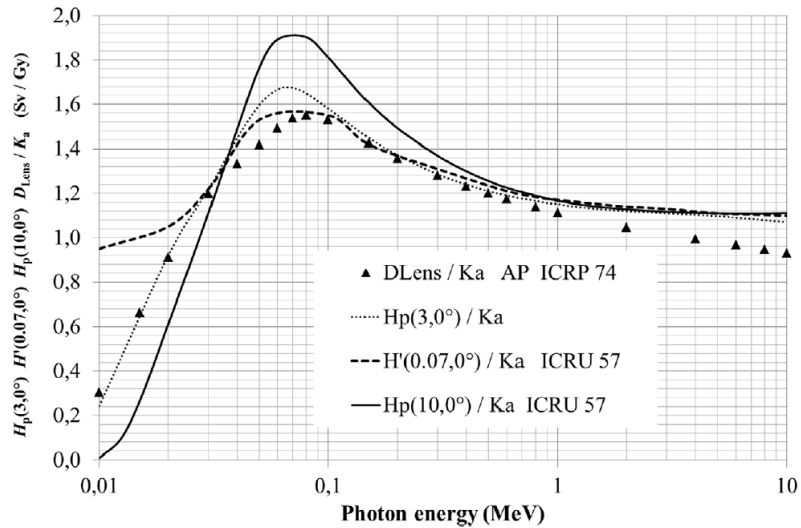


Figure 9.4 - Comparison of dose equivalents at 10 and 0.07 mm depth at 0° taken from the (ICRU report 57, 1995) report and the dose equivalent at 3 mm depth taken from (Daures J., 2009) with the absorbed dose to the eye lens in the anthropomorphic phantom for anterior-posterior (AP) irradiation taken from (ICRP publication 74, 1995). $h'(0.07)$ was plotted instead of $h_p(0.07)$ because $h_p(0.07)$ is not given above one MeV in (ICRU report 57, 1995), but is very similar to $h'(0.07)$ below one MeV (Bordy, 2015).

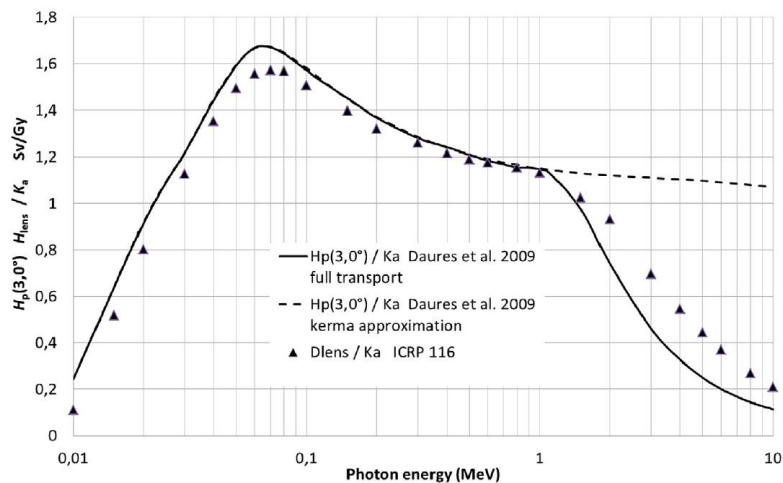


Figure 9.5 - Comparison of dose equivalents at 3 mm depth at 0° taken from (Daures J., 2009) calculated with full transport and kerma approximation with the equivalent dose to the eye lens in the anthropomorphic phantom for anterior-posterior irradiation derived from (ICRP publication 116, 2010, Bordy, 2015).

The dose equivalent $H_p(3)$ defined in the cylindrical phantom and calculated without kerma approximation (secondary charged particles are not transported) is similar to the equivalent dose $H_{lens,ICRP116}$ regardless of the energy or the angle of incidence of the radiation, because of the similarity of the forms of the phantoms used to calculate the values of the conversion coefficients. The same conclusion would be drawn for the directional dose equivalent $H'(3)$, which is very similar to the personal dose equivalent $H_p(3)$ defined in the cylindrical phantom regardless of the angle of incidence or the energy of the radiation because of the similarity of the diameter of the cylinder (20 cm) and the ICRU sphere (30 cm) (Bordy J.M., 2011).

The dose equivalents $H_p(0.07)$ and $H'(0.07)$ are close to the equivalent dose $H_{lens,ICRP74}$ except below approximately 20 keV. In every case (energy and angle), the dose equivalents $H_p(10)$ are worse

estimators of the equivalent dose H_{lens} than the other operational quantities. The same conclusion would be drawn for $H^*(10)$. It should be mentioned that $H_p(10)$ is not defined for angles larger than 75° and that $H^*(10)$ is only for ambient dosimetry as $H'(10)$ is not used even for ambient dosimetry. Therefore, the best choice to monitor $H_{\text{lens,ICRP116}}$ is $H_{p,FT}(3)$ regardless of the energy and angle of incidence (Bordy J.M., 2011).

9.3 Calibration and type testing for a dosimeter to measure $H_p(3)$

In the past years, the scientific community discussed about the best choice of a suitable phantom for calibrating and type testing of a personal dosimeter for the eye lens (Bordy 2015, Gualdrini 2011, Gualdrini 2013, H. Stadtmann 2014, Behrens 2012). It should be considered that a dosimeter designed in terms of $H_p(3)$ quantity and consequently calibrated on the most appropriate phantom should be able to estimate as better as possible the eye lens equivalent dose. It means that it should provide a conservative estimate of the eye lens dose without excessive overestimation. The choice of a suitable phantom should be based on physical considerations on the scattering properties of this phantom compared with the head.

The study of the characteristics of the operational quantities led to the choice of the cylindrical phantom 20 cm in diameter and 20 cm height made of ICRU tissue to define the personal dose equivalent $H_p(3)$. It is obvious for the type testing of personal dosimeters for the eye lens, a water phantom with the same dimension as those used for the definition of the quantity (outer diameter: 200 mm, length: 200 mm, PMMA thickness cylinder walls and end faces: 5 mm, ISO 4037-3 2019). For these reasons the slab phantom $30 \times 30 \times 15 \text{ cm}^3$ is not a good solution to achieve an optimised procedure for eye lens dosimetry. In fact, the dimensions of such a phantom ($13\,500 \text{ cm}^3$) are far larger than a real head volume ($\sim 6\,300 \text{ cm}^3$) with an associated larger quantity of tissue available as a scatterer of the incident radiation. In addition, a thickness of 15 cm is too small to represent the head and this leads to unphysical lack of shield in a posterior-anterior irradiation.

The difference between these two different phantoms can be graphically summarize in Figure 9.6, Figure 9.7, Figure 9.8 and Figure 9.9.

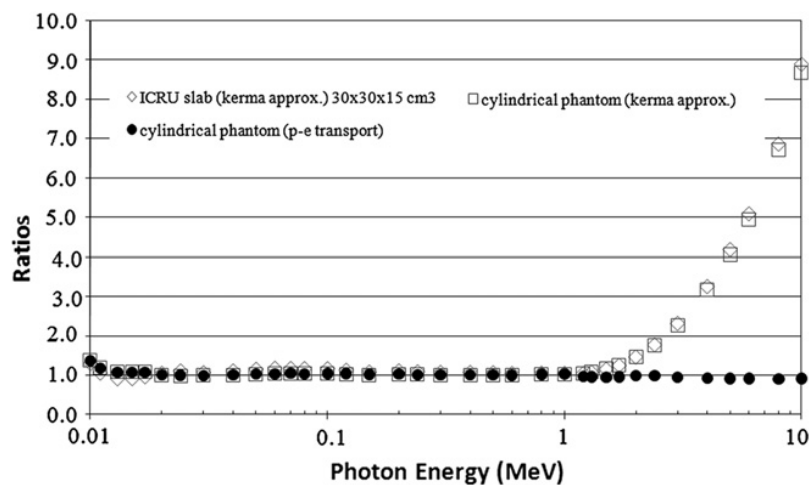


Figure 9.6 - Normally incident photons: comparison between the $H_T(\text{eye lens})$ (R. Behrens 2011) and $H_p(3)$ as obtained using the cylindrical phantom and the traditional $30 \times 30 \times 15 \text{ cm}^3$ slab (E. Till 1995).

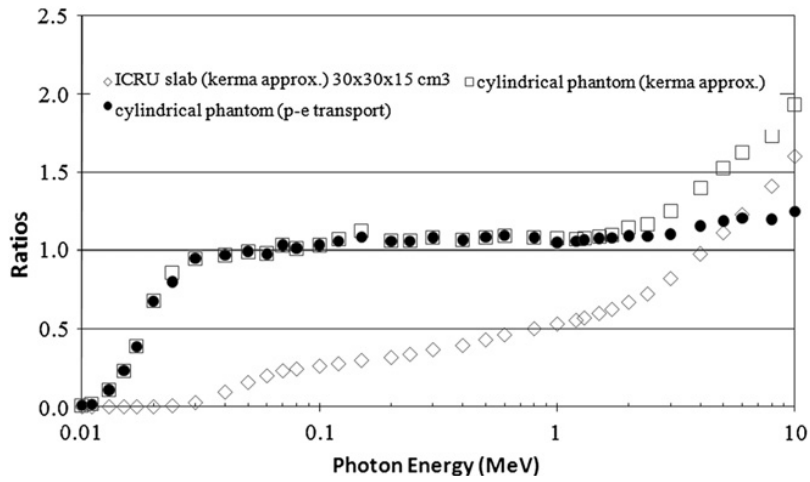


Figure 9.7 - Laterally incident photons: comparison between the H_T (eye lens) (R. Behrens 2011) and $H_p(3)$ as obtained using the cylindrical phantom and the traditional $30 \times 30 \times 15 \text{ cm}^3$ slab (E. Till 1995).

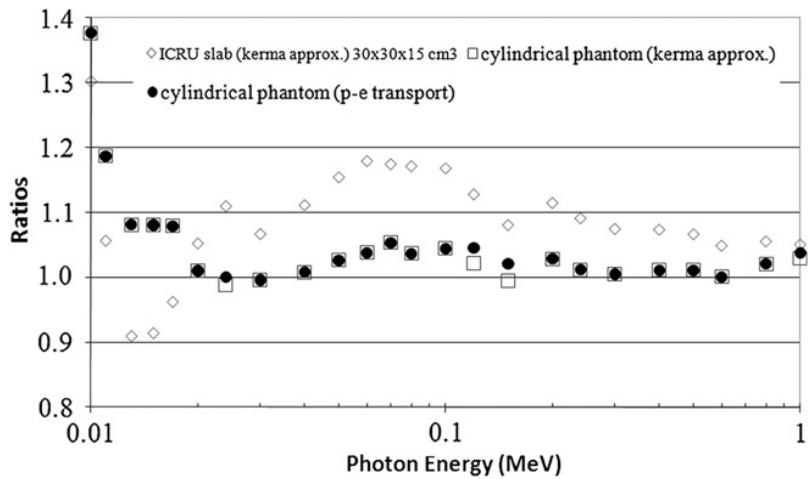


Figure 9.8 - A detail of Figure 9.6 showing the comparison between the H_T (eye lens) (R. Behrens 2011) and $H_p(3)$ as obtained using the cylindrical phantom and the traditional $30 \times 30 \times 15 \text{ cm}^3$ slab (E. Till 1995) below 1 MeV.

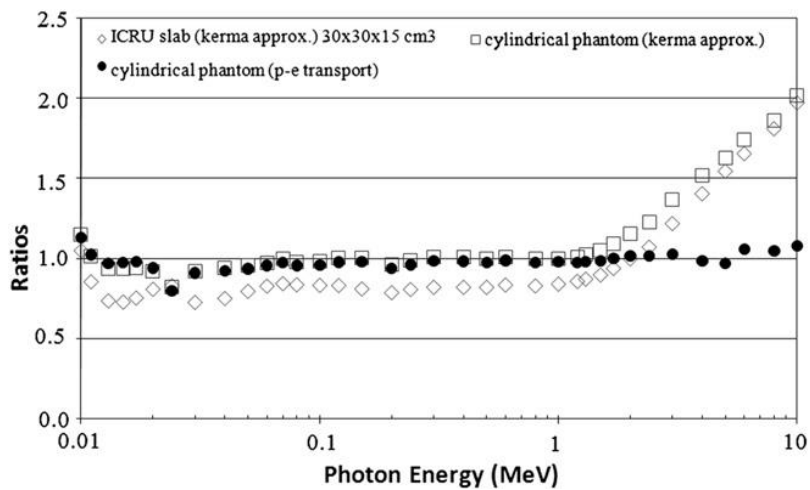


Figure 9.9 - Rotational photon exposure: comparison between the H_T (eye lens) (R. Behrens 2011) and $H_p(3)$ as obtained using the cylindrical phantom and the traditional $30 \times 30 \times 15 \text{ cm}^3$ slab (E. Till 1995).

Nevertheless, a water slab phantom $30 \times 30 \times 15 \text{ cm}^3$, as the one for the calibration of dosimeters for the whole body (see Figure 9.10), can be used because of the similarity of backscatter to the cylindrical phantom (see Figure 9.11) at normal incidence. The standard ISO 29661 (ISO 29661 2012) opens up the possibility of using both phantoms (ISO 12794 2000, ISO 14146 2000, Bordy J.M. 2011) for calibration in agreement with the customer. Note, however, that to conform to the definition of $H_p(3)$ in the cylindrical phantom a correction factor must be applied if the slab phantom is used, and that for angles larger than 75° the slab phantom cannot be used due to the edges. The type testing can be done following the specification of the following standards: IEC 62387 (IEC 62387 2012) and ISO 12794 (ISO 12794 2000). In practice, the IEC 62387 standard is more exhaustive and hence should be preferred (Bordy J.M. 2011).



Figure 9.10 - Four whole-body dosimeters positioned on the front surface of the ISO water slab phantom (H. Stadtmann 2014).

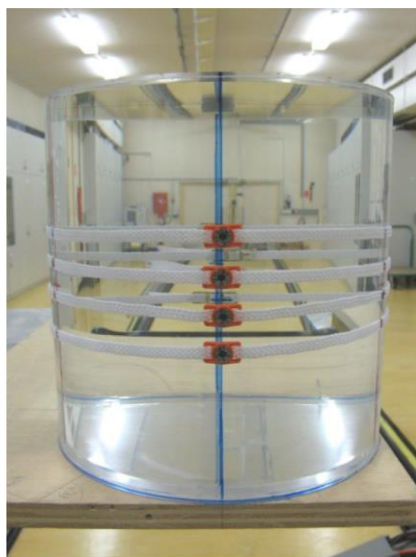


Figure 9.11 - Four head-band dosimeters positioned on the water filled cylindrical head phantom (H. Stadtmann 2014).

9.4 Wearing conditions and state of art

The positioning of the dosimeter for the lens of the eye is important to have a good estimate of the dose to the lens of the eye. The dosimeter for the lens of the eye shall be worn as possible to the eye, if possible in contact with the skin, and facing towards the radiation source. In case of usage in interventional radiology, the side closest to the X-ray tube shall be chosen. The dosimeter must be worn at the level of the eye in a way which cannot underestimate the exposure of the lens. It can be worn to the left or to the right or between the eyes; this has not been specified up to now. Wearing the dosimeter between the eyes would allow, to some extent, an average estimate of the exposure of the two lenses, whereas wearing the dosimeter on the right or on the left is better because it allows measurement of the maximum value of the exposure. If individual protection is used, for example glasses, the dosimeter must be put under this protection to give information about the real exposure to the lens. This is often not very practical, and a dosimeter on the outside or next to the lead glasses can be chosen. In this case, some correction factors should be applied (ISO 15382 2015). A lot of models of glasses are commercially available; one should choose those with lateral and central shields to avoid lateral irradiation, similar to the case of the lack of underside protection for faceguards (Bordy, 2015).

The dosimeters used for monitoring the lens of the eye are generally based on passive techniques and made of thermoluminescent (TL) materials, although, detectors based on other methods, such as film badges, optically-stimulated luminescence (OSL) and radiophoto luminescence (RPL) can be also used. Electronic devices, e.g. made of silicon probes, can be used if they are optimized in terms of $H_p(3)$ with respect to energy and angular dependence. These systems offer the advantage of a direct reading of the dose, which is useful for training and optimization purposes. However, their suitability in pulsed radiation fields shall be confirmed if they are to be used in such fields, e.g. in the vicinity of pulsed X-ray tubes as often used in medical sector (ISO 15382 2015).

To give an idea of the possible choice of dosimeter for eye lens dosimetry, Table 9-2 summarizes the main features of several dosimeters available on the present market. For more detailed information see the individual website.

	Type of detector	Dose range	Energy dependence / range	Angular response / range
EYE-D (Radcard)	MCP-N (LiF:Mg, Cu, P) + 3 mm thick polyamide	Photons 10 μ Sv - 10 Sv	Photons 30 keV – 1.3 MeV <20%	0° - 80° (cylindrical phantom) <20%
UK Rotunda Scientific Technologies	TLD Harshaw “chipstrates” + 3 mm thick PTFE filter			
Health Protection Agency	TLD Harshaw EXTRADTM + 1.5 mm thick PTFE filter (headband version)	Photons 0,15 mSv - 10 Sv	Photons 16 keV – 0.662 MeV	Up to 45°
DOSIRIS (IRSN)	TLD (7LiF:Mg, Ti) + 3 mm thick polypropylene bolus	Beta & Photons 100 μ Sv - 50 Sv	Beta down to 700 keV Photons down to 20 keV - 1.3 MeV *	Up to 60°
VISION (Landauer)	One TLD chip (LiF:Mg,Ti)	Photons 0.10 mSv - 10 Sv	Photons 24 keV – 1.25 MeV	\pm 60° 24 keV – 1.25 MeV

Table 9-2 - State of art for eye lens dosimetry.

9.5 Design a dosimeter for monitoring $H_p(3)$

From the different reasons and the main concepts explained in the previous paragraphs, the fundamental constraint and considerations for the design of an eye lens dosimeter are the following.

- Tissue-equivalent material at the front of the detector should have a thickness of 3 mm; a bolus of hemispherical or similar shape seems to be the most adapted (P. Bilsky 2011). Tissue-equivalent material behind the detector should be sufficient to reproduce the backscatter of the radiation if the dosimeter is not worn next to the skin.
- The composition of the detector itself is more problematic because it is not strictly equivalent to tissue. This can bring the type test results outside the criteria.
- Its composition and/or its shape including the front and rear faces must be adapted so that the criteria for energy and angle responses are fulfilled (i.e. special case around the detector).
- A headband can be used to maintain in the proper position close to the eye for the measurement. Maybe the detector can be equipped on a protective glass in order to be worn together with the fundamental individual protection.

9.6 Eye lens dosimeter prototype based on active detector

This paragraph shows the development of an eye lens dosimeter prototype. The design and the type test for this dosimetric unit, based on the Hamamatsu detector S3590-09 (paragraph 3.2.7), will be shown below. This part of the work is an example of development obtained by using the irradiation facility, in particular the N-series spectra, studied and characterized during this PhD project.

Referring to the description made in 3.2.7, 0 and 3.3 (about the features of the detector and the processing electronics), some measurements of type testing were taken in order to get some preliminary concluding remarks about the energy and angular response of this prototype.

The bare detector is not appropriate as dosimetric device due to its intrinsic response (see Figure 9.12). The detector itself has a response function in energy that depends on the material which is used to build the semiconductor junction: in this situation the device is made of silicon.

The response function, which is the number of detected events (pulses) inside the active volume for this application, is not generally proportional to operational quantities used for radioprotection:

- the detector material is different from the reference biological tissue;
- the detector is not covered by the proper layers used by definition for the operational quantities;
- the radiation interaction with matter inside the detector shows a different efficiency in function of the incident X-ray energy. In particular, for silicon, the intrinsic energy response decreases as the energy grows.

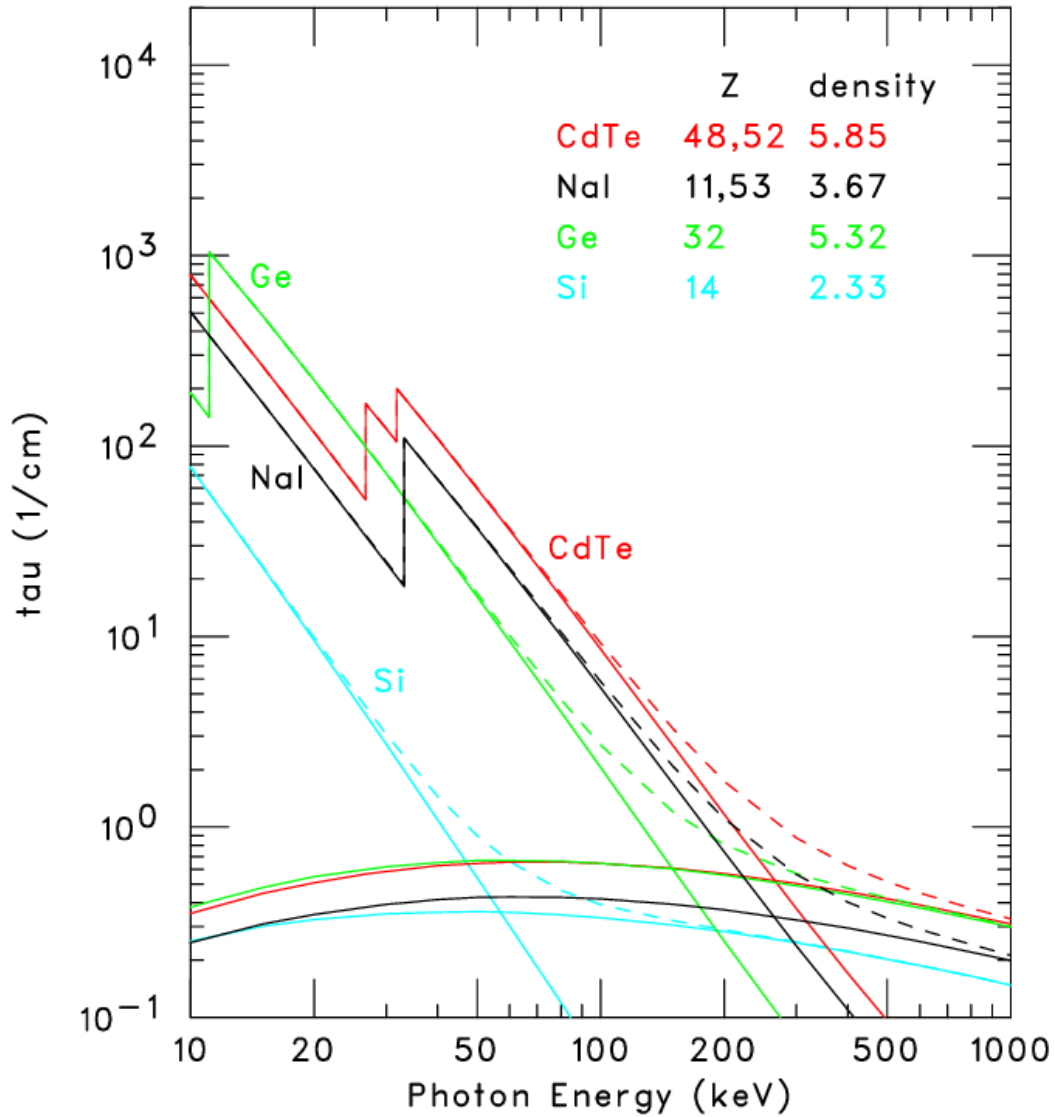


Figure 9.12 - Linear attenuation coefficients for photo absorption and Compton scattering in silicon and other detector materials (Tadayuki Takahashi 2019).

For these reasons the international regulations admit a certain variability for the device response function. For this situation the reference document is the IEC 62387 “Radiation protection instrumentation – Passive integrating dosimetry systems for personal and environmental monitoring of photon and beta radiation” (IEC 62387 2012).

Considering the energy range for medical applications, this tolerance about the response variability is summarised in the following intervals.

$0.69 < R(E, \alpha) / R_{ref} < 1.82$ for photon energy between 33 keV - 65 keV,

$0.71 < R(E, \alpha) / R_{ref} < 1.67$ for photon energy beyond 65 keV.

$R(E, \alpha)$ is the response for several energies (E) and incidence angles (α). R_{ref} is the arbitrary reference value of a situation taken as reference. The ratio $R(E, \alpha)/R_{ref}$ is the relative response of the device under test.

Type tests were made by using at first bare detectors and then some filtrations on the sensitive area. The different filters are metallic. The choice of these materials relies on the behaviour of the

bare detector and its response function that could be improved by adding such a filtration allowing to fulfil the IEC 62387 constraints. Considering the availability of this kind of material in the laboratory, the different filters were designed in order to force a depression of the silicon response at low energies. The chosen filters are: 1 mm lead (Pb), 1 mm lead (Pb) + 0.4 mm copper (Cu) and 1mm lead (Pb) with a 4 mm diameter hole in the centre.

Taking into account the reference calibration condition, previously discussed in paragraph 9.3, the prototype was set on the irradiation line on the surface of the cylindrical phantom (Figure 9.13). Placed the experimental set up at the distance of 2.5 m and performed several runs at 0.5 mA tube current (best situation to avoid pile-up), the N-series spectra, studied and characterized during this PhD project, were used to irradiate the prototype for the type test (Hamamatsu detector: 90 V bias, acquisition system threshold 1.5 V, corresponding to ~ 22 keV).



Figure 9.13 - Experimental setup for irradiating the eye lens dosimeter prototype. The dosimetric unit is placed on the surface of the water filled cylindrical head phantom according the calibration procedure (paragraph 9.3): 2.5 m distant from the tube focus (90 V bias, 1.5 V or ~ 22 keV threshold).

Table 9-3 contains all the conversion coefficients used in this elaboration ($H_p(3, \alpha)$ column). By multiplying these factors and the air kerma values measured by PTW (paragraph 3.2.6) it was possible to obtain the delivered operational quantities values. The columns refer to the three main operational quantities to measure with the proper phantom. For these measurements, only the coefficients corresponding to $H_p(3, \alpha)$ are to be considered.

Beam	Angle (°)	Conversion coefficient $H_p(0.07, \alpha)/K_{air}$, rod phantom (Sv/Gy)	Conversion coefficient $H_p(3, \alpha)/K_{air}$, cylinder phatom (Sv/Gy)	Conversion coefficient $H_p(10, \alpha)/K_{air}$, ICRU slab phantom (Sv/Gy)
N40	0	1.07	1.28	1.21
	30	1.07	1.25	1.16
	45	1.07	1.22	1.06
	60	1.07	1.15	0.883
N60	0	1.11	1.54	1.66
	30	1.11	1.51	1.60
	45	1.11	1.48	1.49
	60	1.11	1.41	1.29
N80	0	1.15	1.66	1.89
	30	1.15	1.64	1.83
	45	1.15	1.60	1.72
	60	1.15	1.54	1.51
N100	0	1.16	1.63	1.88
	30	1.16	1.62	1.82
	45	1.16	1.59	1.73
	60	1.16	1.54	1.53
N120	0	1.17	1.58	1.80
	30	1.17	1.57	1.75
	45	1.17	1.55	1.67
	60	1.17	1.51	1.51

Table 9-3 – Recommended conversion coefficients for the three main operational quantities to measure with the proper phantom. N-series spectra, different angle of incidence, distance from focal spot 2.5 m (ISO 4037-3 2019).

Table 9-4 shows the raw data obtained by several runs using the different filters on the dosimetric unit. The main output of the system can be represented by the measured counts during the different measurements. The delivered $H_p(3)$ values are listed too; the uncertainties are about 10% because of the not avoidable uncertainty of the feedback resistor in the PTW processing electronics (see paragraph 3.2.8).

Beam	Counts	Angle (°)	Dosimetric unit	Ratio ($\mu\text{Gy}/V_{\text{SMON}}$)	Air Kerma (μGy)	$H_p(3)$ (μSv)
N120	45544	0°	Ham	0.422	1.56	2.47 ± 0.25
N100	86124	0°	Ham	0.693	2.23	3.64 ± 0.36
N80	424719	0°	Ham	2.580	6.80	11.3 ± 1.1
N60	1431908	0°	Ham	10.21	15.5	23.9 ± 2.4
N40	3048774	0°	Ham	46.27	21.9	28.1 ± 2.8
N120	17737	0°	Ham+1mmPb	0.422	1.59	2.52 ± 0.25
N100	36673	0°	Ham+1mmPb	0.693	2.48	4.04 ± 0.4
N80	144947	0°	Ham+1mmPb	2.580	6.60	10.9 ± 1.1
N60	308875	0°	Ham+1mmPb	10.21	14.7	22.7 ± 2.3
N40	232270	0°	Ham+1mmPb	46.27	27.4	35.1 ± 3.5
N120	17853	0°	1mmPb+0.4mmCu+Ham	0.422	1.65	2.60 ± 0.26
N100	36956	0°	1mmPb+0.4mmCu+Ham	0.693	2.43	3.96 ± 0.4
N80	150058	0°	1mmPb+0.4mmCu+Ham	2.580	7.14	11.8 ± 1.2
N60	319028	0°	1mmPb+0.4mmCu+Ham	10.21	16.1	24.7 ± 2.5
N40	242961	0°	1mmPb+0.4mmCu+Ham	46.27	28.6	36.6 ± 3.7
N120	22679	0°	1mmPb hole 4mm +Ham	0.422	1.79	2.83 ± 0.28
N100	45182	0°	1mmPb hole 4mm +Ham	0.693	2.44	3.98 ± 0.4
N80	190124	0°	1mmPb hole 4mm +Ham	2.580	7.02	11.6 ± 1.2
N60	513530	0°	1mmPb hole 4mm +Ham	10.21	20.3	31.3 ± 3.1
N40	700253	0°	1mmPb hole 4mm +Ham	46.27	40.4	51.6 ± 5.2
N120	20720	30°	1mmPb hole 4mm +Ham	0.422	1.83	2.87 ± 0.3
N80	174153	30°	1mmPb hole 4mm +Ham	2.580	7.74	12.7 ± 1.3
N40	649333	30°	1mmPb hole 4mm +Ham	46.27	30.2	37.7 ± 3.8
N120	20207	60°	1mmPb hole 4mm +Ham	0.422	1.72	2.60 ± 0.3
N80	162441	60°	1mmPb hole 4mm +Ham	2.580	6.88	10.6 ± 1.1
N40	661755	60°	1mmPb hole 4mm +Ham	46.27	23.8	27.4 ± 2.7

Table 9-4 - From left to right: beam type, measured counts by dosimetric unit, irradiation angle, filter type, ratio of delivered air kerma by monitor unit, delivered kerma in air, $H_p(3)$. Relative uncertainties ~ 10% (related to feedback resistor unc. 10%).

By identifying the “response” of the unit detector+filter with the total number of detected pulses, it was possible to build the different following tables. The $H_p(3, \alpha)$ response, R, is the ratio between the detected counts by the dosimeter and the delivered $H_p(3, \alpha)$ during that specific measurement. With the proper choice of R_{ref} it was finally possible to get the relative response (R/R_{ref}) in the energy intervals, according to the IEC 62387 constraints.

About the choice of R_{ref} : all response values are normalized to the reference radiation quality (in this work N100 is the arbitrary choice) at 0° angle of radiation incidence (Table 9-5, Table 9-6, Table 9-7, Table 9-8, H. Stadtmann 2014).

All irradiations were made at 0° of radiation incidence angle and in addition, for the prototype dosimeter covered by 1 mm Pb with a 4 mm diameter hole showing the best compliance with the limits of IEC 62387, two additional directions of radiation incidence for an angle of 30° and 60° were tested (the left orientation is also equivalent to the right one due to the dosimeter and phantom symmetry).

Beam	Angle (°)	R H _p (3) response (counts/μSv)	R _{ref} Reference response (counts/μSv)	R/ R _{ref} Relative response
N120	0	18444.1	23668.9	0.78
N100	0	23668.9		1.00
N80	0	37618.0		1.59
N60	0	59929.5		2.53
N40	0	108309		4.58

Table 9-5 - Results of type testing of bare dosimetric unit (N100 chosen like R_{ref}). Relative standard uncertainties~ 10%.

Beam	Angle (°)	R H _p (3) response (counts/μSv)	R _{ref} Reference response (counts/μSv)	R/ R _{ref} Relative response
N120	0	7045.07	9066.32	0.78
N100	0	9066.32		1
N80	0	13226.6		1.46
N60	0	13630.8		1.50
N40	0	6625.82		0.73

Table 9-6 - Results of type testing of dosimetric unit covered by 1 mm Pb (N100 chosen like R_{ref}). Relative standard uncertainties~ 10%.

Beam	Angle (°)	R H _p (3) response (counts/μSv)	R _{ref} Reference response (counts/μSv)	R/ R _{ref} Relative response
N120	0	6864.9	9332.95	0.74
N100	0	9332.95		1
N80	0	12669.2		1.36
N60	0	12910.8		1.38
N40	0	6634.22		0.71

Table 9-7 - Results of type testing of dosimetric unit covered by 1 mm Pb + 0.4 mm Cu (N100 chosen like R_{ref}). Relative standard uncertainties~ 10%.

Beam	Angle (°)	R H _p (3) response (counts/μSv)	R _{ref} Reference response (counts/μSv)	R/ R _{ref} Relative response
N120	0	8010.13	11356.4	0.71
	30	7211.71		0.64
	60	7785.93		0.69
N100	0	11356.4		1.00
N80	0	16323.7		1.44
	30	13711.8		1.21
	60	15320.8		1.35
N60	0	16418.8		1.45
N40	0	13556.5		1.19
	30	17201.9		1.51
	60	24173.1		2.13

Table 9-8 - Results of type testing of dosimetric unit covered by 1 mm Pb with a 4 mm diameter hole (N100 chosen like R_{ref}).
Relative standard uncertainties~ 10%.

In Figure 9.14 the response values (ratio of detector counts to the delivered H_p(3)) of the different irradiated prototypes are given for each beam. It is possible to see that the metallic filters produce a flattening in the response profile while the bare sensor, according to silicon behaviour, shows a big variability: over response at low energies and under response at high energies.

Figure 9.15 shows the same trends as before but the values are normalized with a reference condition (R_{ref}) in order to fit the limits range foreseen by IEC 62387. The depicted uncertainty bars are the values standard deviations. The bare detector curve is not depicted due to the too wide variability (clearly outside the IEC 62387 limits) which would modify the graph scale. In Figure 9.16 the relative response values and the corresponding standard deviation (indicated as uncertainty bar) of the prototype filtered by 1 mm Pb with 4 mm diameter hole is drawn together with its angular results. This combination of results for different radiation qualities (representing the energy response) and different irradiation directions (representing the angular response) was called “combined energy and angular response” (H. Stadtmann 2014). In order to compare the results with the requirements laid down in the international standard (IEC 62387 2012), the corresponding response limits for angle and energy dependence are marked in addition in the diagrams (red lines in the following figures).

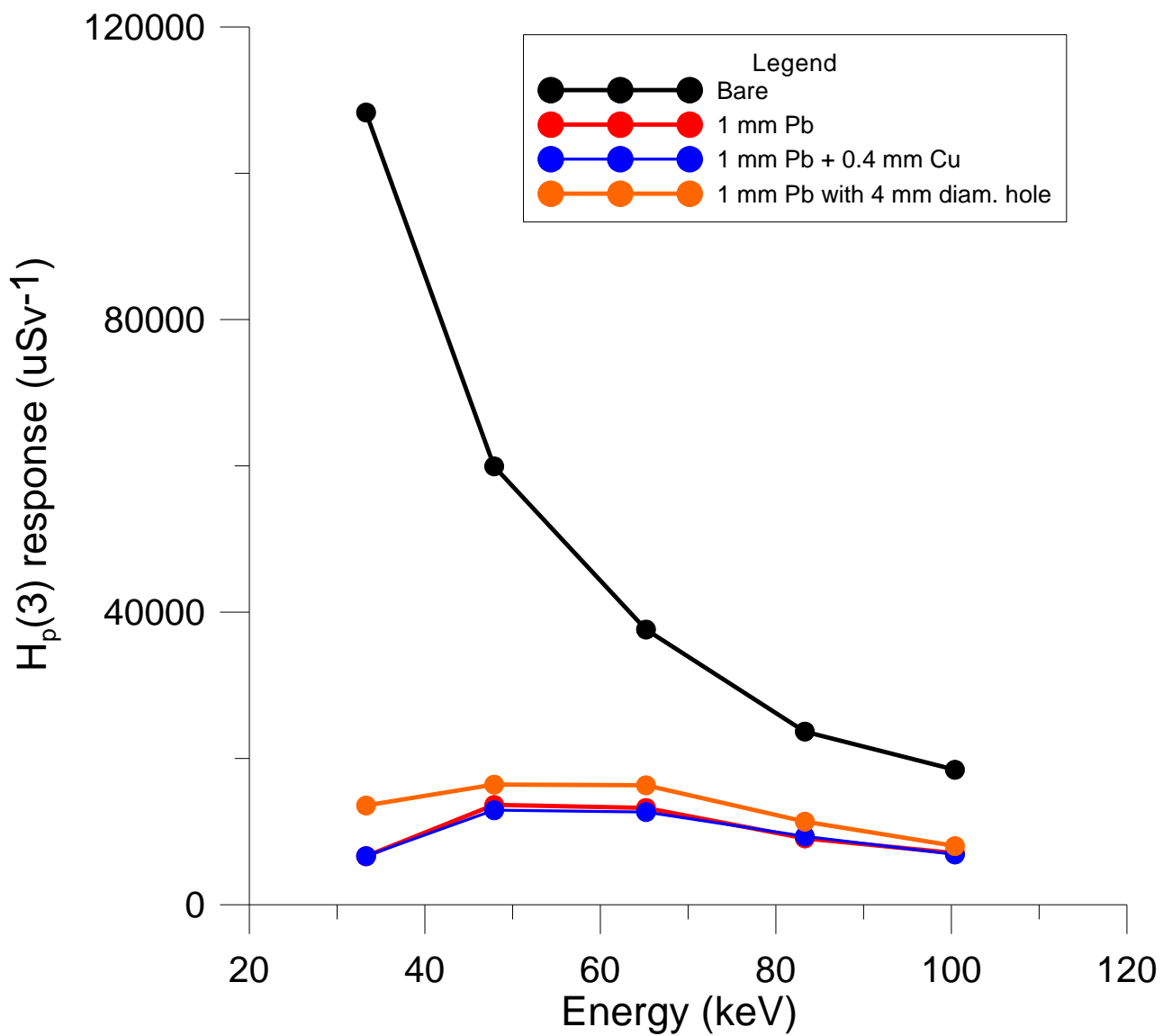


Figure 9.14 - Energy responses of the different prototypes. It is possible to see the flattening profile due to the metallic filters. The bare sensor profile shows a big variability: over response at low energies and under response at high energies. Relative standard uncertainties ~ 10%.

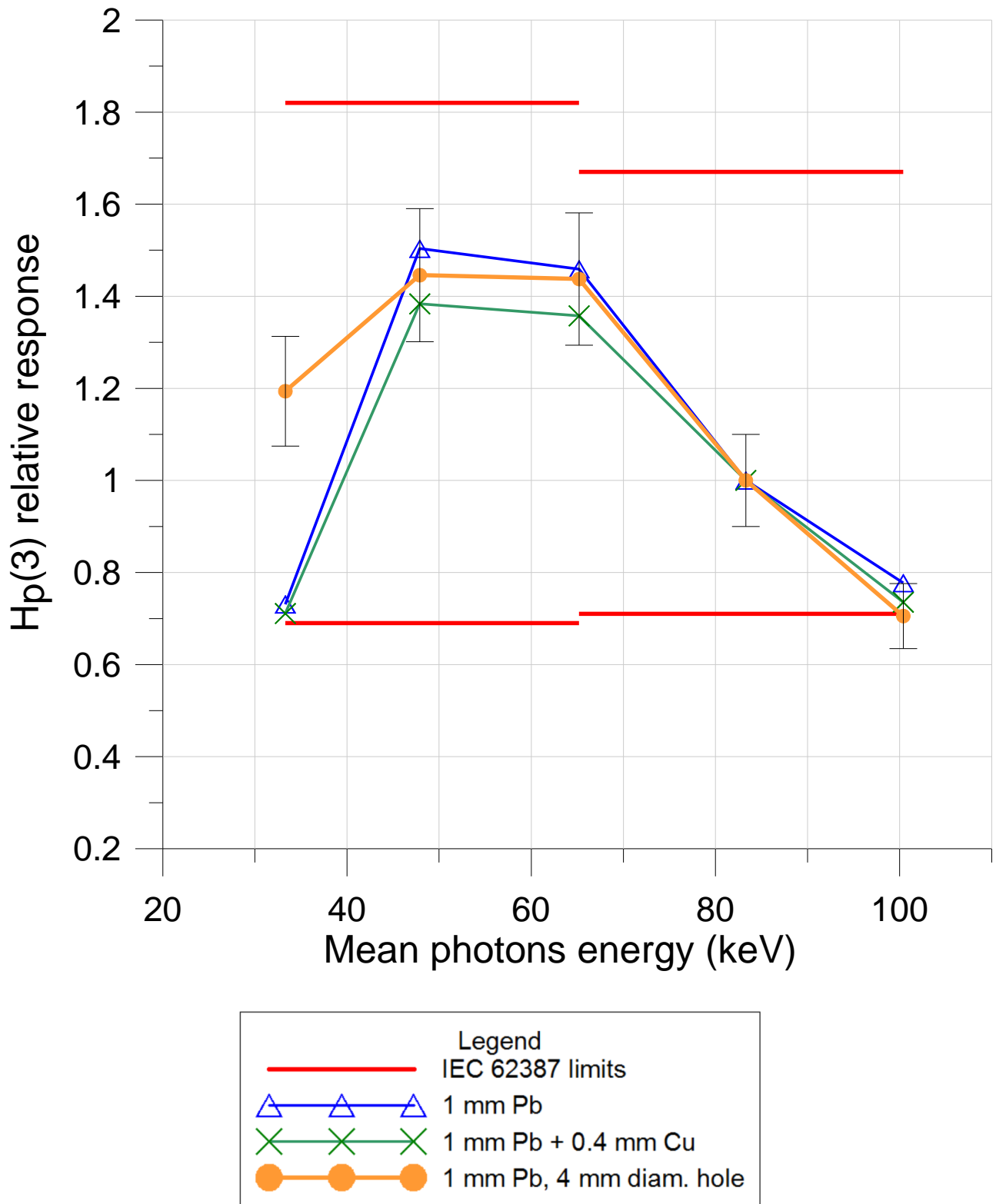


Figure 9.15 - Energy relative responses at 0° of angular incidence for every prototype. All the results fulfil the IEC 62387 limits. Relative standard uncertainties ~ 10%.

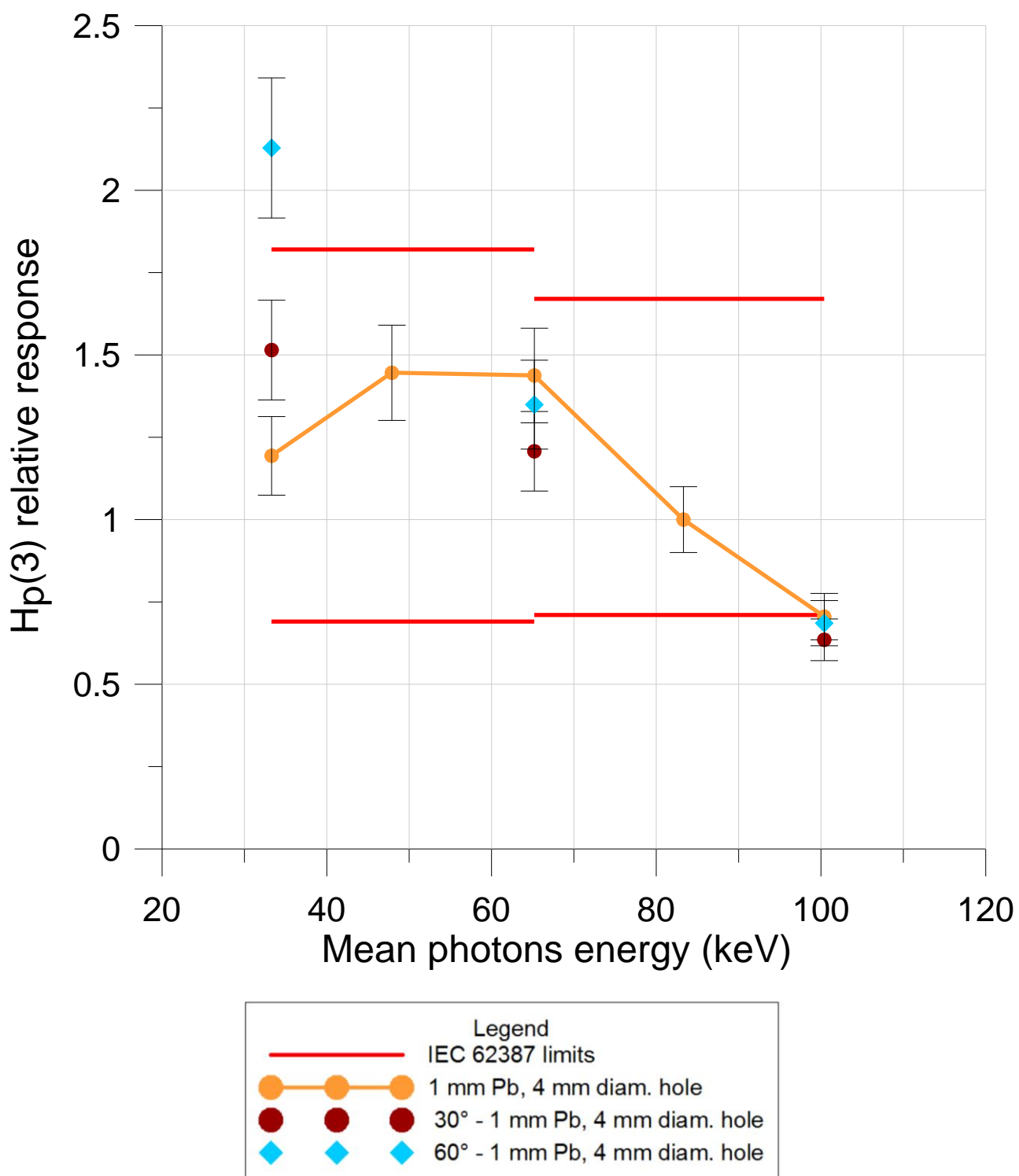


Figure 9.16 - Measured combined energy and angular response for the best resulting eye lens dosimeter prototype (1 mm Pb 4 mm diameter hole due to the low values) calibrated on the cylinder head phantom in terms of personal dose equivalent $H_p(3)$ (relative standard uncertainties ~ 10%).

9.7 Concluding remarks about energy and angular response of the prototype

The energy responses of all the different filters paired with the detector fulfil the requirements of IEC 62387 (IEC 62387 2012) in the diagnostic energy range from about 30 keV to about 100 keV. The intrinsic energy response of the silicon detector (bare detector in the legend) lead to an over response at low photon energies and an under response at high energy regions for the bare dosimeter prototype (silicon response decreasing with the energy growth, Figure 9.12). The filters allow to flatten this intrinsic energy response by mitigating the important over response of silicon at low energies. The behaviour of filter is clearly shown in Figure 9.17: N40 spectrum is substantially depressed in comparison to what happens in the case of N120. In addition, it can be possible to see the effect of the Pb K edge - about 88 keV, (J. P. McCaffrey February 2007) - in N120 spectrum (Figure 9.18) and to see the softly mitigation of the holed Pb filter respect to the full Pb filter in N40 spectrum of Figure 9.17.

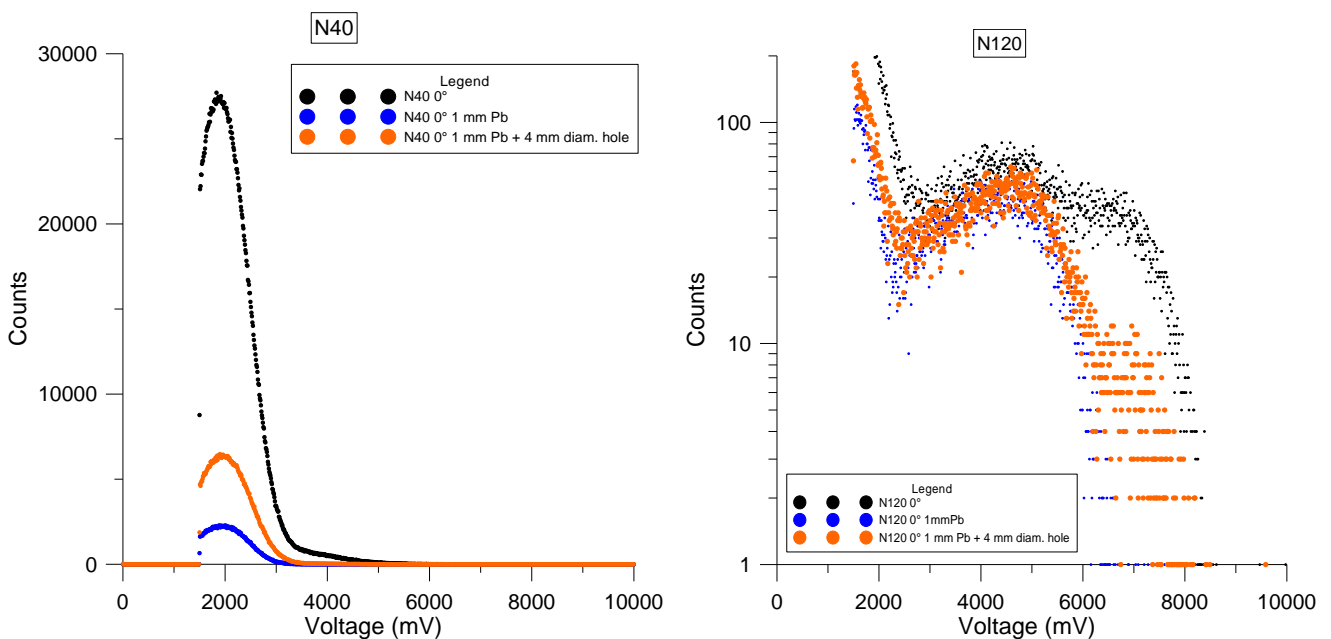


Figure 9.17 – Comparison between unfiltered and some filtered dosimeter prototype in the case of N40 (left) and N120 (right) spectra. The lead hardly suppresses the response at low energies (N40) and softly attenuates the response of silicon at high energies (N120), where the intrinsic response is yet weak. Considering the 4 mm diameter in the 1 mm Pb filter, the mitigation in suppression at the low energy region is clearly visible in the N40 orange curve.

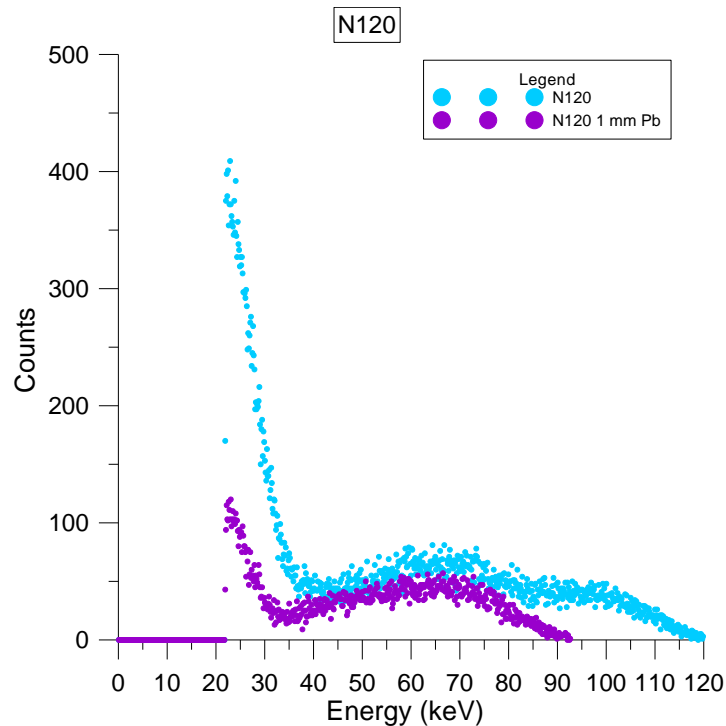


Figure 9.18 - N120 spectrum: comparison between a filtered (1mm Pb) and bare prototype (same irradiation time, 120 s, and same distance, 2.5 m). It is possible to see the cut in the response (violet curve) at about 88 keV due to the K edge of lead (J. P. McCaffrey February 2007).

The only way to optimize the energy response with respect to the given response limits from IEC 62387 2012 was the choice of an appropriate reference radiation energy.

This mean photons energy of 83 keV as reference energy (for this energy the response is, per definition, one), which is the average photons energy of the X-ray radiation quality N100, leads to an optimised dosimeter response within the energy response limits. The dosimetric prototype showing the minor variability (27% as percentual standard deviation, see Table 9-9) is the one coupled with 1 mm Pb with a 4 mm diameter hole in its center. The hole in the filter allows to softly mitigate, respect to the homogenous filters, the depression of silicon response at low energies due to the metallic filter.

Regarding the angular response, the results are good but some points are out of the response limits: N120 - 30°, 60° and N40 - 60°. It is worth noting that a more exhaustive study of the angular response is needed to further understand this problem. Probably it could be necessary a properly shaped filter, maybe like a dome, in order to improve the angular response of this eye lens dosimeter prototype based on active detector.

Dosimetric unit	Mean energy (keV)	Relative response R/Rref	Standard deviation σ	Mean μ	σ/μ
Hamamatsu + 1 mm Pb	100.4	0.78	0.37	1.09	34%
	83.3	1.00			
	65.2	1.46			
	47.9	1.50			
	33.3	0.73			
Hamamatsu + 1mmPb + 0.4 mm Cu	100.4	0.74	0.32	1.04	31%
	83.3	1.00			
	65.2	1.36			
	47.9	1.38			
	33.3	0.71			
Hamamatsu + 1 mm Pb, 4 mm diam. hole	100.4	0.71	0.31	1.16	27%
	83.3	1.00			
	65.2	1.44			
	47.9	1.45			
	33.3	1.19			

Table 9-9 - Synthesis of the results from type testing of different eye lens dosimeter prototypes.
The percentual standard deviation is shown in the last column.

The results of this dosimeter development show that it is possible to measure the dose quantity $H_p(3)$ with a silicon-based dosimeter covered by a proper filter. This feasibility study confirms the possibility to measure $H_p(3)$ with an active dosimeter: this represents the most suitable approach for an accurate dose assessment in real time. With a certain elaboration of the information, it could be also possible to set alarms at dose or dose rate level. The filter allows to flatten the detector response and to fulfil the requirements given in IEC 62387 2012 with a good choice as reference energy. Further investigations on the best shape for improving the filter angular response need to be carried out as possible next development.

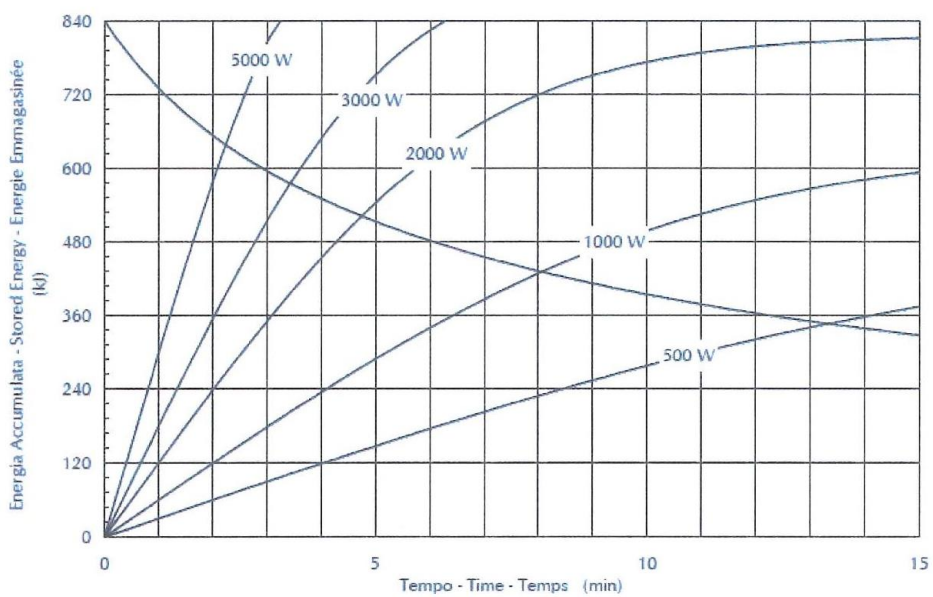
10.1 RTC 1000 HS 0.6/1.2 X-ray tube



Documentazione Tubo a raggi X
Tube Documentation
Documentation du Tube

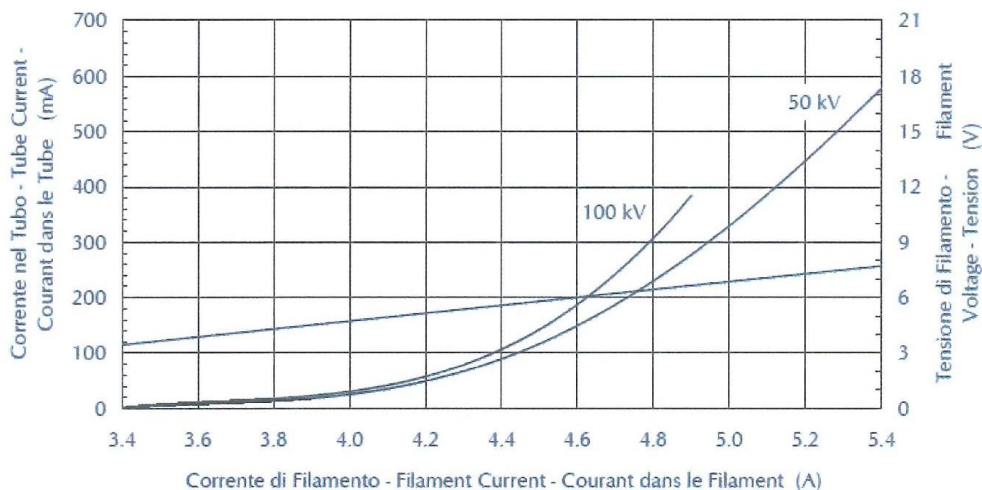
RTC 1000 HS 0.6/1.2

Curve di riscaldamento e raffreddamento dell'anodo
Anode heating and cooling curves
Courbes d'échauffement et de refroidissement de l'anode

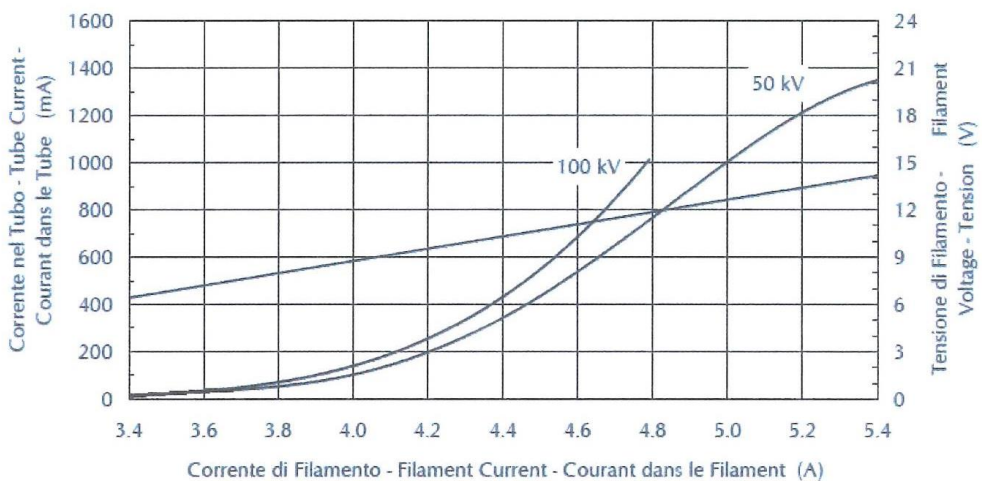




Caratteristica di emissione del catodo
Cathode emission characteristic
Caractéristique d'émission de la cathode
■ 0.6 - 3 ~ - (± 0.2 A)



Caratteristica di emissione del catodo
Cathode emission characteristic
Caractéristique d'émission de la cathode
■ 1.2 - 3 ~ - (± 0.2 A)





Caratteristiche - Specifications - Spécifications

Macchie focali Focal spot Foyer	☐ 0.6 ■ 1.2	(IEC 336, EN 60336)
Velocità di rotazione dell'anodo Anode speed Vitesse de l'anode	3000 min ⁻¹ 10000 min ⁻¹	
Potenza anodica nominale Nominal anode input power Puissance anodique nominale	☐ 26 kW 40 kW ■ 63 kW 100 kW	(IEC 613, EN 60613)
Diametro anodico Anode diameter Diamètre de l'anode	110 mm	
Materiale anodico Anode material Matériau de l'anode	RT-TZM-C	
Angolo anodico Anode angle Pente de l'anode	13°	
Campo di radiazione Radiation field Champ de rayonnement	a 70 cm 32 cm a 100 cm 45 cm	
Filtrazione inerente Inherent filtration Filtration inhérente	0.7 mm Al eq	(IEC 522)
Capacità termica anodica Maximum anode heat content Chaleur maximale accumulée dans l'anode	840 kJ 1120 kHU	
Dissipazione termica continua Continuous heat dissipation Dissipation thermique continue	1200 W 96 000 HU/min	
Dissipazione termica massima Maximum heat dissipation Dissipation thermique maximale	2000 W 160 000 HU/min	
Alta tensione nominale Nominal X-ray tube voltage Haute tension nominale	150 kV	
Massima corrente di filamento Max. filament current Courant dans le filament max.	5.4 A	

I dati forniti nella presente documentazione si intendono riferiti a:

The data indicated in this documentation refer to:

Les données indiquées dans cette documentation sont calculées pour:

Potenza anodica di equilibrio termico
Equivalent anode input power
Puissance anodique d'équilibre thermique

300 W = % della capacità termica anodica
% of maximum anode heat content
% de chaleur max. accumulée dans l'anode

48%

10.2 TZM properties



[ABOUT US](#) [MATERIALS](#) [PRODUCT CATEGORY](#) [NEWS](#) [CONTACT US](#)

TZM and Molybdenum , Molybdenum is similar to tungsten, with a melting point of 2,620 °C (4,753oF), slightly lower than tungsten.

The elongation capacity is better than tungsten, so it is more suitable for producing thin wires. Molybdenum is transformed into TZM by using small amounts of extremely thin carbides, containing more than 99.2% up to 99.5% of Mo, 0.50% and 0.08% of titanium, zirconium and carbide.

TZM is more resistant to pure molybdenum and has a higher re-crystallisation temperature and better sliding resistance. The recommended operating temperatures are between 700 and 1 400 ° C.TZM is used in high temperature applications involving strong mechanical stresses, for example in forging tools.

For its features such as high resistance at high temperatures and good thermal conductivity, the TZM alloy is used to produce mould parts for gravity casting and die casting of aluminum castings or those subject to erosion by liquid metal . TZM matrices are also used in the extrusion of Copper alloys.

Chemical and physical characteristics:

Melting point: 2620 ° C

Density: 10.15 g / cm³

Coeff. Of dilation:

At 20 ° C 6.0 m / m ° C

At 1000 ° C 5.8 m / m ° C

At 1500 ° C 6.5 m / m ° C

Thermal conductivity:

At 20 ° C 125 w / m ° C

At 1000 ° C 95 w / m ° C

At 1500 ° C 85 w / m ° C

Tensile strength: 590-790 MPa

Hardness: 230-320 DPH10

Elongation: 5-15%



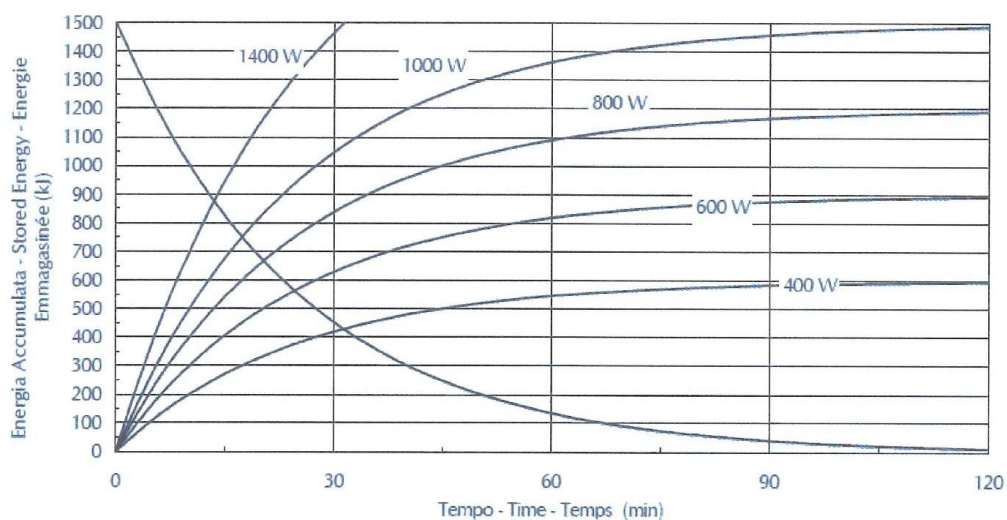
Caratteristiche - Specifications - Spécifications

Lunghezza totale Overall length Longueur totale	524 mm		
Diametro massimo Max. diameter Diamètre maximal	190 mm		
Peso netto del complesso tubo-guaina Tube assembly net weight Poids net de la gaine équipée	29 kg		
Limiti di temperatura per il trasporto e lo stoccaggio Temperature limits for transportation and storage Limites de température pour le transport et le stockage	-10°C + +80°C		
Limiti di umidità per il trasporto e lo stoccaggio Humidity limits for transportation and storage Limites d'humidité pour le transport et le stockage	max. 80%		
Alta tensione nominale Nominal X-Ray tube assembly voltage Haute tension nominale de la gaine équipée	150 kV		
Alta tensione verso massa High voltage to ground Haute tension par rapport à la masse	± 75 kV		
Massima energia accumulabile nel complesso tubo-guaina Maximum tube assembly heat content Chaleur maximale retenue dans la gaine équipée	1500 kJ	2000 kHU	
Dissipazione termica continua massima Maximum continuous heat dissipation Dissipation thermique continue maximale	1000 W	80000 HU/min	
Minima filtrazione inerente nel complesso tubo-guaina Min. tube assembly inherent filtration Min. filtration inhérente de la gaine équipée	1.2 mm Al / 75 kV		IEC 522
Filtrazione addizionale Additional filtration Filtration additionnelle	0.3 mm Al		
Filtrazione totale minima Min. total filtration Min. filtration totale	1.5 mm Al eq		
Fattori di carico per la misura della radiazione di fuga Loading factor for leakage radiation determination Paramètres de charge pour la mesure du rayonnement de fuite	150 kV 7.5 mA		IEC 601.1.3 EN 60601.1.3
Radiazioni di fuga massima a 1 metro dalle macchie focali Maximum leakage radiation at 1 m from focal spots Rayonnement de fuite maximal à 1 m du foyer	0.44 mGy/h (50 mR/h)		

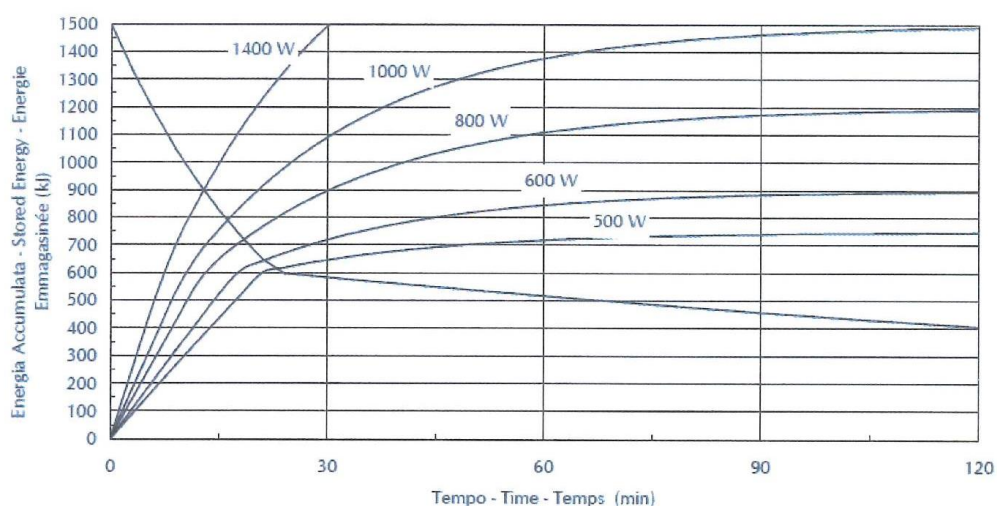


Curve di riscaldamento e raffreddamento della cuffia
Tube-assembly heating and cooling curves
Courbes d'échauffement et refroidissement de la gaine équipée

Ventilatori in funzionamento continuo / Continuously operated fans / Ventilation continueue

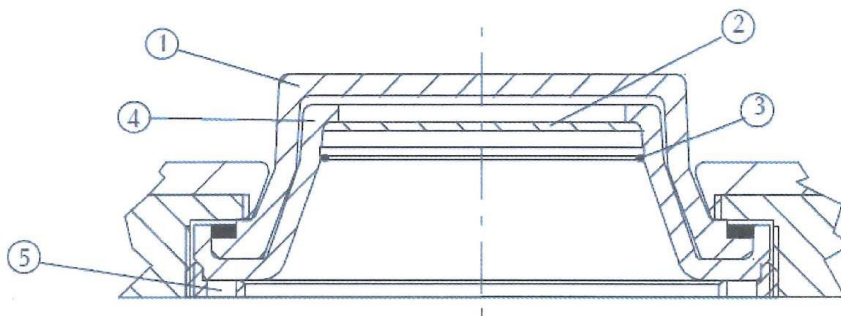


Ventilatori con soglia di intervento / Thermally switched fans / Ventilation intermittente



Massa	Ground terminal	Borne de masse	A
Termostato esterno normalmente chiuso 5 A, 50 V DC 4 A, 250 V AC apre a: 67° C ± 4° C	External thermal switch, normally closed 5 A, 50 V DC 4 A, 250 V AC opens at: 67° C ± 4° C	Sécurité thermique externe, contact fermé au repos 5 A, 50 V DC 4 A, 250 V AC ouvre à: 67° C ± 4° C	B
Termostato interno normalmente chiuso apre a: 80° C ± 4° C	Internal thermal switch, normally closed opens at: 80° C ± 4° C	Sécurité thermique interne, contact fermé au repos ouvre à: 80° C ± 4° C	C
Interruttore polmone 15 A, 125/250 V AC 0.6 A, 125 V DC	Expansions bellow switch 15 A, 125/250 V AC 0.6 A, 125 V DC	Interrupteur de la vessie 15 A, 125/250 V AC 0.6 A, 125 V DC	D
Termostato ventilatore normalmente aperto 4 A, 250 V AC chiude a: 43° C ± 3° C	Fan thermal switch, normally open 4 A, 250 V AC close at: 43° C ± 3° C	Interrupteur thermique contact ouvert au repos 4 A, 250 V AC ferme a: 43° C ± 3° C	E
Pompe 0.11 A, 220 V AC	Pumps 0.11 A, 220 V AC	Pompes 0.11 A, 220 V AC	-
Ventilatori 0.16 A, 220 V AC	Fans 0.16 A, 220 V AC	Ventilateurs 0.16 A, 220 V AC	F

Modifiche alla filtrazione - Modification of filtration - Modification de la filtration



Finestra	Tube-housing window	Fenêtre de la gaine	1
Filtro 0.3 mm Al	Filter 0.3 mm Al	Filtre 0.3 mm Al	2
Molla di fissaggio filtri	Filter clamp	Ressort de fixation du filtre	3
Piombo finestra	Lead window	Fenêtre de plomb	4
Ghiera di fissaggio finestra e cono (non aprire)	Window nut (do not open)	Bague de serrage de la fenêtre (ne pas ouvrir)	5

10.4 PTW ionization chamber



1 l Spherical chamber Type 32002
 10 l Spherical chamber Type 32003
 Spherical chamber TK30 Type 32005
 Measuring Ranges

4 Measuring Ranges

Using the ionization chambers type 32002, 32003 und 32005 together with a PTW universal dosimeter type UNIDOS results in the following measuring ranges. The resolution of the digital display is better than 0.5% of the measuring ranges given.

Measuring range UNIDOS	Measuring range spherical chamber					
	Type 32002		Type 32003		Type 32005	
Dose						
LOW	50.0 nGy ...	5.5 µGy	6.0 nGy ...	660.0 nGy	2.2 µGy ...	243.7 µGy
HIGH	2.5 µGy ...	550.0 µGy	300.0 nGy ...	66.0 µGy	110.8 µGy ...	24.4 mGy
Dose rate						
LOW	18 µGy/h ...	18 mGy/h	2.2 µGy/h ...	2.2 mGy/h	797.4 µGy/h ...	797.4 mGy/h
MEDIUM	900.0 µGy/h ...	900.0 mGy/h ¹⁾	108.0 µGy/h ...	108.0 mGy/h ²⁾	39.9 mGy/h ...	39.9 Gy/h ³⁾
HIGH	90.0 mGy/h ...	90.0 Gy/h ¹⁾	10.8 mGy/h ...	10.8 Gy/h ²⁾	4.0Gy/h ...	4.0 kGy/h ³⁾

¹⁾ The upper limit of the measuring range for a saturation of 99.0% is 440 mGy/h.

²⁾ The upper limit of the measuring range for a saturation of 99.0% is 25 mGy/h.

³⁾ The upper limit of the measuring range for a saturation of 99.0% is 29.4 Gy/h.

6 Technical Specifications

Only values for which tolerances or limits are specified are guaranteed. Values for which no tolerances are specified are for information only.

Ionization chambers	1 l spherical chamber type 32002	10 l spherical chamber type 32003	spherical chamber TK30 type 32005
Manufacturer	PTW-Freiburg		
Application	Stationary radiation protection measurements (area dose) Dose and dose rate measurements free in air for absolute dosimetry in secondary standard laboratories		
Special construction characteristics	vented		
Measuring quantities	Photon equivalent dose and photon equivalent dose rate Kerma and kerma rate Exposure and exposure rate		
Measuring volume	1000 cm ³	10000 cm ³	27.9 cm ³
Reference point for dose and dose rate	Chamber center		
Chamber dimensions	refer to Figure 7	refer to Figure 8	refer to Figure 9
Response	40 µC/Gy	330 µC/Gy	900 nC/Gy
Chamber voltage	± (300 ... 500) V nominal ± 400 V		± (200 ... 1000) V nominal ± 400 V
Leakage current	≤ ± 10 fA		≤ ± 5 fA
Cable leakage	≤ 1 pC/(Gy·cm) (when using PTW connection cables)		
Maximum dose rate at continuous irradiation at 400 V and 99% saturation	0.42 Gy/h	26 mGy/h	29.4 Gy/h
Maximum dose per irradiation pulse at 400 V and 99% saturation	3.1 µGy	0.8 µGy	26 µGy
Ion collection time at 400 V	37 ms	150 ms	4.5 ms
Polarity effect	≤ ± 1%		
Directional dependence	Preferable direction of radiation is perpendicular to the chamber axis.		
for rotation around the chamber axis	≤ ± 0.5%		≤ ± 0.5%
for tilting of the axis up to ± 45°	≤ ± 5%		≤ ± 3%

Ionization chambers	1 I spherical chamber type 32002	10 I spherical chamber type 32003	spherical chamber TK30 type 32005
Energy dependence	$\leq \pm 4\%$ in the range 40 keV to Co-60 refer to Figure 4	$\leq \pm 3\%$ in the range 40 keV to Co-60 refer to Figure 5	$< \pm 5\%$ in the range A60 (48 keV) to Co-60 related to Co-60 refer to Figure 6
Transient periods for Temperature equilibrium Pressure equilibrium	(2 ... 3) min/K ≤ 10 s		
Pre-irradiation	not required		
Stabilization time	The difference between the response after 15 minutes and 2 hours and the response after 1 hour is less than $\pm 0.5\%$.		
Post irradiation leakage	Signal drop to 1% in 5 s after irradiation		
Long term stability	$< \pm 1\%$	$\leq \pm 1\%$	$\leq \pm 0,5\%$
Wall material and thickness	3.0 mm POM (CH ₂ O) _N	2.75 mm POM (CH ₂ O) _N	3.0 mm POM (CH ₂ O) _N graphite coated
Area density	453 mg/cm ³	417 mg/cm ³	453 mg/cm ³
Electrode material	PS graphite coated		PMMA graphite coated
Nominal ambient conditions Energy Temperature Humidity Atmospheric pressure	Photons 25 keV ... 50 MeV (5 ... 40) °C (10 ... 85) % relative humidity; not exceeding 20 g/m ³ (700 ... 1060) hPa		
Environmental conditions for transport and storage Temperature Humidity Atmospheric pressure	(- 20 ... + 60) °C (10 ... 80) %, no condensation (max. 20 g/m ³ absolute humidity) (600 ... 1200) hPa		
Connecting systems	PTW-M system BNT or TNC Triax-connectors		

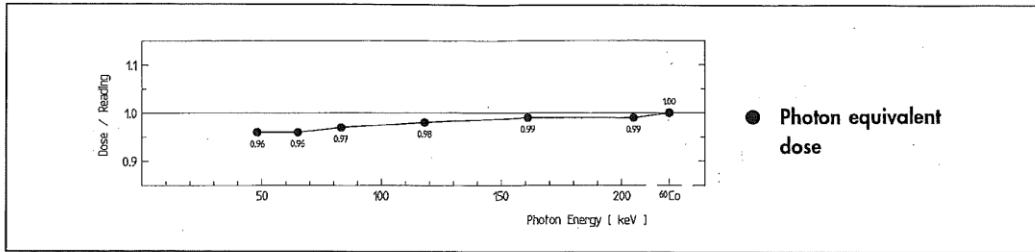


Figure 4: Energy dependence type 32002

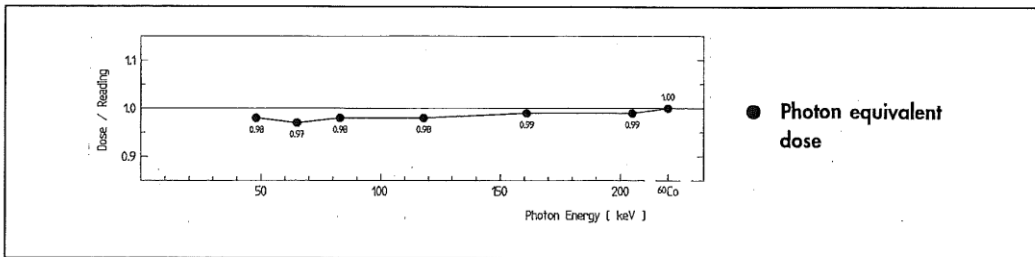


Figure 5: Energy dependence type 32003

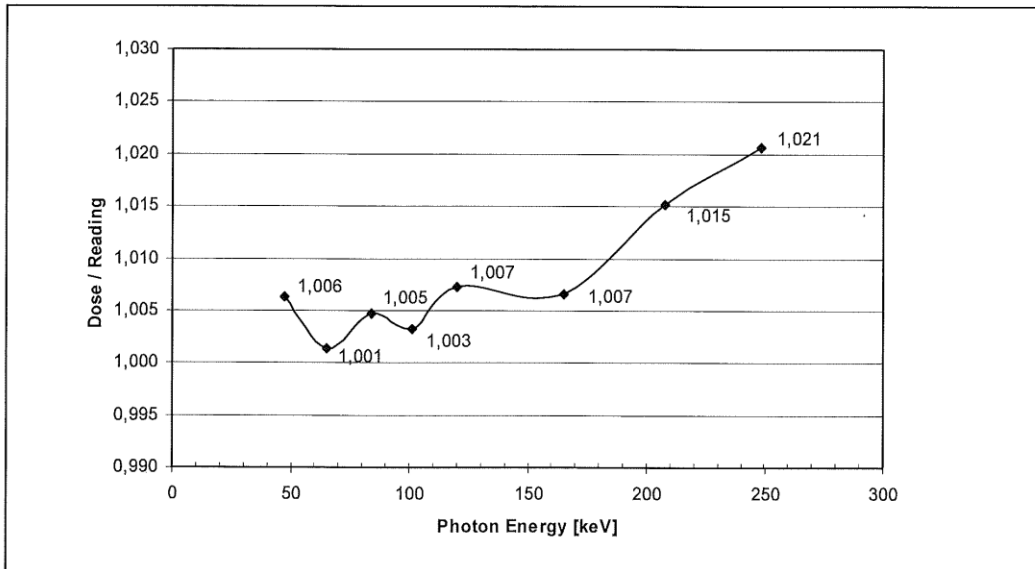


Figure 6: Energy dependence type 32005 referring to ⁶⁰Co

1 l Spherical chamber Type 32002
 10 l Spherical chamber Type 32003
 Spherical chamber TK30 Type 32005
 Technical Specifications

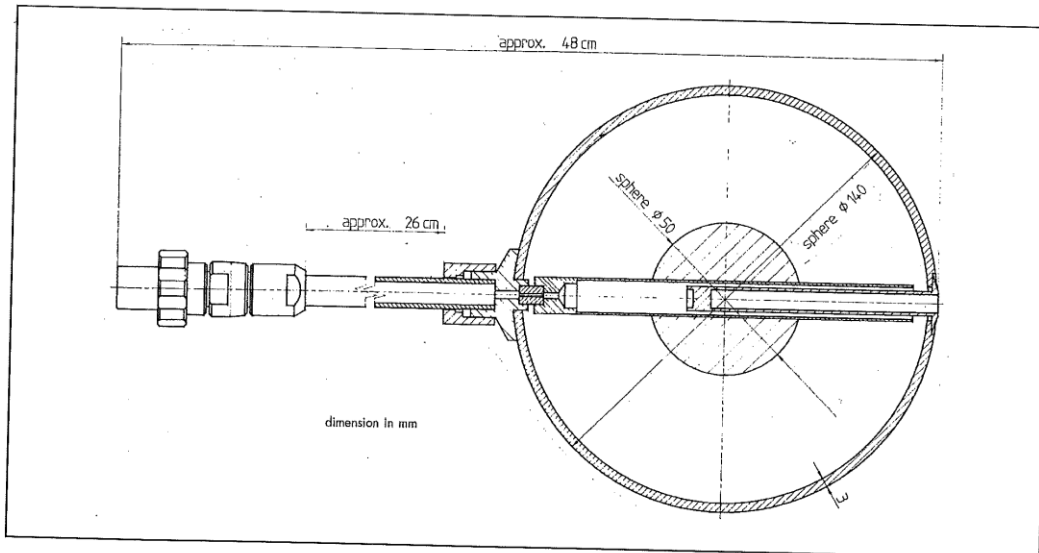


Figure 7: Spherical chamber type 32002 (dimensions in mm)

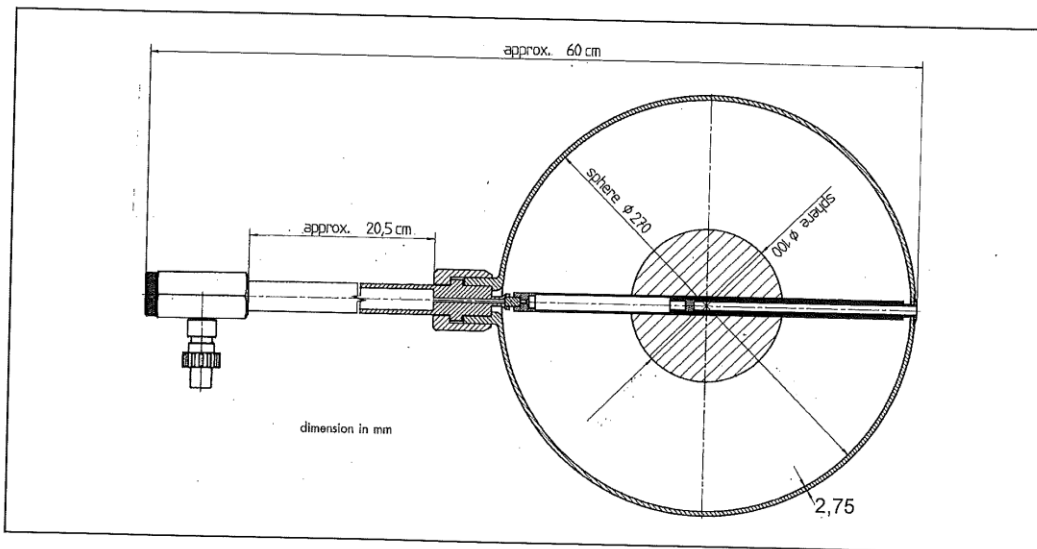


Figure 8: Spherical chamber type 32003 (dimensions in mm)

10.5 PTW calibration certificate

CALIBRATION CERTIFICATE
No. 1601743



PTW-Freiburg, Lorracher Str. 7, 79115 Freiburg, Germany ☎ +49 (0)761-49055-0 FAX +49 (0)761-49055-70 E-Mail info@ptw.de

Calibration Object

Radiation Detector

Detector **[REF] TW32002 [SN] 000591**
Detector Type Ionization Chamber

Manufacturer PTW-Freiburg
Customer Tema Sinergie S.p.A Order No. : AU1601316
Via Malpighi, 120 Order Date : 2016-04-22
I-48018 Faenza (RA)

Calibration Results

Measuring Quantity Air Kerma (K_{air})
Detector Calibration Factor $N_K = 2.448 \cdot 10^4 \text{ Gy / C}$

Beam Quality Correction	Beam Quality	Correction Factor k_Q	Uncertainty
	^{60}Co	1.000	2.5 %

Reference Conditions
 Beam Quality: ^{60}Co
 Temperature: 293.2 K (20°C)
 Air Pressure: 1013.25 hPa
 Relative Humidity: 50%
 Chamber Voltage/Polarity: + 400 V
 Ion Collection Efficiency: 100 %

Calibration Date **2016-04-27**
Recalibration Interval 2 years (recommended)

Freiburg, 2016-04-27
 PTW-Freiburg
 Physikalisch-Technische
 Werkstätten Dr. Pöchlau GmbH

 (Signature)

Calibration Conditions and Set-up

Climatic Conditions	Temperature Range:	(294.2 ± 3) K / (21 ± 3) °C			
	Air Pressure Range:	(1000 ± 50) hPa			
	Rel. Humidity Range:	(40 ± 20) %			
Beam Quality and Geometry	Quality	Filter [mm]	HVL [mm]	SDD [cm]	Size [cm]
	⁶⁰ Co	-	-	300	28 x 28
	Quality:	Beam qualities according to ISO 4037-1 (ISO: N-xxx = PTB: Axxx, e.g. N-100 = A100)			
	Filter:	Total filtration (inherent and additional filters)			
	HVL:	Half value layer at the point of measurement			
	SDD:	Distance between radiation source and reference point			
	Size:	Field size at reference point, diam. = Field Diameter			
Detector Arrangement	Chamber axis perpendicular to radiation beam axis Line on chamber stem faced towards the radiation source Reference point position at stated measuring depth / distance to the radiation source (For further information see manual and data sheet of detector.)				
Dose and Dose Rate	Air kerma :	min.: 5.0 · 10 ⁻³ Gy / max.: 5.0 Gy			
	Air kerma rate :	min.: 0.01 mGy/min / max.: 300 mGy/min			
Saturation Correction Factor	k _S =	1.000			
Leakage	Negligible during calibration				

Remarks

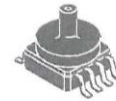
- The uncertainty stated corresponds to the double standard deviation (k=2). The standard deviation was calculated according to ISO GUM from the partial uncertainties arising from the standard used, the calibration procedure, the environmental conditions and short time effects of the object of measurement. The uncertainties stated are composed of the uncertainties of the calibration procedure and those of the specimen during calibration. A share for the long-term instability of the object under calibration is not included.
- The calibration is traceable to national standards of the German National Laboratory, PTB, Braunschweig. This calibration certificate may not be reproduced other than in full except with the permission of the issuing laboratory. This certificate is valid only with the ionization chamber showing the intact sticker with the certificate number. Calibration factors of chambers having been opened for repair are not comparable to previous calibrations. Calibration certificates without signature are not valid.
- The calibration object fully complies with the respective specifications given in the data sheet and user manual.

Media Resistant, Integrated Silicon Pressure Sensor for Manifold Absolute Pressure, Altimeter or Barometer Applications On-Chip Signal Conditioned, Temperature Compensated, and Calibrated

MPXAZ4115A SERIES

INTEGRATED PRESSURE SENSOR
15 to 115 kPa (2.2 to 16.7 psi)
0.2 to 4.8 V Output

SMALL OUTLINE PACKAGE



MPXAZ4115AC6U
CASE 482A



MPXAZ4115A6U
CASE 482

PIN NUMBER

1	N/C	5	N/C
2	V _S	6	N/C
3	Gnd	7	N/C
4	V _{OUT}	8	N/C

NOTE: Pins 1, 5, 6, 7, and 8 are not device connections. Do not connect to external circuitry or ground. Pin 1 is noted by the notch in the lead.

Motorola's MPXAZ4115A series sensor integrates on-chip, bipolar op amp circuitry and thin film resistor networks to provide a high output signal and temperature compensation. The small form factor and high reliability of on-chip integration make the Motorola pressure sensor a logical and economical choice for the system designer.

The MPXAZ4115A series piezoresistive transducer is a state-of-the-art, monolithic, signal conditioned, silicon pressure sensor. This sensor combines advanced micromachining techniques, thin film metallization, and bipolar semiconductor processing to provide an accurate, high level analog output signal that is proportional to applied pressure.

Figure 1 shows a block diagram of the internal circuitry integrated on a pressure sensor chip.

Features

- Resistant to high humidity and common automotive media
- 1.5% Maximum Error over 0° to 85°C
- Ideally suited for Microprocessor or Microcontroller-Based Systems
- Temperature Compensated from -40° to +125°C
- Durable Thermoplastic (PPS) Surface Mount Package

Application Examples

- Aviation Altimeters
- Industrial Controls
- Engine Control
- Weather Stations and Weather Reporting Devices

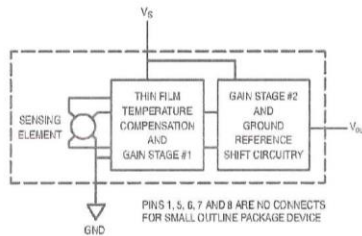


Figure 1. Fully Integrated Pressure Sensor Schematic

Rev 0

© Motorola, Inc. 2001

For More Information On This Product,
Go to: www.freescale.com



MPXAZ4115A SERIES Freescale Semiconductor, Inc.
 ARCHIVED BY FREESCALE SEMICONDUCTOR, INC. 2005

MAXIMUM RATINGS(NOTE)

Parametric	Symbol	Value	Units
Maximum Pressure (P1 > P2)	P _{max}	400	kPa
Storage Temperature	T _{stg}	-40° to +125°	°C
Operating Temperature	T _A	-40° to +125°	°C

NOTE: Exposure beyond the specified limits may cause permanent damage or degradation to the device.

OPERATING CHARACTERISTICS (V_S = 5.1 Vdc, T_A = 25°C unless otherwise noted, P1 > P2. Decoupling circuit shown in Figure 3 required to meet Electrical Specifications.)

Characteristic	Symbol	Min	Typ	Max	Unit
Pressure Range	P _{OP}	15	—	115	kPa
Supply Voltage ⁽¹⁾	V _S	4.85	5.1	5.35	Vdc
Supply Current	I ₀	—	7.0	10	mAdc
Minimum Pressure Offset ⁽²⁾ @ V _S = 5.1 Volts	V _{off}	0.135	0.204	0.273	Vdc
Full Scale Output ⁽³⁾ @ V _S = 5.1 Volts	V _{FSD}	4.725	4.794	4.863	Vdc
Full Scale Span ⁽⁴⁾ @ V _S = 5.1 Volts	V _{FSS}	4.521	4.590	4.659	Vdc
Accuracy ⁽⁵⁾	—	—	—	±1.5	%V _{FSS}
Sensitivity	V/P	—	45.9	—	mV/kPa
Response Time ⁽⁶⁾	t _R	—	1.0	—	ms
Output Source Current at Full Scale Output	I _{OS}	—	0.1	—	mAdc
Warm-Up Time ⁽⁷⁾	—	—	20	—	ms
Offset Stability ⁽⁸⁾	—	—	±0.5	—	%V _{FSS}

NOTES:

- Device is ratiometric within this specified excitation range.
- Offset (V_{off}) is defined as the output voltage at the minimum rated pressure.
- Full Scale Output (V_{FSD}) is defined as the output voltage at the maximum or full rated pressure.
- Full Scale Span (V_{FSS}) is defined as the algebraic difference between the output voltage at full rated pressure and the output voltage at the minimum rated pressure.
- Accuracy is the deviation in actual output from nominal output over the entire pressure range and temperature range as a percent of span at 25°C due to all sources of error including the following:
 - Linearity: Output deviation from a straight line relationship with pressure over the specified pressure range.
 - Temperature Hysteresis: Output deviation at any temperature within the operating temperature range, after the temperature is cycled to and from the minimum or maximum operating temperature points, with zero differential pressure applied.
 - Pressure Hysteresis: Output deviation at any pressure within the specified range, when this pressure is cycled to and from minimum or maximum rated pressure at 25°C.
 - TcSpan: Output deviation over the temperature range of 0° to 85°C, relative to 25°C.
 - TcOffset: Output deviation with minimum pressure applied, over the temperature range of 0° to 85°C, relative to 25°C.
- Response Time is defined as the time for the incremental change in the output to go from 10% to 90% of its final value when subjected to a specified step change in pressure.
- Warm-up Time is defined as the time required for the product to meet the specified output voltage after the pressure has been stabilized.
- Offset Stability is the product's output deviation when subjected to 1000 cycles of Pulsed Pressure, Temperature Cycling with Bias Test.



TSic™ 301/306

Easy to integrate, low power temperature sensor IC

1/4



The Product

The TSic™ series of temperature sensor ICs are specifically designed as a low-power solution for temperature measurement in building automation, medical/pharma technologies, industrial and mobile applications. The TSic™ provides a simple temperature measurement and achieves outstanding accuracy combined with long term stability.

The TSic™ has a high precision bandgap reference with a PTAT (proportional-to-absolute-temperature) output, a low-power and high-precision ADC and an on-chip DSP core with an EEPROM for the precisely calibrated output signal. The TSic™ temperature sensor is fully calibrated, meaning no further calibration effort is required by the customer. With an accuracy of $\pm 0.3K$ in a range of 80K (e.g. 10°C to 90°C), the sensor is more accurate than a class F0.3 (DIN EN 60751) platinum sensor. Extended long wires (> 10m) will not influence the accuracy.

The TSic™ is available as digital (ZacWire, TSic™ x06) or analog (0-1V, TSic™ x01). The low power consumption of about 35µA makes it suitable for many applications.

Features

- Accuracy: $\pm 0.3K$ (TSic™ 30x) in the range of 10°C to 90°C
- Resolution: 0.1K
- Measurement Range: -50°C to 150°C
- Sampling Rate: 10Hz
- Supply Voltage: $V^+ = 3.0V$ to 5.5V, high precision operating range $V^+ = 4.5V$ to 5.5V
- Package: SOP-8, TO92
- Supply Current: typ. 30µA at 25°C and $V^+ = 3.3V$ for minimal self-heating

Custom Specific Calibrations

The accuracy range of 80K (default: 10 C – 90 C) can be shifted, e.g. an accuracy of $\pm 0.3K$ in a range from -30°C to +50°C can be ensured (TSic 30x).

Key Benefits

- No calibration necessary
- Very low power consumption
- Custom calibration and assembly possible
- Digital or analog output signal
- Excellent long term stability



INNOVATIVE SENSOR TECHNOLOGY

IST AG, Industriestrasse 2, CH-9630 Wattwil, Switzerland, Phone (+41 71 987 73 73, Fax (+41 71 987 73 77
e-mail info@ist-ag.com, www.ist-ag.com



TSic™ 301/306

Easy to integrate, low power temperature sensor IC

4/4

Absolute Maximum Ratings

PARAMETER	MIN	MAX	Units
Supply Voltage (V ^s)	-0.3	6.0	V
Voltagess for analog I/O – Pins (V _{INA} , V _{OUTA})	-0.3	V _{DDA} +0.3	V
Storage Temperature Range (T _{stg})	-20	80	°C

Operating Conditions

PARAMETER	MIN	TYP	MAX	Units
Supply Voltage to GND (V ^s)	2.97	5.0	5.5	V
Supply Current (I _{V+}) @ V ^s = 3.3V, RT	25	30	60	µA
Operating Temperature Range (T _{amb})	-50		150	°C
Output Load Capacitance (C _L)			15	nF
External Capacitance between V ^s and GND ¹ (C _{V+})	80	100	470	nF
Output Load Resistance between signal and GND (or V ^s)	47			kΩ

¹Recommended as close to TSic V+ and GND-Pins as possible.

Temperature Accuracies²

TSic 30x	Tol.	Units
T1: +10°C to 90°C	±0.3	K
T2: -20°C to +110°C	±0.3	K
T3: -50°C to +150°C	±0.5	K
TSic 20x	Tol.	Units
T1: +10°C to 90°C	±0.3	K
T2: -20°C to 110°C	±0.4	K
T3: -50°C to 150°C	±0.9	K

²The provided accuracy is applicable for a supply voltage between 4.5V and 5.5V. The accuracy is smaller with a supply voltage between 2.97V and 4.5V. For applications where the best accuracy at 3V is requested, ask for a custom specific 3V calibrated device.

Other TSic™ products with custom specific calibrations are available on request e.g. other temperature range for high accuracy.

Accuracy at delivery; the assembly method can influence the accuracy!

Tolerance out of the measurement range:

Below -50°C / above +150°C: ±3K



INNOVATIVE SENSOR TECHNOLOGY

IST AG, Industriestrasse 2, CH-9630 Wattwil, Switzerland, Phone (+)41 71 987 73 73, Fax (+)41 71 987 73 77
e-mail info@ist-ag.com, www.ist-ag.com

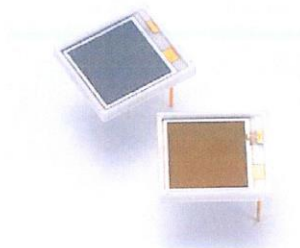


All mechanical dimensions are valid at 25°C ambient temperature, if not differently indicated. All data except the mechanical dimensions only have information purposes and are not to be understood as assured characteristics. Technical changes without previous announcement as well as possible errors. The information on this data sheet was compiled carefully and will be accepted as correct. No liability in case of mis-use. Used with caution: values during a longer period can affect the reliability. All rights reserved. The material contained herein may not be reproduced, copied, transmitted, stored, or used without the prior written consent of the copyright owner. Typing errors and omissions reserved. Product specifications are subject to change without notice. All rights reserved.



Si PIN photodiode

S3590-08/-09/-18/-19



Large active area Si PIN photodiode

Features

- ➔ Sensitivity matching with BGO and CsI (TI) scintillators: S3590-08/-09
- ➔ Sensitivity matching with blue scintillator (LSO, GSO, etc.): S3590-18/-19
- ➔ Bare chip type (unsealed): S3590-09/-19
- ➔ High quantum efficiency: S3590-09 ($\lambda=540$ nm) S3590-19 ($\lambda=400$ nm)
- ➔ Low capacitance
- ➔ High-speed response
- ➔ High stability
- ➔ Good energy resolution

Applications

- ➔ Scintillation detectors
- ➔ Hodoscopes
- ➔ TOF counters
- ➔ Radiation detection
- ➔ X-ray detection

Structure / Absolute maximum ratings

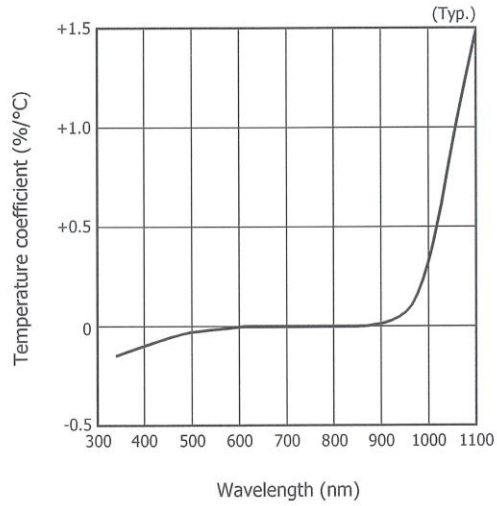
Type No.	Window material	Active area (mm)	Depletion layer thickness (mm)	Absolute maximum ratings			
				Reverse voltage V_R max	Power dissipation P (mW)	Operating temperature T_{opr} (°C)	Storage temperature T_{stg} (°C)
S3590-08	Epoxy resin	10 × 10	0.3	100	100	-20 to +60	-20 to +80
S3590-09	Unsealed						
S3590-18	Epoxy resin						
S3590-19	Unsealed						

Note: Exceeding the absolute maximum ratings even momentarily may cause a drop in product quality. Always be sure to use the product within the absolute maximum ratings.

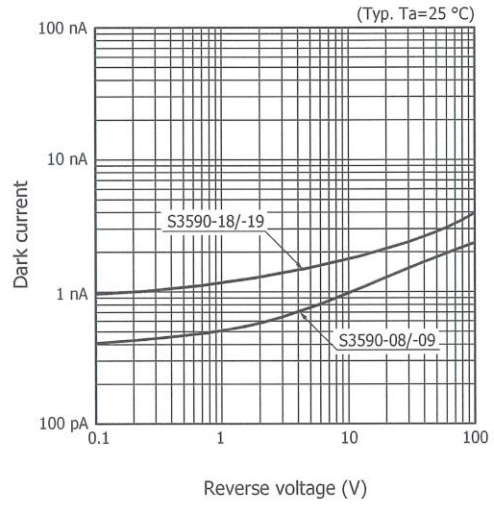
Electrical and optical characteristics (Typ. $T_a=25$ °C, unless otherwise noted)

Type No.	Spectral response range λ (nm)	Peak sensitivity wavelength λ_p (nm)	Photo sensitivity S				Short circuit current I_{sc} 100 lx (μ A)	Dark current I_D $V_R=70$ V		Temp. coefficient of I_D T_{CID} $V_R=70$ V (times/°C)	Cut-off frequency f_c $V_R=70$ V (MHz)	Terminal capacitance C_t $f=1$ MHz $V_R=70$ V (pF)	NEP $V_R=70$ V ($W/Hz^{1/2}$)
			$\lambda=\lambda_p$ (A/W)	LSO 420 nm (A/W)	BGO 480 nm (A/W)	CsI(Tl) 540 nm (A/W)		Typ.	Max.				
S3590-08	340 to 1100	960	0.66	0.20	0.30	0.36	100	2	6	1.12	40	40	3.8×10^{-14}
S3590-09			0.22	0.33	0.41	90							
S3590-18			0.65	0.28	0.34	0.38	100	4	10				
S3590-19			0.58	0.33	0.37	0.4	86						

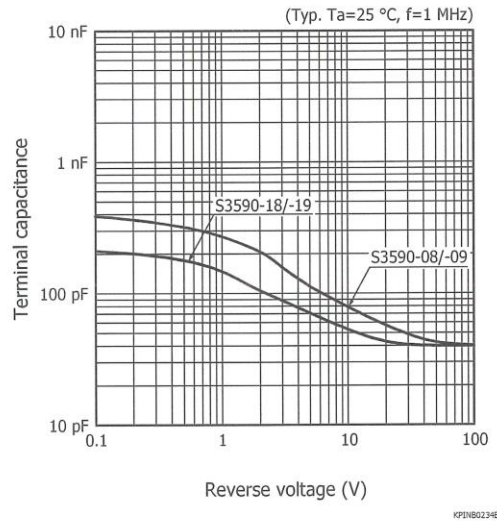
Photosensitivity temperature characteristic



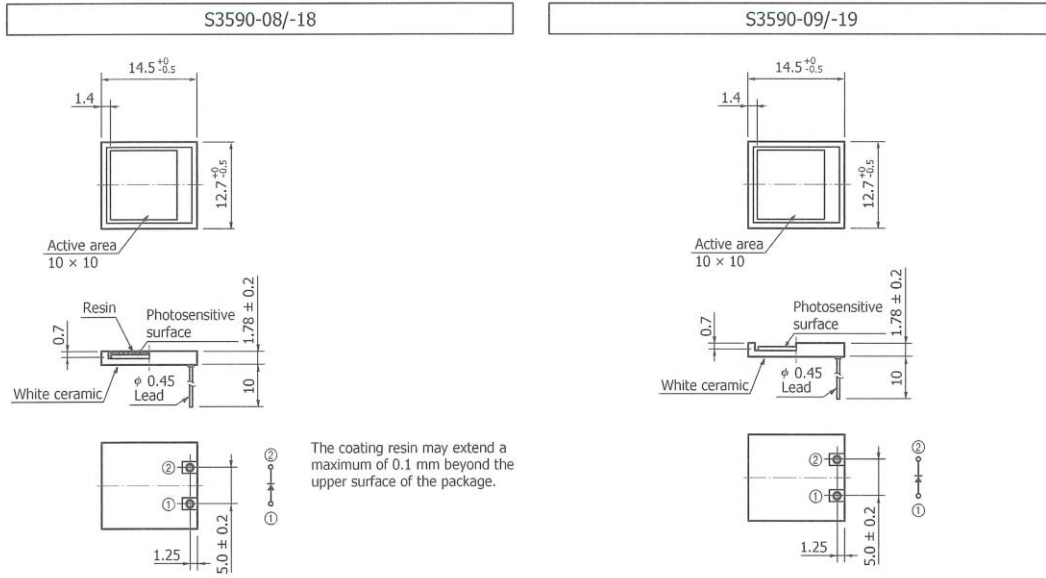
Dark current vs. reverse voltage



Terminal capacitance vs. reverse voltage



Dimensional outline (unit: mm)



KFINA001HEG

KFINA009EE

Information described in this material is current as of July, 2012.

Product specifications are subject to change without prior notice due to improvements or other reasons. Before assembly into final products, please contact us for the delivery specification sheet to check the latest information.

The product warranty is valid for one year after delivery and is limited to product repair or replacement for defects discovered and reported to us within that one year period. However, even if within the warranty period we accept absolutely no liability for any loss caused by natural disasters or improper product use.

Copying or reprinting the contents described in this material in whole or in part is prohibited without our prior permission.

HAMAMATSU

www.hamamatsu.com

HAMAMATSU PHOTONICS K.K., Solid State Division

1126-1 Ichino-cho, Higashi-ku, Hamamatsu City, 435-8558 Japan, Telephone: (81) 53-434-3311, Fax: (81) 53-434-5184

U.S.A.: Hamamatsu Corporation: 360 Foothill Road, P.O.Box 6910, Bridgewater, N.J. 08807-0910, U.S.A., Telephone: (1) 908-231-0960, Fax: (1) 908-231-1218

Germany: Hamamatsu Photonics Deutschland GmbH: Arzbergerstr. 10, D-82211 Herrsching am Ammersee, Germany, Telephone: (49) 8152-375-0, Fax: (49) 8152-265-8

France: Hamamatsu Photonics France S.A.R.L.: 19, Rue du Saule Trapu, Parc du Moulin de Massy, 91882 Massy Cedex, France, Telephone: 33-(1) 69 53 71 00, Fax: 33-(1) 69 53 71 10

United Kingdom: Hamamatsu Photonics UK Limited: 2 Howard Court, 10 Tewin Road, Welwyn Garden City, Hertfordshire AL7 1BW, United Kingdom, Telephone: (44) 1707-294888, Fax: (44) 1707-325777

North Europe: Hamamatsu Photonics Norden AB: Thorshamnsgatan 35 16440 Kista, Sweden, Telephone: (46) 8-509-031-00, Fax: (46) 8-509-031-01

Italy: Hamamatsu Photonics Italia S.R.L.: Strada della Moia, 1 int. 6, 20020 Arese, (Milano), Italy, Telephone: (39) 02-935-81-733, Fax: (39) 02-935-81-741

China: Hamamatsu Photonics (China) Co., Ltd.: 1201 Tower B, Jianning Center, No.27 Dongshanhu Bellu, Chaoyang District, Beijing 100020, China, Telephone: (86) 10-6586-6006, Fax: (86) 10-6586-2866

Cat. No. KPIN1052E09 Jul. 2012 DN

4

10.9 CdTe detector



EURORAD

FICHE D'ENVOI
CdTe Detectors

Customer's Name: CAZZATO Claudio

Order Number : 001/16

Counter

Spectrometer

Reference : S1.1.1U

Serial Number :1100-25A

Size :

Area 1,33 x 1,33 mmxmm

Sensitive thickness 1 mm

Volume : 1 mm³

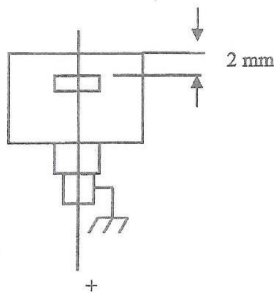
Performance :

Operating bias : 100 V

BIAS positive

BIAS negative

Mounting : BNC Connector



Name : D.FEDER

Date : 12/05/16

Signature :







Référence : F08.06

Indice : 01

Date d'application : 15/09/98

1/1

- Planar spectrometer: (Standard CdTe production)

	TYPE	GRADE	AREA (mm)	THICKNESS	BIAS VOLTAGE (V)	FWHM (keV)
	S.1.1.1.	Standard	1 x 1	1 mm	30 - 50	6 – 10
		Ultimate	1 x 1	1 mm	30 - 50	Below 6
	S.2.2.1.	Standard	2 x 2	1 mm	30 - 50	6 – 10
		Ultimate	2 x 2	1 mm	30 - 50	Below 6
	S.2.2.2.	Standard	2 x 2	2 mm	50 - 100	8 - 12
		Ultimate	2 x 2	2 mm	50 - 100	5 - 8
	S.5.5.1.	Standard	5 x 5	1 mm	30 - 50	6 – 10
		Ultimate	5 x 5	1 mm	30 - 50	Below 6
	S.5.5.2.	Standard	5 x 5	2 mm	50 - 100	8 - 12
		Ultimate	5 x 5	2 mm	50 - 100	5 - 8
	S.5.5.3.	Standard	5 x 5	3 mm	50 - 150	8 - 12
		Ultimate	5 x 5	3 mm	50 - 150	5 - 8

INTRODUCTION

This standard low noise hybrid preamplifier chip is suitable for general spectroscopic applications with all kind of semiconductor detectors.

The preamplifier is equipped with a test input which permits to verify the good running conditions of your spectroscopic chain. The preamplifier can be connected to an standard spectroscopic amplifier or a EURORAD SH1-H.

RECOMMANDATIONS

The charge sensitive preamplifier must be used with the specific cable delivered by EURORAD.

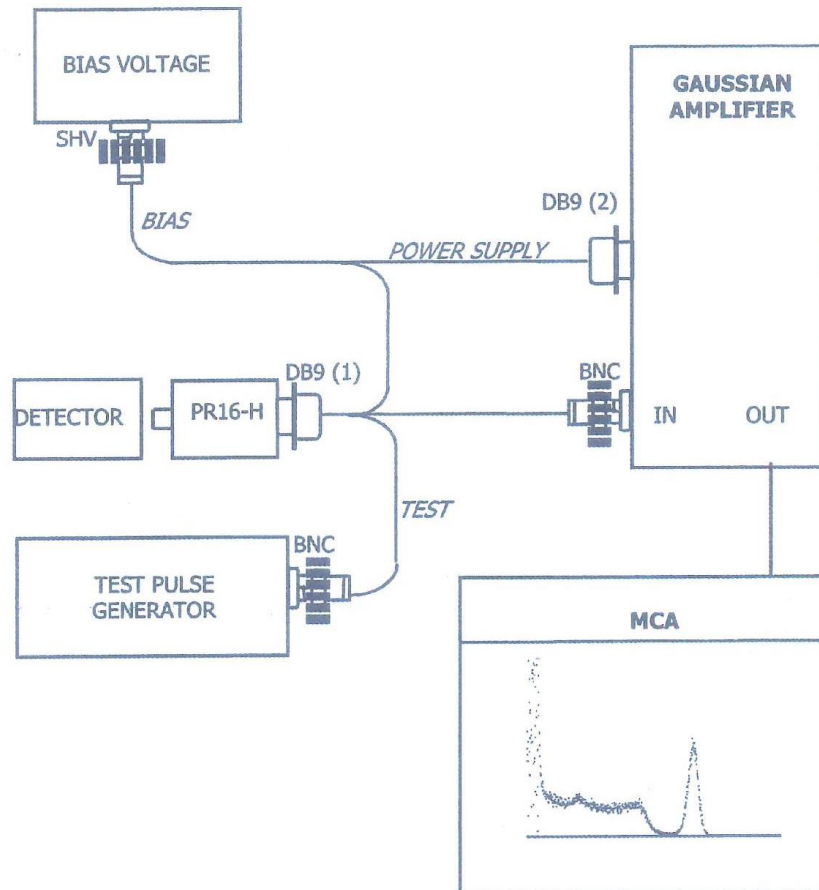
The bias voltage do not exceed +500V, apply the high voltage recommended on the detector datasheet.

ELECTRICAL SPECIFICATIONS

- Power supply : $V_{cc-} = 12$ Volts ($I_{cc-} = 8$ mA)
 $V_{cc+} = 12$ Volts ($I_{cc+} = 16$ mA)
- Output polarity (for a positive charge at the input) : Positive
- Sensitivity: 6,6V/pC
 - for Silicon : 300 mV/MeV
 - for Cadmium Telluride : 240 mV/MeV
- Fall time : 50 μ s
- Output impedance : 50 Ω
- Output coupling : DC
- Input coupling : AC (DC optional order PR16 DC)
- Bias filtering : 1M Ω , 10nF MAX +/-500V
- Polarisation resistor : 100 M Ω (to Bias)
- Support moved away FET : No
- Integrated shaper: No

Capacitance (pF)	Rise Time (ns)	Noise (Si, 1 μ s) (with polarisation resistor)	Noise (Si, 1 μ s) (without polarisation resistor)
0 pF	20 ns	1.5 keV	1.15 keV
56 pF	30 ns	3.2 keV	3 keV
100 pF	75 ns	5 keV	4.7 keV

CONNECTION DIAGRAM



CR-110 charge sensitive preamplifier: application guide

Rev. 2 (May, 2014)

General Description

Crema's CR-110 is a single channel charge sensitive preamplifier module intended for use with various types of radiation detectors including semiconductor detectors (e.g. CdTe and CZT), p-i-n photodiodes, avalanche photodiodes (APDs), and various gas-based detectors. The CR-110 is one of a series of four charge sensitive preamplifiers offered by Crema, which differ from each other most notably by their gain. A guide to selecting the best charge sensitive preamplifier for your application can be found at our web site: <http://cremat.com>. As with all Crema's preamplifier modules, the CR-110 is small (less than one square inch in area), allowing for compact multichannel detection systems to be constructed using a modular design.

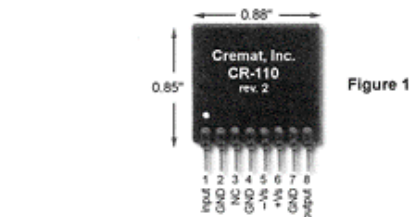
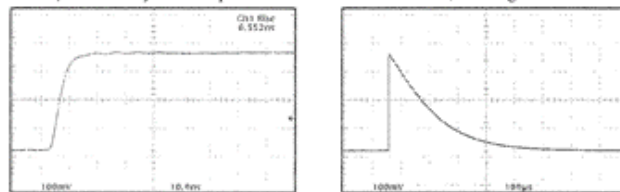
Detector coupling

The CR-110 can be used either in a direct coupled (DC) mode, or an AC coupled mode. If the detector current exceeds 10 nA, it is recommended that an AC coupled mode be used to prevent the resulting DC offset of the preamplifier output from saturating. Low frequency detector current (e.g. 'dark' current, or leakage current) produces an offset in the preamplifier output voltage at a rate of 0.2 V per nA. The use of AC coupling also is useful in improving the counting rate capability of the preamplifier. A schematic diagram of an AC-coupled charge sensitive preamplifier detection circuit can be found at http://www.cremat.com/CSP_application_notes.htm

approximately 7 ns. Furthermore, capacitance at the preamplifier input (i.e. detector capacitance) will further slow the rise time at a rate of 0.4 ns / pF.

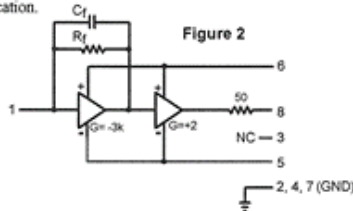
Keep in mind the output rise time will also be limited by the speed of the detector. For example, the detection current pulse from a CsI(Tl)/photodiode scintillation detector has a duration of approximately a couple μ s, so the expected rise time of the charge sensitive preamplifier output will be at least that long.

The output waveform of the CR-110 using a capacitively-coupled fast square wave pulser at the input is shown below to the left. At long time domains, the output decays due to the discharge of the feedback capacitor through the feedback resistor, with an RC time constant of 140 μ s. This decay of the output waveform is also shown below, to the right.



Package Specifications

The CR-110 circuit is contacted via an 8-pin SIP connection (0.100" spacing). Leads are 0.020 inches wide. Pin 1 is marked with a white dot for identification.



Equivalent circuit diagram

Figure 2 above shows a simplified equivalent circuit diagram of the CR-110, which is a two stage amplifier. The first stage is high gain, and the second stage is low gain with an emphasis on supplying sufficient output current to drive a terminated coaxial cable. Pin numbers corresponding with the CR-110 preamplifier are shown. R_f (100 M Ω) and C_f (1.4 pF) are the feedback resistor and capacitor respectively.

Output waveform

Charge sensitive preamplifiers are used when radiation is detected as a series of pulses, resulting in brief bursts of current flowing into or out of the preamplifier input. Depending on the type of detector, this burst of current may be very brief (<1 ns) or as long as a few μ s. For an idealized detection current pulse taking the form of a delta function, the detected charge (time integral of the input current) will ideally take the form of a step function.

The output waveform of an actual charge sensitive preamplifier will of course have a non-zero rise time: for the CR-110 this figure is

Crema Inc, 950 Watertown St. #3
West Newton, MA 02465 USA
+1(617) 527-6590
FAX: +1(617) 527-2849
<http://cremat.com>



Specifications		
Assume temp = 20 °C, $V_s = \pm 6.1V$, unloaded output		
	CR-110	units
Preamplification channels	1	
Equivalent noise charge (ENC)*		
ENC RMS	200	electrons
	0.03	femtoCoul.
Equivalent noise in silicon	1.7	keV (FWHM)
Equivalent noise in CdZnTe	2.4	keV (FWHM)
ENC slope	4	elect. RMS pF
Gain	1.4	volts / pC
	62	mV / MeV(Si)
Rise time **	7	ns
Decay time constant	140	μ s
Unsaturated output swing	-3 to +3	volts
Maximum charge detectable per event	1.3×10^7	electrons
	2.1	pC
Power supply voltage (V_s)		
maximum	$V_s = \pm 13$	volts
minimum	$V_s = \pm 6$	volts
Power supply current (pos)	7.5	mA
(neg)	3.5	mA
Power dissipation	70	mW
Operating temperature	-40 to +85	°C
Output offset	+0.2 to -0.2	volts
Output impedance	50	ohms

* Measured with input unconnected, using Gaussian shaping amplifier with time constant = 1 μ s. With a detector attached to the input, noise from the detector capacitance, leakage current, and dielectric losses will add to this figure.

** Pulse rise time (defined as the time to attain 90% of maximum value) has a linear relationship with input capacitance. Value cited in the table assumes zero added input capacitance. To calculate pulse rise time for practical situations, use the equation: $t_r = 0.4 C_d + 7$ ns, where t_r is the pulse rise time in ns, and C_d is the added capacitance (e.g. detector capacitance) in pF. Keep in mind that others factors within the detection system may further limit this value.

CR-200 Gaussian shaping amplifier: application guide

rev. 2, Jan. 2014

General Description

The CR-200 is a Gaussian shaping amplifier module, and is used to read out the "tail pulse" signals such as from charge sensitive preamplifiers, PMTs, and other similar detection circuits. Gaussian shaping amplifiers are also known as 'pulse amplifiers', 'linear amplifiers', or 'spectroscopy amplifiers' in the general literature. They accept a step-like input pulse and produce an output pulse shaped like a Gaussian function (bell curve). The purpose of these amplifiers is not only to transform the shape of the event pulse from a tail pulse to a bell curve, but also to filter much of the noise from the signal of interest. Use of shaping amplifiers will thereby reduce the fall time of the pulse signals (reducing the incidence of pulse 'pile up') and also improve the signal-to-noise of the detection system.

The CR-200 is available in 9 different shaping times, from 25 ns to 8 μs. The gain and shaping times of these amplifiers are fixed. If additional gain is desired, it is recommended that this be done with the application of an additional broadband amplifier between the preamplifier and the CR-200 shaping amplifier. Cremat offers an evaluation board (CR-160-R7) which includes a multi-stage variable-gain amplifier, as well as all necessary connectors. More information on the CR-160-R7 evaluation board can be found at <http://cremat.com>

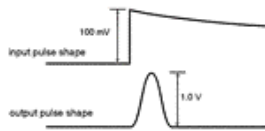


Figure 1. Comparison of sample input and output pulse shapes

The shaping time is defined as the time-equivalent of the "standard deviation" of the Gaussian output pulse. A simpler measurement to make in the laboratory is the full width of the pulse at half of its maximum value (FWHM). This value is greater than the shaping time by a factor of 2.4. For example, a Gaussian shaping amplifier with a shaping time of 1.0 μs would have a FWHM of 2.4 μs.

Equivalent circuit diagram

Figure 2 shows an equivalent circuit. Pin numbers corresponding with the CR-200 shaping amplifier are shown. Input components C_{in} and R_{in} form a differentiating circuit. The following circuitry consists of two Sallen and Key filters, providing 4 poles of integration and signal gain. The numerous integration stages produce an output pulse that approximates a Gaussian function.

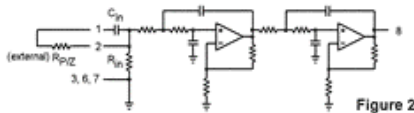


Figure 2

part #	shaping time	output pulse width (FWHM)	R_{in}	C_{in}	gain
CR-200-25ns	25 ns	59 ns	82 Ω	220 pF	4
CR-200-50ns	50 ns	120 ns	220 Ω	220 pF	8
CR-200-100ns	100 ns	240 ns	220 Ω	470 pF	10
CR-200-250ns	250 ns	590 ns	240 Ω	1000 pF	10
CR-200-500ns	500 ns	1.2 μs	510 Ω	1000 pF	10
CR-200-1μs	1 μs	2.4 μs	1.0 kΩ	1000 pF	10
CR-200-2μs	2 μs	4.7 μs	2.0 kΩ	1000 pF	10
CR-200-4μs	4 μs	9.4 μs	1.2 kΩ	3300 pF	10
CR-200-8μs	8 μs	19 μs	2.4 kΩ	3300 pF	10

Pole/Zero Correction

The long decay time of the input pulse creates a small overshoot in the shape of the output pulse unless a pole/zero correction is utilized. This can be done by connecting a resistor ($R_{P/Z}$) between pin 1 (input) and pin 2 (P/Z). This resistor is in parallel with the input capacitor (internal to the CR-200 circuit) and creates a 'zero' in the amplifier's transfer function which cancels the 'pole' created by the charge sensitive preamplifier's feedback resistor. To achieve proper pole/zero cancellation, $R_{P/Z}$ should be selected so that $R_{P/Z} * C_{in}$ is equal to the decay time constant of the preceding charge sensitive preamplifier output signal. Use the equation $R_{P/Z} = R_f * C_f / C_{in}$ where R_f and C_f are the feedback resistor and feedback capacitor of the

charge sensitive preamplifier and C_{in} is the value of the input capacitor in the CR-200. The value of C_{in} for the CR-200 circuit can be found in the provided table.

You may wish to realize $R_{P/Z}$ as a potentiometer so to adjust the value precisely. The effect of $R_{P/Z}$ on the pulse shape can be seen in the pulse waveforms shown in Figure 3.

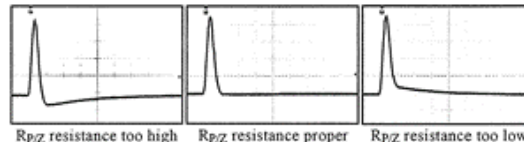


Figure 3

Baseline Restoration (BLR)

The CR-200 does not contain active baseline restoration circuitry. For this reason there will be a negative 'baseline shift' (change in the output DC offset) at high counting rates. In order to determine whether this will be a problem for your application, use the equation (valid for small baseline shifts):

$$S/H = R * \tau * 2.5 \times 10^{-6}$$

where S is the negative baseline shift, H is the pulse height, R is the count rate (counts/sec), and τ is the shaping time of the shaping amplifier (in μs). For example, using a 1 μs shaping amplifier we would predict a 0.025 (2.5%) shift in the baseline at a count rate of 10,000 counts per second.

To address this potential problem, Cremat offers the CR-210 baseline restorer. More information on this circuit can be found at the cremat.com web site.

Package Specifications

The CR-200 circuit is contacted via an 8-pin SIP connection (0.100" spacing). Pin 1 is marked with a white dot for identification.

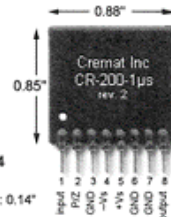


Figure 4

Typical Application

Figure 5 shows the CR-200 in a typical application, coupled to a detector via a CR-110 charge sensitive preamplifier. Depending on the requirements of your application, an AC-coupled amplifier may be added between the preamplifier and shaping amplifier to further increase the signal size. An optional CR-210 baseline restore circuit has been added as well.

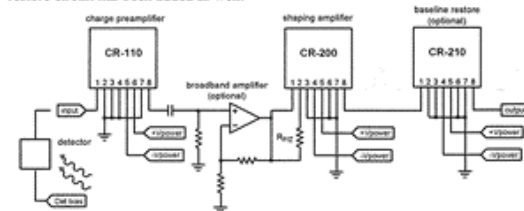


Figure 5

Cremat Inc, 950 Watertown St. #3
West Newton, MA 02465 USA
+1(617) 527-6590
FAX: +1(617) 527-2849
<http://cremat.com>



10.13 ImageJ macro for the coloured uniformity map

```
// This macro takes as input the Gafchromic scanned image, dividedes it in n x m sub-images
// and performs a pseudo-colored map

setBatchMode( true );

dir_portions="/ scripts/MT/cropped_M_T/"; //path to save sub-images
dir_results="/scripts/MT/Results_statistics/"; //path to save statistics results
dir_maps="/scripts/MT/Colored_maps/"; //path to save the final map
//create all the directories
File.makeDirectory(dir_portions);
File.makeDirectory(dir_results);
File.makeDirectory(dir_maps);

open("/scripts/MT/Gaf_26_04_3 1.png"); //open the gafchromic scanned image
run("Conversions...", "scale weighted");
run("8-bit"); // convert it in 8-bit gray
saveAs("Jpeg", "/scripts/MT/" + "Gaf_26_04_3_1_grey" );
id = getImageID();
n=85; //divisions along y
m=100; //divisions along x
a=b=0;
//get the dimensions of the original image
height_gaf= getHeight();
width_gaf= getWidth();

//makes rectangles of fixed height and width strating from the right-top corner of the initial image
//each selected rectangle is saved in dir_portions directory giving a name like the matrix elements
for (y = 0; y < n; y++) {
    offsetY = (y * height_gaf) / n;
    Y_fine = height_gaf/n;
    a=a+1;
    b=0;
    for (x = 0; x < m; x++) {
        offsetX = x * width_gaf / m;
        X_fine = width_gaf/m;
        b=b+1;
        selectImage(id);
        // make rectangle richiede x ed y iniziali e lunghezza ed altezza del quadrato!!
        makeRectangle(offsetX, offsetY, X_fine, Y_fine);
        run("Duplicate...", "title=" + "crop" + a + "_" + b);
        saveAs("Jpeg", dir_portions + "crop" + a + "_" + b);
    }
}

print("all sub-images have been saved :)");

fList = getFileList( dir_portions ); //gets the number of files in the specified folder (numbers of sub-images)
MeanValuesArray = newArray(fList.length); //creates an array to store mean gray values
w=0; //array index
//for every sub-image the mean gray value is measured and saved in the array
```

```

for ( p=1; p <= n; p++ ) {
    for ( i=1; i <= m; i++ ) {
        open( dir_portions + "crop" + p + "_" + i + ".jpg" );
        id = getImageID();
        fileName = File.nameWithoutExtension;
        selectImage(id);
        run("Set Measurements...", "area mean redirect=None decimal=1");
        run("Measure");
        getStatistics(area, mean);
        MeanValuesArray[w]=mean; //salva tutti i valori di media in un array
        close(id);
        w=w+1;
    }
}
saveAs("Results", dir_results + "Results_overall" + ".txt"); //all statistic results are saved in a .txt file

print("Statistics computed and saved");
//
//
//finds the max and min value of the array and makes the difference
//to know how many gray values are displayed in the original image

Array.getStatistics(MeanValuesArray, min_array, max_array);
print(max_array);
print(min_array);
diff= max_array - min_array +1;
n_percento=0.01*diff
perc=n_percento*100/diff;

//create a black image of the same dimensions as the original one
newImage("Colored_map", "32-bit RGB", width_gaf, height_gaf, 1);
run("RGB Color");

j=0; //index for an array

width=width_gaf/m; //width of a square to be colored
height=height_gaf/n; //height of a square to be colored

//for loop to creating the pseudo-colored map
//starting for the top-right corner of the new black image, a rectangle of the same size
//as the previously created sub-images, is selected and colored depending on the corresponding
//mean gray value stored in the array MeanValuesArray.
//colors are assigned as follows: the minimum grey value is the most intense field part (100% of intensity I)
//starting with this value, some intensity ranges are computed, and to each one a color is assigned:
// I<3%: black; 3%<I<5%: blue navy; 5%<I<7%: Blue (Crayola); 7%<I<10%: cerulean blue; 10%<I<15%: cyan;
//15%<I<30%: violet; 30%<I<50%: magenta; 50%<I<70%: purple; 70%<I<90%: orange; 90%<I<100%: yellow.

for (y = 0; y < n; y++) {
    offsetY = y * height ;
    for (x = 0; x < m; x++) {
        offsetX = x * width;
        // make rectangle requires initial x and y, width and height of the rectangle

```

```

makeRectangle(offsetX, offsetY, width, height);

if (MeanValuesArray[j]<=min_array+3*n_percento) {
setForegroundColor(0, 0, 0); //black
run("Fill", "slice");
}
else if (MeanValuesArray[j]<=min_array+5*n_percento) {
    setForegroundColor(0, 0, 139); //blue navy
    run("Fill", "slice");
}
else if (MeanValuesArray[j]<=min_array+7*n_percento) {
setForegroundColor(0, 71, 149); //Blue (Crayola)
run("Fill", "slice");
}
else if (MeanValuesArray[j]<=min_array+10*n_percento) {
setForegroundColor(0, 119, 233); //Cerulean blue
run("Fill", "slice");
}
else if (MeanValuesArray[j]<=min_array+15*n_percento) {
setForegroundColor(0, 174, 252); // cyan
run("Fill", "slice");
}
else if (MeanValuesArray[j]<=min_array+30*n_percento) {
setForegroundColor(102, 0, 204); //violet
run("Fill", "slice");
}
else if (MeanValuesArray[j]<=min_array+50*n_percento) {
setForegroundColor(204, 0, 204); //magenta
run("Fill", "slice");
}
else if (MeanValuesArray[j]<=min_array+70*n_percento) {
setForegroundColor(153, 0, 76); //purple
run("Fill", "slice");
}
else if (MeanValuesArray[j]<=min_array+90*n_percento) {
setForegroundColor(255, 128, 0); //orange
run("Fill", "slice");
}
else {
setForegroundColor(255, 255, 153); //yellow
run("Fill", "slice");
}

j=j+1;
}
}
//save the final pseudo-colored map
saveAs("Jpeg", dir_maps + "Colored_map_variable%_" + n + "x" + m);

print("The pseudo-colored map is done :)");

```

```

//create the map legend
//create a new with image
newImage("Legend_map", "32-bit RGB", 115, 260, 1);
run("RGB Color");
makeRectangle(0, 0, 115, 260);
setForegroundColor(255, 255, 255);
run("Fill", "slice");

//write the title
setFont("Serif", 13, "bold");
setColor(0, 0, 0);
drawString("Uniformity (%)", 1, 20); //text, x and y position

//make the colored rectangles with a black outline

makeRectangle(4, 39, 22, 12);
setForegroundColor(0, 0, 0);
run("Fill", "slice");

makeRectangle(4, 59, 22, 12);
setForegroundColor(0, 0, 0);
run("Fill", "slice");

makeRectangle(4, 79, 22, 12);
setForegroundColor(0, 0, 0);
run("Fill", "slice");

makeRectangle(4, 99, 22, 12);
setForegroundColor(0, 0, 0);
run("Fill", "slice");

makeRectangle(4, 119, 22, 12);
setForegroundColor(0, 0, 0);
run("Fill", "slice");

makeRectangle(4, 139, 22, 12);
setForegroundColor(0, 0, 0);
run("Fill", "slice");

makeRectangle(4, 159, 22, 12);
setForegroundColor(0, 0, 0);
run("Fill", "slice");

makeRectangle(4, 179, 22, 12);
setForegroundColor(0, 0, 0);
run("Fill", "slice");

makeRectangle(4, 199, 22, 12);
setForegroundColor(0, 0, 0);
run("Fill", "slice");

```

```

makeRectangle(4, 219, 22, 12);
setForegroundColor(0, 0, 0);
run("Fill", "slice");

makeRectangle(5, 40, 20, 10);
setForegroundColor(0, 0, 0);
run("Fill", "slice");

makeRectangle(5, 60, 20, 10);
setForegroundColor(0, 0, 139);
run("Fill", "slice");

makeRectangle(5, 80, 20, 10);
setForegroundColor(0, 71, 149);
run("Fill", "slice");

makeRectangle(5, 100, 20, 10);
setForegroundColor(0, 119, 233);
run("Fill", "slice");

makeRectangle(5, 120, 20, 10);
setForegroundColor(0, 174, 252);
run("Fill", "slice");

makeRectangle(5, 140, 20, 10);
setForegroundColor(102, 0, 204);
run("Fill", "slice");

makeRectangle(5, 160, 20, 10);
setForegroundColor(204, 0, 204);
run("Fill", "slice");

makeRectangle(5, 180, 20, 10);
setForegroundColor(153, 0, 76);
run("Fill", "slice");

makeRectangle(5, 200, 20, 10);
setForegroundColor(255, 128, 0);
run("Fill", "slice");

makeRectangle(5, 220, 20, 10);
setForegroundColor(255, 255, 153);
run("Fill", "slice");

//wight the text next to the rectangles

setFont("Serif", 10, "bold");
setColor(0, 0, 0);
drawString("100-97", 35, 52);
drawString("97-95", 35, 72);
drawString("97-95", 35, 92);
drawString("95-90", 35, 112);

```

```
drawString("90-85", 35 , 132);
drawString("85-70", 35 , 152);
drawString("70-50", 35 , 172);
drawString("50-30", 35 , 192);
drawString("30-10", 35 , 212);
drawString("10-0", 35 , 232);

saveAs("Jpeg", dir_maps + "Map_legend");
exit();
```


10.14 Voltage divider

GICI
Greenwich Instrument Co. Inc.
128 Old Church Road
Greenwich CT 06830
(203) 661-0398

CALIBRATION REPORT
Prepared for
RAYNOVA SRL-Consorzio Hypatia
GiCi W.O. Number: 19690
1 Accreditation to ISO 17025
GICI 2000 voltage divider
sn M2381901
1 Federal Express Priority Air

COUNTRY OF ORIGIN: USA
Measuring Equipment
Sch B 9030330040
Shipper US EIN: 06-1246599

Greenwich Instrument Co. Inc. is ISO 17025 Accredited by ANAB

Report Date: 11Apr2016

Last Calibration #: New

This report may not be reproduced, except in full, without the
written approval of Greenwich Instrument Co. Inc.

Page 1

GICI
Greenwich Instrument Co. Inc.
128 Old Church Road
Greenwich CT 06830
(203) 661-0398

Gici W\o : 19690 P.O. #:0

Report date 11Apr2016

www.dynalyzer.com

CERTIFICATE OF CALIBRATION

We hereby certify that this instrument has been calibrated and is in accordance with the specifications set forth for this model, unless otherwise noted. Input and output voltages and currents are traceable to the NIST.

Gici has ISO 17025:2005 laboratory accreditation by ANAB. ISO 17025 includes the elements of ISO 9001. Greenwich Instrument Company, Inc. (Gici) assumes no contingent liability arising from the use of this equipment. Our liability is limited to the fee paid to Gici for the calibration, and repairs, if any, to the instruments referenced below. Terms of service available on request. The referenced test equipment requires recalibration annually, or sooner, if changes in performance are observed.

Description and Serial No. (or No.'s if applicable.)

1 Accreditation to ISO 17025
GICI 2000 voltage divider
sn M2381901
1 Federal Express Priority Air

COUNTRY OF ORIGIN: USA
Measuring Equipment
Sch B 9030330040
Shipper US EIN: 06-1246599

Ambiant Temperature: 12 F. Relative Humidity: 25%

Unit may be calibrated on or prior to shipping date per calibration sticker attached to unit. Calibration interval is one year from shipment, or when changes in performance are noted. Recalibration reminders will be sent periodically if warranted.

Calibration Engineer:



Jonathan S. Shapiro, PhD.

Page 2

Form #F003 Rev.5

GICI
Greenwich Instrument Co. Inc.
128 Old Church Road
Greenwich CT 06830

GICI
Greenwich Instrument Co. Inc.
128 Old Church Road
Greenwich CT 06830
(203) 661-0398

Report Date: 11Apr2016
Your P.O. Number: 0
Our W.O. Number: 19690

RAYNOVA SRL-Consorzio Hypatia
via del Politecnico c/o ASI
00133 ROMA ITALY


Thank you for selecting Greenwich Instrument Company for the calibration of your test equipment. Your instruments were calibrated with our computer controlled test set. All readings were referenced to equipment which is in current calibration, and is traceable to NIST.

Comments:

New voltage divider calibrated and accredited to ISO 17025.

High voltage measurements were made using Spellman constant potential UHV series power supplies.
Attached, if applicable, are reports giving the HVU voltage divider ratio and frequency response, the current transducer (MA) response and the filament circuit calibration.
Also attached, if applicable, is the verification of the digital display calibration for a series of calibrated, simulated exposures.

For Greenwich Instrument Company,


Jonathan S. Shapiro, PhD
President

10.15 Monitor ion chamber operating point measurements

Table 5.1: Monitor chamber voltage scan for 0,5 mA of tube current.

kV	Monitor				PTW			PTW/MON	Corr. Fact.	K_{air} (μGy)	K_{rate} ($\mu\text{Gy/s}$)
	Bias (V)	bsl (V)	Integral (Vs)	Signal (V)	bsl (V)	Integral (Vs)	Signal (V)				
60.45	50	-6.22E-05	-1.028	-0.0172	-8.20E-06	-2.575	-0.0431	2.505	0.972	12.25	0.2049
60.45		-6.15E-05	-1.028	-0.0172	-5.73E-06	-2.58	-0.0431	2.510	0.973	12.29	0.2053
60.57	70	-6.81E-05	-1.099	-0.0184	-4.78E-05	-2.738	-0.0457	2.491	0.974	13.06	0.2179
60.56		-8.24E-05	-1.098	-0.0183	-2.11E-05	-2.731	-0.0456	2.487	0.975	13.04	0.2177
60.56	90	-7.93E-05	-1.100	-0.0184	-3.98E-05	-2.721	-0.0456	2.474	0.975	12.99	0.2177
60.57		-9.62E-05	-1.103	-0.0184	-3.83E-05	-2.73	-0.0456	2.475	0.975	13.03	0.2176
60.45	100	-6.21E-05	-1.056	-0.0176	1.48E-05	-2.586	-0.0432	2.449	0.973	12.32	0.2060
60.45		-7.26E-05	-1.054	-0.0177	1.38E-05	-2.581	-0.0433	2.449	0.973	12.30	0.2062
60.44	200	-6.65E-05	-1.064	-0.0178	2.87E-06	-2.598	-0.0434	2.442	0.973	12.38	0.2064
60.45		-6.63E-05	-1.067	-0.0178	-9.82E-06	-2.604	-0.0435	2.440	0.973	12.40	0.2070
60.46	300	-8.09E-05	-1.063	-0.0178	-2.14E-05	-2.599	-0.0436	2.445	0.973	12.38	0.2071
60.45		-7.28E-05	-1.069	-0.0178	1.48E-05	-2.609	-0.0436	2.441	0.973	12.43	0.2073
60.45	400	-6.70E-05	-1.068	-0.0178	-8.78E-06	-2.616	-0.0437	2.449	0.974	12.47	0.2083
60.45		-6.33E-05	-1.064	-0.0178	9.86E-07	-2.602	-0.0436	2.445	0.974	12.41	0.2083
60.46	500	-6.03E-05	-1.065	-0.0179	-3.60E-05	-2.608	-0.0437	2.449	0.974	12.44	0.2080
60.47		-7.24E-05	-1.067	-0.0179	-2.40E-05	-2.613	-0.0438	2.449	0.974	12.46	0.2089
60.45	600	-8.81E-05	-1.067	-0.0178	-5.36E-06	-2.620	-0.0438	2.455	0.974	12.49	0.2087
60.46		-6.34E-05	-1.070	-0.0179	1.91E-05	-2.627	-0.0439	2.455	0.974	12.53	0.2090
60.47	700	-5.59E-05	-1.067	-0.0179	1.19E-05	-2.625	-0.0440	2.460	0.974	12.52	0.2099
60.46		-5.97E-05	-1.068	-0.0178	5.03E-06	-2.621	-0.0439	2.454	0.974	12.50	0.2096
60.56	800	-1.80E-02	-1.076	-0.0180	8.43E-06	-2.663	-0.0445	2.475	0.974	12.70	0.2120
60.56		-8.36E-05	-1.075	-0.0180	-3.37E-06	-2.656	-0.0445	2.471	0.973	12.65	0.2121
60.46	900	-8.26E-05	-1.072	-0.0180	-2.97E-06	-2.639	-0.0443	2.462	0.973	12.57	0.2109
60.47		-9.48E-05	-1.073	-0.0180	2.27E-07	-2.642	-0.0443	2.462	0.974	12.60	0.2112

Table 5.2: Monitor chamber voltage scan for 1 mA of tube current.

kV	Monitor				PTW			PTW/MON	Corr. Fact.	K_{air} (μGy)	K_{rate} ($\mu\text{Gy/s}$)
	Bias (V)	bsl (V)	Integral (Vs)	Signal (V)	bsl (V)	Integral (Vs)	Signal (V)				
60.28	50	-6.50E-05	-2.647	-0.0442	-1.01E-05	-7.043	-0.1176	2.661	0.974	33.59	0.561
60.27		-6.63E-05	-2.650	-0.0444	-2.49E-05	-7.061	-0.1184	2.665	0.974	33.67	0.565
60.27	70	-7.04E-05	-2.805	-0.0469	-4.01E-05	-7.096	-0.1119	2.530	0.974	33.84	0.533
60.27		-7.86E-05	-2.802	-0.0470	-2.25E-05	-7.086	-0.1188	2.529	0.974	33.79	0.567
60.25	90	-7.30E-05	-2.865	-0.0480	-3.31E-05	-7.076	-0.1187	2.470	0.974	33.74	0.566
60.26		-6.46E-05	-2.874	-0.0482	-2.82E-05	-7.084	-0.1188	2.465	0.974	33.78	0.567
60.27	100	-8.54E-05	-2.909	-0.0486	-3.26E-05	-7.141	-0.1193	2.455	0.974	34.05	0.569
60.27		-6.65E-05	-2.904	-0.0487	-3.61E-05	-7.120	-0.1194	2.452	0.974	33.95	0.569
60.26	200	-7.15E-05	-2.938	-0.0493	-8.59E-06	-7.115	-0.1193	2.422	0.974	33.93	0.569
60.26		300	-6.68E-05	-2.943	-0.0494	8.98E-06	-7.125	-0.1195	2.421	0.974	33.98
60.27	400	-9.17E-05	-2.849	-0.0482	-1.65E-05	-6.914	-0.1169	2.427	0.974	32.97	0.557
60.28		-9.40E-05	-2.927	-0.0491	-3.04E-05	-7.061	-0.1184	2.412	0.974	33.67	0.565
60.26	500	-7.45E-05	-2.932	-0.0492	-1.94E-05	-7.099	-0.1191	2.421	0.974	33.85	0.568
60.26		-8.64E-05	-2.953	-0.0493	-5.11E-06	-7.134	-0.1191	2.416	0.974	34.02	0.568
60.26	600	-6.71E-05	-2.930	-0.0493	1.45E-05	-7.117	-0.1193	2.422	0.974	33.94	0.569
60.26		-8.55E-05	-2.947	-0.0494	8.70E-06	-7.119	-0.1194	2.416	0.974	33.95	0.569
60.26	700	-1.05E-04	-2.940	-0.0493	-3.10E-05	-7.129	-0.1195	2.425	0.974	34.00	0.570
60.26		-1.02E-04	-2.961	-0.0494	-3.31E-05	-7.154	-0.1195	2.416	0.975	34.15	0.570
60.26	800	-8.99E-05	-2.957	-0.0494	-1.78E-05	-7.158	-0.1195	2.421	0.974	34.13	0.570
60.27		-8.27E-05	-2.959	-0.0494	-1.30E-05	-7.164	-0.1196	2.421	0.974	34.16	0.570
60.27	900	-9.89E-05	-2.942	-0.0493	-1.42E-05	-7.136	-0.1197	2.426	0.974	34.03	0.571
60.28		-1.08E-04	-2.946	-0.0494	-9.13E-07	-7.134	-0.1198	2.422	0.974	34.02	0.571

Table 5.3: Monitor chamber voltage scan for 2 mA of tube current.

kV	Monitor				PTW			PTW/MON	Corr. Fact.	K_{air} (μGy)	K_{rate} ($\mu\text{Gy/s}$)
	Bias (V)	bsl (V)	Integral (Vs)	Signal (V)	bsl (V)	Integral (Vs)	Signal (V)				
59.92	50	-6.70E-05	-5.310	-0.0891	-4.60E-05	-15.268	-0.2563	2.875	0.975	72.88	1.223
59.92		-7.29E-05	-5.376	-0.0898	-3.06E-05	-15.468	-0.2584	2.877	0.976	73.91	1.235
59.91	70	-7.97E-05	-5.903	-0.0990	-4.62E-06	-15.471	-0.2595	2.621	0.975	73.85	1.239
59.91		-8.55E-05	-5.929	-0.0994	-3.87E-05	-15.050	-0.2601	2.538	0.975	71.84	1.242
59.91	90	-6.61E-05	-6.177	-0.1037	-5.65E-05	-15.539	-0.2609	2.516	0.976	74.25	1.247
59.91		-6.37E-05	-6.195	-0.1039	-2.99E-05	-15.565	-0.2610	2.513	0.976	74.38	1.247
59.91	100	-6.83E-05	-6.330	-0.1057	-2.33E-05	-15.652	-0.2614	2.473	0.976	74.79	1.249
59.91		-5.48E-05	-6.312	-0.1058	-9.97E-06	-15.589	-0.2614	2.470	0.976	74.49	1.249
59.91	200	-8.88E-05	-6.578	-0.1099	-5.85E-05	-15.681	-0.2619	2.384	0.976	74.93	1.251
59.91	300	-9.73E-03	-6.625	-0.1107	-6.14E-05	-15.693	-0.2621	2.369	0.976	74.99	1.252
59.90	400	-8.24E-05	-6.640	-0.1109	-2.69E-05	-15.698	-0.2622	2.364	0.976	75.01	1.253
59.90	500	-8.50E-05	-6.644	-0.1110	-3.42E-05	-15.696	-0.2621	2.362	0.976	75.00	1.252
59.90	600	-8.95E-05	-6.619	-0.1110	-2.64E-05	-15.650	-0.2625	2.364	0.976	74.78	1.254
59.90	700	-9.77E-05	-6.621	-0.1110	-2.02E-05	-15.657	-0.2626	2.365	0.976	74.82	1.255
59.91	800	-1.17E-04	-6.618	-0.1110	-1.74E-05	-15.664	-0.2626	2.367	0.976	74.85	1.255
59.90	900	-1.50E-04	-6.615	-0.1109	-2.32E-05	-15.666	-0.2626	2.368	0.976	74.86	1.255

Table 5.4: Monitor chamber voltage scan for 3 mA of tube current.

kV	Monitor				PTW			PTW/MON	Corr. Fact.	K_{air} (μGy)	K_{rate} ($\mu\text{Gy/s}$)
	Bias (V)	bsl (V)	Integral (Vs)	Signal (V)	bsl (V)	Integral (Vs)	Signal (V)				
59.75	50	-3.37E-05	-7.316	-0.1221	-1.39E-05	-21.868	-0.3652	2.989	0.971	103.96	1.736
59.75		-4.54E-05	-7.347	-0.1227	-2.71E-05	-22.000	-0.3675	2.994	0.971	104.59	1.747
59.74	70	-5.39E-05	-8.197	-0.1374	-1.87E-05	-22.027	-0.3694	2.687	0.971	104.72	1.756
59.74		-5.93E-05	-8.227	-0.138	-1.87E-05	-22.098	-0.3760	2.686	0.971	105.05	1.788
59.74	90	-6.45E-05	-8.730	-0.1464	-2.64E-05	-22.172	-0.3719	2.540	0.972	105.51	1.770
59.74		-7.33E-05	-8.760	-0.1470	-1.84E-05	-22.240	-0.3729	2.539	0.972	105.84	1.775
59.74	100	-6.24E-05	-8.960	-0.1496	-5.38E-05	-22.347	-0.3733	2.494	0.972	106.35	1.777
59.73		-5.65E-05	-8.942	-0.1499	-1.84E-05	-22.289	-0.3738	2.493	0.972	106.07	1.779
59.72	200	-8.14E-05	-9.472	-0.1582	-3.39E-05	-22.362	-0.3735	2.361	0.972	106.42	1.777
59.73		-6.57E-05	-9.475	-0.1589	-4.87E-05	-22.307	-0.3741	2.354	0.972	106.16	1.780
59.73	300	-8.51E-05	-9.554	-0.1603	-3.52E-05	-22.329	-0.3744	2.337	0.973	106.37	1.784
59.73		-8.91E-05	-9.580	-0.1608	-4.70E-05	-22.333	-0.3750	2.331	0.973	106.39	1.786
59.73	400	-8.40E-05	-9.647	-0.1611	-3.04E-05	-22.466	-0.3752	2.329	0.973	107.02	1.787
59.73		-7.35E-05	-9.630	-0.1616	-3.15E-05	-22.387	-0.3756	2.325	0.973	106.65	1.789
59.74	500	-6.06E-05	-9.636	-0.1616	-8.10E-06	-22.426	-0.3761	2.327	0.973	106.83	1.792
59.73		-9.09E-05	-9.659	-0.1620	-2.69E-05	-22.427	-0.3761	2.322	0.973	106.84	1.792
59.73	600	-8.32E-05	-9.653	-0.1619	-1.28E-05	-22.455	-0.3766	2.326	0.973	106.97	1.794
59.72		-9.06E-05	-9.676	-0.1623	-2.76E-05	-22.476	-0.3769	2.323	0.974	107.18	1.797
59.71	700	-9.76E-05	-9.671	-0.1622	-1.71E-05	-22.463	-0.3767	2.323	0.974	107.12	1.796
59.75		-8.12E-05	-9.749	-0.1628	1.36E-05	-22.665	-0.3786	2.325	0.974	108.08	1.805
59.78	800	-1.05E-04	-9.718	-0.1630	-1.58E-05	-22.721	-0.3810	2.338	0.974	108.35	1.817
59.70		-1.14E-04	-9.790	-0.1635	-2.80E-05	-22.855	-0.3817	2.335	0.975	109.10	1.822
59.78	900	-1.24E-04	-9.742	-0.1634	-1.33E-05	-22.779	-0.3820	2.338	0.975	108.74	1.824
59.78		-1.34E-04	-9.799	-0.1636	-6.96E-06	-22.893	-0.3822	2.336	0.975	109.28	1.824

Table 5.5: Monitor chamber voltage scan for 4 mA of tube current.

kV	Monitor				PTW			PTW/MON	Corr. Fact.	K_{air} (μGy)	K_{rate} ($\mu\text{Gy/s}$)
	Bias (V)	bsl (V)	Integral (Vs)	Signal (V)	bsl (V)	Integral (Vs)	Signal (V)				
59.62	50	-1.94E-05	-9.286	-0.1563	-3.30E-05	-30.488	-0.5094	3.283	0.975	145.54	2.432
59.63		-6.11E-05	-9.409	-0.1577	-6.20E-05	-30.407	-0.5098	3.232	0.975	145.15	2.434
59.63	70	-5.39E-05	-10.879	-0.1825	-2.97E-05	-30.473	-0.5111	2.801	0.975	145.47	2.440
59.63		-7.46E-05	-10.936	-0.1826	-4.91E-05	-30.608	-0.5116	2.799	0.975	146.11	2.442
59.62	90	-5.83E-05	-11.762	-0.1964	-4.20E-05	-30.649	-0.5119	2.606	0.976	146.46	2.446
59.63		-7.25E-05	-11.720	-0.1965	-4.19E-05	-30.534	-0.5121	2.605	0.976	145.91	2.447
59.62	100	-8.18E-05	-12.005	-0.2013	-3.62E-05	-30.560	-0.5124	2.546	0.976	146.03	2.449
59.63		-6.25E-05	-12.068	-0.2015	-5.32E-05	-30.720	-0.5131	2.546	0.976	146.80	2.452
59.63	200	-8.60E-05	-12.998	-0.2171	-4.77E-05	-30.740	-0.5134	2.365	0.976	146.89	2.453
59.63		-9.07E-05	-13.046	-0.2179	-6.70E-05	-30.779	-0.5141	2.359	0.976	147.08	2.457
59.63	300	-9.19E-05	-13.208	-0.2206	-3.41E-05	-30.815	-0.5146	2.333	0.977	147.40	2.462
59.63		-8.87E-05	-13.184	-0.2211	-5.32E-05	-30.664	-0.5143	2.326	0.977	146.68	2.460
59.63	400	-1.10E-04	-13.277	-0.2218	-3.27E-05	-30.812	-0.5146	2.321	0.977	147.39	2.462
59.62		-8.60E-04	-13.256	-0.2223	-3.01E-05	-30.725	-0.5153	2.318	0.977	146.97	2.465
59.62	500	-9.84E-05	-13.324	-0.2226	-2.61E-05	-30.859	-0.5154	2.316	0.977	147.61	2.465
59.63		-9.49E-05	-13.359	-0.2231	-4.22E-05	-30.516	-0.5159	2.284	0.977	145.97	2.468
59.62	600	-1.33E-04	-13.342	-0.2228	-4.88E-05	-30.898	-0.5159	2.316	0.977	147.80	2.468
59.62		-1.07E-01	-13.312	-0.2233	-6.62E-05	-30.785	-0.5163	2.313	0.978	147.41	2.472
59.62	700	-1.05E-04	-13.360	-0.2232	-3.24E-05	-30.916	-0.5164	2.314	0.978	148.03	2.473
59.62		-9.96E-05	-13.331	-0.2235	-4.80E-05	-30.798	-0.5164	2.310	0.978	147.47	2.473
59.61	800	-1.20E-04	-13.358	-0.2233	-2.75E-05	-30.903	-0.5167	2.313	0.979	148.12	2.477
59.62		-1.35E-04	-13.391	-0.2236	-3.93E-05	-30.965	-0.5171	2.312	0.979	148.42	2.479
59.62	900	-1.43E-04	-13.322	-0.2235	-3.92E-05	-30.828	-0.5171	2.314	0.979	147.76	2.479
59.62		-1.41E-04	-13.353	-0.2240	-6.26E-05	-30.885	-0.5181	2.313	0.979	148.04	2.483

Table 5.6: Monitor chamber voltage scan for 5 mA of tube current.

kV	Monitor				PTW			PTW/MON	Corr. Fact.	K_{air} (μGy)	K_{rate} ($\mu\text{Gy/s}$)
	Bias (V)	bsl (V)	Integral (Vs)	Signal (V)	bsl (V)	Integral (Vs)	Signal (V)				
59.46	50	-4.30E-05	-11.435	-0.1922	-5.23E-05	-39.728	-0.6637	3.474	0.979	190.42	3.181
59.46		-5.54E-05	-11.541	-0.1935	-6.70E-05	-39.638	-0.6648	3.435	0.980	190.19	3.190
59.46	70	-6.12E-05	-13.620	-0.2284	-4.76E-05	-39.689	-0.6657	2.914	0.980	190.43	3.194
59.46		-7.85E-05	-13.698	-0.2287	-5.66E-05	-39.909	-0.6665	2.913	0.980	191.49	3.198
59.45	90	-6.80E-05	-14.882	-0.2496	-3.09E-05	-39.740	-0.6665	2.670	0.980	190.68	3.198
59.46		-5.99E-05	-14.966	-0.2499	-5.37E-05	-39.963	-0.6674	2.670	0.980	191.75	3.202
59.47	100	-5.90E-05	-14.756	-0.2502	-1.82E-05	-38.256	-0.6488	2.593	0.981	183.74	3.116
59.47		-5.97E-05	-15.110	-0.2534	-2.69E-05	-39.186	-0.6573	2.593	0.986	189.17	3.173
59.47	200	-7.66E-05	-16.667	-0.2797	-5.84E-05	-39.437	-0.6615	2.366	0.986	190.38	3.193
59.47		-7.09E-05	-16.767	-0.2812	-5.17E-05	-39.544	-0.6633	2.358	0.986	190.90	3.202
59.40	300	-9.34E-05	-17.101	-0.2857	-3.61E-05	-39.482	-0.6595	2.309	0.986	190.60	3.184
59.40		-6.37E-05	-17.101	-0.2868	-3.04E-05	-39.398	-0.6608	2.304	0.986	190.19	3.190
59.39	400	-6.64E-05	-17.292	-0.2889	-3.53E-05	-39.614	-0.6616	2.291	0.986	191.23	3.194
59.40		-7.89E-05	-17.274	-0.2897	-3.76E-05	-39.543	-0.6631	2.289	0.986	190.89	3.201
59.40	500	-1.07E-04	-17.380	-0.2903	-4.33E-05	-39.741	-0.6637	2.287	0.984	191.46	3.197
59.40		-1.07E-04	-17.332	-0.2910	-4.69E-05	-39.563	-0.6643	2.283	0.984	190.60	3.200
59.39	600	-1.29E-04	-17.438	-0.2913	-4.55E-05	-39.814	-0.6649	2.283	0.983	191.62	3.200
59.40		-1.33E-04	-17.406	-0.2919	-5.66E-05	-39.712	-0.6661	2.282	0.984	191.32	3.209
59.40	700	-1.47E-04	-17.480	-0.2920	-6.46E-05	-39.903	-0.6664	2.283	0.983	192.04	3.207
59.40		-1.31E-04	-17.518	-0.2926	-4.36E-05	-39.958	-0.6673	2.281	0.983	192.31	3.212
59.40	800	-1.40E-04	-17.430	-0.2923	-5.56E-05	-39.771	-0.6671	2.282	0.983	191.41	3.211
59.41		-1.57E-04	-17.740	-0.2931	-5.39E-05	-39.850	-0.6685	2.246	0.983	191.79	3.217
59.40	900	-1.59E-04	-17.463	-0.2929	-2.45E-05	-39.878	-0.6687	2.284	0.983	191.92	3.218
59.41		-1.67E-04	-17.567	-0.2934	-8.11E-05	-40.080	-0.6694	2.282	0.983	192.90	3.222

Conclusions

This work showed the assembly and the complete qualification, under a metrological point of view, of an X-ray tube together with all the necessary equipment to build an irradiation line able to make tests and experiments on several devices using the spectra of N-series of ISO 4037.

The assembling phase represented the practical application of the theoretical background of this PhD work (Part I - Chapter 1, 2 and 3): the installing and assembling of the X-ray unit and its HV generator, the preparation of the rooms for the research activity and setting up the measurement equipment were successfully done in order to study and to deeply characterize this X-ray irradiation facility.

The characterization and the qualification under a metrological point of view (Part II), following the recommendations of ISO 4037, showed the main characteristics and features of this irradiation line.

The custom monitor ionization chamber (Chapter 4) to measure and to control the time-dependant output of the X-ray tube was designed and developed at the beginning of this work. This ion chamber was always operative as monitor of the X-ray tube during all the PhD period, performing successfully its main function.

The qualification was based to investigate the main figures of merit and features of the irradiation line.

- The tube focus position was determined to have a proper and precise reference point (Chapter 5).
- It was possible to go back to the first and second HVL values (Chapter 6), which are listed in Table 6-3 and Table 6-4, together with the homogeneity coefficient. As shown, the accordance between theory and experiment is very good: the discrepancy is less than about 5%. This proves that with the choice of these kiloVolt- filtration combinations written in the tables is possible to achieve well-identified radiation qualities, as specified by relevant international standards. These are the quasi monochromatic spectra of the N series, the narrow series of ISO 4037, useful as calibrating reference.
- The total field variability (Chapter 7) is about 11% within a central region of 8 cm radius. This area corresponds to the most important region where the air kerma measurements are usually taken by PTW chamber. The two different measurement techniques - Gafchromic and Si detector - agree as can be observed in Figure 7.10, Figure 7.11, Figure 7.12 and Figure 7.13). The global variability is confirmed also in these plots.
- The measurements by Si and CdTe led a role for having a reasonable idea of the spectral components in addition to the quality measurements of HVLs: in particular of the continuum shape of bremsstrahlung spectrum and the endpoint energies. Considering the typical distortions of these semiconductor detectors, good interpretations on the resulting spectra was explained in Chapter 8.

Thanks to the physical qualification of the X-ray tube under a metrological point of view, it was possible to use this irradiation facility as test bench for the development and type testing (study on energy and angular response) of a semiconductor-based prototype of an eye-lens dosimeter developed during this PhD work (Part III - Chapter 9). The results of this dosimeter development show that it is possible to measure the dose quantity $H_p(3)$ with a silicon-based dosimeter covered by a proper filter. The filter allows to flatten the detector response and to fulfil the requirements given in IEC 62387 2012 with a good choice as reference energy. This innovative part of my PhD work represented a R&D study on a need for operational dosimetry.

Bibliography

- A. Endo. «Operational quantities and new approach by ICRU.» *ICRP Annals*, 2015: 178-187.
- A. Tomal, J.C. Santos, P.R. Costa, A.H. Lopez Gonzales, M.E. Poletti. «Monte Carlo simulation of the response functions of CdTe detectors to be applied in X-ray spectroscopy.» *Applied Radiation and Isotopes* 100, 2015: 32-37.
- Amptek, R. Redus,. *CdTe Measurement of X-ray Tube Spectra: Escape Events, Application Note ANCDTE1 Rev A1*. 04 02 2008. <https://www.amptek.com/internal-products/cdte-measurement-of-x-ray-tube-spectra-escape-events> (consultato il giorno 07 5, 2019).
- Bartolomeo, A.Di. «Master in Verifiche di Qualità in Radiodiagnostica, Medicina Nucleare e Radioterapia.» 2007.
- Behrens, R. «Monitoring the Eye Lens.» Paper to talk presentation at IRPA13, Glasgow, 2012.
- Bordy J.M., et al. «Proposals for the type tests and calibration methodology of passive eye lens dosimeters in interventional cardiology and radiology workplaces.» *Radiat. Meas.* 46 (11), 2011: 1235-1238.
- Bordy, J.-M. «Monitoring of eye lens doses in radiation protection.» *Radioprotection* 50(3), 2015: 177-185.
- Chodick, G., et al. «Risk of cataract after exposure to low doses of ionizing radiation: a 20 year prospective color study among US radiologic technologists.» *Am J. Epidemiol.* 168, 2008: 620-631.
- Ciraj-Belac, O., Rehani, M., Sim, K., Liew, H., Vano, E., Kleiman, N. «Risk for radiation-induced cataract for staff in interventional cardiology: is there reason for concern?» *Catheterization and Cardiovascular Interventions* 76 (6), 2010. 826-834.
- D.R. Dance, S. Christofides, A.D.A. Maidment, I.D. McLean, K. H. Ng. *Diagnostic radiology physics : a handbook for teachers and students*. Wien: International Atomic Energy Agency (IAEA), 2014.
- Dalba, Giuseppe. *La Fisica dei Raggi X*. Università di Trento: Dipartimento di Fisica, a.a. 1999-2000.
- Daures J., et al.,. «Conversion coefficients from air kerma to personal dose equivalent Hp(3) for eye-lens dosimetry, ISSN-0429-3460,» *CEA-R-6235 Saclay, France*, 2009.
- Daures J., et al.,. «Monte Carlo determination of the conversion coefficients Hp(3)/Ka in a right cylinder phantom with penelope code. Comparison with "mcnp" simulations.» *Radiat. Prot. Dosim.* 144 (1-4), 2011: 37-42.
- Di Castro, E., Pani, R., Pellegrini, R., Bacci, C.,. «The use of cadmium telluride detectors for the qualitative analysis of diagnostic X-ray spectra.» *Phys. Med. Biol.* 29 (9),, 1984: 1117-1131.
- Dietze, G. «Dosimetric Concepts and Calibration of Instruments.» 2019.
<http://www.irpa.net/irpa10/pdf/E03.pdf> (consultato il giorno 07 06, 2019).
- E. Till, M. Zankl, G. Drexler. «Angular dependence of depth dose in a tissue slab irradiated with monoenergetic photons.» Neuhenberg, Germany: GSF-National Research Centre for the Environment and Health, 1995.
- «EURATOM.» *Basic Safety Standards for protection against the dangers arising from exposure to ionizing radiation*. European directive 2013/59, 2013.

- «European Commission.» *Council Directive 96/29 EURATOM of 13 May 1996 laying down basic safety standards for the protection of health of workers and the general public against dangers arising from ionizing radiation.* Official Journal 159, 1-114., 1996.
- Grodzins L., Grodzins H. *X-ray fluorescence analyzer.* 2002.
- Gualdrini G., et al. «A new cylindrical phantom for eye lens dosimetry development.» *Radiat. Meas.* 46, 2011: 1231-1234.
- Gualdrini G., et al. «Air kerma to Hp(3) conversion coefficients for photons from 10 keV to 10 MeV, calculated in a cylindrical phantom.» *Radiat. Prot. Dosim.* 154 (4), 2013: 517-521.
- Guy. *The principle of Medical Imaging.* IV edition. Brescia: Pippo, 2000.
- H. Stadtmann, C. Hranitzky. «Test and optimization of two routine dosimeters for the dose quantity Hp(3).» *Radiation Measurements* 71, 2014: 451-455.
- Hendee, William R., e E. Russell Ritenour. *Medical Imaging Physics.* New York: Wiley-Liss Inc., 2002, Fourth edition.
- IAE X-ray tubes RTC000. 2019. <https://www.iae.it/product-details/rtc1000/#characteristics> (consultato il giorno 06 29, 2019).
- IAEA. *Calibration of radiation protection monitoring.* Vol. Safety Reports Series No. 16. Vienna: International Atomic Energy Agency, 2000.
- «ICRP 2011» *Statement on Tissue Reactions.* ICRP Reference 4823-3093-1464, 2011.
- «ICRP 103» *The 2007 Recommendations of the International Commission on Radiological Protection, vol. 103.* Vol. Volume 37/2-4, 2008. ICRP Publication. Ann. ICRP 37 (2-4), 2007.
- «ICRP 118» *ICRP on tissue reactions/early and late effects of radiation in normal tissues and organs - threshold doses for tissue reactions in radiation protection context.* ICRP 41(1/2), 2012.
- «ICRP 74» *Conversions coefficients for use in radiological protection against external radiation.* Publication 74. Ann. ICRP 26 (3/4), 1996.
- «ICRP 85» *Avoidance of Radiation Injuries from Medical Interventional, vol. 85.* ICRP Publication. Ann. ICRP 30 (7-67), 2000.
- «ICRP publication 116» *Conversion coefficients for radiological protection quantities for external radiation exposures.* ICRP, 2010.
- «ICRP publication 60» *International Commission on Radiological Protection, 1991. 1990 Recommendations of the International Commission on Radiological Protection.* Oxford, United Kingdom: Pergamon Press, 1991.
- «ICRP publication 74» *Conversion coefficients for use in radiological Conversion coefficients for use in radiological.* ICRP, 1995.
- «ICRU 39» *Determination of dose equivalents resulting from external radiation sources.* Bethesda: ICRU, 1985.
- «ICRU 51» *ICRU Report 51 - Quantities and Units in Radiation Protection Dosimetry.* Bethesda: ICRU, 1993.
- «ICRU 84» *Reference data for the validation of doses from cosmic-radiation exposure of aircraft crew.* J. ICRU 10(2), 2010.

- «ICRU 85» *Fundamental quantities and units for ionizing radiation (revised)*. Oxford University Press, October 2011.
- «ICRU report 43» *Determination of dose equivalents from external radiation sources- Part 2*. Bethesda, 1988.
- «ICRU report 47» *Measurement of dose equivalent from external photons and electron radiations*. Bethesda, 1992.
- «ICRU report 57» *Conversion coefficients for use in radiological protection against external radiation*. ICRU, Bethesda, 1995.
- «IEC 62387» *Radiation protection instrumentation - Passive integrating dosimetry systems for environmental and personal monitoring*. 2012.
- «ISO 12794» *Individual thermo luminescence dosimeters for extremities and eyes*. ISO, Geneva, 2000.
- «ISO 14146» *Criteria and performance limits for the periodic evaluation of processors of personal dosimeters for X and gamma radiation*. ISO, Geneva, 2000.
- «ISO 15382» *Radiological protection - Procedures for monitoring the dose to the lens of the eye, the skin and the extremities*. International Standard, 2015.
- «ISO 29661» *Reference radiation fields for radiation protection - Definitions and fundamental concepts*. ISO, Geneva, 2012.
- «ISO 4037-1» *X and gamma reference radiation for calibrating dosimeters and dose rate meters and for determining their response as a function of photon energy – Part 1: Radiation characteristics and production methods*. International organization for standardization, 2016.
- «ISO 4037-3» *Radiological protection - X and gamma reference radiation for calibrating dosimeters and dose rate meters and for determining their response as a function of photon energy - Part 3*. International Standard, 01 2019.
- J. P. McCaffrey, H. Shen, B. Downton, E. Mainegra-Hing. «Radiation attenuation by lead and nonlead materials used in radiation shielding garments.» *Medical Physics*, Vol. 34, No. 2, , February 2007: 530-537.
- J. T. Bushberg, J. A. Seibert, E. M. Leidholdt Jr., J. M. Boone. *The Essential Physics of Medical Imaging*. Philadelphia: LIPPINCOTT WILLIAMS & WILKINS, a WOLTERS KLUWER business, 2012.
- J.P. Seuntjens, W. Strydom, K. R. Shortt. *Review of Radiation Oncology Physics: A Handbook for Teachers and Students*. n.d.
- Johns, e Cunningham. *The Physics of radiology*. s.d.
- Junk, A.E., Kyrychenko, O.Y., Musijachenko, N.V., et al. «Risk of cataract after exposure to low doses of ionizing radiation: a 20-Year prospective cohort study among US.» *Radiologic Technologists American Journal of Epidemiology* 168 (6), 2008. 620-631.
- K. Neriishi, E. Nakashima, A. Minamoto, S. Fujiwara, M. Akahoshi, H. K. Mishima, T. Kitaoka, and R. E. Shore. «Postoperative cataract cases among atomic bomb survivors: Radiation dose response and threshold.» *Radiation Research*, 2007: 168(4):404-408; doi: <http://dx.doi.org/10.1667/RR0928.1>.
- Kim, K.P., Miller, D.L. «Minimising radiation exposure to physicians performing fluoroscopically guided cardiac catheterisation procedures: a review.» *Radiat. Prot. Dosim.* 133 (4), 2009: 227-233.

- Kim, K.P., Miller, D.L., Balter, S., Kleinerman, R.A., Linet, M.S., Kwon, D., Simon, S.L. «Occupational radiation doses to operators performing cardiac catheterization procedures.» *Health Phys.* 94 (3), 2008: 211-227.
- Kutkov, Vladimir. *Dosimetry for Use in Preparedness and Response to Radiological and Nuclear Emergency*. 3 October 2018. <https://www.intechopen.com/online-first/dosimetry-for-use-in-preparedness-and-response-to-radiological-and-nuclear-emergency> (consultato il giorno 07 24, 2019).
- L. T. J. Chylack, L. E. Peterson, A. H. Feiveson, M. L. Wear, F. Keith Manuel, W. H. Tung, D. S. Hardy, L. J. Marak, and F. A. Cucinotta. «NASA Study of Cataract in Astronauts (NASCA). Report 1: Cross-Sectional Study of the Relationship of Exposure to Space Radiation and Risk of Lens Opacity.» *Radiation Research.*, 2009.: 172(1):10-20; doi: <http://dx.doi.org/10.1667/RR1580.1>.
- Lutz, Gerhard. *Semiconductor Radiation Detectors. Device Physics*. Springer, 1999.
- Mariotti F., et al. «ORAMED project eye-Lens dosimetry, a new Monte Carlo approach to define the operation quantity Hp(3).» *RT/2009/1/BAS ENEA Rome*, 2009: ISSN/0393-3016.
- Markowicz, A. «X-ray physics.» In *Handbook of X-ray Spectrometry, 2nd Edition*, di A. Markowicz, 58. R.A. Van Grieken, A.A. Markowicz, Marcel Dekker, 2002.
- Martin, C.J. «A review of radiology staff doses and dose monitoring requirements.» *Radiat. Prot. Dosim.* 136 (3), 2009: 140-157.
- Matsumoto, M., Yamamoto, A., Honda, I., Taniguchi, A., Kanamori, H.,. «Direct measurement of mammographic X-ray spectra using a CdZnTe detector.» *Med.Phys.* 27 (7), 2000: 1490–1502.
- Medical, Integrity. *GE OEC 9900 Elite 12" Vascular MTS C-Arm*. 2019. <https://integritymed.com/product/ge-oec-9900-elite-12-vascular-mts-c-arm> (consultato il giorno 07 12, 2019).
- Miyajima, S., Imagawa, K.,. «CdZnTe detector in mammographic X-ray spectroscopy.» *Phys.Med.Biol.*47(22), 2002: 3959–3972.
- Nakashima, E., Neriishi, K., Minamoto, A. «A reanalysis of atomic-bomb cataract data, 2000-2002: a threshold analysis.» *Health Phys.* 90, 2006: 154-60.
- National Nuclear Data Center, NuDat 2 database*. 2019. <http://www.nndc.bnl.gov/nudat2/> (consultato il giorno 06 30, 2019).
- P. Bilsky, et al.,. «The new eye-dTM dosimeter for measurements of Hp(3) for medical staff.» *Radiat. meas.* 46 (11), 2011: 1239-1242.
- Papadopoulos, C. *Solid-State Electronic Device, an Introduction*. 2014.
- Paulo Márcio C. Oliveira, Peterson L. Squair, Maria do S. Nogueira, Teógenes A. da Silva. «Uniformity and field size of filtered X-ray beams.» *2007 International Nuclear Atlantic Conference - INAC 2007*, 2007: 978-85-99141-02-1.
- R. Behrens, G. Dietze. «Dose conversion coefficients for photon exposure of the human eye lens.» *Phis. Med. Biol.* 56, 2011: 415-437.
- R. Redus, J. Pantazis, T. Pantazis, A. Huber, B. Cross. «Characterization of CdTe Detectors for Quantitative X-ray Spectroscopy.» *IEEE Trans Nucl Sci*, 2008.
- Radiology C. - Mammography*. 2019. <https://www.radiologycafe.com/radiology-trainees/frcr-physics-notes/mammography> (consultato il giorno 08 28, 2019).

- Radiopaedia - Heel effect*. 2019. <https://radiopaedia.org/articles/anode-heel-effect> (consultato il giorno 06 28, 2019).
- Radiopaedia - Space charge*. 28 06 2019. <https://radiopaedia.org/articles/space-charge>.
- Radiopaedia - Space charge*. 2019. <https://radiopaedia.org/articles/space-charge> (consultato il giorno 06 28, 2019).
- «Real Decreto 783/2001» *Real Decreto 783/2001, de 6 de julio, por el que se aprueba el Reglamento sobre proteccion sanitaria contra radiaciones ionizantes*. BOE 178, 2001., 6 07 2001.
- S. B. Gudennavar, Daisy Joseph, Bubbly sg. «K β to K α Intensity Ratio and Total Vacancy Transfer Probabilities of Molybdenum and Silver.» *Universal Journal of Physics and Application* 1(2), 2013: 83-87.
- Shah, M.R. Squillante and K.S. «Other Materials: Status and Prospects, Chap 12 in Semiconductors for Room Temperature Nuclear Detector Applications.» In *Other Materials: Status and Prospects, Chap 12 in Semiconductors for Room Temperature Nuclear Detector Applications*, di M.R. Squillante and K.S. Shah, 470. T.E. Schelsinger and R.B. James, Academic Press, 1995.
- Sordo, S. Del. «Progress in the Development of CdTe and CdZnTe Semiconductor Radiation Detectors for Astrophysical and Medical Applications.» *Sensors* 9, 2009: 3491–3526.
- Tadayuki Takahashi, Shigeto Watanabe. *Recent progress in CdTe and CdZnTe detectors, Research Gate*. 2019. Linear attenuation coefficients for photo absorption and Compton scattering in Si and other detector materials. (consultato il giorno 08 11, 2019).
- Thom T., et al. «Heart disease and stroke statistics 2006 updated a report from the American Heart Association Statistics Committee and Stroke Statistics Subcommittee.» *Circulation* 113, 2006: E85-E151.
- Togni, M., Balmer, F., Pfiffner, D., Meier, W., Zeiher, A.M., Meier, B. «Percutaneous coronary interventions in Europe 1999-2001.» *Eur. Heart J.* 25, 2004: 1208-1213.
- Vanhavere, F., Carinou, E., Donadille, L., Ginjaume, M., Jankowski, J., Rimpler, A., Sans Merce, M. «An overview on extremity dosimetry in medical applications.» *Radiat. Prot. Dosim.* 129 (1-3), 2008: 350-355.
- Vañó, E., González, L., Guibelalde, E., Fernández, J.M., Ten, J.I. «Radiation exposure to medical staff in interventional and cardiac radiology.» *Brit. J. Radiol.* 71, 1998: 954-960.
- Vano, E., Kleiman, N., Duran, A., Rehani, M., Echeverri, D., Cabrera, M. «Radiation cataract risk in interventional cardiology.» *Radiation Research* 174 (4), 2010. 490-495.
- Worgul, B.V., Kundiyeu, Y.I., Sergiyenko, N.M., Chumak, V.V., et al. «Cataracts among Chernobyl clean-up workers: implications regarding permissible eye exposures .» *Radiation Research* 167, 2007: 233-243.

Ringraziamenti

Per la sempre generosa ospitalità, per l'utile e valido confronto scientifico e accademico, ringrazio il Professor Carles Domingo Miralles: il suo sostegno è stato sicuramente importante per il completamento di questo progetto di dottorato.

Ringrazio il Dottor Roberto Bedogni per avermi seguito durante lo svolgimento di questo lavoro, che ha rappresentato l'occasione di completare la mia formazione e il mio percorso di studi presso i Laboratori Nazionali di Frascati dove, all'interno del suo gruppo e del suo laboratorio, ho potuto condurre attività sperimentale in modo sempre vario e istruttivo.

Il ringraziamento più importante e più grande va a Mariele che, più di chiunque altro, mi è stata vicina in ogni occasione, dandomi sempre la forza, l'aiuto e la serenità necessari per superare qualsiasi difficoltà, spesso a scapito dei suoi impegni: hai rappresentato un confronto fondamentale e illuminante per le questioni tecniche e scientifiche, oltre ad essere la ragazza premurosa, attenta e dolce che ogni ragazzo desidererebbe accanto a sé. Grazie a te sono riuscito a portare a termine questo progetto, di cui sei stata parte fondamentale ed essenziale.

L'altra persona che devo certamente ringraziare per la partecipazione attiva nelle misure e nelle attività di questo progetto di dottorato è Oriol, collega e compagno di laboratorio durante l'esperienza a Frascati: grazie per la spensieratezza e la vivacità che sei sempre stato capace di portare in laboratorio, oltre all'aiuto e alla fantasia da "softwerista".

Un grazie speciale va sicuramente alla mia famiglia, in particolare ai miei genitori, che con affetto, impegno e dedizione mi hanno saputo instillare da sempre l'amore e la passione per lo studio, sostenendomi passo dopo passo fino al dottorato, senza mai farmi mancare il loro appoggio.

I miei amici, tutti in modo diverso e vario, hanno contribuito in maniera importante a non farmi mai mancare il loro prezioso sostegno. Gabriella, in particolare, ha rappresentato un saldo sostegno e, come sempre, si è dimostrata fonte di validi e accorti suggerimenti. A Stefano, Carlo, Irma, Jesse e Francesco vanno i miei ringraziamenti per aver condiviso insieme, durante serate di svago e lunghe conversazioni, momenti di riflessione su questo lavoro e su quest'ultima fatica accademica.

Ricordare e descrivere i vari momenti, che si conservano nel cuore e nella mente, non è semplice e non può essere sicuramente fatto nello spazio ristretto di una pagina. Nonostante la limitatezza di questi ringraziamenti, spero e confido che tutti sappiano quanto affetto e riconoscenza nutra verso le persone che, durante questi anni, mi hanno aiutato, ognuno in modo diverso e mai scontato. Grazie!